Title	Fundamental Investigation on Polishing of Internal Structures Made by Laser-based Powder Bed Fusion
Authors(s)	Shen, Mingyue
Publication date	2023
Publication information	Shen, Mingyue. "Fundamental Investigation on Polishing of Internal Structures Made by Laser-Based Powder Bed Fusion." University College Dublin. School of Mechanical and Materials Engineering, 2023.
Publisher	University College Dublin. School of Mechanical and Materials Engineering
Item record/more information	http://hdl.handle.net/10197/24890

Fundamental Investigation on Polishing of Internal Structures Made by Laser-based Powder Bed Fusion

By

Mingyue Shen, BEng, MEng

The thesis is submitted to University College Dublin

in fulfilment of the requirements for the degree of

DOCTOR OF PHILOSOPHY

IN

NATIONAL UNIVERSITY OF IRELAND,
UNIVERSITY COLLEGE DUBLIN,
COLLEGE OF ENGINEERING & ARCHITECTURE,
SCHOOL OF MECHANICAL & MATERIALS ENGINEERING.

Supervisor: Professor Fengzhou Fang

March 2023

Table of Contents

Abstract

This study aims at utilizing a self-developed hybrid polishing system to establish polishing capabilities of electropolishing (EP), abrasive fluid polishing (AFP), multiple polishing in different sequences and innovative hybrid polishing for the internal structures prepared by laser-based powder bed fusion (L-PBF). By studying polishing effects on various inner surfaces, the relationships between polishing processes and material removal mechanisms of L-PBF surface features are established considering microstructural differences of surface features. The thesis starts with a comprehensive introduction of the project and then a literature review outlining L-PBF process, application of typical L-PBF internal structures, surface characteristics, advantages and limitations of current polishing methods for L-PBF inner surfaces. Breakthroughs in the surface finish of L-PBF internal structures are required in order to improve surface quality to meet the specific requirements of product performance. It is notified that EP and AFP exhibit complementary advantages in the polishing of internal structures among various polishing technologies. In the chapter 3, different types of inner surfaces for fundamental investigation and typical internal structures for application development are designed, and prepared by L-PBF using 316L stainless steel and Ti6Al4V powders. Then, un-sintered powders and sintered area are characterized as common surface features on L-PBF top, face up, side and face down surfaces considering the differences of morphology and microstructure. Meanwhile, an innovative hybrid polishing system which could carry out EP, AFP, their multiple polishing and hybrid polishing is established for the surface improvement of the L-PBF inner surfaces and internal structures. In the chapter 4, a polishing mode consisting of two-step EP is developed by using different potentials and polishing time for L-PBF 316L stainless steel and Ti6Al4V inner surfaces after parametric study in the developed polishing system. Based on material removal characteristics of surface features, the effectiveness and high efficiency of the two-step EP are demonstrated. Considering polishing characteristics of AFP, the inlet design of polishing chamber is improved and the material removal process of various L-PBF internal surfaces are discussed by

analyzing the evolution of surface morphology, roughness and microstructure on cross sections in the chapter 5. In the chapter 6, multiple polishing in different sequences and hybrid polishing based on EP and AFP are investigated for L-PBF inner surfaces. It is found that L-PBF inner surfaces after single polishing can be further improved by multiple polishing in different sequences because of the complementary characteristics of EP and AFP in removing L-PBF surface features. In addition, hybrid polishing can perform EP and AFP simultaneously without interfering with each other, showing great potential in improving polishing efficiency of L-PBF inner surfaces. In the chapter 7, different polishing processes are applied to three typical L-PBF internal structures. The superiority of multiple polishing in different sequences and hybrid polishing for L-PBF inner structures is verified. Overall, it is confirmed that the self-developed innovative hybrid polishing system is capable of polishing various L-PBF internal structures with reliable results. Fundamental research on material removal characteristics of L-PBF surface features during polishing provides a theoretical basis for the applications of multiple and hybrid polishing based on EP and AFP. High efficiency and cost-effectiveness make the hybrid polishing system a strong candidate for industrial implementation in the surface finish of L-PBF internal structures.

Statement of Original Authorship

I hereby certify that this submitted thesis is my own work which was completed while registered as a candidate for the degree stated on the Title Page. I further declare that I have not obtained a degree elsewhere on the basis of the research presented in this submitted work.

Acknowledgement

List of Figures

List of Tables

List of Abbreviations

EP	Electropolishing
AFP	Abrasive fluid polishing
L-PBF	Laser-based powder bed fusion
AM	Additive manufacturing
CAD	Computer-aided design
AFM	Abrasive fluid machining
LAM	Laser additive manufacturing
LS	Laser sintering
LMD	Laser melting deposition
3D	Three-dimensional
FCC	Face centered cubic
VC	Vertex cube
ECC	Edge centre cube
MPB	Molten pool boundaries
SEM	Scanning electron microscopy
BCC	Body-centered cubic
MAF	Magnetic abrasive finishing
BF	Barrel finishing
CP	Chemical polishing
HCAF	Hydrodynamic cavitation abrasive finishing
ECMP	Electrochemical mechanical polishing
ECP	Electrochemical polishing
OECP	Overpotential electrochemical polishing
OM	Optical microscopy
LCPR	Limiting current density plateau region

Chapter 1 Introduction

1.1 Background & motivation

Delicate internal structures such as honeycomb with cellular structures and natural bone with gradient porosity are designed to achieve specific functions in the nature. In contemporary industries, metallic parts with internal structures such as curve channels [1] and lattice structures [2] are in high demand due to their advantages such as light weight, high cooling efficiency and superior energy absorption property [3, 4]. However, it is difficult, time-consuming and costly to apply traditional subtractive technologies to the fabrication of complex interior structures [5, 6]. Since the technique of additive manufacturing (AM) became available in the late 1980s [7], AM processes based on material incremental approaches have experienced rapid development in the subsequent decades. Among various AM technologies, laser-based powder bed fusion (L-PBF), also known as selective laser melting, is a process in which a laser beam with high power is used to scan a powder bed. With the help of computer-aided design (CAD), desired models with intricate structures can be fabricated layer by layer until the entire component is finished. Due to its advantages such as geometric freedom and high material utilization ratio, L-PBF is widely utilized in the fabrication of various materials and more preferable for the preparation of customized parts that require complex internal structures. It is worth noting that a majority of research work has focused on L-PBF titanium alloys, steel and nickel-based alloys, and some of which material and process combinations have reached maturity for practical applications [7]. Among various alloys, 316L stainless steel has been widely studied due to its excellent ductility, weldability, corrosion and oxidation resistance, biocompatibility, relatively low cost and various applications in different industries [8], while Ti6Al4V is known as the most commonly used titanium alloy which has a unique combination of strength, toughness and corrosion resistance, low specific weight and biocompatibility [9]. Thus, 316L stainless steel and Ti6Al4V have attracted a lot of attention and showed great application potential for their L-PBF internal structures [10-13]. Despite the advantages

of L-PBF, it still faces an apparent limitation in terms of poor surface quality which limits its applications in various industries.

Surface quality of L-PBF parts is generally inferior due to the adhesion of partially melted powders and rough sintered area related to the behavior of molten pool. Meanwhile, various effects such as gravity and staircase effect also influence the final surface of L-PBF components. Owing to the same deposition approach, internal and outer surfaces on L-PBF parts actually possess similar surface quality and features. Generally, surface roughness and morphology such as quantity of adhered powders could vary significantly with different deposition angles. Although the optimization of raw powders and process parameters could be helpful to reduce balling phenomena and surface defects, it is hard to eliminate the adhesion of powders and the unevenness of molten pools due to the use of powder bed and layer-by-layer principle of L-PBF. In fact, the characteristics of surface features are relevant to L-PBF process and require further characterization considering comprehensive differences in morphology, topography and microstructure. Furthermore, surface analysis of L-PBF internal structures also needs to consider the complexity of specific internal structure. Given that surface quality has significant influence on multiple functions, such as biological response, mechanical properties and fluid dynamics, it is crucial and in high demand to develop and apply appropriate polishing methods to improve the surface quality of L-PBF components with internal structures.

Numerous polishing technologies has been utilized to improve internal surface quality of L-PBF parts in recent years. Compared to outer surfaces that could use techniques such as milling and blasting for surface finish, it is more challenging to apply proper polishing process to improve the quality of interior surfaces. Traditional abrasive flow machining (AFM) has generally used on L-PBF inner surfaces [1]. In the meantime, techniques such as abrasive fluid polishing (AFP) [14], electropolishing (EP) [15] and hybrid polishing technologies [16-18] are gradually applied to enhance L-PBF interior surface quality. It is worth noting that these polishing methods have their own advantages and limitations in the polishing of L-PBF internal structures. Although obsessive attention has been paid to the improvement of internal surface quality, the

material removal mechanism of L-PBF surfaces during polishing has not been studied in-depth. For example, Zhang et al. [19] investigated the cross section of attached powders on L-PBF Inconel 718 alloy surface during EP and their results identified disparate material removal mechanisms of attached powders and half melted powders. However, the characterization of mechanical polished cross section could only distinguish different types of adhered powders, without considering microstructural differences in powders and sintered area as well as their impact on the EP process. Thus, it is typically necessary to investigate and establish the relationship between L-PBF surface features and their corresponding material removal mechanisms during polishing. In addition to surface features, the internal structures increase the difficulty of designing and establishing appropriate polishing equipment for L-PBF parts. More efforts should be devoted to the development of innovative polishing systems or machines in order to improve polishing efficiency and final surface quality of L-PBF internal structures.

In this thesis, fundamental investigation on polishing of various L-PBF inner surfaces using an innovative self-developed hybrid polishing system is presented. After the literature review, it is notified that EP and AFP have complementary advantages and show great potential to combine with each other to develop a new hybrid polishing process for L-PBF internal structures. Considering L-PBF process and application requirements, inner surfaces and structures of L-PBF 316L stainless steel and Ti6Al4V have been prepared. To facilitate the study, a hybrid polishing system combining EP and AFP has been established. By developing and using different types of environmentally friendly polishing media, the hybrid polishing system is capable of conducting EP, AFP, multiple polishing in different sequences and hybrid polishing for L-PBF internal structures. Considering the surface complexity of inner structures, L-PBF top, face up, side and face down inner surfaces with various deposition angels are designed and prepared for fundamental study. Surface features of L-PBF 316L stainless steel and Ti6Al4V are characterized considering the differences of morphology and microstructure. By using the developed hybrid polishing system, polishing process and material removal mechanism of EP and AFP on L-PBF internal

surfaces are investigated. Based on the analysis of EP and AFP, material removal process of L-PBF surface features during multiple polishing in different sequences and hybrid polishing are studied. Finally, typical L-PBF internal structures are polished for developing applications. The establishment of relationships between various L-PBF inner surfaces and polishing processes based on EP and AFP is crucial for the application of the developed polishing system in the polishing of internal structures such as lattice structures, thin-walled straight and conformal channels prepared by powder bed fused technologies.

1.2 Thesis layout

The thesis is accomplished in 8 chapters, including introduction, literature review, surface features and polishing system, fundamentals of EP, AFP, multiple and hybrid polishing respectively, application development and final conclusions. Following the present introductory chapter, the outline of the thesis is given as follows:

- **Chapter 2** provides a literature survey on advances in polishing of internal structures fabricated by L-PBF. Process, surface and polishing methods for L-PBF internal structures are comprehensively reviewed. The causes of poor surface quality and surface morphology of L-PBF inner structures are presented. Strength and weakness of various polishing technologies for L-PBF inner surfaces and structures are compared, along with a discussion of challenges for the improvement of interior surface quality on L-PBF parts.

- **Chapter 3** presents characterization of internal surface features and a developed hybrid polishing system for L-PBF internal structures. Designed CAD models and printing parameters of 316L stainless steel and Ti6Al4V are provided. Then, surface features on L-PBF top, face up, side and face down surfaces are characterized in detail considering differences of morphology and microstructure. Corresponding to the designed samples, an innovative polishing system combining EP and AFP is established to study the polishing of L-PBF inner surfaces and internal structures.

- **Chapter 4** studies EP process on various internal surfaces made by L-PBF 316L stainless steel and Ti6Al4V. Before performing EP on the hybrid polishing system, EP effects on flat L-PBF 316L stainless steel surfaces are studied using a conventional in-beaker EP system. Then, parameter optimization and material removal mechanism of various internal surfaces on L-PBF 316L stainless steel and Ti6Al4V during EP are studied using the developed hybrid polishing system.

- **Chapter 5** investigates AFP process on various internal surfaces made by L-PBF 316L stainless steel and Ti6Al4V. AFP parameters are optimized firstly and then utilized to L-PBF inner surfaces. The design of the inlet of polishing chamber could achieve uniform material removal along the whole polishing area in AFP. Material removal characteristics of L-PBF internal surface features during AFP is studied and analyzed in detail.

- **Chapter 6** presents multiple polishing in different sequences and hybrid polishing of EP and AFP on various internal surfaces made by L-PBF 316L stainless steel and Ti6Al4V. Based on the study in chapter 3 and 4, the material removal processes of multiple polishing and hybrid polishing are investigated. In addition, characteristics of single polishing and hybrid polishing for L-PBF inner surfaces are discussed.

- **Chapter 7** applies different polishing process to L-PBF straight channels with small inner diameter, lattice structures and conformal channels using the hybrid polishing system. Considering materials, inner surfaces and specific internal structures, polishing capabilities of multiple and hybrid polishing for different L-PBF internal structures are demonstrated.

- **Chapter 8** summarizes scientific and technological deliverables, gives the final remarks and recommendations for further research.

1.3 Original contribution

The work presents the following defenses of scientific novelty as the original contribution of this thesis:

- Develop a hybrid polishing system that can perform EP, AFP, multiple polishing in different sequences and innovative hybrid polishing for L-PBF internal structures on the same system.

- Characterize un-sintered powders and sintered area as common surface features for various L-PBF surfaces with different printing angles, providing analytical solutions for surface evaluation of L-PBF parts considering printing orientation and characteristic of specific structure.

- Study EP parameters and effects on various L-PBF inner surfaces in the hybrid polishing system that enables high-speed circulation of electrolytes, extending the possibility and applicability of EP and EP-based hybrid polishing to complex internal structures.

- Establish the relationships between material removal mechanism of L-PBF surface features and various polishing processes (EP, AFP, multiple and hybrid polishing), providing a theoretical basis for improving polishing efficiency and achieving flexible control of inner surface finish.

- Investigate characteristics of the innovative hybrid polishing on L-PBF inner surfaces, demonstrating that it can combine the advantages of single polishing and perform EP and AFP simultaneously without interfering with each other.

- Develop environmentally friendly electrolytes and polishing media for L-PBF 316L stainless steel and Ti6Al4V in the established hybrid polishing system.

Chapter 2. Literature Review

2.1 Introduction

Internal structures of metallic products are crucially important in realizing functional applications in various industries. For example, conformal cooling channels could improve cooling efficiency by achieving more uniform heat transfer in mould industry, while the design of lattice structure could reduce the weight of parts in aerospace and medical industries. Compared with traditional manufacturing technologies [20, 21], L-PBF is more attractive because of layer principle and no geometrical limitations in preparing parts with complex internal structures. Despite the advantages of L-PBF, it faces an apparent limitation in terms of poor surface quality. Considering that surface finish of products is important to real applications, it has high demand and is essential to achieve good surface finish of L-PBF internal structures in order to obtain satisfactory products with specific requirements.

The objective of this literature review is to understand the surface characteristics of L-PBF metallic parts and progress on polishing of L-PBF internal structures, as well as the research challenges and prospects. It presents the state of the art of the development of interior surface finish for L-PBF parts.

2.2 Process, internal structures and applications

2.2.1 L-PBF process

As a type of laser additive manufacturing (LAM) technology, L-PBF was developed from laser sintering (LS). Table 2.1 summarizes various LAM technologies according to their mechanisms. In general, materials are partially melted in LS due to the low energy input of laser. Hence, low melting point materials are used as binders to bond un-melted solid cores with high melting point during LS. As a result, LS components usually possess low density and inhomogeneous microstructure which means good combination of parameters and post-treatment such as hot isostatic pressure are essential to LS products [7, 22]. In comparison to LS, a more powerful laser is used in L-PBF, therefore L-PBF is capable of depositing fully dense parts with better

mechanical properties and surface finish. In terms of laser melting deposition (LMD), the powders are supplied by a coaxial feeding system that is completely different from the powder bed. Apart from powder supply, high power laser and large-size laser spot during LMD lead to large molten pools and result in higher surface roughness than L-PBF samples [7]. Thus, L-PBF is currently the preferred technology for manufacturing intricate components, especially those requiring complex internal geometries and good surface quality [5].

Table 2.1 Classification of various LAM processes.

Process	Mechanism	Powder supply
LS	Partial melting of powder	Pre-spreading of powder before laser scanning (Powder bed)
L-PBF	Complete melting of powder	Pre-spreading of powder before laser scanning (Powder bed)
LMD	Complete melting of powder	Coaxial powder feeding with synchronous laser scanning

Different from conventional subtractive manufacturing techniques, L-PBF is based on a material incremental manufacturing strategy. There are several steps from the virtual model creation to the finish of the three-dimensional (3D) object. In the first step, CAD model of the product is produced mathematically. Then, specialized software slices this model into cross-sectional layers, generates the tool path and sends the generated file to the L-PBF machine. Finally, the designed model can be fabricated layer by layer until the 3D component is completed. The schematic diagram of L-PBF apparatus is shown in Figure 2.1. A L-PBF apparatus generally consists of a laser, an automatic powder spreading system, a computer for the process control, an inert gas protection system and other accessorial systems such as substrate and powder bed preheating system [7, 23]. Before the printing process, the substrate is leveled and fixed on the building platform firstly in the L-PBF machine. Then, the protective inert gas is fed into the building chamber to reduce oxidation during L-PBF. After a thin layer of powder is spread on the substrate, the laser beam would melt the powders selectively according to the CAD model. Due to the alternate repetition of powder

spreading and laser processing, powders on the top layer are fused onto the previously melted layer until the part is finished [24]. As the energy of laser beam is high enough to melt the powder and form a molten pool, the rapid solidification of molten pools would leave sintered tracks on L-PBF surfaces after laser scanning. Generally, L-PBF parameters such as layer thickness, laser scanning speed and hatch spacing are adjusted for different printing materials [25]. In addition, the combination of various parameters is effective on the volumetric energy density of the laser-material interaction which is important for the microstructure and properties of final 3D products [26-29].
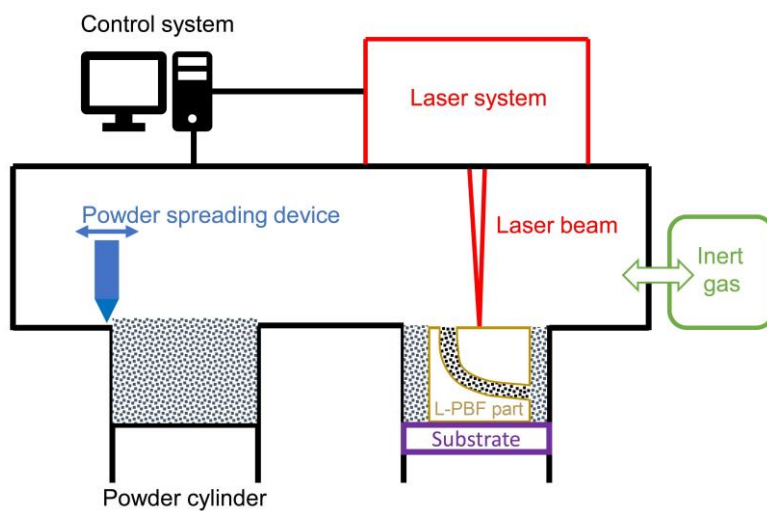
Figure 2.1 The schematic diagram of L-PBF apparatus.

Based on the rapid melting and solidification mechanism, the printing process is crucially relied on the behaviors of molten pool during L-PBF. As mentioned, a result of the interaction of powder bed and the high-powered laser is the forming of a molten pool. In general, the molten pool has a circular or segmental cylinder shape due to surface tension [30]. In order to reduce the surface energy, the molten area has the tendency to break up and therefore usually possesses an irregular geometry. Thus, process parameters and the properties of raw powders influence the behavior of molten pool significantly because molten region follows Plateau Rayleigh instability [31]. In addition, the shape of the molten area is also relevant to Marangoni convection [25]. Plateau Rayleigh instability suggests that liquid cylinders with high aspect ratio tend to fracture to reduce surface energy. It was found that the breakup time of metals

with a temperature above the melting temperature has a relationship with its geometry, surface tension, density and viscosity [31]. Apart from Plateau Rayleigh instability, Marangoni convection represents that the direction of a flow inside a molten pool depends on the gradient of fluid surface tension. If the flow is radially outward, a shallow and wide molten region can be formed while a deep and narrow molten area is generated when the flow is radially inward [32]. After laser scanning, molten pools generally experience rapid solidification and shrinkage with a cooling rate of 10^3 to 10^6 K/s [5]. The rapid cooling process leads to the phase transition in a non-equilibrium state which greatly affects the microstructure, mechanical properties and surface morphology of final L-PBF parts. In this way, L-PBF components can be fabricated through the melting, overlapping and solidification of molten pools [33].

The principle and mechanism of L-PBF make it an effective technology for preparing fully dense parts with complex internal structures. Moreover, based on the complete melting/ solidification mechanism [7], L-PBF has demonstrated the capability of manufacturing a wide range of materials such as titanium [34, 35], steel [36, 37], cobalt chrome [38], aluminum alloys [39-41], nickel based alloys [42, 43], hard alloys [44, 45], ceramics [46] and composites [47, 48]. Due to the expanded degrees of freedom in the design of functional features, objects with desired geometry and intricate structures are allowed to be prepared by L-PBF for various applications [6].

2.2.2 Basic forms of L-PBF internal structures

The development of L-PBF technology has expanded the degrees of freedom in designing and manufacturing 3D objects with complex internal structures in one fabrication process. Industrial components with complex inner geometry and structures such as hydraulic valve manifold [49], conformal cooling channels [1] and heat exchanger [50, 51] are currently prepared by L-PBF for various applications [13, 52, 53]. Despite the complexity of the interior structures of these products, they are usually composed of multiple basic forms. In general, channels and cellular structures are the two basic forms of L-PBF internal structures.

L-PBF is capable of fabricating straight and curve channels with different sizes and shapes of cross-section [54, 55]. In terms of straight channels with different deposition angles, the inner diameter or size may change gradually (Figure 2.2a and c). For a curve channel, the centerline of the channel is curved, where conformal channel is a passageway that follows the external shape or contour of the component [56, 57]. In addition, L-PBF is suitable for the preparation of complex channels (Figure 2.2b and d).
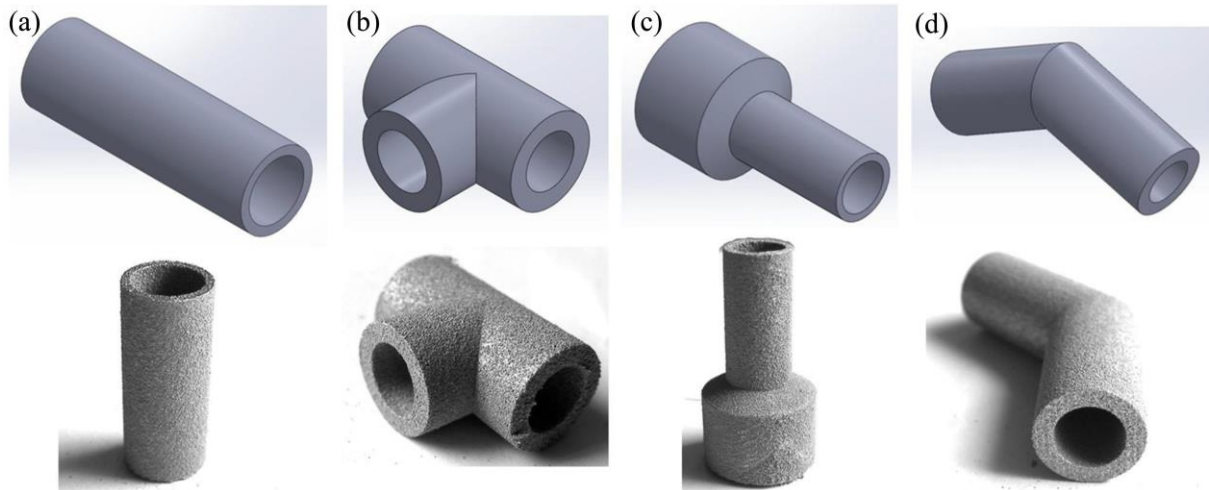
Figure 2.2 Various L-PBF tubes: (a) straight, (b) horizontal t-shape, (c) vertical t-shape, and (d) reduction of size [58].

Due to the great potential for light-weighting, noise reduction and energy absorption applications, L-PBF cellular structures have been investigated for many years to determine the relationship between geometry and their physical properties [5, 59]. In general, cellular structure consists of stochastic foams and lattice structures. It should be noted that the porosity distribution is random in a stochastic foam. Apart from stochastic foams, L-PBF demonstrates unique superiority in fabricating periodic lattice structures [60] with various types of unit cells, such as face centered cubic [61]. Furthermore, lattice structures with uniform and graded densities have also been investigated, as can be seen in Figure 2.3. Currently, the combination of mechanical and functional properties of L-PBF cellular structures needs to be considered during the design and fabrication process [62-64].
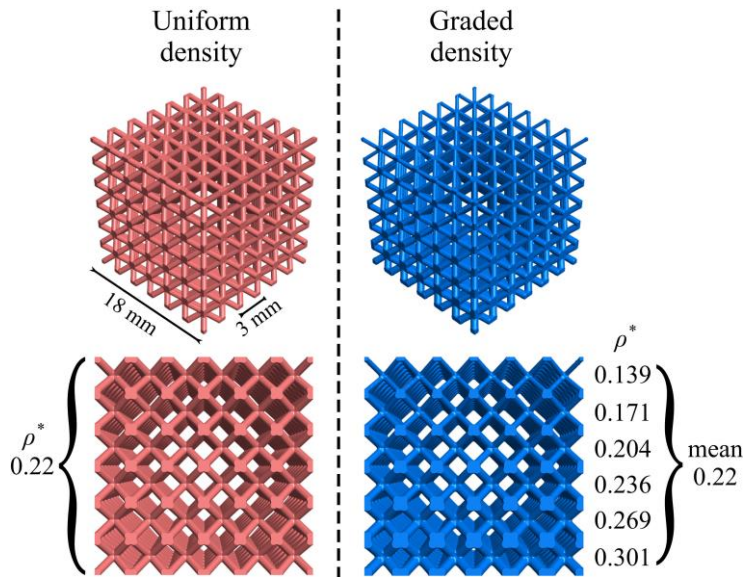
Figure 2.3 CAD models of uniform (left) and graded density (right) lattice structures [60].

Maconachie et al. [65] reviewed the design, fabrication and performance of L-PBF lattice structures and emphasized the importance of design and topography optimization. In fact, fabrication limitations such as dimensional inaccuracies are particularly prone to occur on L-PBF internal structures [66, 67]. Thus, aspects such as model design, raw powder size, melt pool size, deposition parameters, support structure, performance and dimension prediction models need to be considered for L-PBF internal structures [68, 69]. Based on channels and cellular structures, L-PBF is used to manufacture components with various internal structures for applications.

2.2.3 Applications of L-PBF internal structures

L-PBF is becoming an effective process for manufacturing components with various internal structures for automotive, medical, and aerospace industries [70-74]. Given that straight channels are widely used, Romei et al. [50] analyzed the critical features of L-PBF heat exchanger and indicated that the control of feature size below 200 µm was achieved on 316L stainless steel. As can be seen in Figure 2.4a, General Electric company has applied L-PBF to prepare engine fuel nozzles with complex internal channels [75]. For medical applications, Langi et al. [76] investigated the microstructure and mechanical properties of L-PBF 316L stainless steel tubes with thin wall thickness for stent applications. Moreover, straight channels with diameters of 200, 300 and 500 µm were designed and prepared by L-PBF on drug-delivering implants to

12

reduce or avoid infection [77]. Apart from straight channels, curve channels that manufactured by L-PBF exhibit excellent cooling uniformity and efficiency in hydraulic [78] and mould [79] industries as illustrated in Figure 2.4b. The current focus of L-PBF manifolds with curve channels is to investigate the relationship between microstructure and mechanical properties [78]. In terms of cellular structures, Yan et al. [80] fabricated L-PBF Ti6Al4V with different lattice structures for bone implant and found that the modulus and porosity of the lattices could be tailored to mimic human bones. Xiao et al. [81] designed three types of topology-optimized lattice structure as shown in Figure 2.4c and tested their energy absorption efficiencies. Except for uniform lattice structures, Maskery et al. [60] also prepared and examined the mechanical behavior of graded L-PBF AlSi10Mg lattices in Figure 2.3. In addition, open cell foams with large surface area-to-volume ratios have exhibited superior performance in enhancing heat transfer efficiency. Ho et al. [51] researched the heat transfer performance of different types of L-PBF lattice structures and proposed Rhombi-Octet lattice structure for improving single-phase forced convection cooling. Moreover, Jafari et al. [74] reviewed the application of L-PBF technology on heat transfer devices and summarized the successful cell structures. In comparison to basic forms of internal structures, the combinations of different forms have also been designed and fabricated by L-PBF for practical applications as can be seen in Figure 2.5.
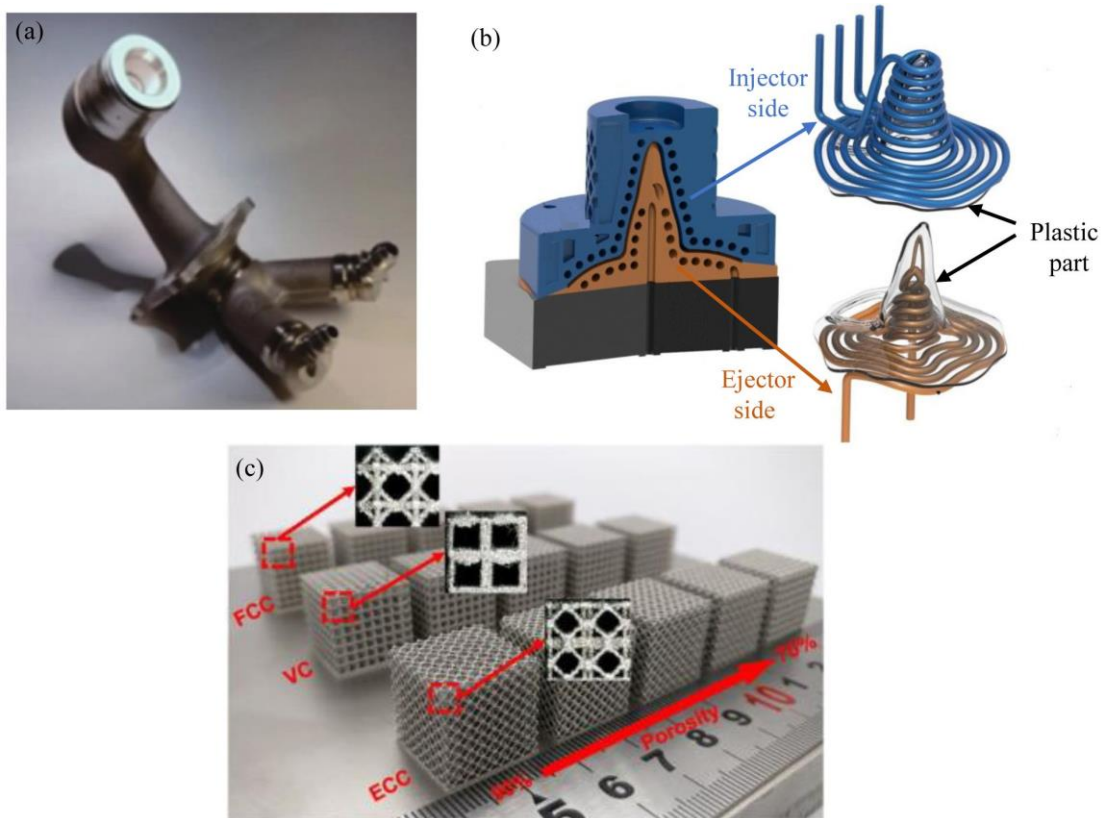
Figure 2.4 Three typical part structures (a) fuel nozzle with internal channel from General Electric company [75], (b) ejector side (orange) and injector side (blue) of mold with incorporated conformal cooling channels near to cavity [82] and (c) as built face centered cubic (FCC) structure, vertex cube (VC) and edge centre cube (ECC) structures [81] that prepared by L-PBF.
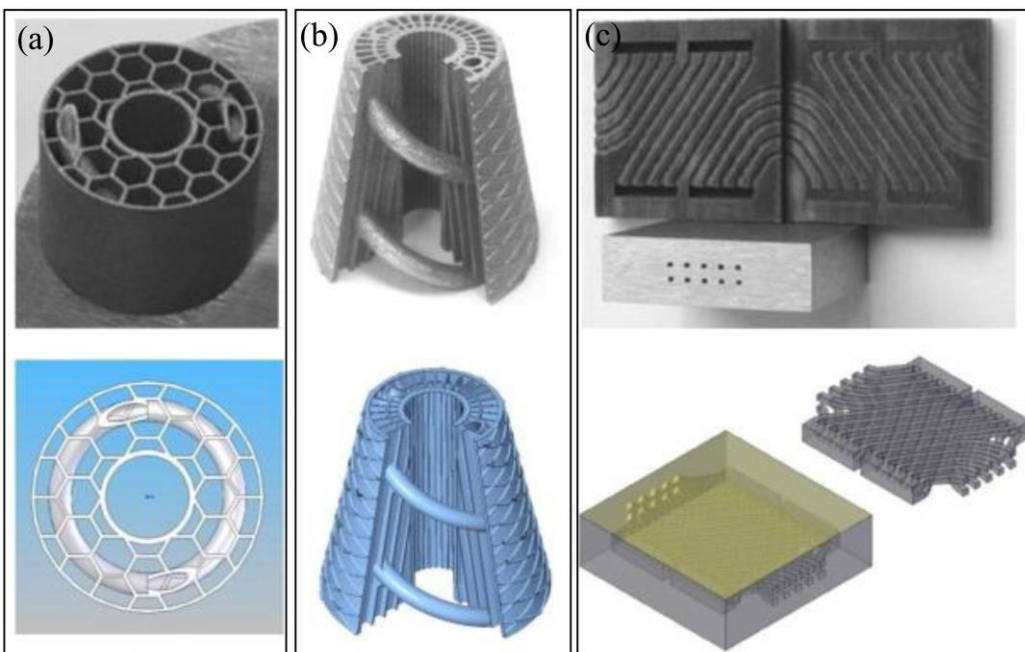
Figure 2.5 L-PBF parts (top) and their CAD models (bottom) combined with different forms of internal structures: (a) cylinder with honeycomb inner structure and two spiral channels from 316L stainless steel, (b) conical frustum object with ribs and one spiral inner channel from 904L stainless steel, and (c) heat exchanger with complex cooling channels from Inconel 625 [83].

Although the working principle of L-PBF provides excellent flexibility for the manufacture of various internal structures, there are limitations for applying L-PBF interior structures to specific applications. The main problems are the high internal surface roughness, low dimensional accuracy and shape distortion since L-PBF is an asymmetric fabrication method that depends on print direction. In addition, limited studies and inaccurate prediction of the overall performance of L-PBF internal structures have resulted in the lack of acceptance of this technology [84].

2.3 Surfaces of L-PBF internal structures

Given that surface quality has significant influence to various properties of products in practical applications [85-87], it is fundamental to learn the causes of poor surface quality and the characteristics of surface features on L-PBF parts in order to facilitate the surface improvement of its products. It should be noted that L-PBF outer and internal surfaces are formed based on the same mechanism and are affected by various effects such as staircase effect and balling [25]. As a result, outer and internal surfaces on L-PBF parts also have similar surface features. In order to systematically analyze the surface quality of L-PBF internal structures, it is necessary to consider the combination of different types of surfaces and the complexity of specific internal structures.

2.3.1 Mechanism of causing poor surface quality

The behavior of molten pool and deposition angles are related to the final surface quality of L-PBF parts. As illustrated in Figure 2.6, L-PBF surfaces can be categorized into horizontal (top), up-facing (face up), vertical (side) and down-facing (face down) surfaces [88] according to the different printing orientations. Due to the interaction of powder bed and laser, raw powders on the powder bed would be attracted by molten pools during L-PBF process because of surface tension, resulting in adhered powders on the surface. After laser scanning, molten pools also solidify rapidly and leave uneven sintering tracks on L-PBF surface. Generally, the temperature gradient mechanism is used to explain the unevenness of molten pools considering the property of previously solidified layers and the top layer being processed. Due to the rapid

heating of the top layer by the laser beam and its low heat conductivity, a steep temperature gradient develops between the melt and solidified part. As the free expansion of molten pool is restricted by surrounding materials, the top layer would bend away from the laser beam. Nevertheless, the compressed upper layers become shorter and form a bending angle towards the laser beam during the rapid solidification as illustrated in Figure 2.7 [89]. Thus, the topography of molten pools on top surfaces is usually uneven. Furthermore, the irregular shape of liquid molten pool is also retained on side, face up and face down surfaces after solidification.
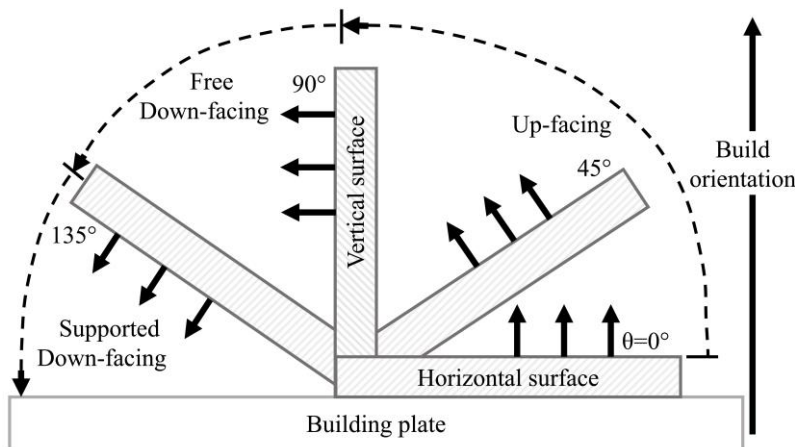
Figure 2.6 Schematic diagram of the different types of L-PBF surfaces according to their printing orientations [88].
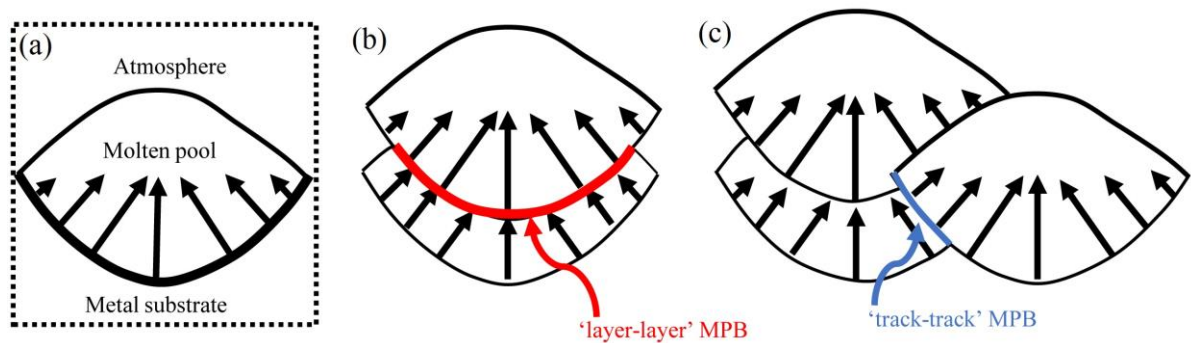
Figure 2.7 Schematic diagrams of the crystallization and solidification of molten pools during L-PBF process: (a) single molten pool; (b) "layer–layer" molten pool boundaries (MPB); (c) "track–track" MPB. The arrows represent the grain orientations [33].

It should be noted that staircase effect is more pronounced on face down surfaces than other surfaces. Cabanettes et al. [25] built samples with different inclinations and showed the visible staircase on an inclined surface (Figure 2.8a). Strano et al. [24] studied L-PBF surface morphology and indicated that staircase effect was obvious at

intervals of about 230 µm (Figure 2.8b) on a 5º inclined surface. Despite the optimization of layer thickness and sloping angle can weaken staircase effect, these parameters are generally constrained by many other factors such as building orientation, residual stresses, CAD design and production rate. Thus, it is hard to change these parameters directly to reduce the impact of staircase effect.
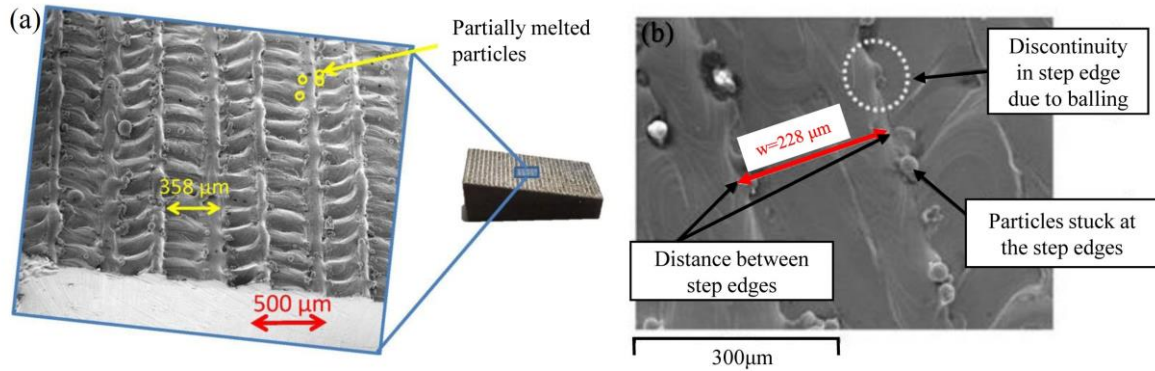
Figure 2.8 Scanning electron microcopy (SEM) images of (a) an inclined sample with staircase effect clearly visible [25] and (b) a 5º inclined surface [24].

Balling effect is the spheroidization phenomena of molten pool due to the instability of melts during L-PBF process. The occurrence of balling is related to Plateau Rayleigh instability and Marangoni convection [31]. During the first laser scanning, powder bed can absorb energy from laser beam, and form a thermal gradient between the molten material and surrounding powders. Then, the powder bed with a relatively low temperature tends to cause the melt to break up into metallic agglomerates with spherical shape in order to reduce surface energy. Balling phenomenon could increase the surface roughness by forming surface protrusions which may cause discontinuous or coarse laser scanning tracks [90]. In addition, pores are easily formed between discontinuous metallic balls, resulting in the poor mechanical properties of L-PBF parts. It should be noted that severer balling may cause the failure of powder spreading step when the paving roller is scratched by the rough surface [24, 91]. Balling effect can be influenced by many factors such as laser scanning speed, oxygen content, laser power and powder characteristics [91, 92]. The oxygen content and wetting ability between the melt and the pre-processed layer is crucial for a successful deposition process. In fact, the oxide on the surface of melts and sintered layers could impede the wettability

of powders and cause balling because contamination layers could attribute to the radially inward Marangoni flow at higher dissolved oxygen contents [7, 31]. Thus, it is mandatory to conduct L-PBF process in a protective atmosphere with inert gases. In terms of laser scanning speed, discontinuous sintering tracks and balling could be formed in the condition of lower energy input and worse wetting ability with higher scanning speed [91]. The effect of oxygen content is indicated in Figure 2.9, where an increase in oxygen content aggravated the size and degree of balling.
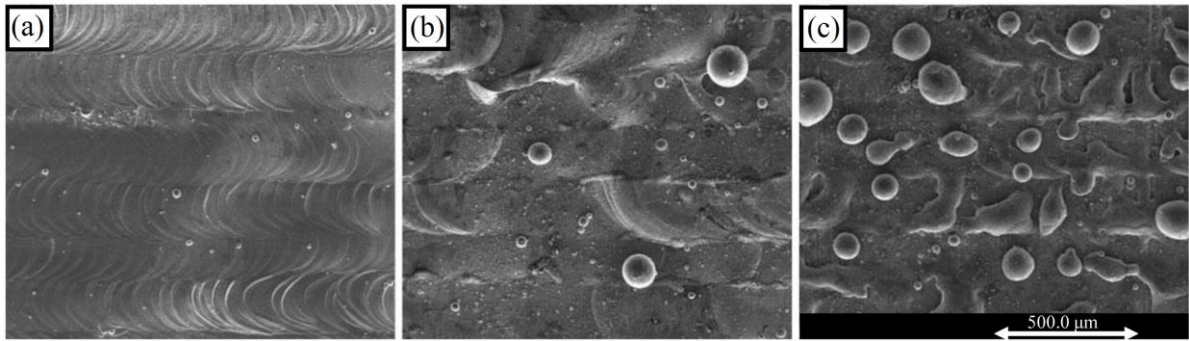
Figure 2.9 SEM images of balling characteristics with different oxygen contents during L-PBF: (a) 0.1%, (b) 2% and (c) 10% [91].

2.3.2 Surface features

Because of surface tension, raw powders on the powder bed would be attracted by molten pools during L-PBF process, resulting in the adhesion of partially melted powders on L-PBF surfaces. It is a widely held view that the area ratios of adhered powders vary on top, face up, side and face down surfaces considering the effects of staircase, heat conduction, gravity and overhang. Bai et al [93]. applied L-PBF to fabricate top and side surfaces of 316L stainless steel, and found that the top surface had less adhered powders than the side surface. Due to the spherical shape of raw powders, the spherical protrusions on L-PBF surface were normally considered as adhered powders. However, it is impossible to identify the sintering degree of a powder by simply observing its spherical morphology on L-PBF surfaces. Figure 2.10 shows the surface microstructure of L-PBF AlSi7Mg (Figure 2.10a) on L-PBF side surface (Figure 2.10b) [94] and the adhered powder showed a microstructure transition from the raw powder to the sintered area throughout the spherical morphology (Figure 2.10c and d). Moreover, the bonding state and bonding strength of adhered powders on L-

PBF surface may also vary due to the complicated solidification process. Thus, the sintering degree and bonding conditions of adhered powders should be precisely characterized and identified for further surface feature analysis.
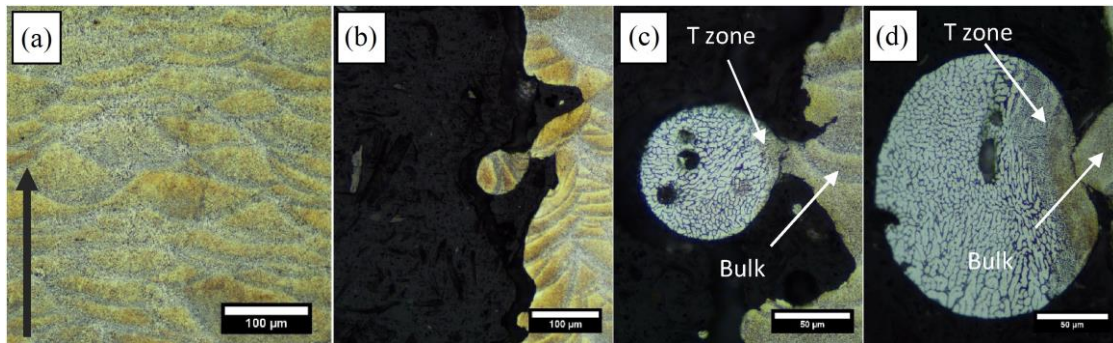
Figure 2.10 Optical images of cross-sectional (a) bulk AlSi7Mg microstructure, (b) balling on the surface, (c and d) partially melted spatters with spherical morphology on the surface. The arrow in (a) shows the build direction, T zone means transition zone [94].

After laser scanning, the molten material solidifies rapidly and then forms sintered area on L-PBF surfaces. Despite the existing of partially melted powders, the morphology of sintered area such as the melt track is still visible on various surfaces. Compared to top, face up and side surfaces, the sintered area of face down surfaces usually possesses the highest roughness since heat conduction and gravity play more influential roles for overhanging face down surfaces [25, 95]. Except for the sintered zone left by the solidification of molten pools, adhered powders may be partially sintered during L-PBF. Nasab et al. [94] carried out the nano hardness profiles of a partially melted powder, and a transition zone between un-sintered powder and sintered area was proposed according to the changes of hardness values. Given that the sintered area has strong effect on the surface quality and applications, more detailed research should be carried out for the investigation of this surface feature.

Surface defects such as cracks and pores [96] can also occur if the fusion during L-PBF is not well controlled. A good combination of L-PBF parameters and inert atmosphere are helpful to avoid defects on L-PBF surfaces. In addition, the influences of edge effect, gravity, overhanging surfaces, heat transfer etc. on L-PBF surface quality also need to be considered.

2.3.3 Surface analysis of internal structures

Surface quality of L-PBF parts varies on different types of surfaces. Notably, roughness of L-PBF surfaces can be affected by building angles (Figure 2.11), materials and printing parameters. Moreover, area ratios of sintered area and adhered powders are different on top, face up, side and face down surfaces. Pakkanen et al. [58] studied the internal channel surface roughness and concluded that the surface roughness of L-PBF internal channels depended on their printing angles. Compared to other surfaces, the sintered area of face down surfaces generally possesses the highest roughness [25, 95].
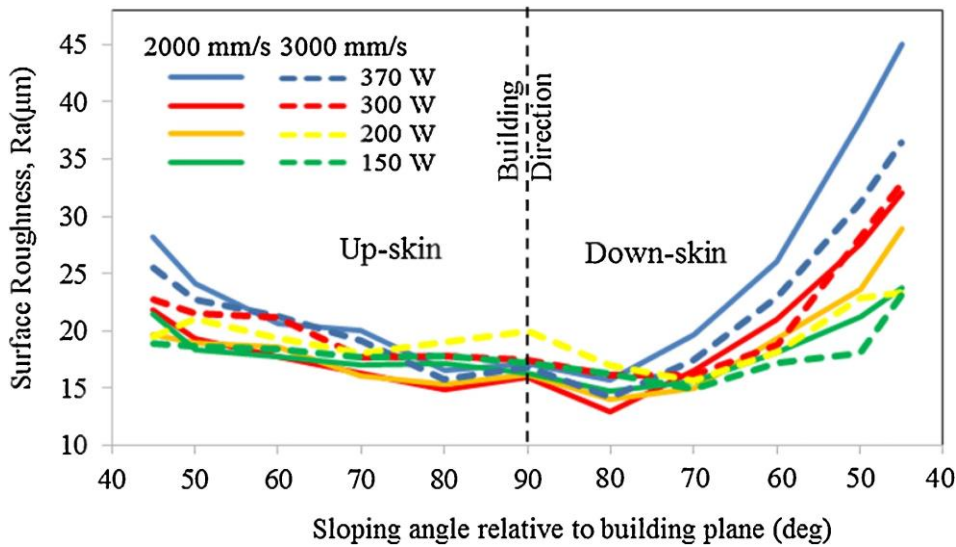
Figure 2.11 Data graphs of roughness on face up and face down surfaces of L-PBF Hastelloy X samples with different printing inclinations (45° to 90°) [95].

Since different printing angles are usually included in L-PBF internal structures, and L-PBF surface quality can be affected by various effects and printing angles, it is important to identify the types of surfaces on internal structures for comprehensive surface analysis. For example, there are two types of surfaces on the internal cross-section of a straight channel in Figure 2.12a. In terms of cellular structures, face up and face down surfaces on the unit cell of a body-centered cubic (BCC) lattice structure can be clearly identified in Figure 2.12b. Not only the face up and face down surfaces, but also the morphology of top surface can be characterized at the connection points of the struts in Figure 2.12c. Based on the above views, when looking back on Figure 2.12b, the four connection points of the struts on the four sides of the BCC lattice

structure should possess characteristics of L-PBF side surface. Therefore, L-PBF components with internal structures in Figure 2.4 and Figure 2.5 actually contain different types of surfaces. It should be noted that consideration of L-PBF specific structure is crucial for a comprehensive analysis of the internal and outer surface quality of L-PBF components.
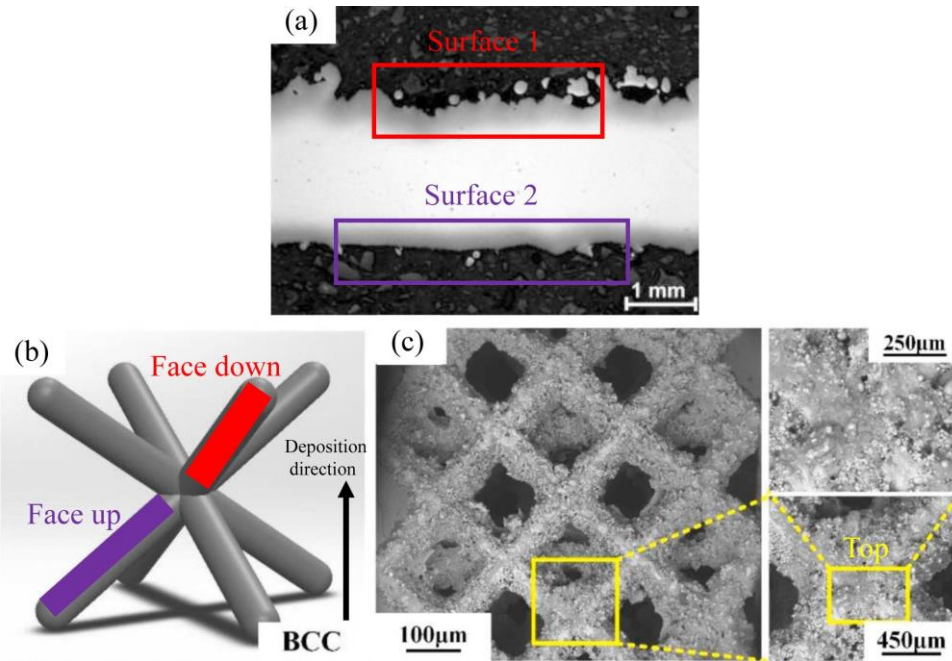
Figure 2.12 Different types of surfaces of (a) a L-PBF straight channel with its inner cross-sectional optical micrograph [78], (b) a unit cell of body-centered cubic (BCC) lattice structure and (c) the top view of a L-PBF BCC lattice structure [97].

Given that poor surface quality of L-PBF parts hinders the engineering applications, appropriate post treatments are required to improve surface quality for L-PBF parts, especially for L-PBF components with internal structures [95]. In addition, the complexity of L-PBF internal surfaces and structures make it challenging for post processing.

2.4 Polishing of L-PBF internal structures

The inferior surface quality of L-PBF components with internal structures is an obstacle to apply this technique to real industry production [19]. Since surface quality is critical for meeting specifications and tolerances [98], researchers have studied different approaches to improve the interior surface quality of L-PBF parts [99, 100]. The typical approach is to optimize the fabrication strategy which includes the design

of raw powders [101], the optimization of L-PBF parameters [102-106], the use of laser re-melting during L-PBF and others such as the control of oxygen content in the atmosphere [107]. Although the optimized fabrication strategy is helpful to reduce balling and other surface defects, the adhesion of partially melted powders and rough sintered area are difficult to avoid completely. Another approach is the development of a hybrid process in which L-PBF and a subtractive process such as milling are integrated to fabricate parts layer by layer [108-110]. However, combining L-PBF and subtractive machining into one process is costly and limited to a few materials because distortion issue of components can easily occur due to the absence of stress relief procedures during hybrid processing. Compared to fabrication optimization and hybrid processing technique, surface polishing methods based on material removal mechanisms are more economic and efficient to remove adhered powders and smooth sintered area. Unlike L-PBF outer surfaces that could use various methods such as blasting and laser polishing for surface improvement [111], it is in high demand and more challenging to polish interior surfaces on L-PBF parts. In recent years, researchers have developed different polishing techniques for L-PBF internal structures. The existing polishing methods for L-PBF internal structures can be categorized to three aspects according to the mechanisms, including mechanical, chemical-based and hybrid methods [112, 113].

2.4.1 Mechanical methods

Mechanical polishing methods generally utilize power-driven abrasive media as cutting tools to smooth L-PBF interior surfaces. Nowadays, AFM, magnetic abrasive finishing (MAF), AFP and barrel finishing (BF) have been applied to improve surface finish of L-PBF parts with internal structures. Despite there are some common features such as the independence of raw surface quality among these mechanical polishing processes, each technology has its specific polishing characteristics and is suitable for different types of interior structures.

AFM is a machining process that can be used to deburr, polish and remove recast layer. By using two vertically opposed cylinders, surface material on the fixed

workpiece can be removed when the pressurized semi-solid laden with hard abrasive particles repeatedly flows through a restricted passageway (Figure 2.13a). Based on the working principles of AFM, it is considered for finishing components with complex geometries and internal structures. The use of AFM parameters such as extrusion pressure, number of cycles and media composition need to be considered for parts with different hardness, geometry and initial surface quality [114]. Nowadays, AFM has been widely used for the polishing of L-PBF straight and curve channels. Han et al. [1, 115] applied AFM to L-PBF conformal cooling channels in mold industry and indicated that AFM was more efficient to remove protruding features than valleys on L-PBF surface [1]. In terms of the residual stress and fatigue performance, it is reported that AFM was capable of improving the fatigue resistance of L-PBF channel by increasing its compressive stress [115]. Apart from experiments, Ferchow et al. [116] proposed a pressure-velocity-based model to quantitatively simulate the roughness and thickness reduction during AFM for L-PBF curve channels. Nevertheless, it is hard to expand AFM to thin wall channels or cellular structures because the use of high pressure is easily to damage these structures. Moreover, the viscous media with high pressure in AFM may remain or embed into L-PBF surface and cause contamination. Furthermore, it is difficult for AFM to achieve uniform material removal on L-PBF channels with varied geometries.

MAF [117] applies magnetic abrasive particles to grind workpiece surface. For L-PBF straight channels, the magnetic abrasive media is generally pressed against the surface by magnetic force. Meanwhile, the rotation of workpiece and linear vibration of magnets induce relative motion between the abrasive particles and sample surface as can be seen in Figure 2.13b. Thus, the abrasive particles are acted as a flexible magnetic abrasive brush and dragged along the internal surfaces to remove materials. Guo et al. [117] investigated MAF process on a straight tube that prepared by L-PBF Inconel 718 alloy. Polishing results indicated that MAF could remove partially melted powders efficiently and decrease the surface roughness from 7 μm to less than 1 μm in Ra. Although MAF is a promising polishing method for L-PBF internal structures, its drawback lies in the limitation on suitable materials for processing. For example, the

polishing effect of MAF is negligible on ferromagnetic material such as cobalt alloys. Furthermore, MAF is more suitable for polishing internal features with rotational symmetry, rather than complicated features and protrusions because magnetic abrasive particles cannot navigate around these internal features [118].
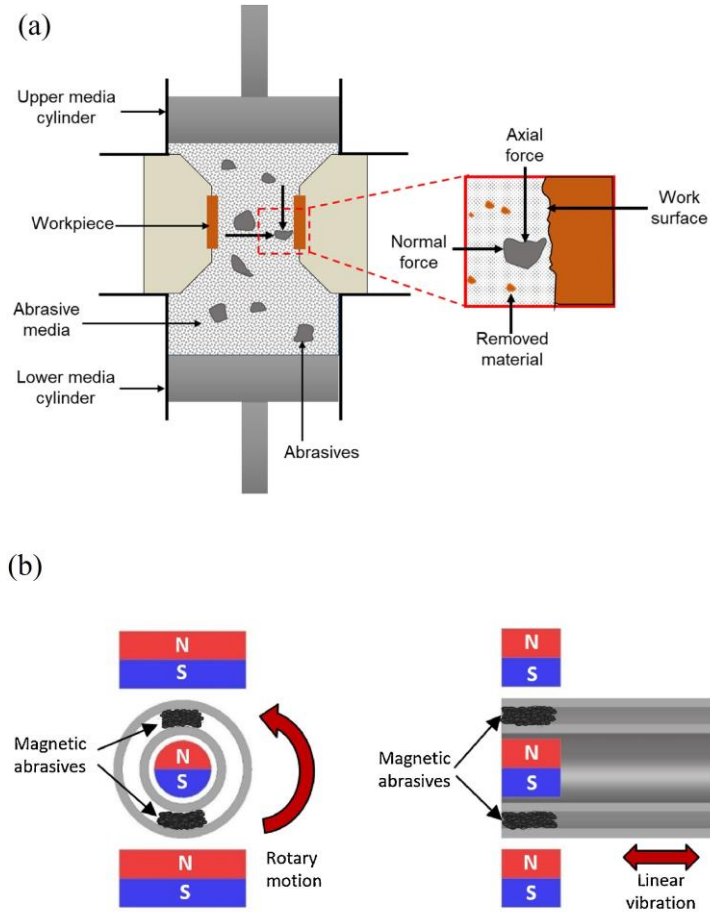
Figure 2.13 Schematic diagrams of (a) AFM [119] and (b) MAF [117].

AFP is a finishing process by the combination of liquid impingement and abrasion from abrasive particles. In AFP process, the surface is polished when the fluid with free abrasive grains passes through the workpiece. Because of its working mechanism, AFP is capable of polishing surfaces with various initial conditions. Due to the mechanical removal mechanism, AFP could also be applied for various L-PBF materials. Compared with traditional AFM which uses high pressure and an abrasive laden media as the tool, a lower pumping pressure and viscosity fluid as well as a higher flow velocity are utilized in AFP [120]. Moreover, unlike the limitations such as contamination and abrasive agglomeration in AFM, AFP is more suitable for polishing

thin-walled and lattice structures without damage and contamination [18]. Thus, AFP is preferable for polishing L-PBF parts with various internal structures in aerospace and mould industries [121]. In order to improve the poor surface quality of L-PBF parts, researchers investigated material removal mechanism and various parameters of AFP in the polishing of L-PBF internal structures. Furumoto et al. [14] developed an AFP apparatus and found the efficiency of AFP decreased with an increase in polishing time. Naglingam et al. [18] investigated liquid impingement and absolute abrasion, respectively. They found that liquid impingement and particle abrasion were effective in removing loose powders and partially melted particles on L-PBF straight channels. The limitations of AFP, for instance, the long polishing time and low processing efficiency, come from the use of low pressure and solution viscosity. Besides, the performance of AFP depends on the hardness and wear property of materials. Thus, AFP is more applied to low hardness alloys such as AlSi10Mg currently.

BF, also known as tumble finishing, generally reduce the surface roughness by the mechanical rotation of a barrel containing a mixture of samples and grinding media [111]. Because no part fixing is required, various materials with L-PBF complex geometries can be processed [23]. Boschetto et al. [122] applied different size of ceramic media in BF and found that the prominent reduction of surface roughness achieved after 20 hours of BF on a L-PBF Ti6Al4V impeller. Khorasani et al. [123] investigated the effects of various BF parameters and confirmed that the roughness of L-PBF various surfaces reduced by more than 50% after wet abrasive centrifugal BF process. Compared to AFM, MAF and AFP, BF is more applicable to structures with large internal size because the polishing media in BF usually have millimeter scale. In addition, BF needs hours of polishing to reduce surface roughness which means the polishing efficiency of BF is lower than other mechanical methods.

2.4.2 Chemical-based methods

Chemical treatment is mainly based on chemical reactions occurring at the interface between surface and reactive chemicals. Benefiting from the fluidity of the solution, polishing media of chemical polishing (CP) and EP can contact with the inner

surface, hence making them suitable candidates for surface improvement of L-PBF internal structures [124].

In the process of CP, the uneven areas on metal or alloy surfaces are selectively dissolved by chemical etching in order to achieve leveling effect. The equipment of CP is simple and it is capable of dealing with channels, cellular structures or combined complex internal structures. It is reported that CP could reduce the peak-to-valley spacing on L-PBF Ti6Al4V surface, and form a passivation film for the improvement of surface corrosion resistance in the meantime [125]. Generally, the process of CP for L-PBF titanium alloys utilizes etchants with hydrofluoric acid and nitric acid. Lyczkowska et al. [124] used CP to improve surface quality of L-PBF Ti6Al7Nb components with lattice structure. It was found that the removal of adhered powders and reduction of surface roughness were influenced mostly by chemical composition and concentration. Despite the process is effective, CP tends to erode material indiscriminately hence compromising the dimensional accuracy of L-PBF components [126]. Although the addition of strong acid with high concentration to chemical etchants could accelerate chemical reactions, it is harmful to environment and may influence the performance of medical products after CP [125, 126].

EP is a finishing process for metals or alloys to get smooth and bright surfaces based on anodic dissolution. During EP, the material is dissolved ion by ion from workpiece due to the combination of electricity and chemical reaction. Final EP results are influenced by many factors such as current density, temperature, electrolyte type and initial surface roughness [127]. In general, EP is composed of anodic levelling (macro-smoothening) and brightening (micro-smoothening) [128]. And the surface quality of part is improved after EP attributing to the removal of the original layer and the formation of a new homogenous oxide film. Different from traditional mechanical finishing techniques such as milling, EP is a non-contact and damage free process. Moreover, EP also has characteristics such as simplicity of device, flowability of electrolyte, designability of cathode tool and high material removal rate, making it suitable for polishing L-PBF channels and cellular structures [129]. Chang et al. [15] proposed a combination of overpotential and conventional EP processes to remove

adhered powders and smooth the struts on L-PBF 316L stainless steel lattice structures. Dong et al. [130] also investigated the effect of EP parameters on L-PBF Ti6Al4V lattice structures via Taguchi method. It is obvious that EP is capable of polishing L-PBF internal surfaces, particularly for removing partially melted powders and smoothing laser sintering tracks as shown in Figure 2.14. The effects of EP on various L-PBF alloys e.g. Ti-based alloys [88], Al-based alloys [15], nickel-based alloys [19], Fe-based alloys [15] and CoCr alloys [131] have also been studied in recent years.
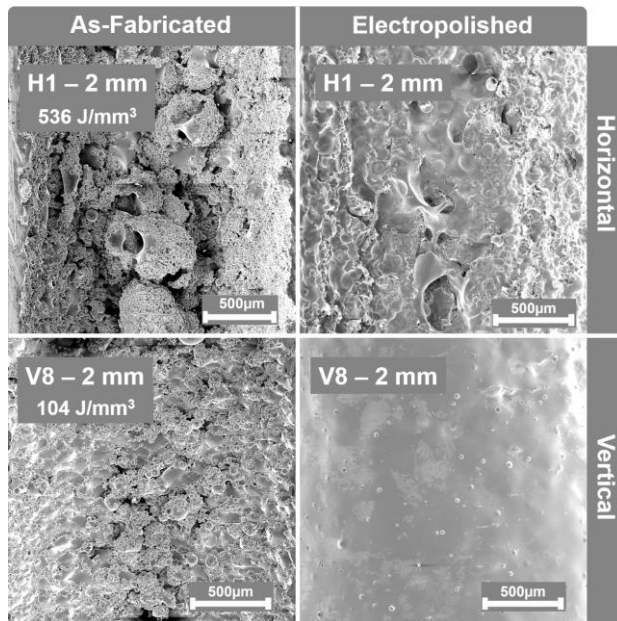
Figure 2.14 SEM images of interior surface morphology of a L-PBF horizontal channel and a L-PBF vertical channel before and after EP [132].

Despite the advantages and wide applications of EP, there are also limitations and challenges for this technology in the post-treatment of L-PBF internal structures. Since the surface roughness of L-PBF components usually varies from 10 to 20 µm in Ra [133], the rough initial surface will impede a fast and effective EP process[128]. In terms of L-PBF internal structures with high complexity, EP is hard to achieve uniform surface finish due to the limited accessibility of cathode tool [18]. Most EP experiments or applications are usually performed in open vessels with low flow rates or low stirring speeds. Moreover, there is still no available theory to explain EP mechanisms well due to the complexity of current, chemical reactions, ion transport and diffusion at workpiece-electrolyte interface [128]. In addition, environmentally friendly electrolytes which also take EP efficiency into account are expected due to safety concerns. Thus,

in-depth study of EP and development of innovative technologies based on EP are strongly necessary in order to benefit the production process of L-PBF.

2.4.3 Hybrid methods

Hybrid polishing technologies are generally developed on the basis of various single polishing process in order to overcome the weakness of one method or improve its polishing performance. It should be noted that the hybrid methods presented in this section refer to combining different polishing processes into one polishing procedure. Current hybrid polishing technologies are classified into AFP-based and EP-based hybrid polishing processes for L-PBF internal structures.

Researchers developed various hybrid polishing processes based on AFP to improve their polishing efficiency recently [18]. Neda et al. [16] combined AFP and CP for interior surface of L-PBF Inconel 625 alloy. In polishing experiments, chemical abrasive fluid is mixed and then pumped to pass through the sample chamber to finish polishing process. Surface roughness data showed that chemical flow polishing resulted in a higher reduction of surface roughness compared to single CP process. Although the efficiency of hybrid polishing is improved, it has the similar limitations as CP, such as the use of strong acid. Unlike using hazard chemicals to facilitate polishing efficiency, Arun et al. [18] applied hydrodynamic cavitation in AFP and proposed hydrodynamic cavitation abrasive finishing (HCAF) technique for L-PBF straight channels. As can be seen in Figure 2.15, a cavitation inducer is placed upstream at the inlet of the HCAF chamber to induce a hydrodynamic cavitation stream in the fluid flow. The investigation indicated that the synergistic effects showed higher material removal rate on L-PBF straight channels than single cavitation and abrasion process. Despite the development of AFP-based hybrid polishing methods exhibit higher polishing efficiency for channels, the mechanism and controllability of hybrid polishing based AFP are more complicated at the same time and worthy of further study.
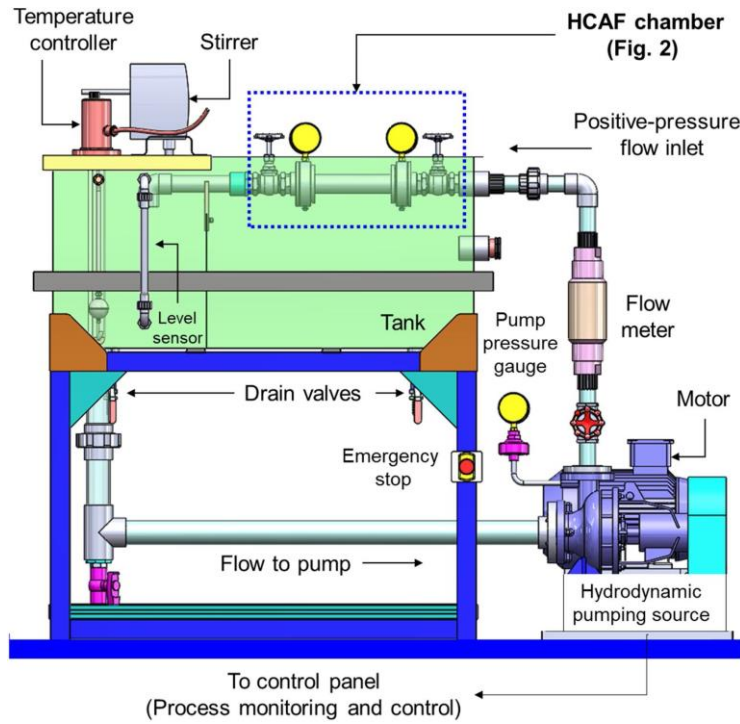
Figure 2.15 Schematic diagram of HCAF apparatus [18].

EP-based hybrid polishing techniques for various L-PBF internal structures are attractive because they possess the advantages of EP, such as high material removal rate. Zhao et al. [17] proposed an electrochemical mechanical polishing (ECMP) process for L-PBF internal holes to by using a metallic wire as cathode and nylon filaments as flexible abrasive. During ECMP, the electrochemical reaction takes place while nylon filaments that fixed on the cathode could mechanically scratch the internal surface following the movement of the wire. However, it is hard to extend this technique to complex curve channels or lattice structures due to the use of nylon filaments and rigid metallic wire. In addition, the polishing effect and mechanism of dry mechanical-electrochemical polishing [93] was also studied, but the smallest internal features that can be polished are limited to the size of the dry electrolyte media particles.

2.4.4 Comparison of various methods

Based on the mechanism differences, various polishing methods have their own polishing characteristics for L-PBF internal structures. In order to compare the polishing effect and efficiency of different polishing techniques, the materials, polishing time, and surface roughness of L-PBF internal structures before and after polishing are

summarized in Table 2.2. In general, EP and EP based hybrid polishing methods have higher material removal rate than other methods due to the use of electricity. Moreover, EP based methods are more suitable for internal structures that facilitate the placement of cathodes. Due to the use of high pressure, AFM is more suitable to polish L-PBF complex channels with a certain wall thickness, while AFP based methods could be used to polish lattice structures and thin-walled channels. In addition, the properties of the polishing medium also affect the suitability of polishing techniques. CP based methods have been applied to polish various internal structures because of the high fluidity and low viscosity of the polishing solution. Compared with CP and EP based methods, AFP, MAF and BF could be applied to internal structures with different internal dimensions considering the size of abrasive particles.

Due to the difference of material removal characteristics, the use of various polishing methods could alter the topography of L-PBF inner surfaces. Polishing methods may also affect the shape and size of internal structures. Ferchow et al. [116] prepared straight channels with face up and face down surfaces by L-PBF and measured the diameter and roughness of the channel at different positions before and after AFM. As can been seen in Figure 2.16a, the removed thickness changed at different positions of the channel after AFM. It was found that the material removal rate at the inlet or entrance of the channel was higher than the intermediate region during AFM. As a result, the diameter of the two ends of the channel were enlarged. Compared with AFM, the polishing pressure during HCAF process is much lower and Figure 2.16b compared the internal surface topography of a L-PBF channel before and after HCAF. The results showed that HCAF could effectively remove adhered powders and reduce surface roughness. Considering the high material removal rate, poor EP parameters may affect dimensional accuracy or even damage the internal structure with thin strut (Figure 2.16c). To accurately evaluate the effect of polishing on surface topography and dimension of L-PBF internal structures, it is essential to measure the topography, roughness, and size of multiple identical locations before and after polishing.

In order to facilitate the productization process of L-PBF components with inner structures, the medical industry generally adopts chemical methods. Moreover, almost all polishing methods can be used for various applications, such as AFP for conformal cooling channels in the mold industry. Considering the surface and structural complexity of L-PBF internal structures, current polishing methods were presented for the polishing of simple or single-form internal structures. Based on the above literature study, it is clear that the polishing technologies for L-PBF internal structures still have a lot of room for further development to expand the applications.

Table 2.2 Polishing methods, materials, polishing time, surface roughness before and after polishing of L-PBF internal structures.

Polishing method	Materials	Internal structures	Raw surface roughness (µm)	Polishing time (minutes)	Polished surface roughness (µm)
AFM [1]	Maraging steel 300	Φ 3mm Curve channel	Sa= 9.70	≈ 80	Sa =3.30
MAF [117]	Inconel 718	Φ 24 mm Straight channel	Ra= 7.22	180	Ra= 0.23
AFP [14]	Alloy	Φ 5 mm Straight channel	Rz ≈ 110.00	133	Rz ≈ 20.00
CP [134]	316L stainless steel	Straight channel	Sa= 13.80	45	Sa =5.22
EP [15]	316L stainless steel	Lattice structure	Ra ≈ 8.00	40	Ra ≈ 0.18
HCAF [135]	AlSi10Mg	5mm*5mm Straight channel with square corss-section	Ra ≈ 18.00	180	Ra ≈ 4.00
ECMP [17]	304 stainless steel	Φ 10 mm Straight channel	Sa=14.51	2.86	Sa=9.09

Notes: Ra: arithmetical mean deviation of line; Rz: average of the vertical distances from the highest peak to the lowest valley; Sa: arithmetical mean deviation of surface area.
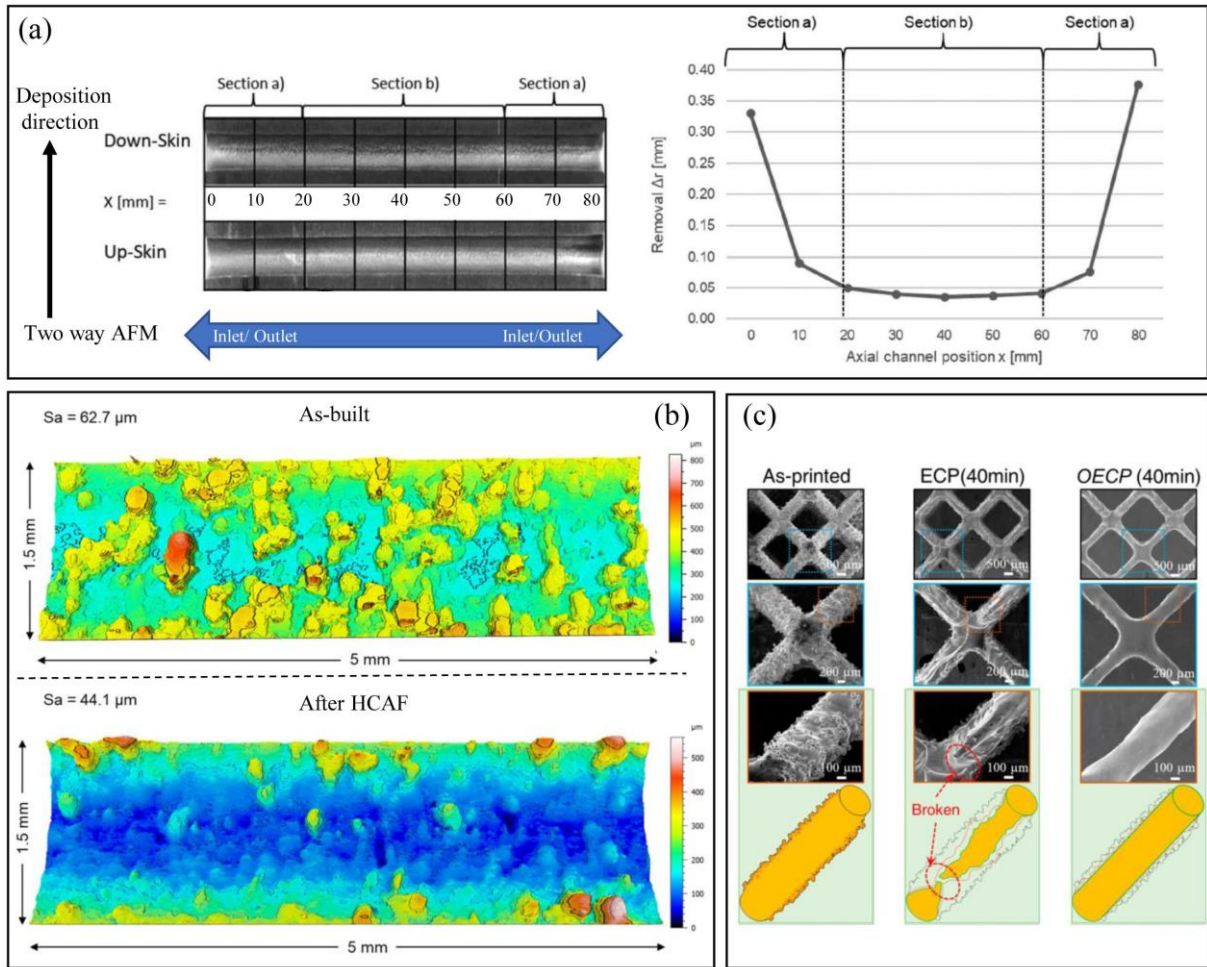
Figure 2.16 Part images of (a) quantitative results showing diameter removal differences at different position of a L-PBF channel after two-way AFM [116], (b) inner surface topography of L-PBF channels before and after HCAF process [136], and (c) morphology comparison of L-PBF BCC lattice structures before and after electrochemical polishing (ECP) and overpotential electrochemical polishing (OECP) [15].

2.5 Objectives

Based on the use of a high-power laser, complete melting mechanism and layer principle, L-PBF has been widely utilized to fabricate various materials with complex internal structures. Channels and cellular structures are typical interior structures that have been used on L-PBF metallic parts due to their specific functionality in practical applications. However, poor surface quality of L-PBF internal structures has seriously affected their applications in industry. Although polishing is an effective and economical way for internal surface improvement, current methods have their drawbacks in the polishing of L-PBF internal structures, especially for thin-walled inner structures. Moreover, the relationship between L-PBF surface features and their corresponding

32

material removal mechanisms during polishing has not been well established. Thus, it is of great significance to develop an innovative polishing system or technology with high polishing efficiency for L-PBF internal structures. Given the complexity of L-PBF surfaces and internal structures, different inner surface types are essential to be investigated in order to comprehensively analyze the surface characteristics of L-PBF internal structures. Furthermore, in-depth research on parameter optimization, material removal mechanism etc. is required for the polishing of L-PBF internal structures in order to improve the efficiency of surface finish. The objectives of this thesis are drawn as follows.

(1) Comprehensive characterization of L-PBF surface features: to establish relationship between surface features and polishing process.

(2) Develop an innovative polishing system which could combine EP and AFP for hybrid polishing for L-PBF internal structures: investigate EP, AFP, multiple polishing in different sequences and hybrid polishing, and demonstrate the possibility of combining EP and AFP for L-PBF internal structures.

(3) Study on EP of various inner surfaces prepared by L-PBF 316L stainless steel and Ti6Al4V with environmentally friendly electrolytes: to investigate EP characteristics and its material removal mechanism for L-PBF internal surfaces.

(4) Study on AFP of various inner surfaces prepared by L-PBF 316L stainless steel and Ti6Al4V with environmentally friendly polishing media: to investigate AFP characteristics and its material removal mechanism for L-PBF internal surfaces.

(5) Investigation of multiple polishing with different sequences and hybrid polishing based on EP and AFP for L-PBF various inner surfaces using environmentally friendly polishing media: to investigate material removal characteristics of multiple polishing and hybrid polishing on L-PBF internal surfaces based on the study of single EP and AFP.

(6) Polishing of typical internal structures fabricated by L-PBF 316L stainless steel and Ti6Al4V using the developed polishing system: to demonstrate the capability and high efficiency of combing EP and AFP in the polishing of L-PBF internal structures for application development.

Chapter 3. L-PBF Surface Features and Establishment of Polishing System

3.1 Sample preparation

3.1.1 CAD design

In general, there are L-PBF top, face up, side and face down surfaces with different deposition angles. Moreover, internal and outer surfaces of L-PBF parts should have similar surface features considering the same deposition principle. In this study, L-PBF cuboid samples and 1/6 straight channels with top, face up, side and face down surfaces were prepared. The CAD models and their angles between the surface and the horizontal plane are summarized in Table 3.1. Cuboid samples have the same dimension of 5x2x10 mm and 1/6 straight channels possess an inner diameter of 5 mm with a length of 10 mm. It should be noted that internal surfaces of different 1/6 straight channels were used for the fundamental study of polishing for various L-PBF inner surfaces. Apart from the CAD models in Table 3.1, straight channels, lattice structures and conformal channels were designed and printed for application development of polishing for L-PBF internal structures in Chapter 7. The CAD models of straight channel, multiple BCC lattice structure, single BCC lattice structure and conformal channel with corresponding materials and dimensions for application development are illustrated in Table 3.2. Note that all samples were taken off from substrate through cutting supporters by a wire saw.

Table 3.1 Different L-PBF surface types and their corresponding angles between surface and horizontal plane.
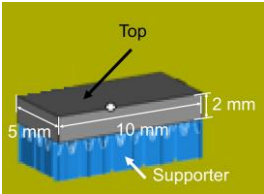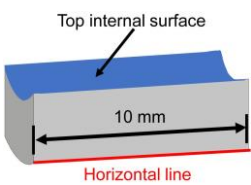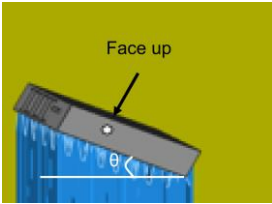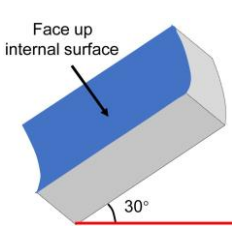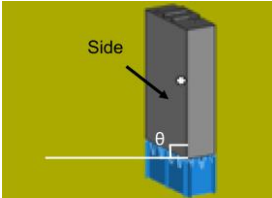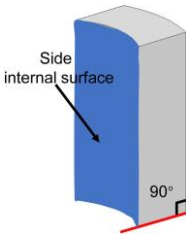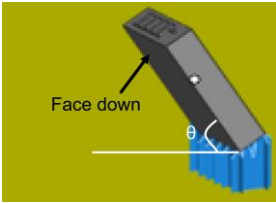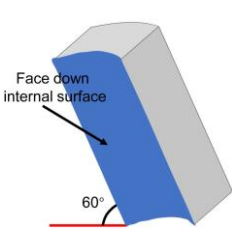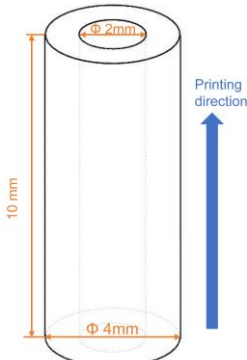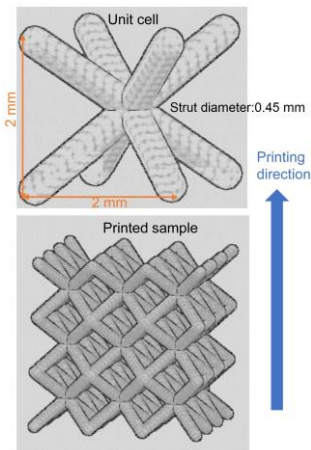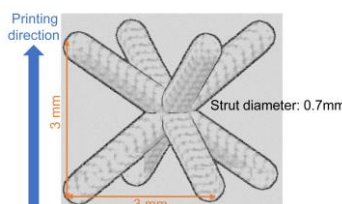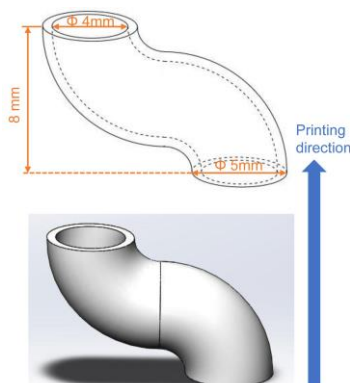
Surface type	Angle θ with horizontal plane	CAD models of cuboid samples	CAD models of 1/6 straight channels with various internal surfaces marked in blue
Top	0°		
Face up	30°		
Side	90°		
Face down	60°		

Table 3.2 CAD models for chapter 7.

Type	CAD models	Material
Straight channel		Ti6Al4V
Multiple lattice structure		316L stainless steel; Ti6Al4V
Single lattice structure		316L stainless steel
Conformal channel		316L stainless steel

3.1.2 316L stainless steel

Generally, morphology, size and distribution of raw powders can affect powder flowability, laser energy absorption and the thermal conductivity of the powder bed [137]. Higher powder bed packing densities are preferred for L-PBF process due to lower internal stress, part distortion, porosity and surface roughness of printed parts. A wider powder size distribution enables a higher powder bed packing density because the gaps between larger powders can be filled in with smaller powders. Moreover, a spherical powder morphology improves the flowability of the powder to achieve a high packing density in the powder bed. Hence, gas-atomized powders with a spherical shape are widely used in L-PBF process [138]. To achieve optimum process, a balance between powder size and shape needs to be considered because large powders require more energy for proper melting. Considering the above analysis, most research on L-PBF steel, nickel-based and titanium-based alloys typically apply spherical powders with 10 to 45 µm in diameter [139].

SEM images and the composition of gas atomized 316L stainless steel powders (Sandvik, Sweden) which used for L-PBF process are shown in Figure 3.1 and Table 3.3, respectively. Most of the powders have a near-spherical shape with particle distribution from 5 to 50 µm. 316L stainless steel specimens were fabricated using a laser powder bed fusion system (EOS GmbH, Germany). The selected deposition parameters were as 195 W in laser power, 20 µm in layer thickness, 1083 mm/s in scanning speed and 90 µm in hatch space. A stripe partition with S scanning tracks of laser in each layer and a scanning rotation of 45° between successive layers were used. In terms of contour scanning, a laser power of 110 W and a scanning speed of 800 mm/s were applied during L-PBF.
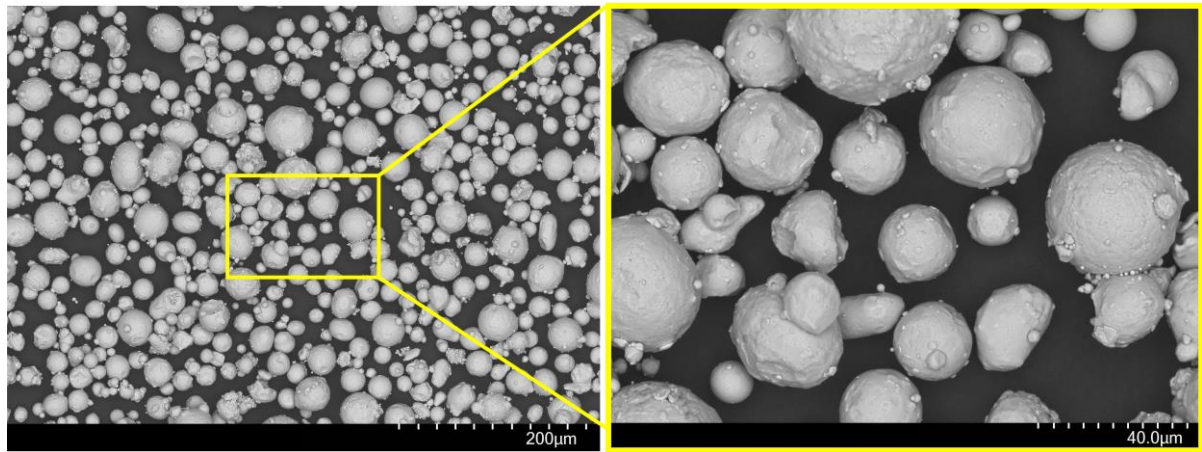
Figure 3.1 Raw 316L stainless steel powders used for L-PBF process.

Table 3.3 Alloy composition with mass percentage (wt%) of raw 316L stainless steel powders.

Element	Fe	Cr	Ni	Mo	Mn	Si	P	C	N	S
%	Balance	16.76	10.65	2.36	1.05	0.72	0.022	0.017	0.074	0.0053

3.1.3 Ti6Al4V

SEM images and the composition of gas atomized Ti6Al4V powders (Peshing New Metal (Changzhou) Co., Ltd., China) which used for L-PBF process are shown in Figure 3.2 and Table 3.4,respectively. Most of the powders have a near-spherical shape with particle distribution from 10 to 50 μm. Ti6Al4V specimens were fabricated using the same laser powder bed fusion system (EOS GmbH, Germany) as 316L stainless steel. The selected deposition parameters were as 280 W in laser power, 30 μm in layer thickness, 1200 mm/s in scanning speed and 140 μm in hatch space. A stripe partition with S scanning tracks of laser in each layer and a scanning rotation of 45° between successive layers were used. In terms of contour scanning, a laser power of 150 W and a scanning speed of 1250 mm/s were applied during L-PBF.
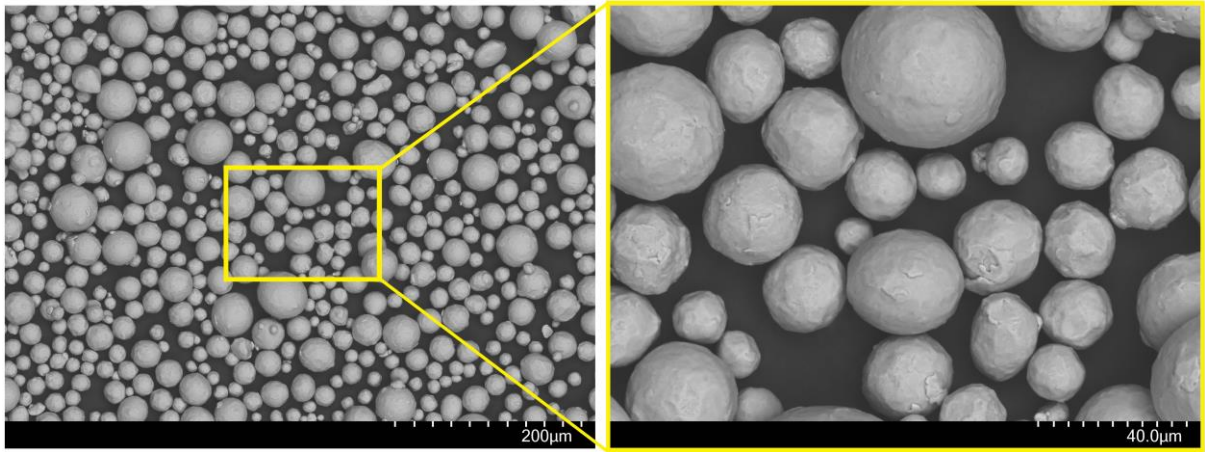
Figure 3.2 Raw Ti6Al4V powders used for L-PBF process.

Table 3.4 Alloy composition with mass percentage (wt%) of raw Ti6Al4V powders.

Element	Ti	Al	V	Fe	O	N	H	C
Mass (wt%)	Balance	6.2234	4.4044	0.1574	0.0886	0.0038	0.0021	0.0043

3.2 Surface features

In this section, outer surfaces on flat cuboid samples and internal surfaces on 1/6 straight channels were characterized considering the differences of morphology and microstructure. It should be noted that morphology of sample surfaces was characterized by using a confocal optical microscope (VHK-5000, Keyence, Japan), a white-light interferometer (Bruker NPFLEX, USA) and two scanning electron microscopes, one is TM4000Plus (Hitachi, Japan) and another one is Sigma 300 (ZEISS, Germany). Phase identification was performed by a D500 X-ray diffractometer (Siemens, Germany) with Cu Kα radiation at 40 kV and 30 mA. The cross sections of L-PBF 316L stainless steel samples and some original 316L stainless steel powders were sequentially mounted, ground, polished and etched in a solution that consists of HCl (37 %), HNO_3 (65 %) and Glycerin (99 %) with volume ratio of 3:1:1 before morphological characterization. The cross sections of L-PBF Ti6Al4V samples and some original Ti6Al4V powders were sequentially mounted, ground, polished and etched in a solution that consists of HF (48 %), HNO_3 (65 %) and distilled water with volume ratio of 1:5:10 before morphological characterization. In terms of surface roughness, although white-light interferometer can be used to measure surface area roughness such as Sa, it is not suitable to use this equipment to measure rough surface
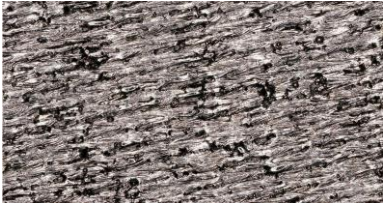
roughness because the information of the measured surface is difficult to be completely collected. Hence, L-PBF surface roughness values in this study were measured via a contact surface roughness tester (SJ210, Mitutoyo, Japan). Generally, SJ210 can measure various surface roughness such as Ra, Rq and Rz. Ra, which is widely accepted in industries, represents an average length between peaks and valleys and the deviation from the mean line on surface. Rq is the square root of the sum of the squares of the individual heights and depths from the mean line. Rz presents a vertical distance from the highest peaks to the lowest valleys. Considering that polishing process may show different effects on peaks and valleys on rough L-PBF surfaces, Ra and Rz are more suitable for this study. Thus, Ra and Rz values were measured on the same sample before and after polishing to study polishing effects. The measuring conditions are specified in ISO 1997 as follows: cut-off wavelength of shortwave filter is 2.5 µm and cut-off value is 0.8 mm. The evaluation length was 4 mm for each measurement and the values of Ra and Rz were calculated by averaging five measurements.

3.2.1 Surface features of flat 316L stainless steel samples

Raw flat surfaces on various cuboid samples of L-PBF 316L stainless steel are rough with various surface features according to the optical microscopy (OM) images in Table 3.5. Raw morphologies of different surfaces were further measured as presented in Figure 3.3. It is obvious that both adhesion of powders and sintered area can be found on various surfaces. The existence of laser scanning traces on top surface (Figure 3.3a) is due to its last deposition sequence while the adhered powders are caused by surface tension from molten pools [25]. What is noteworthy is that the area ratios of adhered powders and sintered area vary on different surfaces. To be more specific, area proportion of adhered powders and sintered areas are in the order as follows. The sintered area is most obvious on top surface, then becoming less and less on face up (Figure 3.3b) and side surfaces (Figure 3.3c), finally almost disappears on face down surface (Figure 3.3d). In terms of adhered powders, their area ratio shows an opposite trend. The top surface has the minimal adhesion of powders while

the face down surface has the maximum. The explanation for different ratios of adhered powders is that apart from the top surface, all the other surfaces are surrounded by powders during the whole printing process [93]. In addition, heat conduction and gravity droop have stronger effects on face down and side surfaces than face up surfaces [95]. Comparing with the top surface that powders exhibit single adhesion state (Figure 3.3a), powders tend to have multi-powders adhesion on the face up surface (Figure 3.3b). The multi-powders aggregation state might be caused by the staircase effect on an inclined surface.

Table 3.5 Information and OM images of flat surfaces on L-PBF 316L stainless steel cuboid samples at 200x magnification.

Surface type	Angle θ with horizontal plane	OM images of raw surfaces
Top	0°	
Face up	30°	
Side	90°	
Face down	60°	

500μm
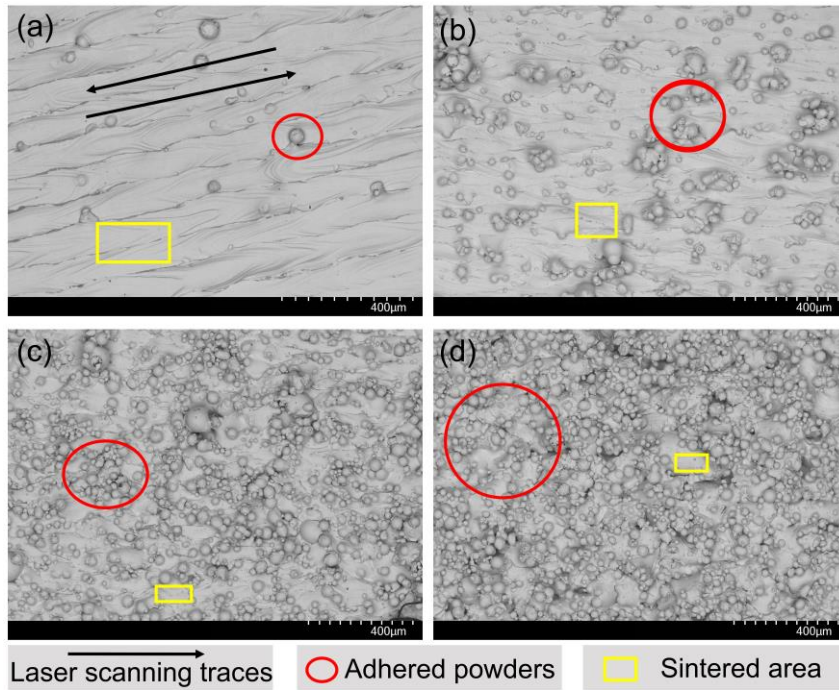
Figure 3.3 SEM images of raw flat (a) top, (b) face up, (c) side and (d) face down surfaces of L-PBF 316L stainless steel.

In order to identify the differences between adhered powders and sintered area, phase and microstructure characterization of original 316L stainless steel powders and raw L-PBF surfaces have been carried out. X-ray diffraction spectra of raw powders, flat top, face up, side and face down surfaces are shown in Figure 3.4. The patterns clearly show that both 316L stainless steel powders and L-PBF built surfaces are characterized by the only presence of FCC austenite phase. Figure 3.5 shows cross section morphology of the same 316L stainless steel powder after mechanical polishing and then etching. The mechanically polished powder shows a spherical morphology while the etched powder exhibits a coarser dendritic microstructure. The microstructure of raw powder is caused by its gas atomized preparation process. By investigating the cross sections of raw surfaces, morphologies of adhered powders and sintered areas are illustrated in Figure 3.6. Two cross sections with different lengths on top sample were selected to show surface features. The printing lengths of top cross section 1 and 2 are 10 mm and 5 mm, respectively (Table 3.1). As highlighted by black arrows, laser scanning traces are visible on cross section 1 (Figure 3.6a) while molten pools with clear curved edges could also be noticed on cross section 2 (Figure 3.6b). Adhered powders with spherical morphology and sintered area consisting of the

edges of molten pools can be found on top (Figure 3.6b), face up (Figure 3.6c), side (Figure 3.6d) and face down (Figure 3.6e) surfaces. Furthermore, the staircase effect derived from layer principle of L-PBF is apparent on both face up and face down surfaces (Figure 3.6c and e). In terms of the microstructure of adhered powder and sintered area, it seems that the adhered powder has a coarser microstructure and different etching color comparing to the sintered area on various L-PBF surfaces. It should be noted that although the spherical adhesives at location I and II in Figure 3.6d show similar morphology, their etched microstructures are different.
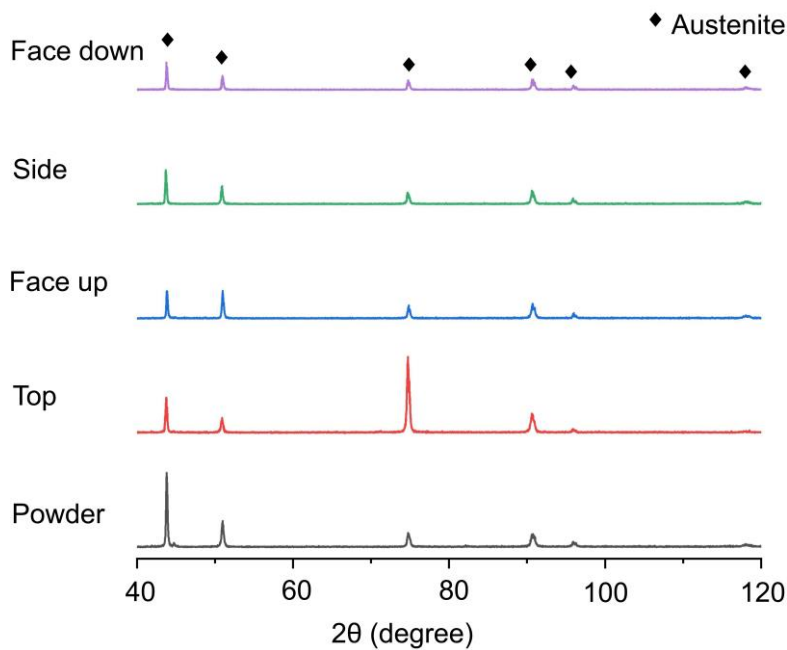
Figure 3.4 X-ray diffraction patterns of raw 316L stainless steel powders, L-PBF flat top, face up, side and face down surfaces of 316L stainless steel.
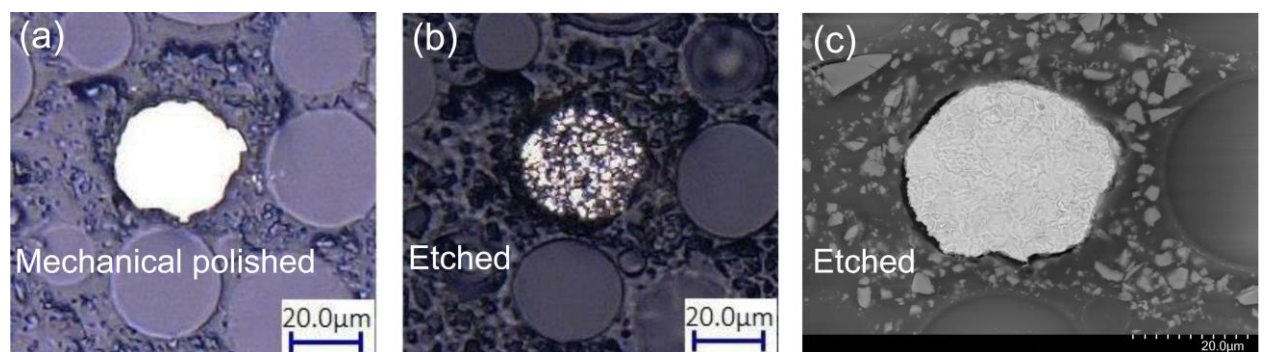
Figure 3.5 Cross-sectional morphologies of a mounted 316L stainless steel raw powder showing (a) OM image after mechanical polishing, (b) OM image of the powder in (a) after etching, and (c) SEM image of the etched powder in (b).

For clear morphology identification of L-PBF surface features, two spherical protrusions (I and II) in Figure 3.6d have been further characterized and shown in Figure 3.7. Their mechanically polished cross sections are illustrated in Figure 3.7a and d, respectively. It can be seen that I (Figure 3.7a) and II (Figure 3.7d) protrusions have similar spherical morphology after mechanical polishing. Then, the polished cross sections were etched as can be seen in Figure 3.7b and e, where some differences can be observed. With high magnification images from SEM in Figure 3.7c and f, it is clear that etched un-sintered part has the same coarser dendritic structure as raw 316L stainless steel powder while sintered area shows a fine cellular and dendritic microstructure. The finer microstructure of sintered area is believed to be caused by rapid melting and solidification during L-PBF [140]. It is also found that spherical protrusion I (Figure 3.7c) is in fact consisted of partially melted powder and sintered area while II (Figure 3.7f) is an un-sintered powder. Thus, it is inaccurate to tell whether it is an un-sintered powder or sintered area by simply observing the spherical morphology on L-PBF surfaces. The sintering degree and bonding state of surface features should be precisely identified through etched cross sections or other treatment methods.

Based on the microstructural differences of un-sintered powders and sintered area, when looking back on Figure 3.6, it is clear that un-sintered powders and sintered areas on various L-PBF surfaces can be easily distinguished because they possess different etched microstructures. As can be seen in Figure 3.6a and b, there are minimal adhesion of un-sintered powders on the top surface. The asperity of sintered area is a result of fluctuations in the upper part of molten pools. On the face up surface (Figure 3.6c), there are more adhered un-sintered powders than the top surface. Meanwhile, the partially overlapped edges of molten pools increase the asperity of sintered area. Although there are more un-sintered powders on side surface (Figure 3.6d), the roughness of sintered area is lower than the face up surface. This is due to that staircase effect on the face up surface causes higher roughness of sintered area when comparing with the side surface. In Figure 3.6e, there are plenty of un-sintered

powders which almost cover the whole face down surface, and the sintered area on the face down surface exhibits the maximum roughness.
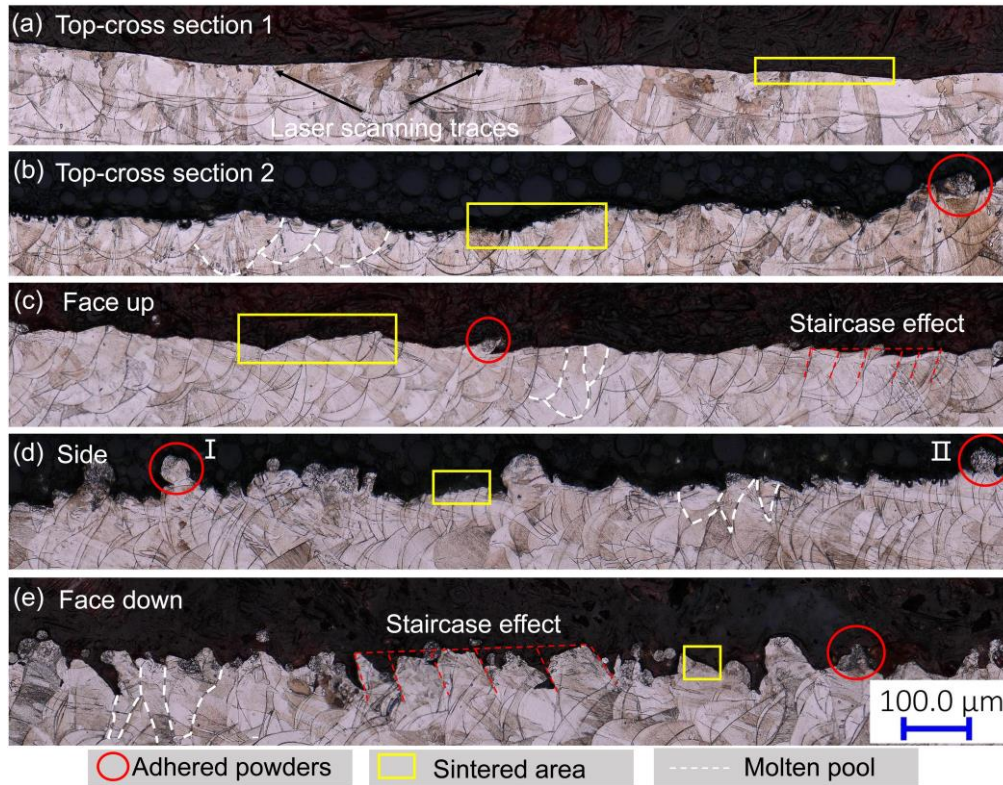
Figure 3.6 Morphologies of etched cross sections on raw L-PBF (a) top cross section 1, (b) top cross section 2, (c) face up, (d) side and (e) face down surfaces of L-PBF 316L stainless steel flat samples.
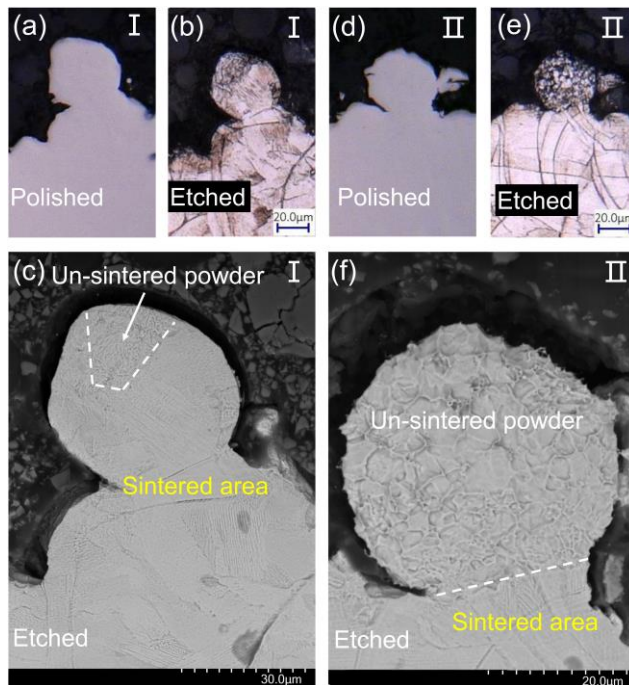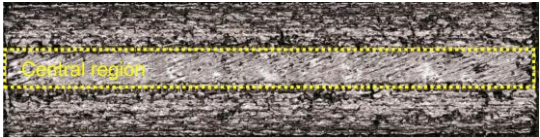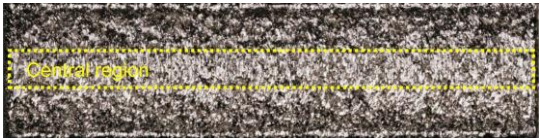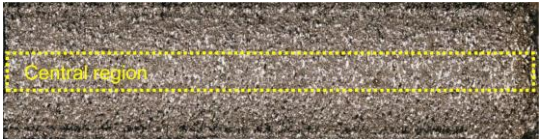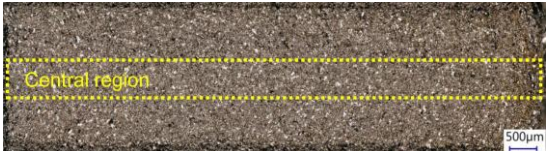
Figure 3.7 Morphologies of (a) mechanically polished, (b) then etched cross section, (c) high magnification of the etched cross section at position I and (d) mechanically polished, (e) then etched cross section, (f) high magnification of etched cross section at position II in Figure 3.6d.

3.2.2 Surface features of 316L stainless steel

Straight 1/6 channels with L-PBF internal top, face up, side and face down surfaces (Table 3.1) were prepared and the angles between inner surfaces and the horizontal plane are summarized in Table 3.6. According to the OM images in Table 3.6, it is obvious that a central region with a width of about 500 μm on the top inner surface maintains the same uniform morphology as the L-PBF flat top surface [141].

Table 3.6 Information and OM images of various inner surfaces on L-PBF 316L stainless steel 1/6 straight channels with magnification of 200.

Surface type	Angle θ with horizontal plane	OM images of raw inner surfaces marked as blue in Table 3.1 and their central regions
Top	0°	
Face up	30°	
Side	90°	
Face down	60°	

Higher magnification of OM and SEM images for the inner central regions of as-built 1/6 straight channels are shown in Figure 3.8 and Figure 3.9,respectively. Similar surface features such as adhered powders and sintered areas with different area proportions are presented on various L-PBF surfaces. The behavior of molten pools and deposition angles are related to the final surface quality of L-PBF parts. Because of the interaction of powder bed and laser, raw 316L stainless powders on the powder bed would be attracted by molten pools during printing process due to surface tension, resulting in the adhesion of powders [89]. After laser scanning, molten pools solidify rapidly and form sintered area. It is noted that laser scanning traces on top surface

(Figure 3.9a) are caused by laser scanning process since top surface is the last deposited layer [89, 94]. In terms of surface characteristics, adhered powders have the lowest area proportion and minimum quantity on top surface (Figure 3.9a), then becoming more and more on face up (Figure 3.9b) and side surfaces (Figure 3.9c), finally shows the maximum quantity on face down surface (Figure 3.9d). The area ratios of sintered area exhibit an opposite trend to adhered powders on L-PBF surfaces (Figure 3.8 and Figure 3.9) because of the influences of staircase effect, edge effect, gravity, overhanging effect etc. [25, 31, 95]. Furthermore, all inner surface areas of the side 1/6 straight channel possess uniform morphology based on the same printing angle.
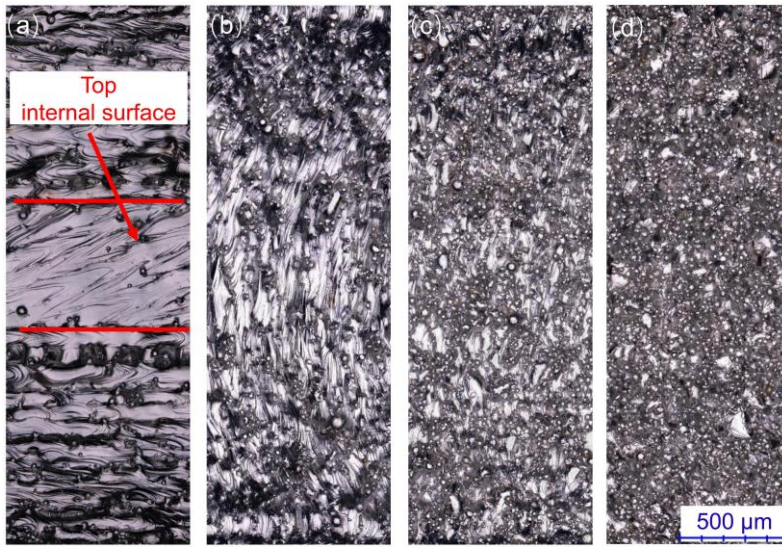
Figure 3.8 OM images of internal (a) top, (b) face up, (c) side and (d) face down surfaces on raw L-PBF 316L stainless steel 1/6 straight channels.
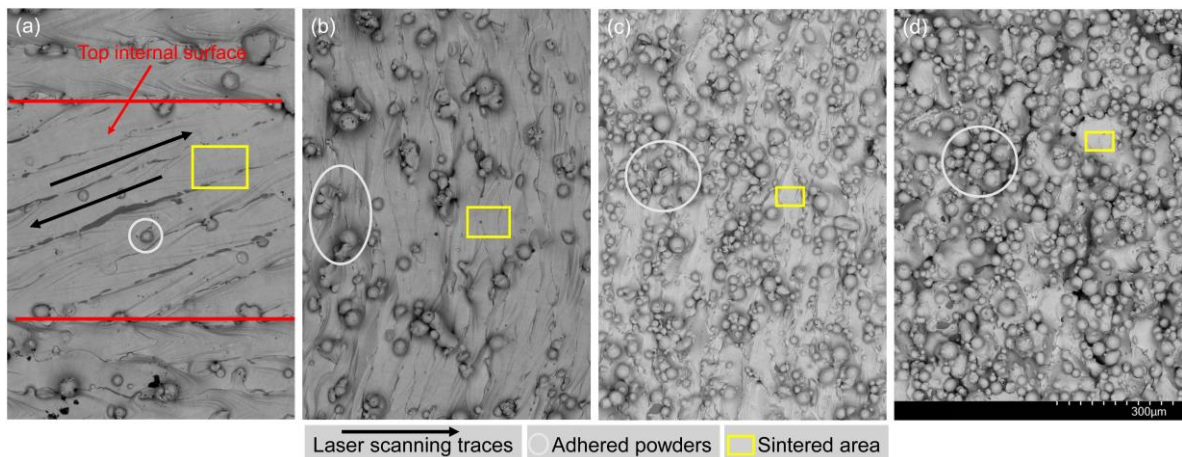
Figure 3.9 SEM images of the central region of internal (a) top, (b) face up, (c) side and (d) face down surfaces on raw L-PBF 316L stainless steel 1/6 channels.

Figure 3.10 and Figure 3.11 show surface features on etched cross sections of the central regions of as-printed various 1/6 straight channels. Consistent with the characterization results on various flat 316L stainless steel surfaces made by L-PBF in section 3.2.1 [141], there are un-sintered powders and sintered area on various internal surfaces [25]. It can be seen that the microstructure of un-sintered powders is different from the sintered area and exhibits varied etching color in optical images. Clear identification of morphology is shown in Figure 3.11, where un-sintered powders have a coarser dendritic microstructure, while sintered area on various 316L stainless steel inner surfaces shows a fine cellular and dendritic microstructure [140]. Un-sintered powders on L-PBF surfaces display the same microstructure as raw 316L stainless steel powders, which is caused by their gas atomized preparation process [141]. Compared with un-sintered powders, the microstructure of sintered area is a result of rapid melting and solidification during laser scanning [89]. Based on the microstructure differences of surface features, when looking back on Figure 3.8 and Figure 3.9, the face up and side surfaces have higher quantity of un-sintered powders than the top surface. And the maximum quantity of un-sintered powders is found on the face down surfaces. In comparison to un-sintered powders, the area ratios of sintered area exhibit an opposite trend on different L-PBF surfaces since the top surface shows the highest area proportion of sintered area while the face down surface has the lowest area ratio of sintered area. In addition, surface features with narrow connections occur more frequently on the face up surfaces compared to other surfaces. It should be noted that the central region of different 1/6 channels possess the same morphology and surface features as their corresponding flat and outer L-PBF surfaces [141]. Thus, the central region on inner surfaces of various L-PBF 316L stainless steel 1/6 channels will be characterized in chapter 4, 5 and 6 for fundamental study.
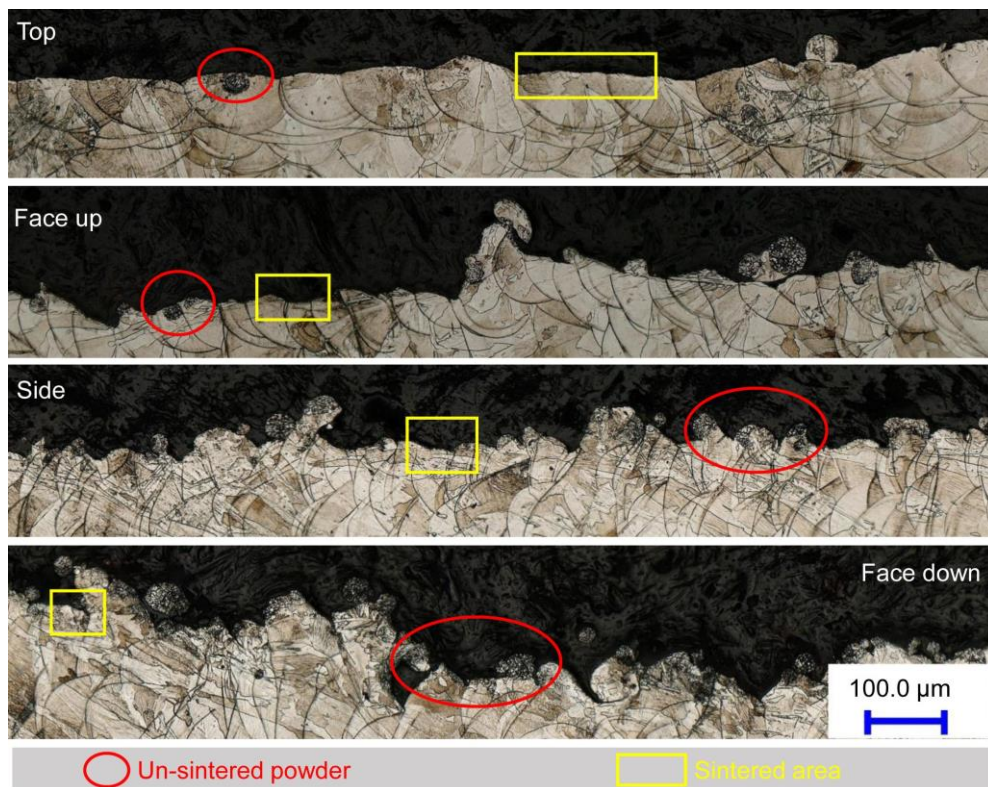
Figure 3.10 OM images of raw cross section on central regions of various L-PBF 316L stainless steel inner surfaces.
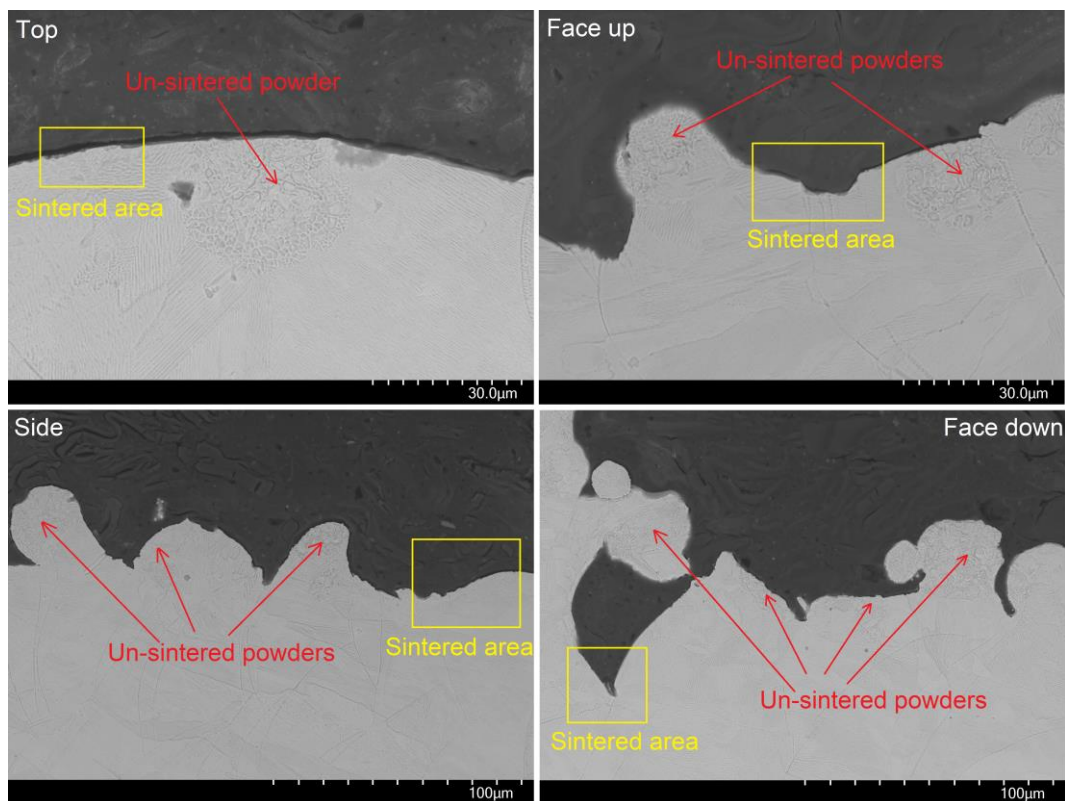
Figure 3.11 SEM images of raw cross sections on central regions of various L-PBF 316L stainless steel inner surfaces.

3.2.3 Surface features of Ti6Al4V

According to the surface characterization results in section 3.2.1 and 3.2.2, surface features and morphology of raw L-PBF flat or outer surfaces with specific deposition angles are identical to the corresponding inner surfaces. Surface morphology of L-PBF Ti6Al4V with various flat surfaces on cuboid samples and internal surfaces on 1/6 straight channels are shown in Figure 3.12 and Figure 3.13, respectively. Notably, flat surfaces and internal surfaces with the same printing angles of L-PBF Ti6Al4V also possess similar surface morphology. Moreover, a central region with a width of about 500 μm on the top inner surface of L-PBF Ti6Al4V 1/6 channel maintains the same morphology as the L-PBF flat top surface. It is obvious that there are adhered powders and sintered area on each type of L-PBF surfaces. Laser scanning traces on top surface (Figure 3.12a and Figure 3.13a) is formed because of its last deposition sequence while the adhered powders are caused by surface tension from molten pools [25]. In addition, area ratios of adhered powders and sintered area vary on different surfaces. In terms of area proportion of adhered powders and sintered areas, the sintered area is most obvious on the top surface, then becoming less and less on the face up (see Figure 3.12b and Figure 3.13b) and side surfaces (see Figure 3.12c and Figure 3.13c), finally have the lowest area proportion on the face down surface (see Figure 3.12d and Figure 3.13d).For adhered powders, their area ratio shows an opposite trend. The top surface has the minimal adhesion of powders while the face down surface has the maximum. Please note that adhered powders on the top surface exhibit single adhesion state, while other surfaces show multi-powders adhesion.
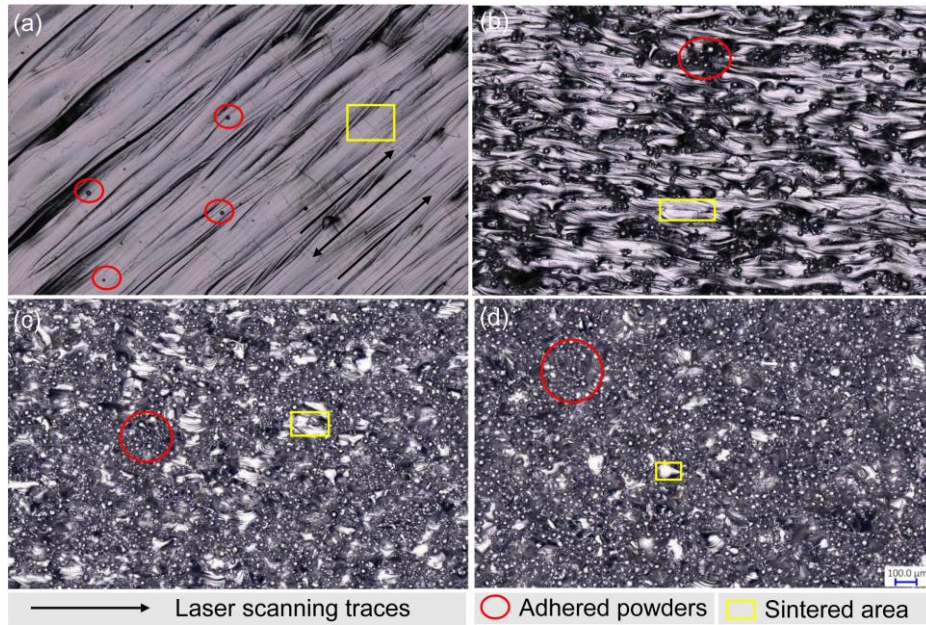
Figure 3.12 OM images of (a) top, (b) face up, (c) side and (d) face down surfaces of flat L-PBF Ti6Al4V cuboid samples in which laser scanning traces are marked by black arrows, adhered powders are marked by red circles and sintered areas are marked by yellow boxes.
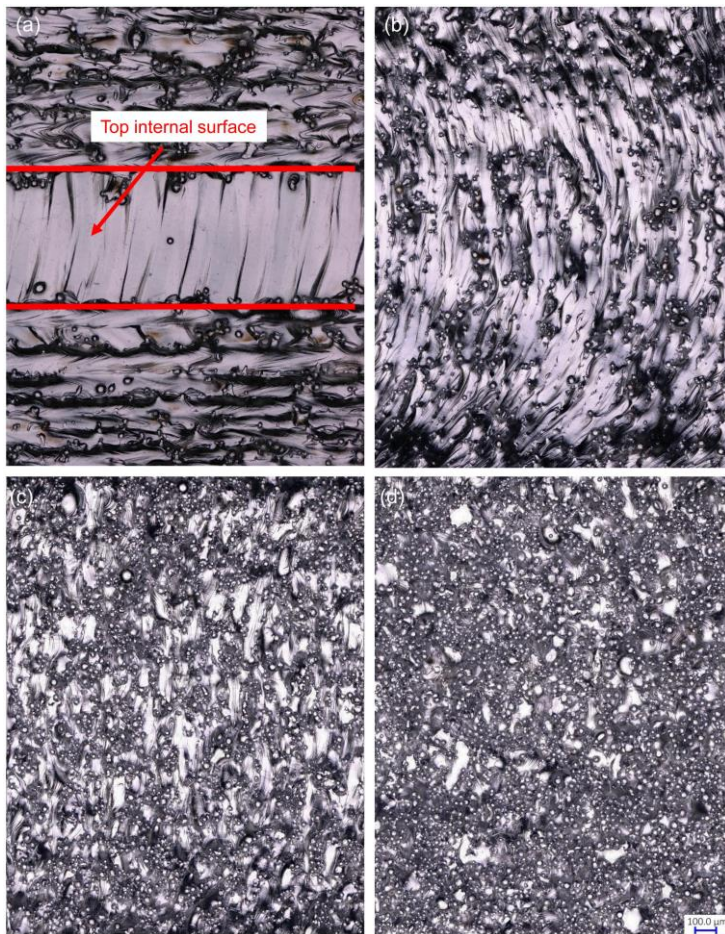
Figure 3.13 OM images of internal (a) top, (b) face up, (c) side and (d) face down surfaces on raw L-PBF Ti6Al4V 1/6 straight channels.

To characterize surface features of L-PBF Ti6Al4V in detail, cross section microstructure of the central regions of various internal channels was analyzed as shown in Figure 3.14. It is worth noting that L-PBF Ti6Al4V surfaces with specific printing angles exhibit similar morphology to that corresponding L-PBF 316L stainless steel surfaces on cross sections. In addition, microstructure of un-sintered powders is slightly different from sintered area and exhibits varied etching color on the cross sections of various L-PBF Ti6Al4V surfaces as can be seen in Figure 3.14. Higher magnification of microstructure of raw Ti6Al4V powders and microstructure of a raw L-PBF Ti6Al4V inner side surface are shown in Figure 3.15 and Figure 3.16, respectively. It can be seen that raw Ti6Al4V powders have lamellae α phase with a relatively coarse microstructure, while sintered area of L-PBF Ti6Al4V possesses acicular α phase [142]. Based on the contrast of secondary electron image and the same area with backscattered electron image in Figure 3.16, sintered area and un-sintered powders on L-PBF Ti6Al4V surface can be identified because un-sintered powders on surface have the same microstructure as raw Ti6Al4V powders. It should be noted that the central region of different 1/6 channels possess the same morphology and surface features as their corresponding flat and outer L-PBF surfaces. Thus, the central region on inner surfaces of various L-PBF Ti6Al4V 1/6 channels will be characterized in chapter 4, 5 and 6 for fundamental study.
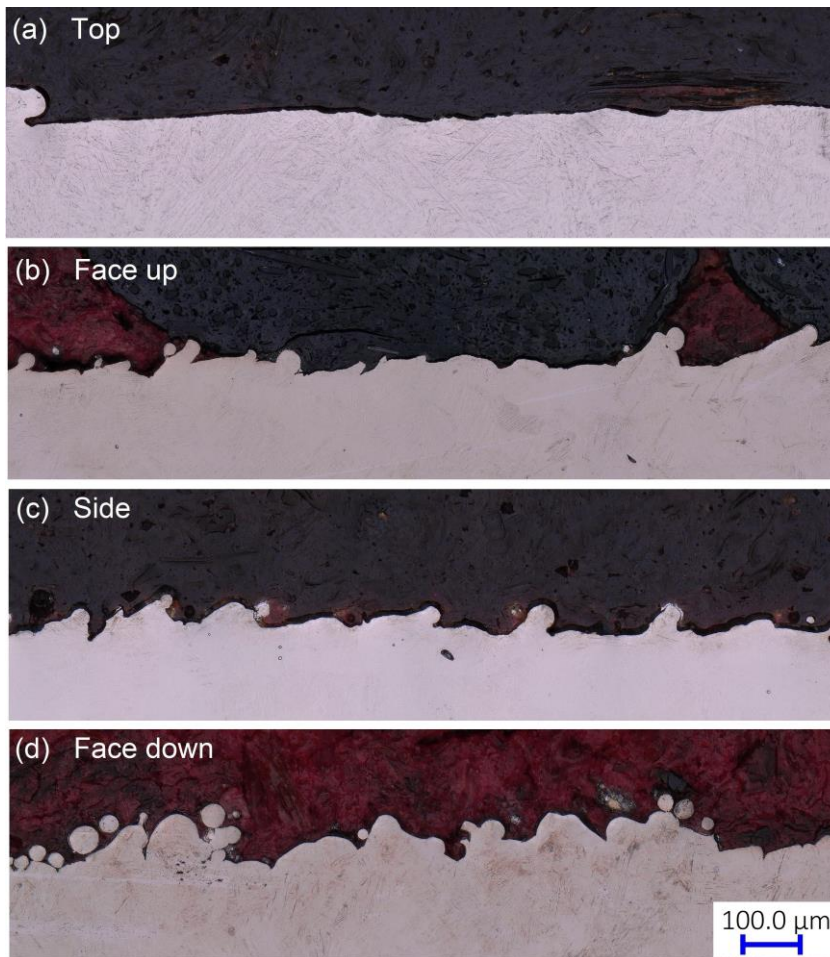
Figure 3.14 Raw morphologies of etched cross sections of central regions on various L-PBF Ti6Al4V internal (a) top, (b) face up, (c) side and (d) face down surfaces.
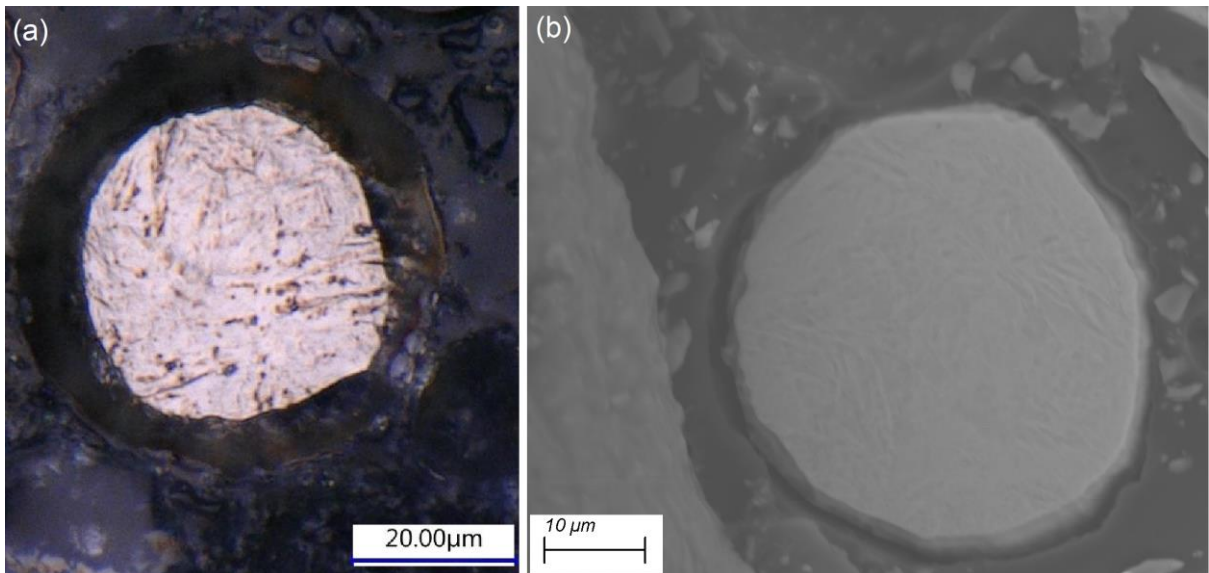
Figure 3.15 Cross-sectional morphologies of mounted Ti6Al4V raw powders (a) after etching under OM and (b) after etching under SEM.
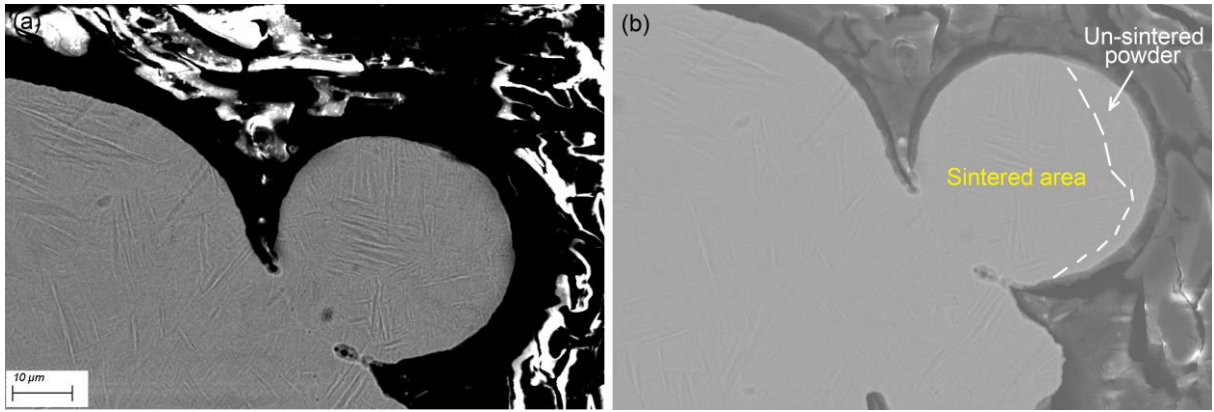
Figure 3.16 Surface features of an etched cross section in (a) secondary electron image and the same area in (b) backscattered electron image on the inner central region of a raw L-PBF Ti6Al4V side 1/6 channel.

3.2.4 Raw surfaces of internal structures

CAD models with various internal structures in Table 3.2 have been printed, as can be seen in Figure 3.17 for the application development of polishing in Chapter 7. Considering that single BCC lattice structure has the same surface features as multiple BCC lattice structure, only raw surfaces of multiple BCC lattice structures were characterized in this section to represent surface characteristics of L-PBF BCC lattice structure. Morphology of raw inner surfaces of multiple BCC lattice structures and channels has been characterized to analyze internal surfaces on these L-PBF structures. According to the complexity of internal structures and their printing orientations, there are one or mixed surface types on different L-PBF internal structures.
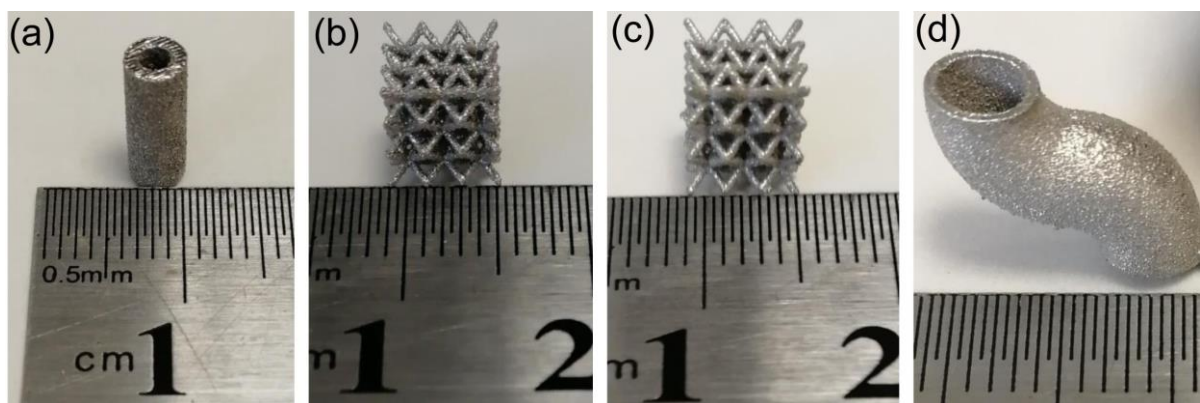
Figure 3.17 Pictures of L-PBF (a) Ti6Al4V straight channel with inner diameter of 2 mm, (b) Ti6Al4V BCC lattice structure, (c) 316L stainless steel BCC lattice structure and (d) 316L stainless steel conformal channel based on the CAD models in Table 3.2.

Inner surface of straight Ti6Al4V channel shows a uniform surface along the whole channel (Figure 3.18a). It is clear that internal surface of the straight channel (Figure 3.18b) have the same morphology as L-PBF Ti6Al4V side surface (Figure 3.12 and Figure 3.13) due to the same printing angle.
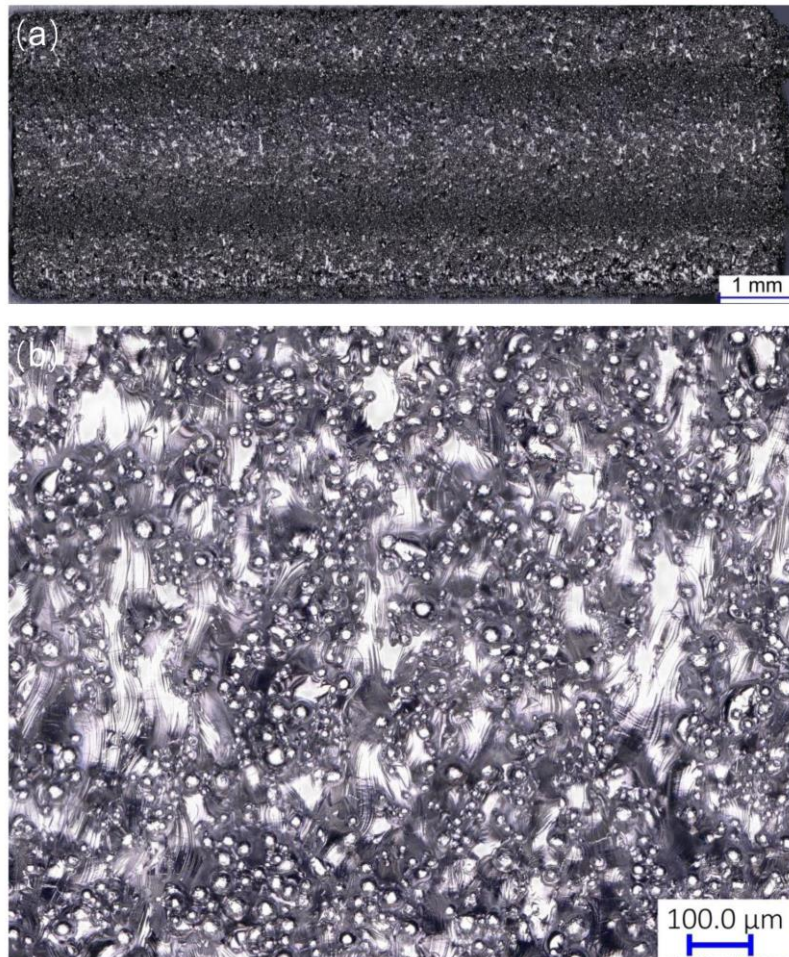
Figure 3.18 OM images of inner surfaces of (a) a sectioned straight Ti6Al4V channel with inner diameter of 2 mm with magnification of 200 and (b) its morphology with magnification of 500.

In terms of BCC lattice structures, schematic diagrams of different views and struts on side view are illustrated in Figure 3.19. Correspondingly, OM images of top, side and bottom views of L-PBF BCC lattice structures with different printing materials are shown in Figure 3.20 and Figure 3.21, respectively. For Ti6Al4V BCC lattice structure (Figure 3.20), connections of struts on the top view have the same morphology as L-PBF Ti6Al4V top surfaces (Figure 3.12 and Figure 3.13), while struts showed similar surface morphology with L-PBF Ti6Al4V face up surfaces (Figure 3.12 and Figure 3.13). On the side view, connections of struts possess the same morphology with L-PBF

Ti6Al4V side surfaces (Figure 3.12 and Figure 3.13). Apart from connections, upper struts (Figure 3.20) have mixed morphology with L-PBF Ti6Al4V side and face down surfaces (Figure 3.12 and Figure 3.13), while lower struts (Figure 3.20) show similar morphology with L-PBF Ti6Al4V side and face up surfaces. Different from the top and side views, all area on the bottom view (Figure 3.20) has similar morphology with L-PBF Ti6Al4V face down surfaces. As the same CAD models were used for printing, surface characteristics on different views of L-PBF 316L stainless steel BCC lattice structures also exhibit consistent combinations of various surface types (Table 3.6 and Figure 3.8) with Ti6Al4V BCC lattice structures as illustrated in Figure 3.21.
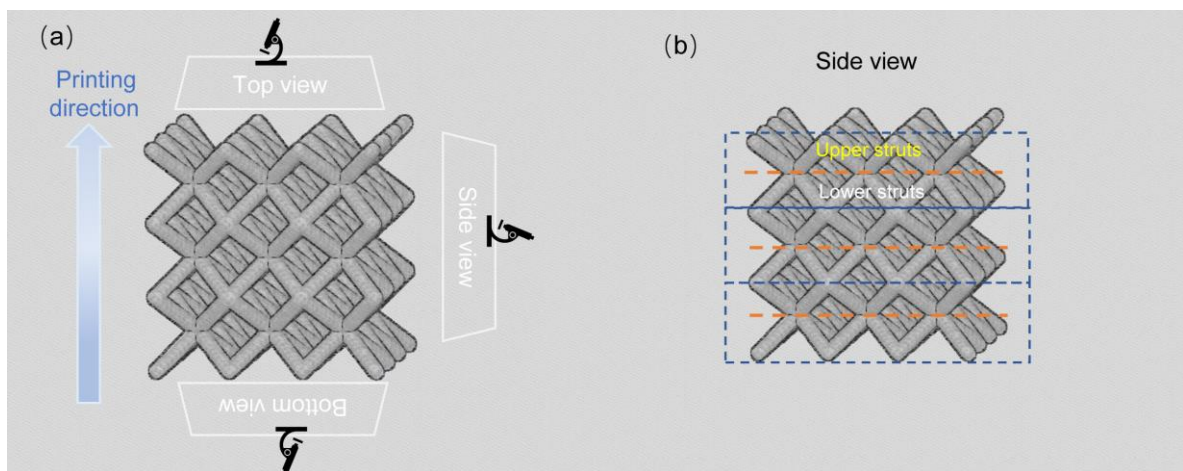
Figure 3.19 Schematic diagrams of (a) top, side and bottom views of BCC lattice structures and (b) upper and lower struts on the side view.
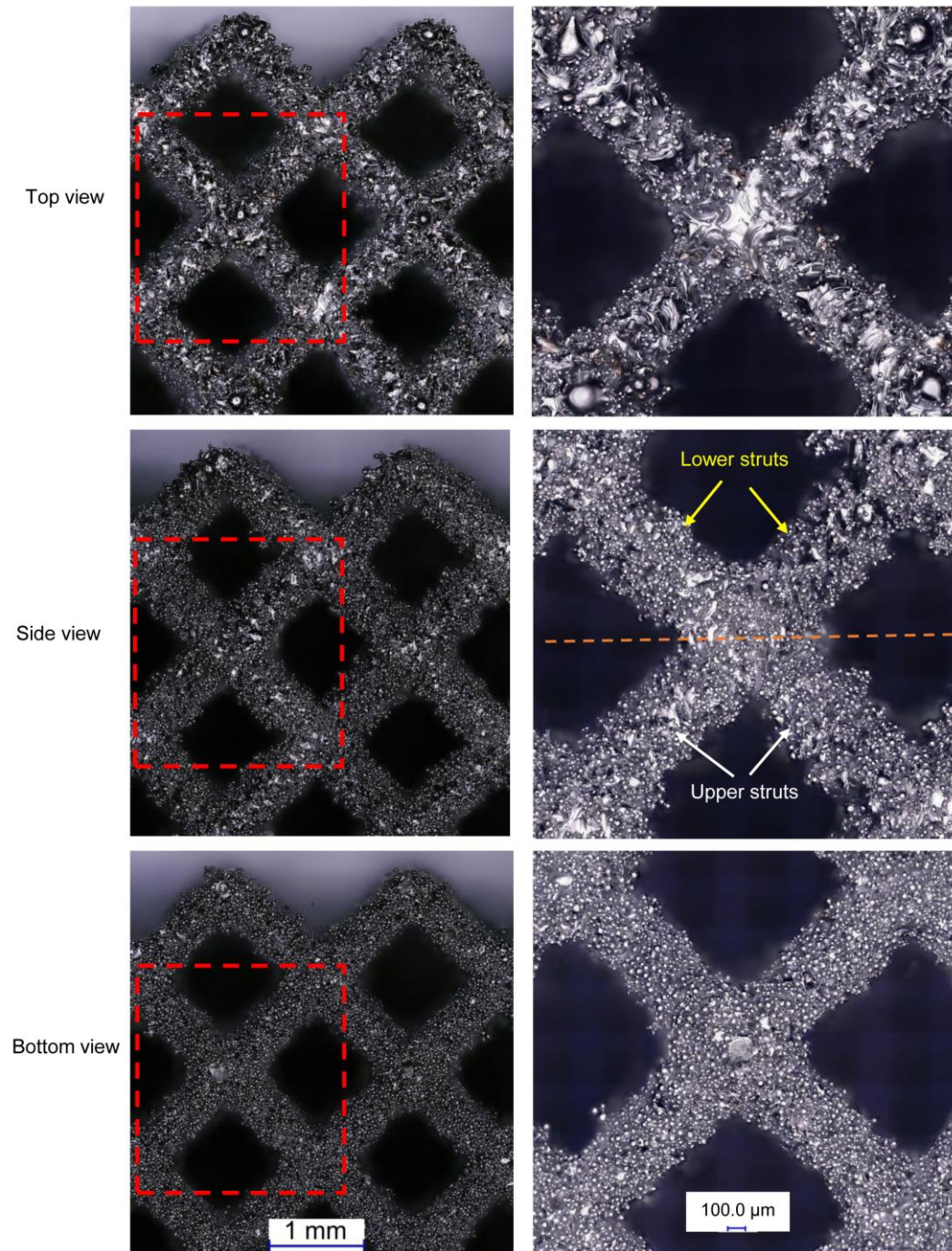
Figure 3.20 Surface morphology of top, side and bottom views of L-PBF Ti6Al4V BCC lattice structures in which the OM images on the left side with a single cell in a red box are at magnification of 200, and the right images are morphology in the red box at a magnification of 500.
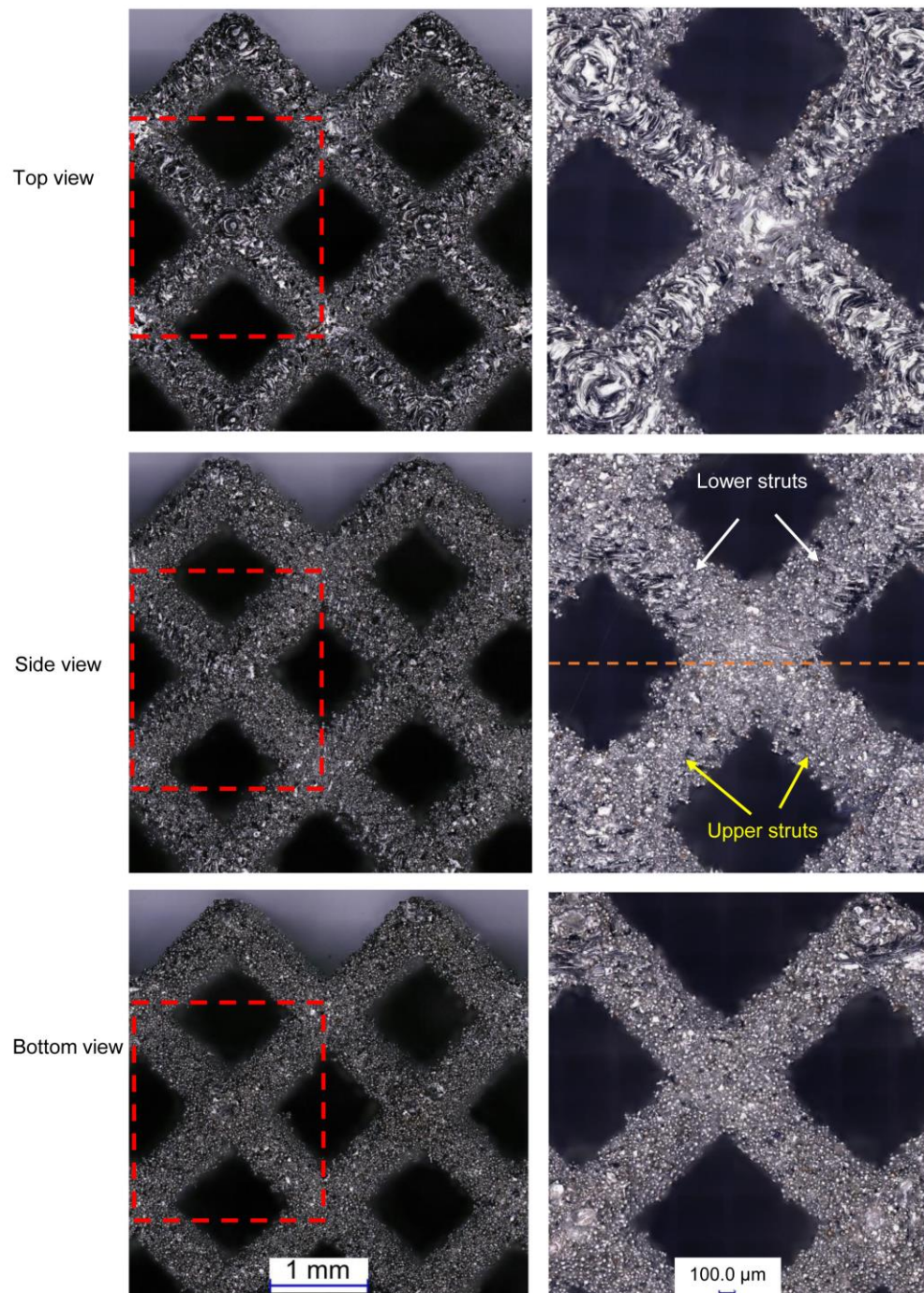
Figure 3.21 Surface morphology of top, side and bottom views of L-PBF 316L stainless steel BCC lattice structures in which the OM images on the left side with a single cell in a red box are at magnification of 200, and the right images are morphology in the red box at a magnification of 500.

OM images of the internal surface of a L-PBF 316L stainless steel conformal channel are shown in Figure 3.22. There are different types of surfaces on its inner surface considering the changes of deposition angles during L-PBF. Based on the surface characteristics of L-PBF 316L stainless steel face up, side and face down

surfaces (see Table 3.6 and Figure 3.1), different types of inner surfaces can be clearly distinguished on the conformal channel (see Figure 3.22).
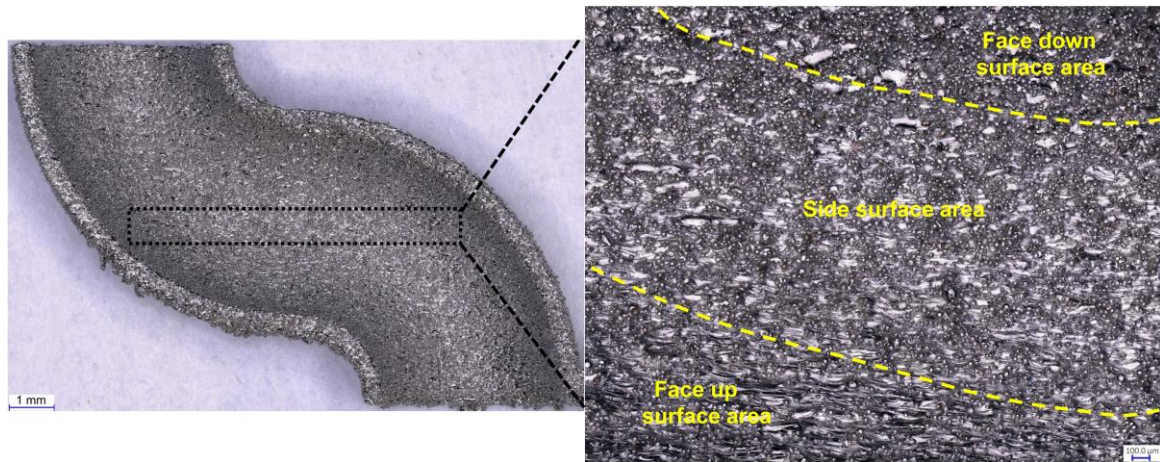
Figure 3.22 OM images of the inner surface of a half L-PBF 316L stainless steel conformal channel with magnification of 200, and the inner surface area marked with a black box with magnification of 500.

3.3 The development of polishing system

Given that the complexity of L-PBF surfaces would affect polishing process, as well as surface finish, the lack of appropriate polishing methods hinders the productization process of L-PBF internal structures. It is therefore essential to develop an efficient polishing system or method for L-PBF internal structures. Compared to single polishing process, hybrid methods usually exhibit superior polishing ability according to the literature review in Chapter 2. Although hybrid polishing methods show great potential to achieve good surface finish of L-PBF internal structures, the selection of appropriate single polishing method for the hybrid process is important, meanwhile, the development of an innovative polishing system or machine is also challenging. Based on the literature review, it can be understood that EP and AFP show great potential in developing an effective hybrid polishing process for L-PBF internal structures. In this section, the potential of combing EP and AFP for an innovative hybrid polishing process and the development of an innovative hybrid polishing system are analyzed and presented.

3.3.1 Combination of EP and AFP

As reviewed in Chapter 2, EP and AFP both apply flowable media for polishing as seen in Figure 3.23. In EP, a sample (anode) and a cathode tool are immersed in an aqueous electrolyte. Moreover, the electrolyte is generally stirred or in a flow cycle that is driven by a pump. In terms of AFP, an external power such as a pump generally drives a mixture of abrasive particles and fluid passing through the sample surface to achieve material removal process. Therefore, the flowability of solution is the basic potential for combining these two methods for hybrid polishing.

Apart from the polishing media, EP and AFP also have complementary polishing characteristics based on their working principles. The limitations of AFP such as the long polishing time and low processing efficiency come from the use of low pressure and solution viscosity. Besides, the performance of AFP depends on the hardness and wear property of L-PBF materials. Although EP possesses a higher material removal rate than AFP attributing to the external power supply, a rough initial surface could impede a fast and effective EP process. In addition, EP is hard to achieve uniform surface finishing for workpieces with intricate geometries due to the limited accessibility of cathode tool. As summarized in Table 3.7, AFP is more suitable for polishing complex internal structures than EP since the placement of the cathode needs to be considered in EP. Although EP shows higher material removal rate than AFP, EP can be affected by much more factors such as electrolyte composition, temperature, initial surface roughness, inter-electrode gap and microstructure of workpiece. Despite the differences in polishing principle, the complementarity of single polishing process shows a promising combination of EP and AFP for L-PBF internal structures.
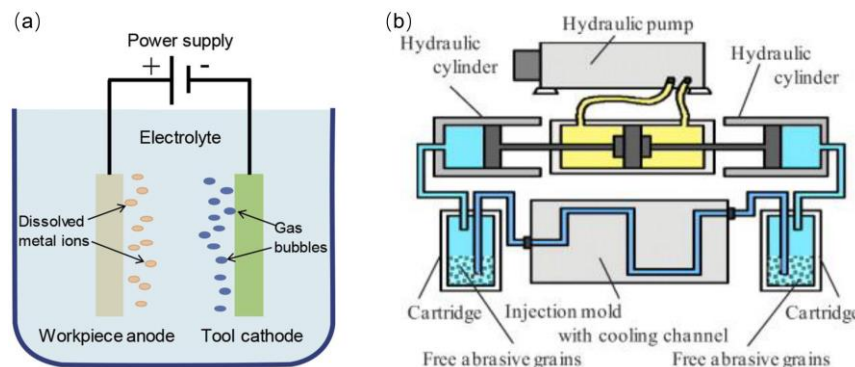
Figure 3.23 Schematic diagrams of (a) EP [143] and (b) AFP [14].

Table 3.7 Complementary polishing characteristics of EP and AFP.

Polishing character	EP	AFP
Suitability for polishing internal structures	Medium level	High level
Material removal rate	High level	Low level
Factor dependence	High level	Low level

Given that the combination of EP and AFP shows great potential, there are still challenges of combining EP and AFP as a new hybrid polishing process for L-PBF internal structures. In order to conduct EP, AFP and hybrid polishing, a polishing system consisting of various components needs to be developed first. Moreover, different components in the polishing system should be well connected and matched with each other.

3.3.2 Polishing system

To achieve EP, AFP, multiple polishing in different sequences and hybrid polishing for L-PBF internal structures, a hybrid polishing system that composes of various components has been developed. The schematic diagram of the hybrid polishing system is shown in Figure 3.24. Abrasive fluid containing abrasive particles and environmental-friendly liquid will be stirred, mixed and heated to a specific temperature in a storage tank. A pump with a maximum flow capacity of 20 L/ min will drive abrasive fluid passing through a polishing chamber to complete polishing process. To combine EP and AFP on the same system, a closed polishing chamber and corresponding fixture have been designed and fabricated by using insulating material and conduction elements in order to make them suitable for fixing samples and connecting electricity with an external electrochemical workstation. A pressure valve is installed before the polishing chamber in order to monitor the pressure of abrasive fluid inside the polishing chamber. A flowmeter is installed in the system loop to monitor the flow rate and temperature of polishing media in real-time.
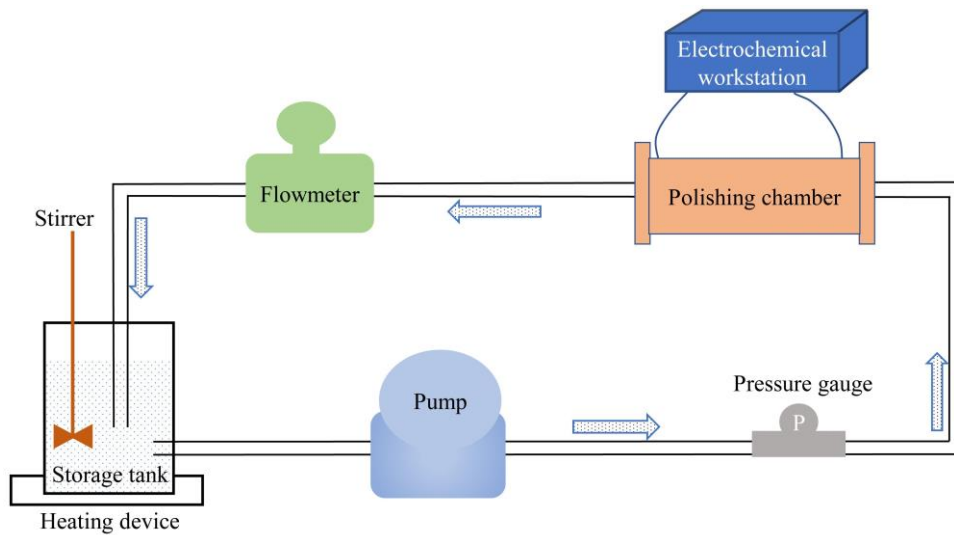
Figure 3.24 Schematic diagram of the developed hybrid polishing system.

The schematic diagrams of the cooperation between polishing chamber, corresponding fixture, L-PBF parts and cathodes are illustrated in Figure 3.25 and Figure 3.26. The inside of the chamber is designed to place L-PBF parts, cathode and the fixture. It should be noted that the inner surface of a L-PBF 1/6 straight channel and a plastic fixture could be combined into a whole straight channel with an inner diameter of 5 mm as can be seen in Figure 3.25a. During various polishing processes, different L-PBF samples will be fixed inside the chamber. In terms of EP and hybrid polishing, the position of cathode needs to be considered. The relative positions of a straight channel and a rod titanium cathode is shown in Figure 3.25b for inner surface polishing of L-PBF 1/6 straight channels and the whole Ti6Al4V straight channel with an inner diameter of 2 mm (see Table 3.2). In terms of other L-PBF internal structures, a titanium cylindrical wall is made as the cathode for BCC lattice structures (see Figure 3.25c), while a conformal cathode made of titanium wires is designed, fabricated and then used for conformal channels (see Figure 3.25d). For AFP and hybrid polishing, the direction of AFP and relative positions of L-PBF samples and fixture are indicated in Figure 3.26.
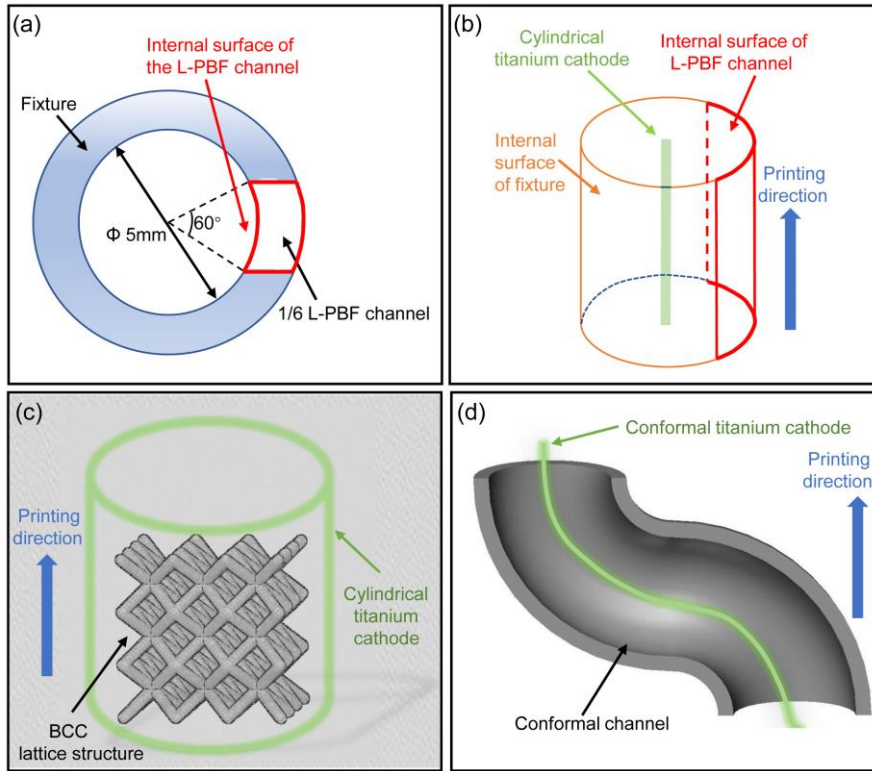
Figure 3.25 Schematic diagrams of the relative positions of (a) fixture and L-PBF 1/6 channels in the chamber, (b) cathode and straight channels, (c) BCC lattice structures and cathode and (d) conformal channels and cathode in the polishing of EP and hybrid polishing.
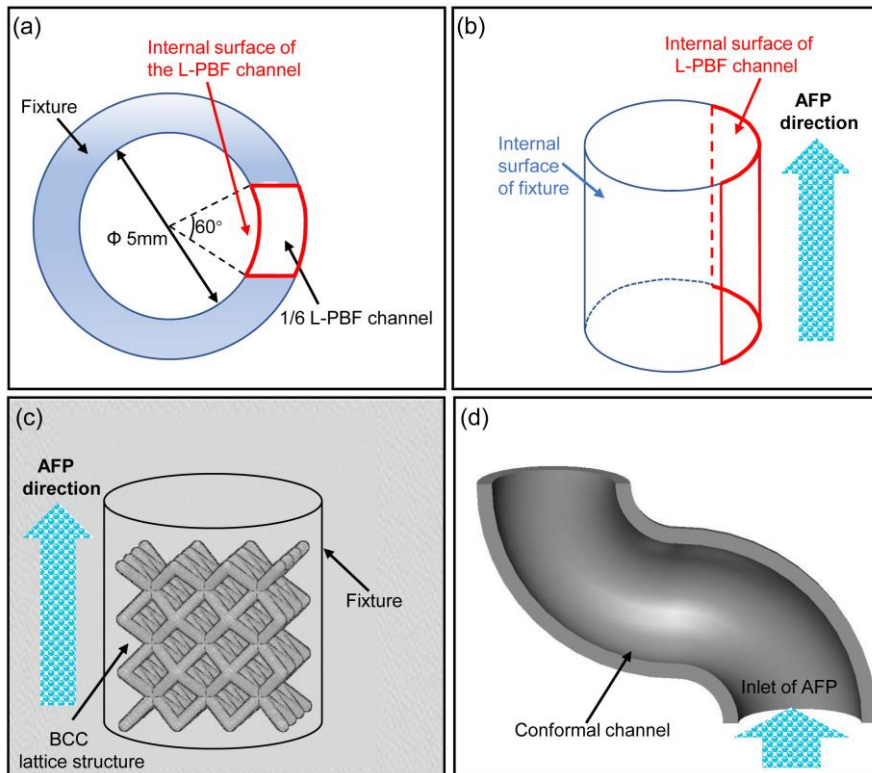
Figure 3.26 Schematic diagrams of the relative position of (a) fixture and L-PBF 1/6 channels in the chamber, (b) AFP direction and straight channels, (c) BCC lattice structures and AFP direction and (d) conformal channels and inlet of AFP during the polishing of AFP and hybrid polishing.

3.3.3 Polishing processes

By combining different types of liquid and abrasive particles in Table 3.8, the established hybrid polishing system can carry out EP, AFP and hybrid polishing, respectively. In this study, there are two ways for the combination of EP and AFP. The first one is multiple polishing in different sequences, which means that EP and AFP would be carried out in different sequences for L-PBF internal structures on the hybrid polishing system. The second is to combine EP and AFP into one polishing process, called hybrid polishing.

Table 3.8 Different types of polishing on the developed hybrid polishing system.

Solution	Abrasive particles	Polishing type
Electrolyte	No	EP
Water	Yes	AFP
Electrolyte	Yes	Hybrid polishing

3.4 Summary

This chapter delivers preparation of L-PBF samples, characterization of L-PBF surface features and the establishment of the hybrid polishing system for L-PBF internal structures. Main conclusions are summarized as follows:

(1) Despite the differences of printing parameters and materials, L-PBF 316L stainless steel and Ti6Al4V show similar surface morphology with specific printing angle. The central regions with a width of about 500 μm on various L-PBF inner surfaces maintain the same morphology of corresponding flat surfaces, and are used to study polishing effects in chapter 4, 5 and 6 respectively.

(2) Un-sintered powders and sintered area are common surface features on L-PBF top, face up, side and face down surfaces. In addition, one or more different inner surfaces are present on L-PBF internal structures based on the variation of printing angles on specific inner structures.

(3) The established hybrid polishing system can be employed to carry out EP, AFP, multiple polishing in different sequences and hybrid polishing based on EP and AFP. The designed L-PBF samples and corresponding fixtures can cooperate with each other in the polishing chamber during various polishing processes.

Chapter 4. EP of L-PBF Internal Surfaces

4.1 EP of 316L stainless steel flat surfaces

4.1.1 Experimental and simulation approaches

EP experiments were conducted in a beaker with a three-electrode cell as illustrated in Figure 4.1. A CS310 electrochemical workstation (Wuhan CorrTest, China) was used to provide a potential of 2 V versus an Ag/ AgCl reference electrode (Fisher Scientific, Ireland). The counter electrode was made of titanium mesh in order to benefit the mixing of electrolyte. The electrolyte in this study mainly contained H_3PO4 (85 %), glycerol (99 %) and distilled water in which the proportion of distilled water was 40 percent. The selected electrolyte does not contain strong acid which means it is environmentally friendly. A stable experiment temperature of $60°C$ was controlled by using a hotplate stirrer, in which an optimized magnetic stirring speed of 480 RPM was applied. Different types of L-PBF flat surfaces on cuboid samples were facing the counter electrode with the same inter-electrode distance in all EP tests. Different types of L-PBF flat 316L stainless steel specimens in Table 3.1 were cleaned using distilled water in an ultrasonic agitation bath for 10 minutes and dried by air blowing before and after EP.
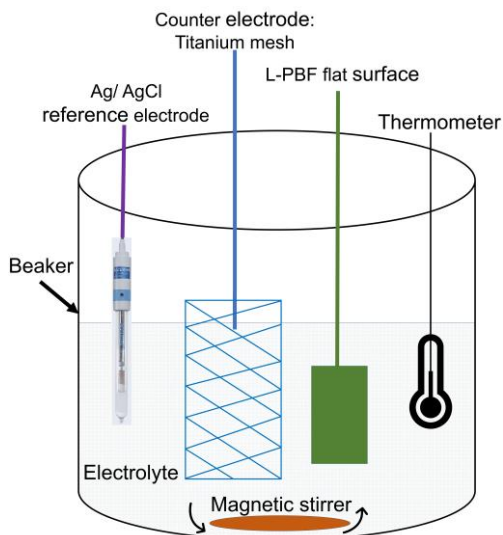
Figure 4.1 Experimental setup for EP process in the beaker.

To facilitate the analysis of material removal mechanism of L-PBF surfaces, a two-dimensional model was established in Ansys (18-2 Version) Electric Analysis System

to simulate current distribution of L-PBF surface during EP, seen in Figure 4.2. Rough L-PBF surface was functioned as the anode boundary. In addition, corresponding cathode and electrolyte boundaries were set to be insulated. To simplify simulation operations without loss of generality, the following assumptions were made [141].

(1) Current distribution at electrodes depends entirely on Ohm's law I= U/R, where I is current, U is the applied potential and R is the resistance of electrolyte. Noted that the electrodes are defined as equipotential surface. Therefore, the primary current distribution is simulated.

(2) The electrolyte is considered to have the same conductivity, temperature and concentration everywhere.

The resistivity of electrolyte was calculated by $\rho=R\cdot S/L$, where R is the resistance of electrolyte, S is sectional area which is the surface area of workpiece, L is the distance between workpiece and cathode during EP. R was obtained from experimental results because the applied potential, the distance between workpiece and cathode, workpiece surface area and current density were set in EP system or measured by the electrochemical workstation. Based on settings and calculations, the potential difference between two electrodes was set as 2V and the isotropic resistivity of electrolyte was set as 0.08 ohm*m.
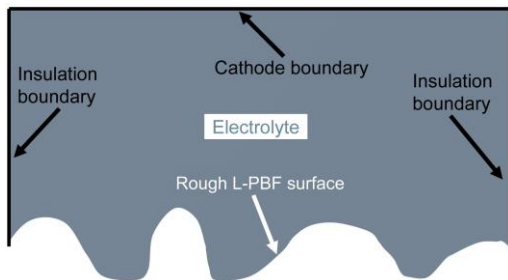
Figure 4.2 The two-dimensional model of raw L-PBF surface with electrochemical effect.

4.1.2 EP effects on various L-PBF flat surfaces

EP effects on morphology of various flat L-PBF 316L stainless steel surfaces after different processing times are shown in Figure 4.3. It is clear that the spherical adherents on L-PBF surfaces dissolve after EP of 2.5 and 5 minutes, while sintered area on top and face up surface typically remains its original morphology in the first 5 minutes. The results indicate that spherical adherents process a higher dissolution rate

than sintered area during EP. With the dissolution of spherical adherents, area proportion of exposed sintered area on face up, side and face down surfaces increases during this period. With an increase in EP time, laser sintering traces on the top surface are gradually blurred. Meanwhile, L-PBF surfaces become brighter after EP for 10 minutes. With EP for 20 minutes, the side and face down surfaces are much brighter than that of 10 minutes. However, some etching traces are noticed on the top and face up surfaces, and hence affect their brightness. It is believed that the appearance of etching trace is a result of the high-water concentration in electrolyte. In addition, most of the sintered area on the top and face up surfaces are electropolished from the beginning of EP due to the higher ratio. Thus, comparing with the side and face down surfaces, the longer EP time of sintered area on the top and face up surface is more prone to surface etching.
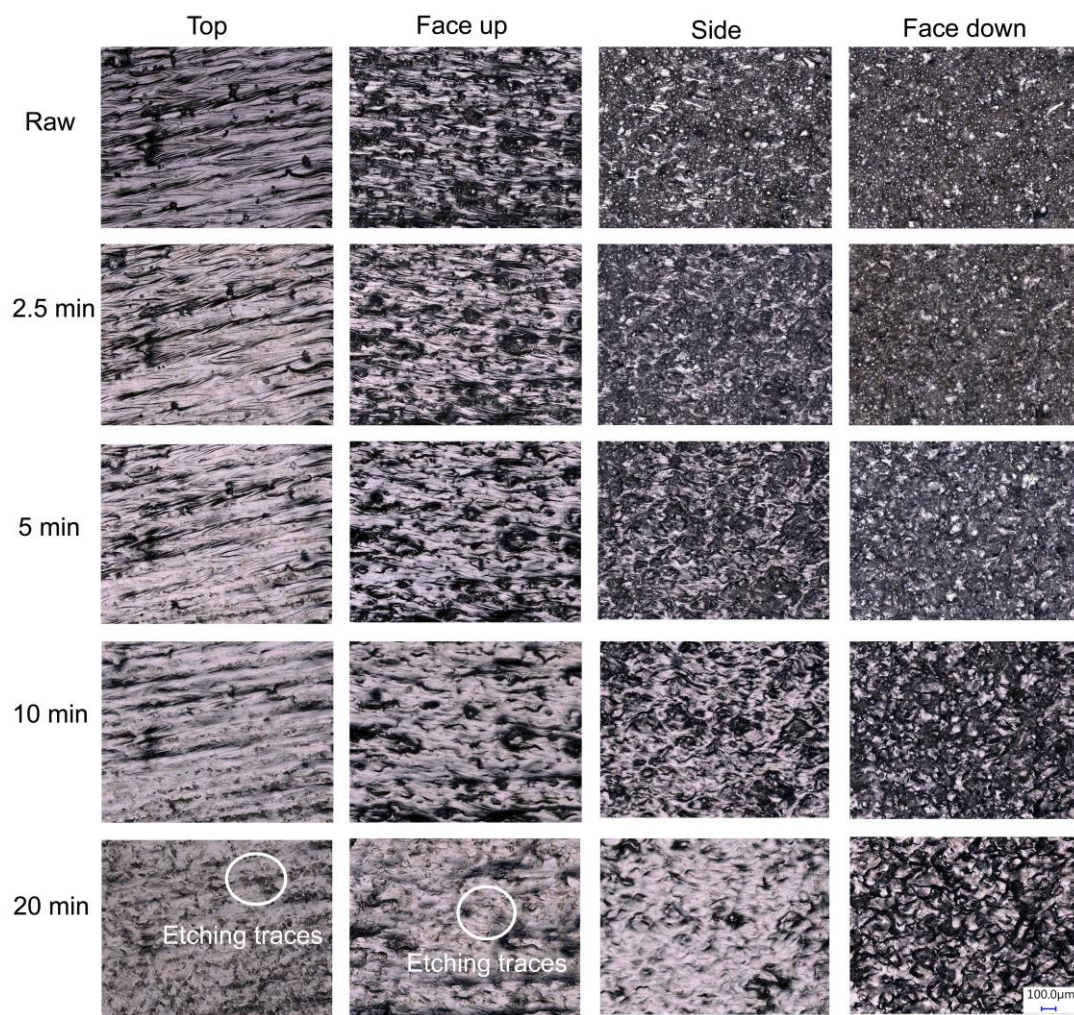
Figure 4.3 OM images of different flat surfaces of L-PBF 316L stainless steel before and after EP for 2.5, 5, 10 and 20 minutes, respectively.

Figure 4.4 shows the topography evolution of different L-PBF surfaces over EP processing time. It can be seen that various surfaces are gradually levelled over time. The adhesion of single spherical protrusion is obvious on raw top surface, while adhesion of protrusion aggregation is apparent on face up surface. Compared with the top and face up surfaces, there are more spherical protrusions on raw side and face down surfaces. The reason for high area ratio of spherical protrusions is the large quantity of adhered powders on side and face down surfaces. In the first 2.5 and 5 minutes, the size of most spherical protrusions on various surfaces get smaller gradually due to the dissolution by EP effect. The number of spherical protrusions on the top and face up surfaces is reduced significantly after EP for 10 minutes. Meanwhile, more uneven sintered area shows up on the side and face down surfaces. With an extension of EP time, various surfaces can be further levelled after 20 minutes.
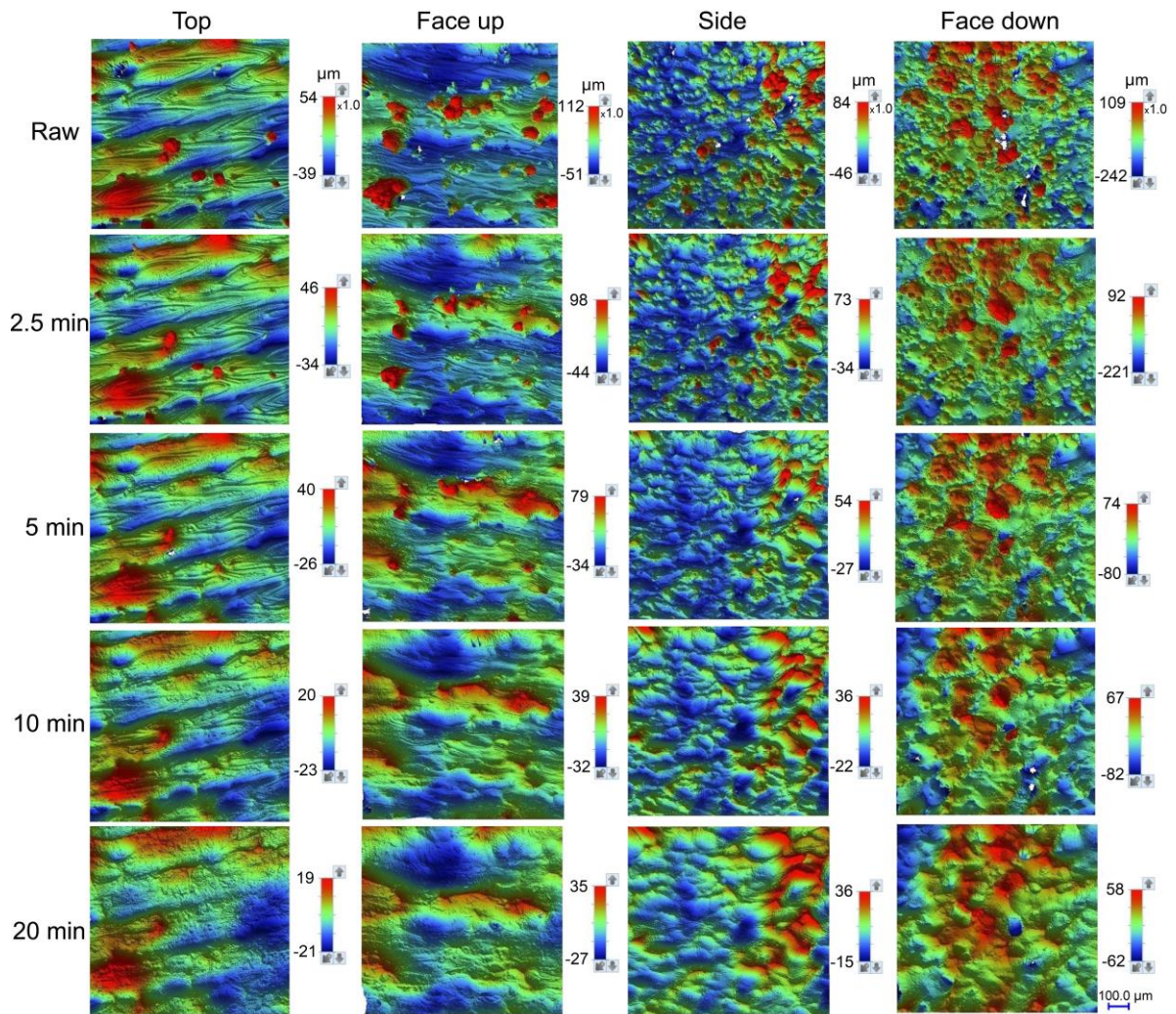
Figure 4.4 Topography of different flat surfaces of L-PBF 316L stainless steel before and after EP of 2.5, 5, 10 and 20 minutes, respectively.

4.1.3 Material removal process

Figure 4.5 shows morphologies of etched cross sections on various L-PBF flat surfaces after EP. According to the results in section 3.2.1, Figure 4.3 and Figure 4.4, it can be found that the un-sintered powders possess a different microstructure to the sintered area, un-sintered powders have different degrees of dissolution while sintered area almost keeps raw morphologies in the first 2.5 and 5 minutes of EP. After 10 minutes of EP, some un-sintered powders still remain on face down surface due to the massive adhesion of un-sintered powders. In terms of top, face up and side surfaces, only sintered area can be observed. From 5 to 10 minutes, protruding sintered areas are electropolished gradually on the top, face up and side surface. Then, the remaining sintered area on these surfaces would be levelled after 20 minutes. Compared with other surfaces, EP progress of the face down surface is slower because of a large quantity of un-sintered powders and high roughness of sintered area. It is observed that most of the sintered area on the face down surface only shows up after 10 minutes of EP because of the removal of adhered powders. In the next stage, the protruding sintered area on the face down surface could be electropolished from 10 to 20 minutes of EP.

High magnification images of un-sintered powders and sintered area after EP were characterized to further investigate material removal mechanisms. Figure 4.6 shows morphologies of typical un-sintered powders on various L-PBF surfaces after EP of 2.5 and 5 minutes. During this period, some un-sintered powders have experienced partially or mostly dissolution on L-PBF surfaces. Note that the bonding area with narrow connections on L-PBF surfaces is also partly dissolved. In other words, un-sintered powders with narrow connections with L-PBF surfaces show both dissolution of powder and bonding area in EP. To study the material removal process of sintered area during EP, morphologies of sintered area on L-PBF surfaces after EP of 5, 10 and 20 minutes are shown in Figure 4.7. Protruding sintered area is observed on all surfaces after EP of 5 minutes. With 10 minutes of EP, the protruding sintered areas are levelled on top, face up and side surfaces. In terms of face down surface, partially

dissolved un-sintered powders can still be seen after 10 minutes and remaining sintered areas are further levelled on various surfaces after 20 minutes. It is found that protruding sintered areas would be removed first, followed by the remaining sintered area. Again, the observation proves the dominant role of microstructure on material removal mechanisms of EP.
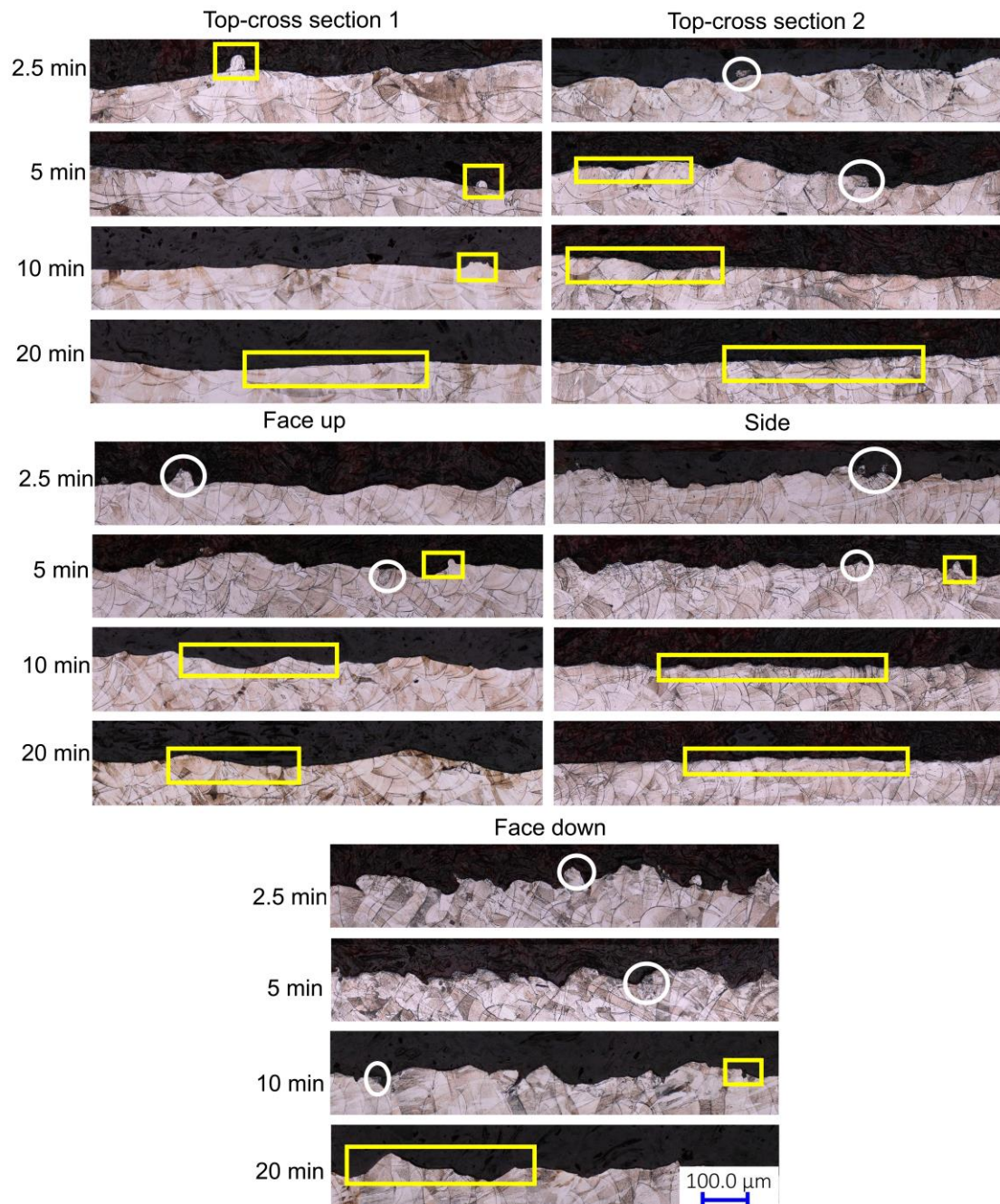
Figure 4.5 OM images of cross sections on L-PBF 316L stainless steel flat surfaces after different time of EP. The un-sintered powders are marked inside white circles while sintered area are marked by yellow boxes.
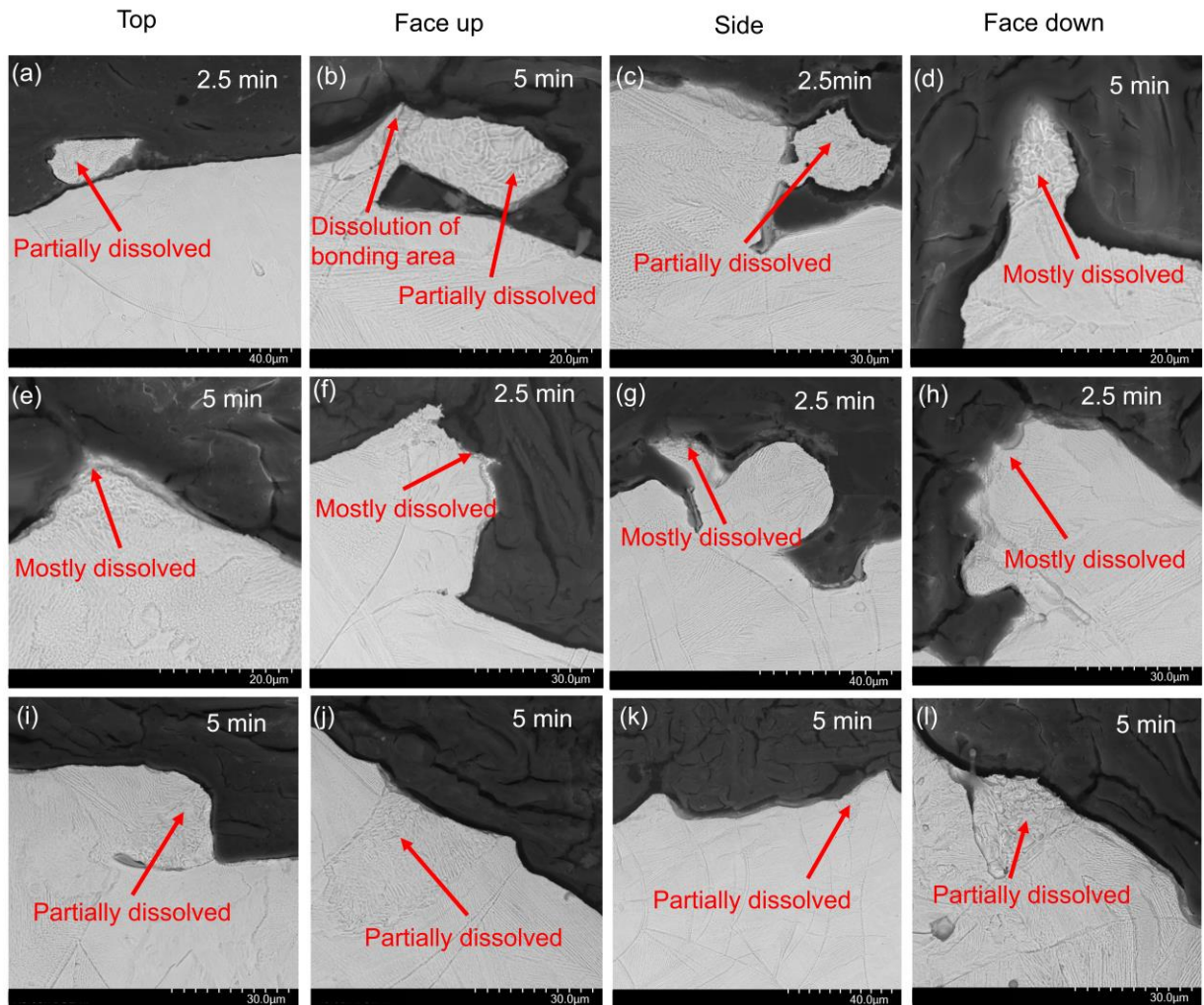
Figure 4.6 SEM images of dissolution of un-sintered powders on etched cross sections of L-PBF 316L stainless steel flat surfaces after EP of 2.5 and 5 minutes, respectively.
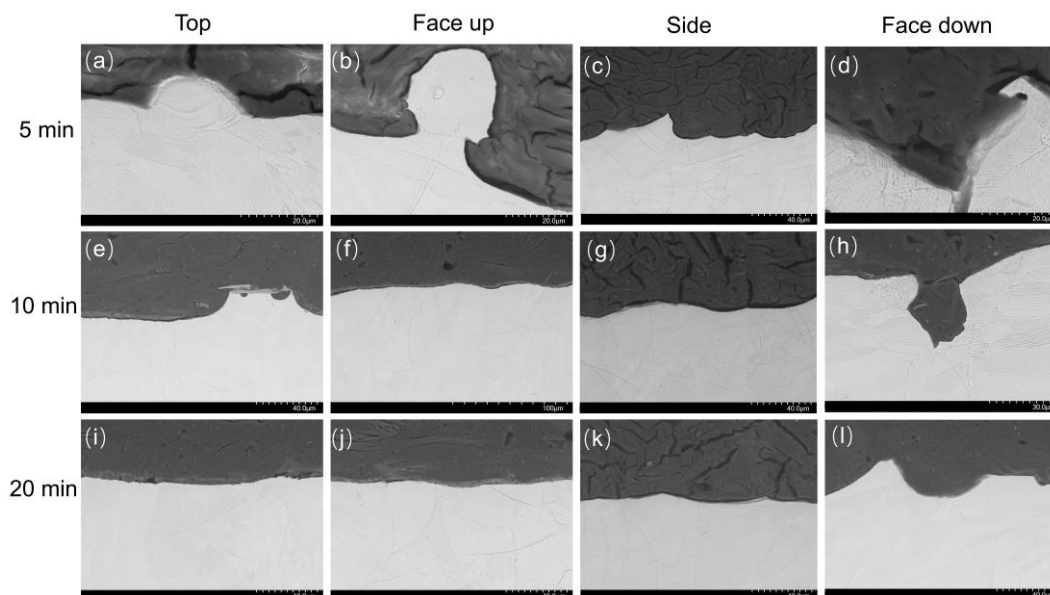
Figure 4.7 SEM images of sintered area on etched cross sections of L-PBF 316L stainless steel flat surfaces after EP of (a-d) 5 minutes, (e-h) 10 minutes and (i-l) 20 minutes, respectively.

According to the evolution of L-PBF surface features during EP, the decrease of roughness on various surfaces in Figure 4.8 could be well explained. Raw roughness values of L-PBF surfaces mainly depend on the superimposed effect of un-sintered powders and sintered area. With an action of EP, the removal of un-sintered powders generates newly exposed sintered area, which influences the surface roughness. In the case of top surface polishing, the newly exposed sintered area has insignificant effect on its roughness because un-sintered powders are rarely existed on the raw top surface (Figure 4.3). After processing for 5 minutes, the prominent decrease of roughness on the top surface (Figure 4.8a) is attributed to the fast removal of un-sintered powders. Then, the downward trend of Ra and Rz become insignificant due to a lower dissolution rate of sintered area. For face up surface, the newly exposed sintered area has limited effect on roughness during EP. The explanation is that sintered area has higher area ratio than un-sintered powders on face up surfaces (see Figure 4.3). A remarkable decrease of roughness on the face up surface is observed after 5 minutes of EP (see Figure 4.8b), attributing to the dissolution of most aggregated un-sintered powders (see Figure 4.4). Then, a reduction of Ra and Rz values shows up in the period of 5 to 20 minutes owing to the levelling of sintered area. Despite the area ratio of adhered powders on the side surface is higher than the face up surface (see Figure 4.3), raw surface roughness of side surfaces have lower values (Figure 4.8c) due to the combination of more evenly distributed powders and lower raw roughness of sintered area. After the dissolution of un-sintered powders in the first 5 minutes of EP, the decreasing trend of roughness on the side surface becomes more gradual from 5 to 20 minutes because of the lower dissolution rate of sintered area (see Figure 4.5). Un-sintered powders have contributed significantly to raw roughness on face down surface resulting from a coverage status of powders as shown in Figure 4.3. With the dissolution of most un-sintered powders after 10 minutes of EP (see Figure 4.5), sintered area shows a strong impact on its roughness values. Due to the highest degree of asperity of sintered area among various L-PBF surfaces, the face down surface has the highest Ra and Rz values after 10 minutes of EP. Then, the sintered area can be further levelled from 10 to 20 minutes as shown in Figure 4.8d.

Although there are different ratios of un-sintered powders and sintered area, raw roughness of face up and face down surfaces are influenced by the combination of un-sintered powders and sintered area. As a result, original face up and face down surfaces were measured with similar surface roughness values as shown in Figure 4.8b and d. With the extension of EP time, the asperity of sintered area plays a dominant role on Ra and Rz values. Because the sintered area of face down surfaces has higher asperity degree than face up surfaces, the face down surface shows higher Ra and Rz values than the face up surface after 20 minutes of EP in Figure 4.8.
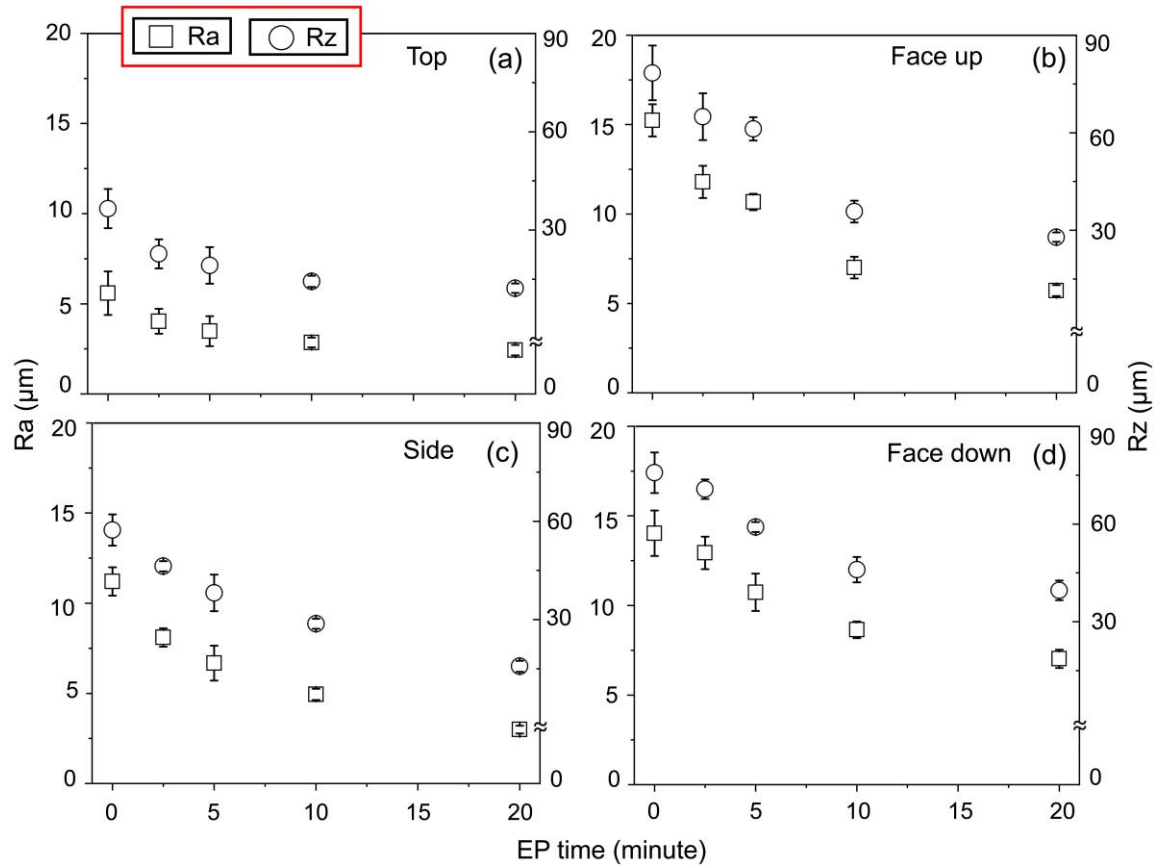
Figure 4.8 Ra and Rz values of flat (a) top, (b) face up, (c) side and (d) face down surfaces of L-PBF 316L stainless steel before and after EP of 2.5, 5, 10 and 20 minutes, respectively. Note that the left vertical axis represents Ra and the right vertical axis represents Rz.

4.1.4 Material removal mechanism

To further study EP material removal mechanisms of L-PBF surface features, un-sintered powders and sintered area for simulation are functioned as anode boundary shown in Figure 4.9a and b, respectively. The dimension, morphology, and location distribution of L-PBF surface features in the simulation are consistent with the surface

characterization results in Chapter 3. A 'fine' setting was used to generate the mesh of the built models as can be seen in Figure 4.9c and d, respectively. Current density simulations of typical un-sintered powders and sintered areas during EP are presented in Figure 4.9e and f [141], respectively. Based on the 2-dimensional models in Figure 4.9a and b, it could be seen that protruding and recessed positions on L-PBF surfaces have different current density distribution during EP, which could lead to different polishing effects. Some un-sintered powders that located at protruding positions have higher current density distribution and therefore dissolve first during EP. As a result, un-sintered powders which possess recessed locations exhibit higher material removal resistance than other un-sintered powders in EP. It should be noticed that tip area on an un-sintered powder has higher current density and would dissolve faster than the other area of the powder. Moreover, if bonding area is the tip area, there would be higher current density distribution on the bonding area as simulated in Figure 4.9e. Therefore, the removal of some un-sintered powders that have narrow bonding connections with L-PBF surfaces includes both the dissolution of the powders and bonding area. The simulation of un-sintered powders in Figure 4.9e is consistent with experimental results in Figure 4.6. Simulated current density distribution for sintered area is shown in Figure 4.9f. It could be seen that protruding sintered area has higher current density distribution and would dissolve faster than other sintered area. The simulation analysis for sintered area has conformity with EP results in Figure 4.7. Despite the current mesh size is helpful to analyse the differences in current density distribution of L-PBF surface features, the structured mesh size can be further improved considering the mesh sensitivity.
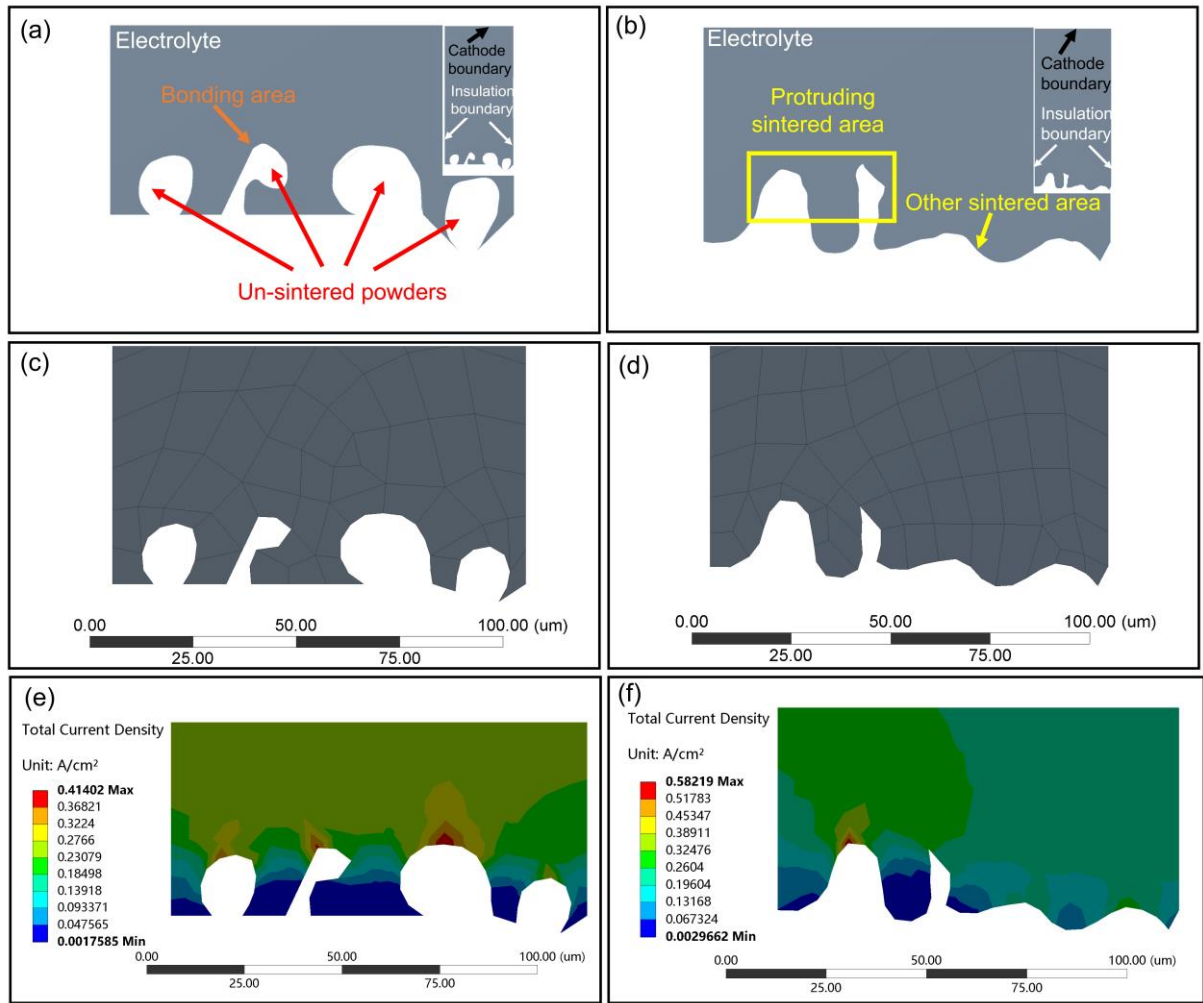
Figure 4.9 A two-dimensional model of (a) un-sintered powders, and (b) sintered area, (c) mesh of the model of un-sintered powders, (d) mesh of the model of sintered area, (e) simulated current density distribution of the un-sintered powders in EP; and (f) current density distribution of the sintered area during EP [141].

The higher reduction degree of Rz than Ra on face up and face down surfaces from 10 to 20 minutes of EP could be interpreted with the simulation results. After dissolution of un-sintered powders, obvious current distribution differences could be generated on remained sintered area if there exists high roughness. As can be seen in Figure 4.9f, peaks on sintered area have higher current distribution than valleys. After removal of un-sintered powders during EP, the levelling process of sintered area is continued from 10 to 20 minutes on face up and face down surfaces. The high asperity of sintered area on the face up and face down surfaces causes significant current distribution differences on protruding and valley positions. Thus, EP leads to the decreased height difference of sintered area and causes a bigger impact on Rz

than Ra as can be seen in Figure 4.8b and d. It should be noted that decrease of Ra and Rz values on specific L-PBF surface during EP are caused by various reasons considering the location, proportion and asperity of different surface features.

Based on experimental and simulation results, the material removal process of L-PBF flat 316L stainless steel surfaces during EP is shown in Figure 4.10. Considering the microstructure and location differences, features on raw L-PBF surfaces are illustrated as un-sintered powders and sintered area in Figure 4.10a. During EP, area on L-PBF surfaces that contacts with electrolyte would be dissolved. Because of the different dissolution rates of un-sintered powders and sintered area, un-sintered powders are dissolved firstly and have different degree of dissolution at the initial stage of EP as shown in Figure 4.10b. As EP progressed, un-sintered powders are removed and protruding sintered area is continued to be electropolished (see Figure 4.10c). Then, remained un-sintered area can be further levelled owing to the current distribution differences during EP as shown in Figure 4.10d.
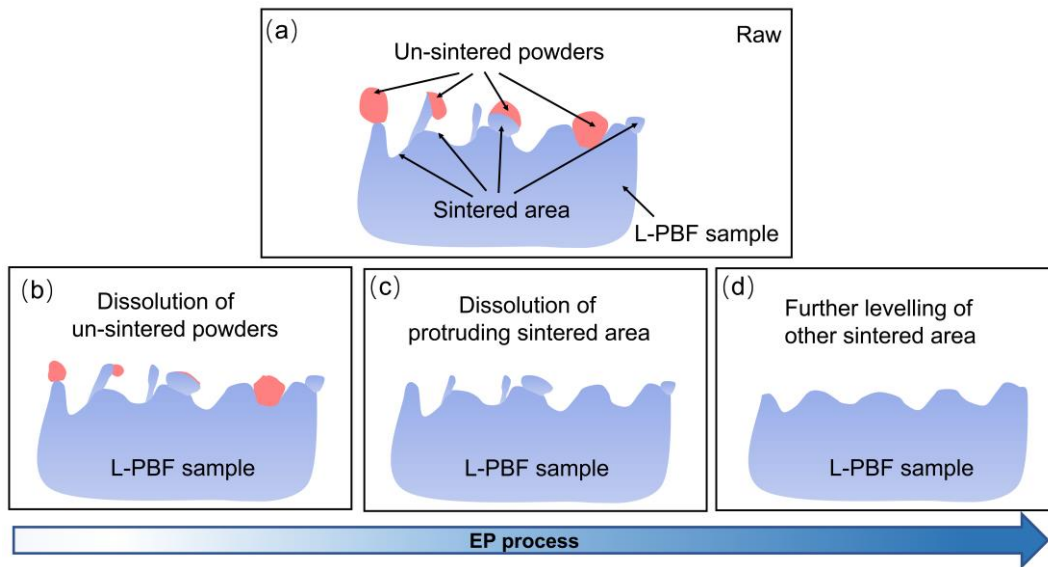
Figure 4.10 Schematic diagram of (a) raw surface features and (b-d) material removal process on L-PBF surfaces during EP.

4.2 EP process optimization for 316L stainless steel internal surfaces

Considering that EP is influenced by many factors, it is essential to study the polishing effects of EP parameters and optimize various parameters in the developed

polishing system. Given that only the internal surface of side 1/6 channels has uniform morphology, EP parameter optimization for 316L stainless steel surfaces was studied using L-PBF side inner surfaces.

4.2.1 Length of cathode

Considering the use of 1/6 straight channels, there are two selections of the length of cathode as illustrated in Figure 4.11. One is to use a long cathode (see Figure 4.11a) in which a cylindrical titanium cathode is located in the center of the chamber along the whole channel. The other one is to apply a short cathode (see Figure 4.11b), where the end of the cathode is placed at one end of the channel.

By applying different lengths of cathodes, inner side surfaces of L-PBF 316L stainless steel were electropolished. The electrolyte contained H_3PO_4 (85 %) and glycerol (99 %) with a ratio of 2:1 and the temperature of electrolyte was 55 ℃ during EP. A flow rate of 0.180 L/s was used for electrolyte circulation. With these two types of cathodes, the internal surfaces of side channel after EP of 30 minutes by using a potential of 2V are shown in Figure 4.12. A uniform morphology with bright surface could be obtained by using the long cathode (see Figure 4.12a and b), while a gradient surface shows up with the short cathode as shown in Figure 4.12c. It should be noted that the farther the inner surface was from the cathode, the less effective of EP could be identified (see Figure 4.12d, e and f). This can be explained that the electrolyte resistance increased with the increase of inter-electrode gap, therefore, current density distribution during EP decreases as the inter-electrode gap increased [141, 143]. Thus, a long cathode is more suitable for EP, multiple and hybrid polishing in this study.
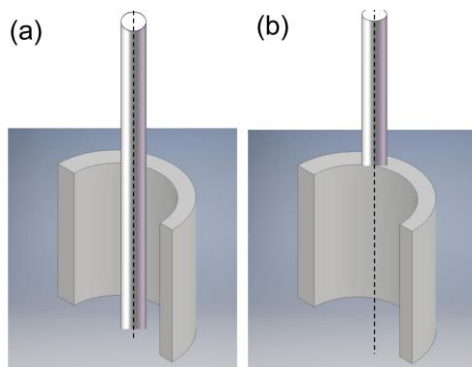
Figure 4.11 Schematic diagrams of relative positions of a channel and a cathode by using (a) long cathode and (b) short cathode in EP.
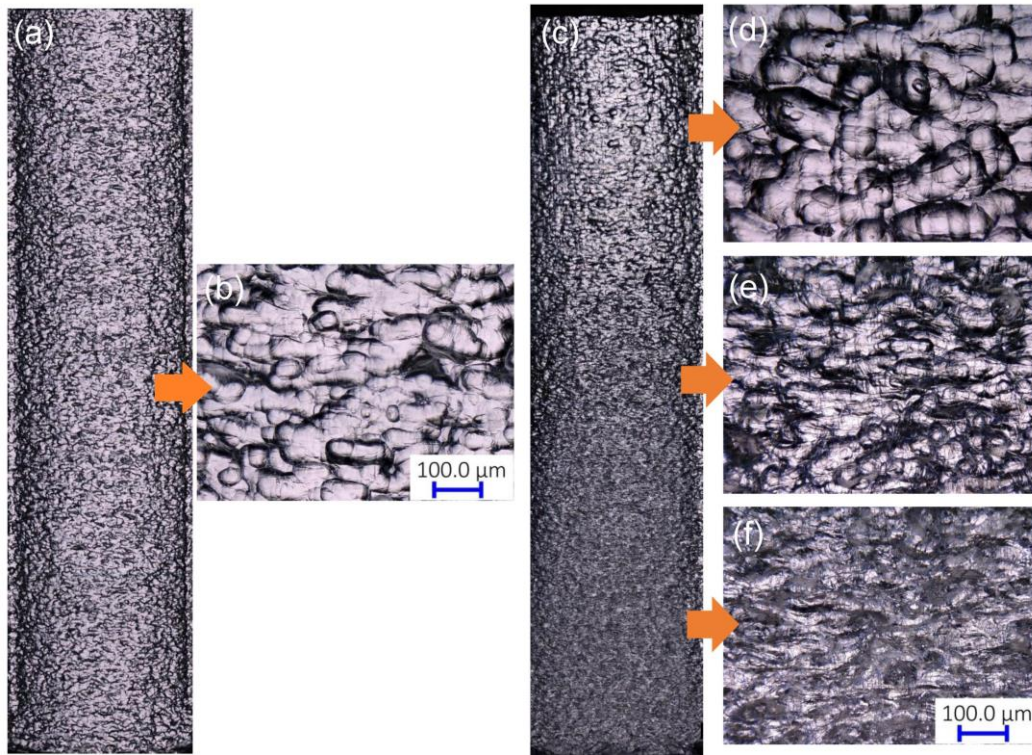
Figure 4.12 OM images of L-PBF 316L stainless steel internal surfaces of (a) a whole side channel and (b) the morphology with high magnification of (a) using a long cathode, and (c) another whole side channel, (d), (e) and (f) the morphology at different positions of (c) with high magnification using a short cathode.

4.2.2 Composition of electrolyte

Because composition of electrolyte would influence the resistance of electrolyte, as well as the distribution of current density and final EP result, it is essential to optimize the composition of electrolyte for internal surfaces of L-PBF 316L stainless steel. Since the mixture of H_3PO_4 and glycerol have shown good polishing effects for 316L stainless steel [141, 144], three different ratios were tested. The volume ratios are 3:1:1, 3:1:0 and 3:2:0 of H_3PO_4, glycerol and deionized water. The temperature of electrolyte was 55 ℃ during EP. A flow rate of 0.180 L/s was used for electrolyte circulation and the internal surfaces of side channel were electropolished for 30 minutes using a potential of 2V. As seen in Figure 4.13, there are etching traces on Figure 4.13a and b, meanwhile, the polished surfaces are not bright. Compared with others, the electrolyte with the ratio of 3:2 of H_3PO_4 and glycerol could obtain a bright surface without etching traces (Figure 4.13c). Thus, the electrolyte for L-PBF 316L stainless steel surfaces is a mixture of H_3PO_4 and glycerol with a volume ratio of 3:2.
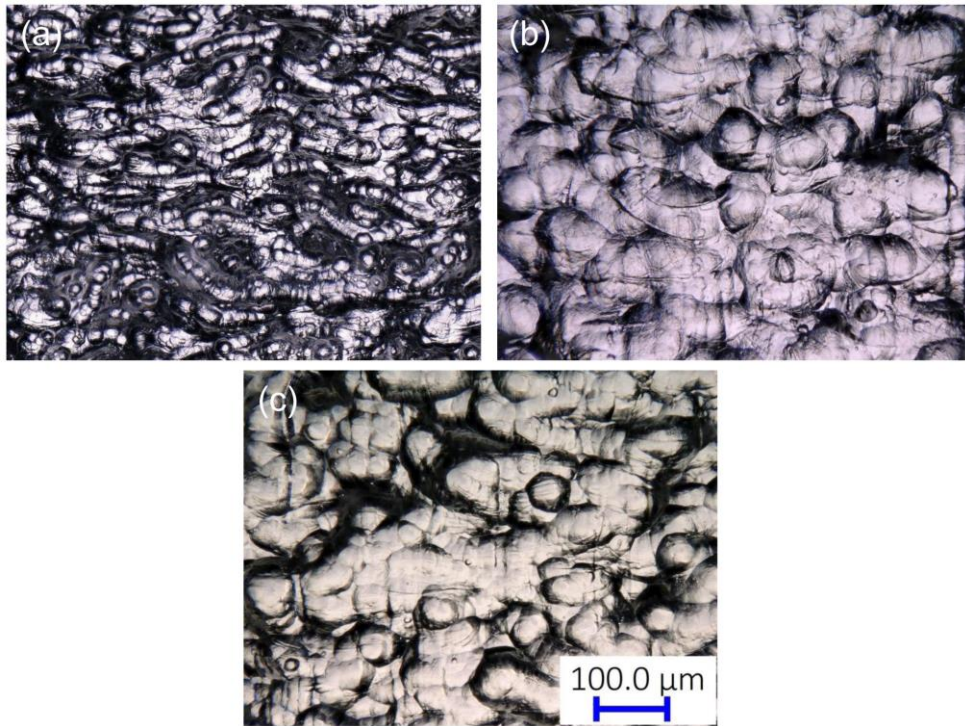
Figure 4.13 OM images of L-PBF 316L stainless steel side internal surfaces after EP using electrolytes containing H_3PO_4, glycerol and deionized water with volume ratios of (a) 3:1:1 (b) 3:1:0 and (c) 3:2:0, respectively.

4.2.3 Temperature of EP

Temperature of electrolyte during EP can affect final polishing result because it influences diffusion rate of ions, thickness of viscous layer, resistance of electrolyte etc. [144]. After testing, the electrolyte circulation temperature of the polishing system can be stabilized at a maximum of 55 ℃, therefore, a mixture of H_3PO_4 and glycerol with the ratio of 3:2 was heated to 40 and 55 ℃ respectively for EP. A flow rate of 0.180 L/s was used for electrolyte circulation and the morphologies of side internal surfaces after EP of 25 minutes by using a potential of 2V are shown in Figure 4.14. Compared with raw side surface (Figure 4.14a) and the polished surface at 55 ℃ (Figure 4.14c), EP 25 minutes at 40 ℃ (Figure 4.14b) is inefficient polishing. Thus, 55 ℃ would be used for subsequent EP, multiple and hybrid polishing of L-PBF 316L stainless steel internal surfaces.
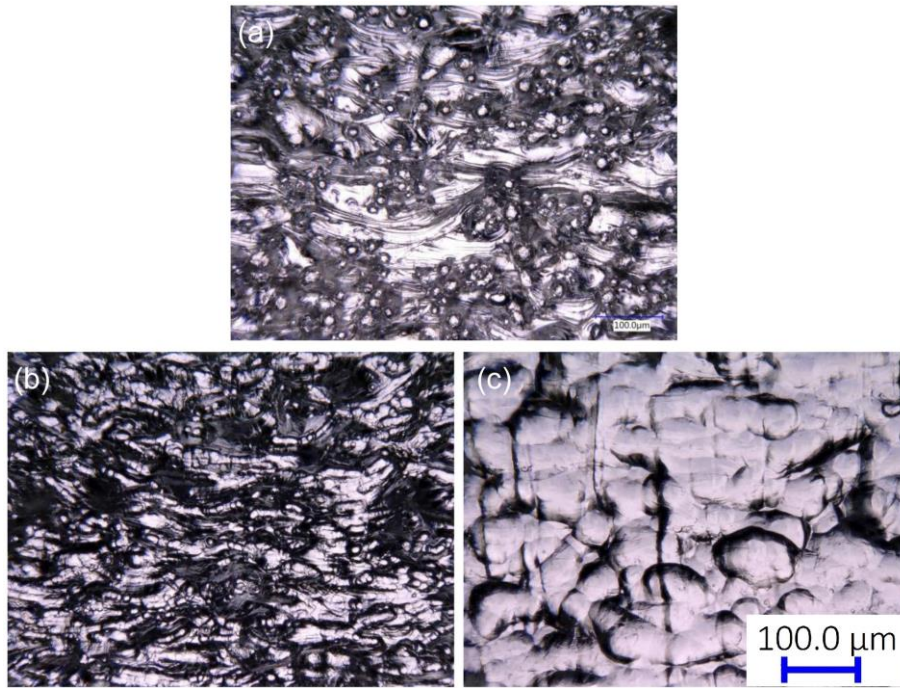
Figure 4.14 OM images of (a) a raw L-PBF 316L stainless steel side internal surface and side internal surfaces after EP at (b) 40 ℃ and (c) 55 ℃, respectively.

4.2.4 Flow rate of electrolyte

Given that polarization curve is a valuable tool in quantifying behaviors of metals and alloys in EP [145], raw side inner channels were selected to measure the polarization curves with different flow rates as seen in Figure 4.15. Note that the potentiodynamic polarization curves were measured by sweeping the potential from 3.5 to 0.5 V (versus Ag/AgCl$_{sat}$) at a scan rate of -20 mV/ s. In general, polarization curve in a typical EP process is usually divided into four regions, the etching, passivating, limiting current density plateau region (LCPR), and gas evolution region with the increase of potential, as reported by Han et al. [143]. In the LCPR, the current is almost stable when changing the applied potential. Thus, normal EP is usually carried out in this region due to the better EP effect. Although different flow rates were tested in Figure 4.15, a distinct LCPR shows up in various polarization curves. Note that current density at LCPR also increases with an increase in the flow rate. Moreover, the LCPR is more stable in flowing electrolyte. In general, a viscous film layer would be formed on workpiece surfaces due to that dissolved metal ions need time to diffuse away from the workpiece surface. With an increase in the flow rate, the diffusion

process can be accelerated and resulted in a thinner viscous film. Thus, the decrease of inter-electrode gap resistance led to an increase in the current density [144]. Because of use of a peristaltic pump in the developed EP system, flow oscillations could easily occur at low flow rate and the degree of oscillation can be greatly weakened with the increase of the flow rate. Therefore, the polarization curve at 0.06 L/s clearly oscillated. In order to obtain a stable LCPR for EP experiments and mechanism study, a flow rate of 0.18 L/s was selected for various L-PBF surfaces. Since the potential range of LCPR at 0.18L/s is between 1.95 and 2.15V in Figure 4.15, a potential of 2V along the LCPR is used in normal EP process for various L-PBF 316L stainless steel inner surfaces.
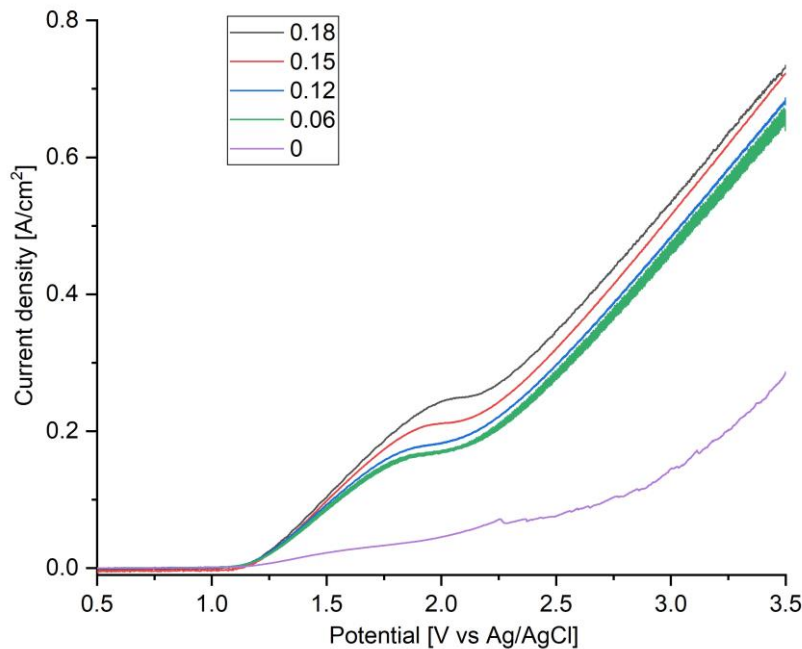
Figure 4.15 Polarization curves of L-PBF 316L stainless steel side internal surfaces with flow rates of 0, 0.06, 0.12, 0.15, 0.18 L/s at 55 ℃.

4.3 EP of 316L stainless steel internal surfaces

4.3.1 Experimental approaches

EP of L-PBF 316L stainless steel internal surfaces was carried out using the developed polishing system as illustrated in Figure 3.24, Figure 3.25a and b. A 1/6 straight channel and a cathode could be connected to a CS310 electrochemical workstation (Wuhan CorrTest, China). A three-electrode system was used in this study

with an Ag/ AgCl reference electrode (Fisher Scientific, Ireland) placed in the storage tank. It should be noted that the 1/6 straight channel of L-PBF 316L stainless steel and a plastic fixture could be combined into a whole straight channel with an inner diameter of 5mm. Electrochemical impedance was measured using the CS310 electrochemical workstation, and the measured impedance diagrams were fitted with the accessory software. Please note that the electrochemical impedance was measured at a constant applied potential along the LCPR. A potential amplitude of 10 mV was used with a frequency range of 100 kHz to 1 Hz. The electrolyte in this study only contained H_3PO_4 (85 %) and glycerol (99 %) with volume ratio of 2:1. Different types of L-PBF inner surfaces were facing the long counter electrode in all EP tests. A stable flow rate of 0.18 L/ s and a temperature of 55 ℃ were controlled during EP and impedance diagram measurements. L-PBF inner surfaces were cleaned using distilled water in an ultrasonic agitation bath for 10 minutes and dried by air blowing before and after EP.

4.3.2 Normal EP

Given that only the internal surface of side 1/6 channels has uniform surface morphology, polishing characteristics and material removal rate of normal EP on side inner surfaces were studied firstly. EP effects on morphology of a side internal surface after different processing times are shown in Figure 4.16. It is clear that adhered powders dissolve after EP of 2.5, 5 and 7.5 minutes. As a result, more sintered area shows up correspondingly. Compared with adhered powders, the sintered area typically remains its original morphology in the first 10 minutes. Consistent with our study of EP characteristics of L-PBF 316L stainless steel surface features in section 4.1 [141], un-sintered powders would dissolve first since they process a higher dissolution rate than sintered area during EP because of the microstructure difference. As the EP time increases from 10 to 30 minutes, the sintered area continues to be polished and the side internal surface becomes smoother, indicating that normal EP is suitable for polishing the sintered area.

Figure 4.17 shows changes of surface roughness values and material removal rate of the side inner surface measured in normal EP. It should be noted that both Ra and

Rz decrease by about 50% in the first 7.5 minutes of EP which mainly attribute to the removal of un-sintered powders. After the dissolution of un-sintered powders, the decrease of roughness values becomes slower from 10 to 20 minutes because sintered area with higher polishing resistance would be electropolished continuously. After polishing for 20 minutes, surface roughness remains basically stable. In terms of material removal rate, the early 7.5 minutes of EP achieves higher material removal rate. Then it decreases slowly with the prolongation of EP time. Since most of un-sintered powders dissolve after 7.5 minutes, the higher material removal rate should be more attributable to the dissolution of un-sintered powders. Then, continuous EP of the sintered regions results in a lower material removal rate because the dissolution rate of sintered area is lower than un-sintered powders. In addition, the reduction of surface roughness values of sintered area can weaken EP effect, resulting in a gradual decrease in material removal rate with the extension of EP time.

As seen from the experimental results above, although un-sintered powders possess a higher dissolution rate than sintered area during EP, it still takes about half the time to remove the un-sintered powders before the surface roughness of L-PBF side surface reaches a stable level. Moreover, the presence of un-sintered powders and high surface roughness may be risky for applications [112, 146] due to un-stable bonding or differences in microstructure from the host material [141]. Thus, it is significant to develop a process to rapidly remove the un-sintered powders on L-PBF surface to improve polishing efficiency of EP.

Figure 4.16 OM images of (a) raw morphology of a L-PBF 316L stainless steel side channel and the same area after (b) 2.5, (c) 5, (d) 7.5, (e) 10, (f) 15, (g) 20, (h) 25 and (i) 30 minutes of EP, respectively.
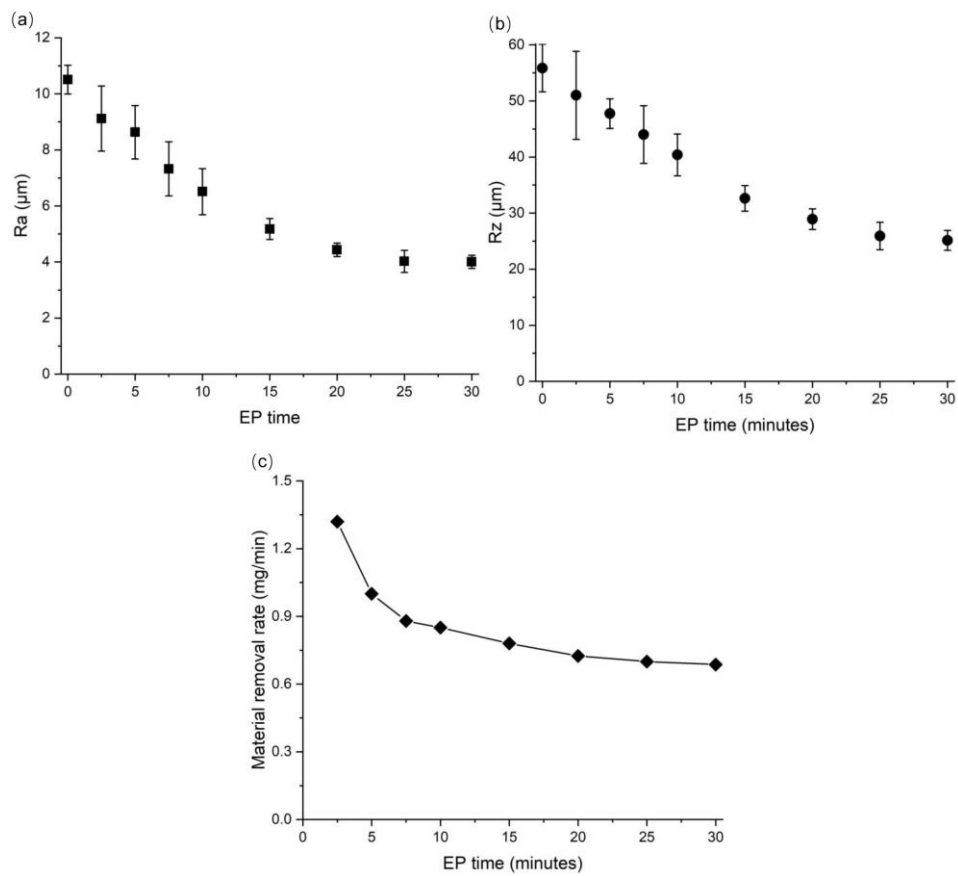
Figure 4.17 Changes of surface roughness (a) Ra, (b) Rz and (c) material removal rate of the L-PBF 316L stainless steel side inner surface in Figure 4.16 before and after different time of EP, respectively.

4.3.3 Optimization for removing un-sintered powders

To improve the removal process of un-sintered powders, different potentials of EP were used as the first step EP for L-PBF side inner surfaces. Figure 4.18 shows the morphology of side inner surfaces before and after polishing at different voltages and Figure 4.19 demonstrates the changes of surface roughness. It can be seen that some spherical adhesions remain on the surface after 2V and 3V (see Figure 4.18b and c), while a morphology similar to Figure 4.16e could be obtained after 4, 5 and 6V, respectively as shown in Figure 4.18c, d and e. Therefore, EP for 5 minutes at 3V is difficult to remove most of un-sintered powders, which is consistent with the results shown in Figure 4.19 that the roughness reduction percentage at 2V and 3V are close to each other. Despite un-sintered powders are removed after EP 5 minutes at 4, 5 and 6V, the highest reduction of Ra and Rz shows up at 4V. Then, the decrease in roughness is smaller at 5V and the lowest reduction percentage occurs at 6V. In general, when the potential is higher than LCPR, the current density increases with an increase of potential [143]. Because 4, 5 and 6V are higher than the LCPR in Figure 4.15, the current at protrusions and valley positions on rough L-PBF surfaces at 5 and 6V should be much higher than at 4V. Thus, the surface roughness changes in Figure 4.19 can be explained that an excessive voltage could cause large amount of material removal at protruding and valley locations at the same time and worsen L-PBF surface roughness [141, 143]. As a result, 5 minutes of EP at 4V in this study can effectively dissolve most of un-sintered powders with a maximum reduction in surface roughness on L-PBF 316L stainless steel side inner surfaces.
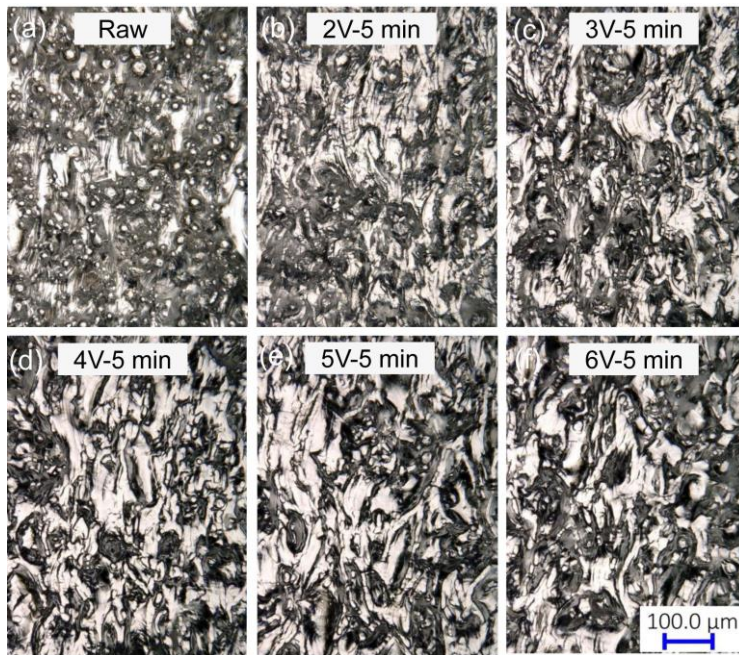
Figure 4.18 OM images of L-PBF 316L stainless steel side inner surfaces (a) before and after EP of 5 minutes at (b) 2V, (c) 3V, (d) 4V, (e) 5V and (f) 6V, respectively.
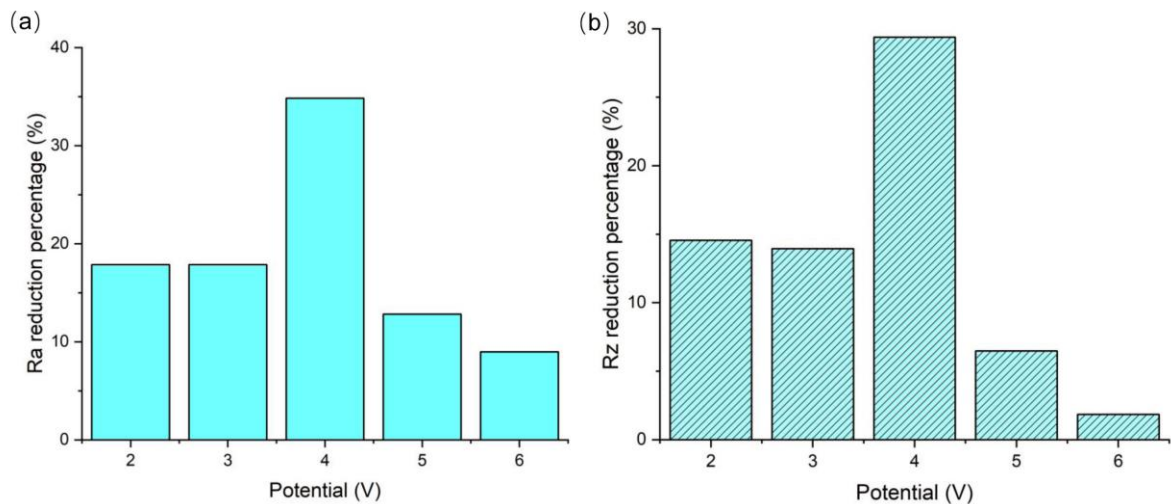
Figure 4.19 Reduction percentages of (a) Ra and (b) Rz of L-PBF 316L stainless steel side inner surfaces after EP of 5 minutes at different voltages.

The optimal parameter for removing un-sintered powders is also validated on other L-PBF 316L stainless steel inner surfaces as seen in Figure 4.20. Un-sintered powders on top, face up and face down surfaces of L-PBF internal channels are effectively removed after 5 minutes of EP at 4V. Thus, it is proposed to use this parameter as the first step EP for various internal surfaces prepared by L-PBF 316L stainless steel.
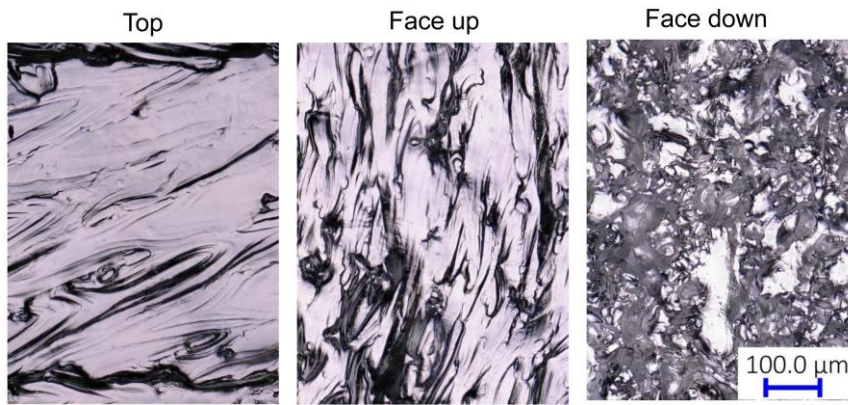
Figure 4.20 OM images of inner top, face up and face down surfaces on L-PBF 316L stainless steel channels after EP of 5 minutes at 4V.

4.3.4 Two-step EP

Considering the material removal characteristics of L-PBF surface features during EP, a two-step EP process is developed for the polishing of various L-PBF internal surfaces. The aim of the first step is to remove almost un-sintered powders by using a potential of 4V for 5 minutes of polishing, while the second step is to further level the remaining sintered area and obtain a smooth surface. Given that LCPR is generally used for better EP effect and shows good surface finish, a potential of 2V was applied in the step two. Please note that area on L-PBF surfaces that contact with electrolyte would be polished during the two-step EP.

Morphologies of various L-PBF surfaces on the same sample before and after the two-step EP are illustrated in Figure 4.21. It is clear that most of spherical adhesions dissolve after the step 1 and sintered area gets smoother on different surfaces as shown in Figure 4.21. It could be seen that laser sintering traces on top surface are blurred after 5 minutes of EP in the step 1. However, some etching marks appear in the original sintered area on top surface during the second step of EP, which is a result of longer EP time for sintered area [141, 145]. In comparison with the top surface, the sintered area on face up, side and face down surfaces are much smoother after 10 and 20 minutes of EP in the step 2. It should be noted that the morphologies of various surfaces change slightly during the second step of EP which demonstrates that most of un-sintered powders have been effectively removed in the first step of EP.
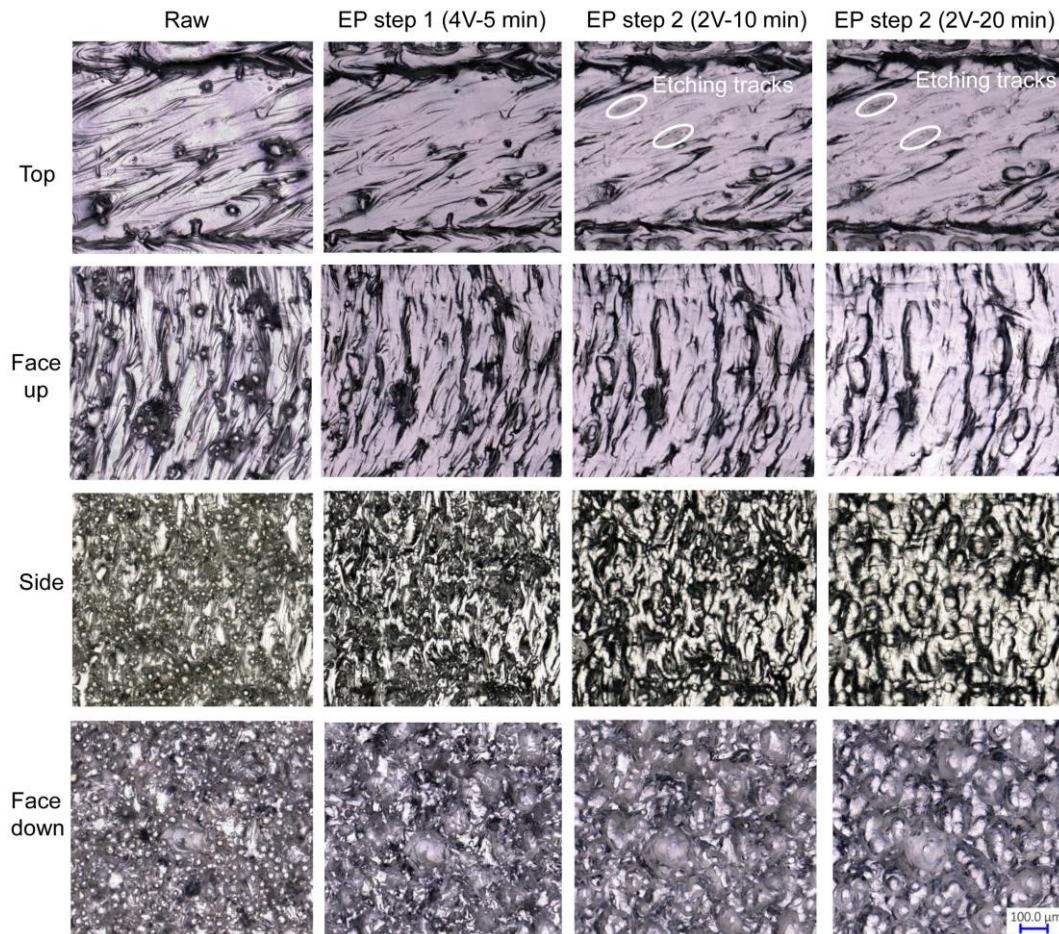
Figure 4.21 OM images of the same area on L-PBF 316L stainless steel various internal surfaces before and after different time of two-step EP.

Figure 4.22 shows the topography evolution of surfaces over EP processing time. It can be seen that L-PBF surfaces are gradually levelled with the extension of time. After the step 1, some spherical adhesions on top surface are disappeared, while the topography of other surfaces changes greatly. From the perspective of vertical scale in Figure 4.22, the reduction of the vertical scale is obvious on top, face up and side surfaces after the step 1 of EP, while face down surface is basically unchanged. In the step 2 of EP, sintered areas on the face up, side and face down surfaces are further polished and their vertical scales significantly decrease with the extension of EP time. However, the vertical scale on the top surface almost remains at similar values. Both Ra and Rz values of original and polished surfaces were measured after the two-step of EP, as shown in Figure 4.23. The raw surface roughness values vary with different L-PBF internal surfaces due to the differences of un-sintered powders and roughness

of sintered area which is consistent with the analysis in section 4.1 [141]. After step 1 of EP, Ra and Rz values on top, face up and side surfaces show markedly decrease due to the removal of un-sintered powders. Different from other surfaces, the values of surface roughness on the face down surface after step 1 is almost the same as before polishing. Then, the roughness of the face up, side and face down surfaces continues to decrease with increasing EP time in the step 2, but Ra and Rz values of the top surface remains almost unchanged. Please note that the changes in roughness values of different L-PBF inner surfaces during the two-step EP are consistent with the variation of vertical scales in Figure 4.22.
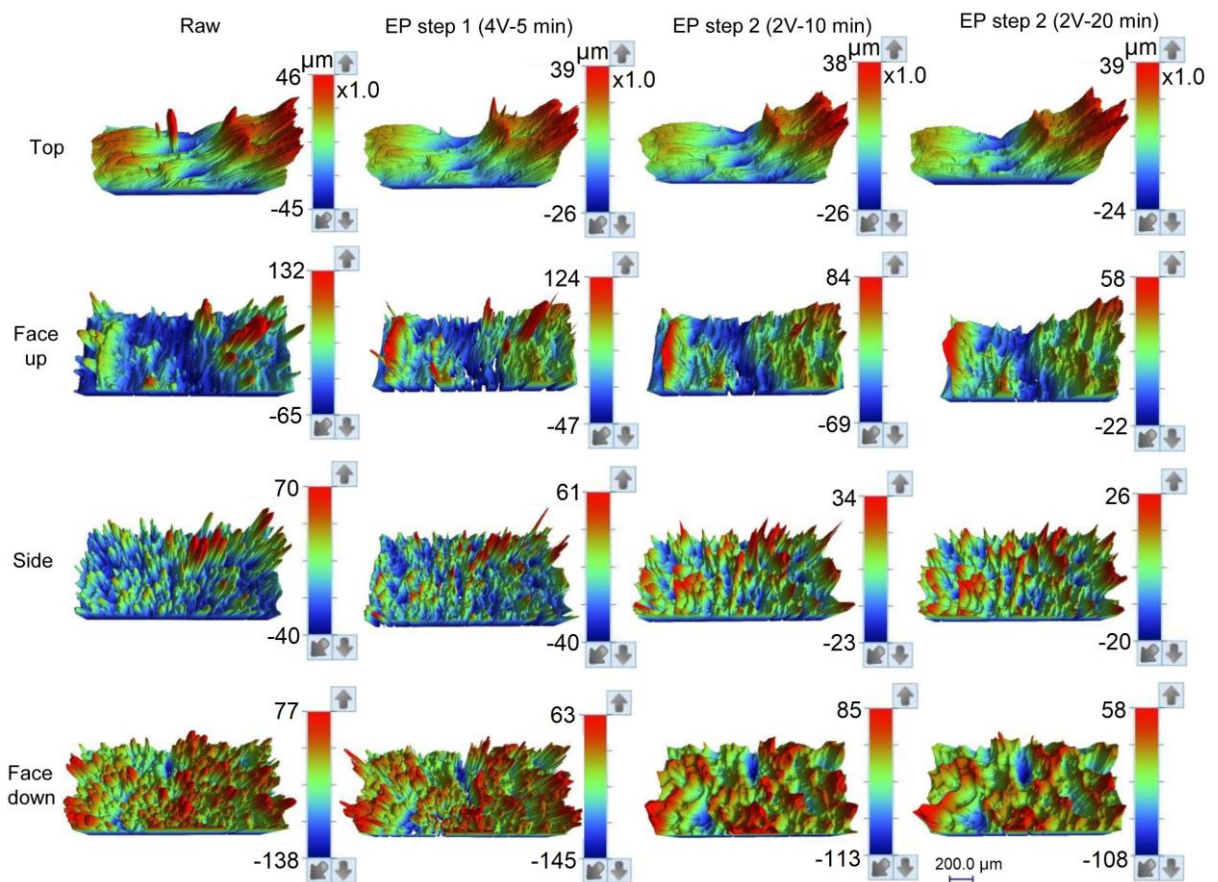
Figure 4.22 Topography of the same area on different L-PBF 316L stainless steel internal surfaces before and after different time of two-step EP.

Figure 4.23 Ra and Rz values of L-PBF 316L stainless steel internal (a) top, (b) face up, (c) side and (d) face down surfaces before and after different time of two-step EP. Note that the left vertical axis represents Ra and the right vertical axis represents Rz.

4.3.5 Material removal process

To further study the material removal process, the etched cross sections of various L-PBF internal surfaces after two-step EP are shown in Figure 4.24 and Figure 4.25. After step 1, only a few un-sintered powders are residual on various L-PBF inner surfaces, which means step 1 has effectively removed most of the un-sintered powders. With step 2 of EP, all un-sintered powders are dissolved, and only sintered area appears on different inner surfaces after 10 minutes. Then, sintered area on face up, side and face down surfaces are noticeably levelled after 20 minutes, except for top surface. Based on the characterization of cross sections, the changes in roughness in Figure 4.23 could be well explained. Raw roughness values of different L-PBF surfaces mainly depend on the combined effect of un-sintered powders and sintered area [141]. With the action of the step 1 of EP, the removal of most un-sintered powders allows newly sintered areas appear on various surfaces which has a strong impact on their Ra and Rz values. Compared with other surfaces, sintered area on the face down

90

surface generally shows the maximum roughness since heat conduction and gravity have a greater effect on overhanging face down surfaces [25, 95]. Therefore, the face down surface exhibits similar roughness values to the original surface after the step 1 (Figure 4.23). In terms of the polishing of sintered area in step 2, the varied levelling degrees of the top and other surfaces can be explained by the different dissolution rates of sintered area at the convex and concave positions. Since other surfaces have higher roughness of sintered area than the top surface, higher current distribution differences at the protruding and valley positions generates a stronger polishing effect on their surfaces during the step 2 of EP [143].
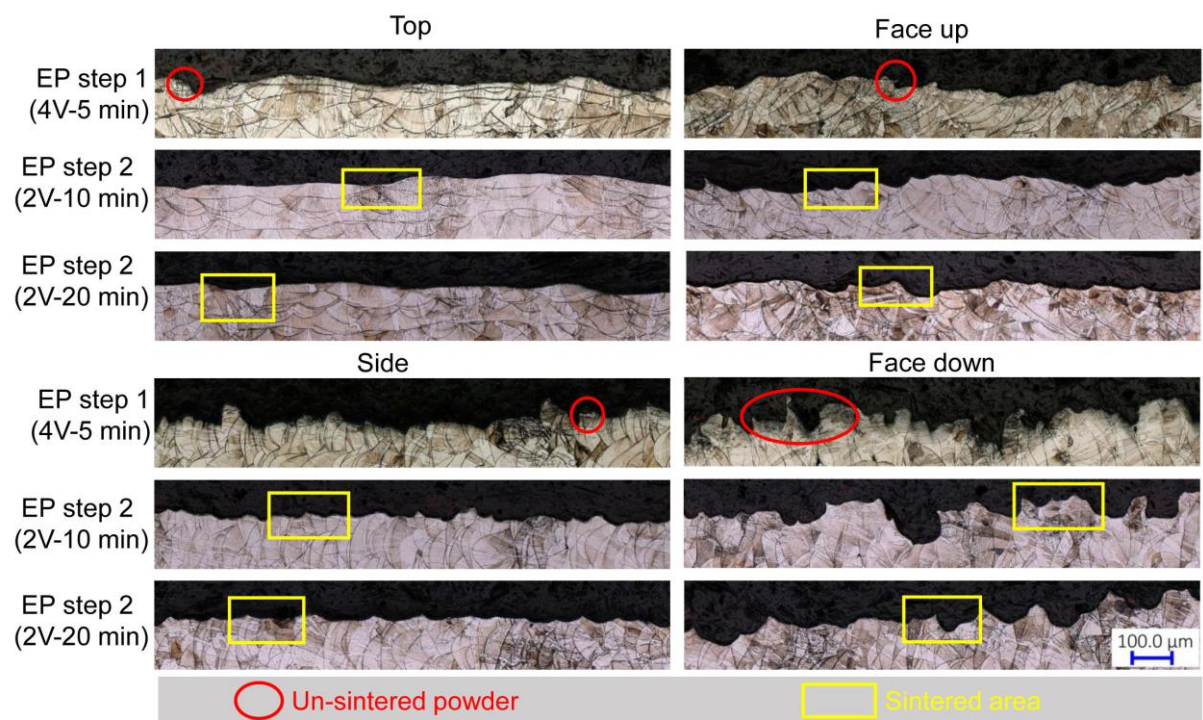
Figure 4.24 OM images of cross sections on L-PBF 316L stainless steel various internal surfaces after processing for different time of two-step EP.
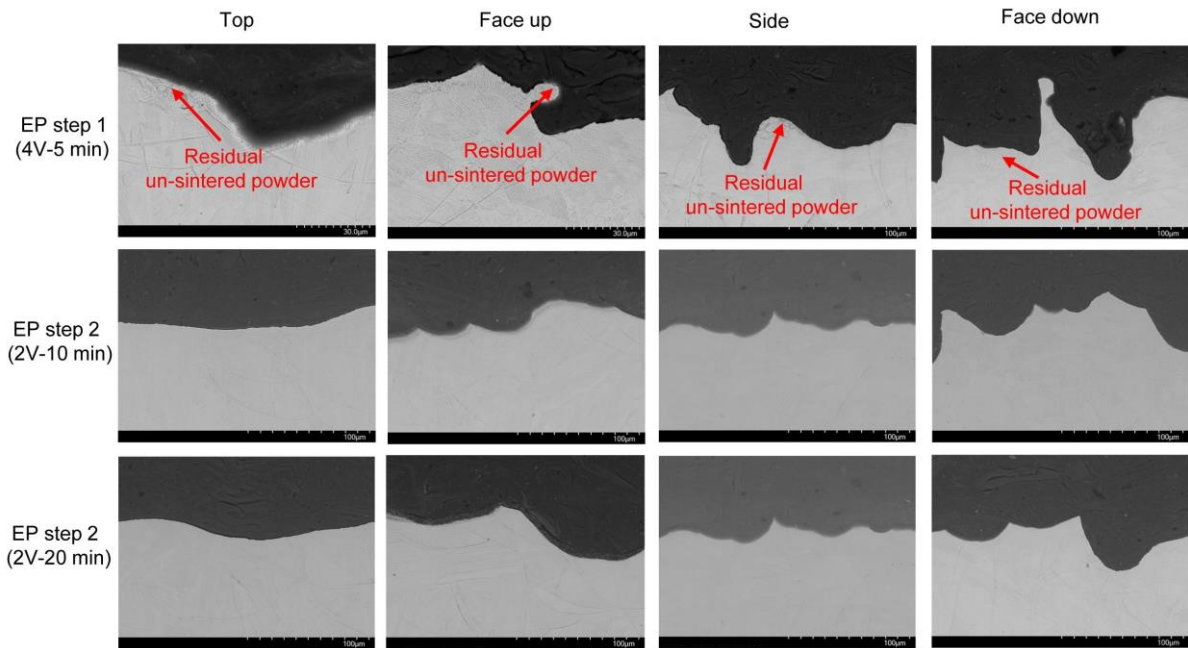
Figure 4.25 SEM images of cross sections on L-PBF 316L stainless steel various internal surfaces after processing for different time of two-step EP.

Based on above results and discussion, the material removal process of L-PBF 316L stainless steel internal surfaces during the two-step EP is illustrated in Figure 4.26. Considering that microstructure differences result in a higher dissolution rate of un-sintered powders than sintered area on various L-PBF surfaces (see Figure 4.26a), the step 1 of EP removes most of the un-sintered powders by using a higher potential than LCPR, while minimizing the roughness as shown in Figure 4.26b. In order to obtain a bright and smoother final surface, a potential along LCPR is applied in the second step of EP. Generally, the sintered area would be levelled gradually with the extension of EP time as shown in Figure 4.26c and d. Notably, the selection of EP parameters needs to be considered according to the differences of various L-PBF surfaces. For example, the polishing time in step 2 of EP needs to be controlled for top surfaces to avoid etching traces, but for face down surfaces, the time can be appropriately extended.
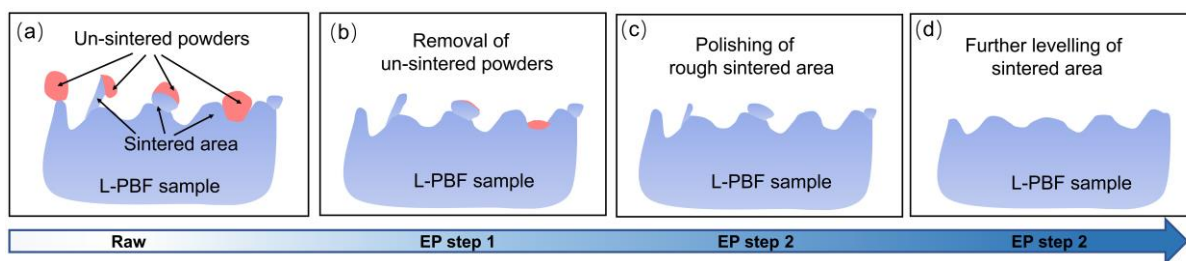
Figure 4.26 Schematic diagram of (a) raw surface and (b-d) material removal process of L-PBF internal surfaces during two-step EP.

4.3.6 Impedance diagram analysis

The mass transport limitations for anodic dissolution, such as salt film theory and adsorbate acceptor system, can be used to analyze EP mechanism by measuring electrochemical impedance spectroscopy [145, 147]. In general, the characteristic features of impedance diagrams could be used to identify its mechanism because the shapes of Nyquist plots for salt film and adsorbate acceptor theories are different. Figure 4.27a shows the impedance diagram at high frequency by using a side internal surface with a potential of 2V. The first and second arcs are visible and are significantly distinct at high frequency, which exhibits similar features to the diagram of absorbate acceptor model. Considering the impedance spectra, the left semi-circle at high frequencies is related to the charge transfer process, Figure 4.27b and c illustrate a schematic Nyquist diagram and an equivalent circuit of the impedance diagram at high frequency, respectively. R_p is the polarization resistance determined by the diameter of the circle, R_s is the electrolyte resistance, and C_{dl} is the double layer capacitance which is calculated by $C_{dl}= 1/ (\omega \cdot R_p)$ where ω is the frequency at the top of the semi-circle. The calculated values of R_s, C_{dl} and R_p from measured impedance diagrams at high frequency with different potentials along the LCPR are shown in Figure 4.28a, b and c. It should be noted that the electrolyte resistance R_s hardly changed with different potentials which also proves that it should behave as an ohmic resistance rather than a porous film during EP. Not only the values of R_s, but the constant values of C_{dl} and R_p also suggest that the mass transport limitation mechanism in this study should be an adsorbate acceptor model [143, 145, 148]. In addition, the mass transport limitation species were water, water-related species or some other species require further study.
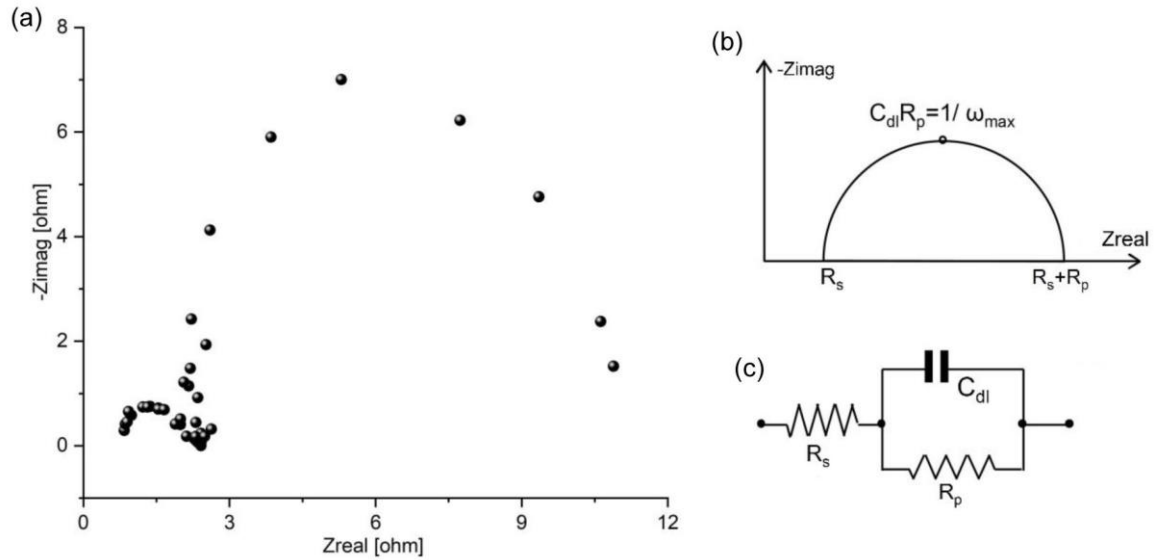
Figure 4.27 Images of (a) an impedance diagram of 2V at high frequency by using L-PBF 316L stainless steel side internal surfaces, (b) Nyquist plot of impedance diagram at high-frequency [145], and (c) equivalent circuit of impedance diagram at high frequency [145].
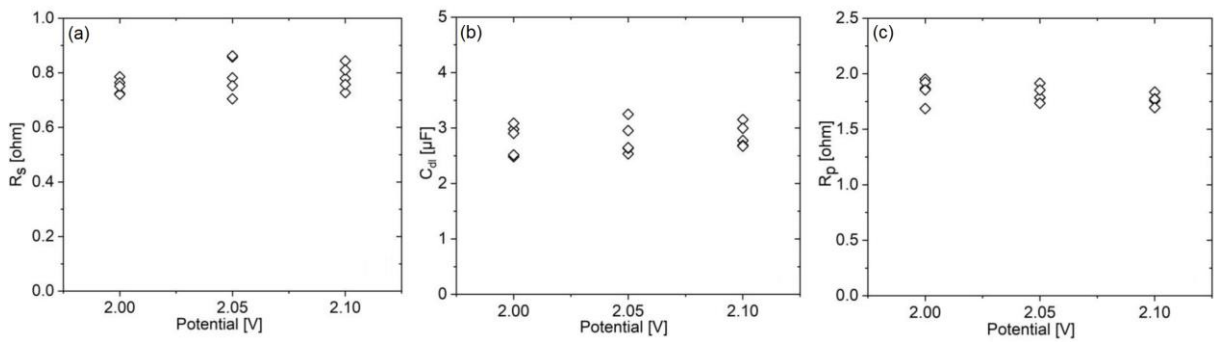
Figure 4.28 Calculated values of (a) R_s, (b) C_{dl} and (c) R_p from the high frequency part of the impedance diagrams at different voltages along the LCPR by using L-PBF 316L stainless steel side internal surfaces.

4.4 EP of Ti6Al4V internal surfaces

4.4.1 Experimental approaches

EP of L-PBF Ti6Al4V internal surfaces on printed 1/6 channels was carried out using the developed polishing system in Figure 3.24, Figure 3.25a and b. A 1/6 straight channel and a cathode could be connected to the electrochemical workstation of IviumStat.XRe (ALVATEK LTD, UK). A three-electrode system was used in this study with an Ag/ AgCl reference electrode (Fisher Scientific, Ireland) placed in the storage tank. It should be noted that the 1/6 straight channel of L-PBF Ti6Al4V and a plastic fixture could be combined into a whole straight channel with an inner diameter of 5mm. The potentiodynamic polarization curves were measured by sweeping the potential

from 10 to 50 V (versus Ag/AgCl$_{sat}$) at a scan rate of 20 mV/ s. The electrolyte in this study is a mixture of NaCl powder (99 %) and ethylene glycol solution (99 %) without acid and the concentration of Cl$^-$ was 0.6 M. Different types of L-PBF surfaces were facing the long counter electrode in all EP tests. A stable flow rate of 0.18 L/ s and a temperature of 25 ℃ were applied during EP. L-PBF inner surfaces were cleaned using distilled water in an ultrasonic agitation bath for 10 minutes and dried by air blowing before and after EP.

4.4.2 Process optimization

EP behaviors of Ti6Al4V in chloride-containing ethylene glycol electrolyte were discussed by researchers [149, 150] considering its environmentally friendly character. Based on the use of this environmental-friendly electrolyte, EP parameters were optimized using side inner surfaces of L-PBF Ti6Al4V 1/6 channels.

Figure 4.29 is the polarization curves from 10 to 50V at different flow rates and LCPR shows up from 44 to 50V at a flow rate of 0.18 L/s. Moreover, changes in flow rates have less effect on LCPR. Then, EP of a side inner surface at 44V was carried out and morphological evolution is shown in Figure 4.30. After 5 minutes of EP, some area has been polished to be smooth, while some raw sintered area still remains. Then, area ratio of smooth surface increases with prolongation of EP time. However, the polishing effect is not uniform after different EP times. Original morphology (marked with white circles in Figure 4.30) still shows up after 5 and 10 minutes. Insufficient polishing areas (marked with yellow boxes in Figure 4.30) are also obvious after 15 minutes of EP. Nonuniform polishing phenomenon may be caused by excessive current density distribution at LCPR. Although the potential along LCPR could be used to obtain smooth and bright surface, combined effects of high current density at 44V, high surface roughness and complexity of raw L-PBF Ti6Al4V side surfaces could lead to nonuniform polishing. Moreover, continued prolongation of EP time at 44V may result in excessive material removal. Thus, the selection of potential for various L-PBF Ti6Al4V inner surfaces should be further investigated.
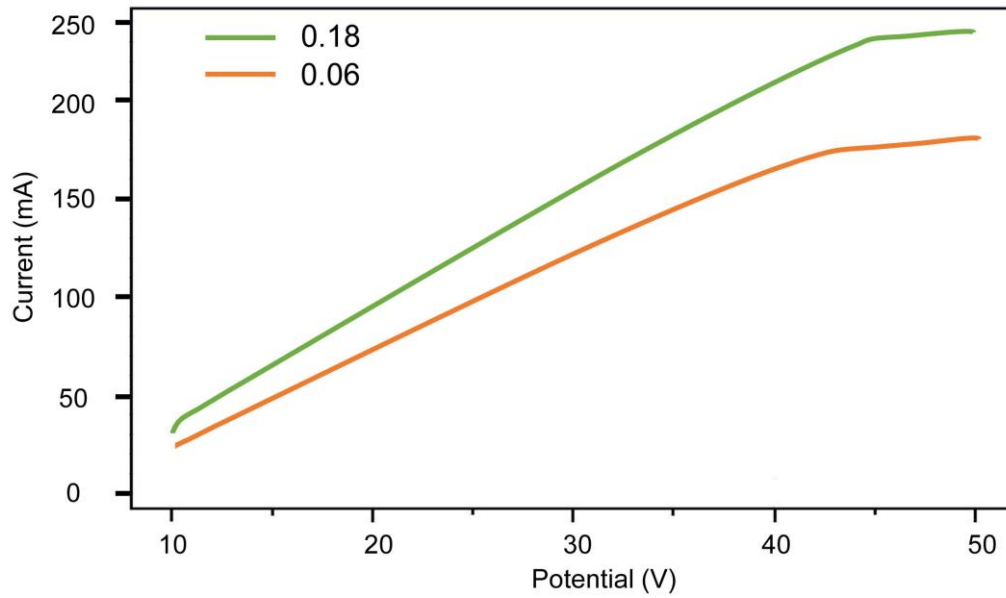
Figure 4.29 Polarization curves of L-PBF Ti6Al4V side internal surfaces with flow rates of 0.18 L/s and 0.06 L/s at 25 ℃.
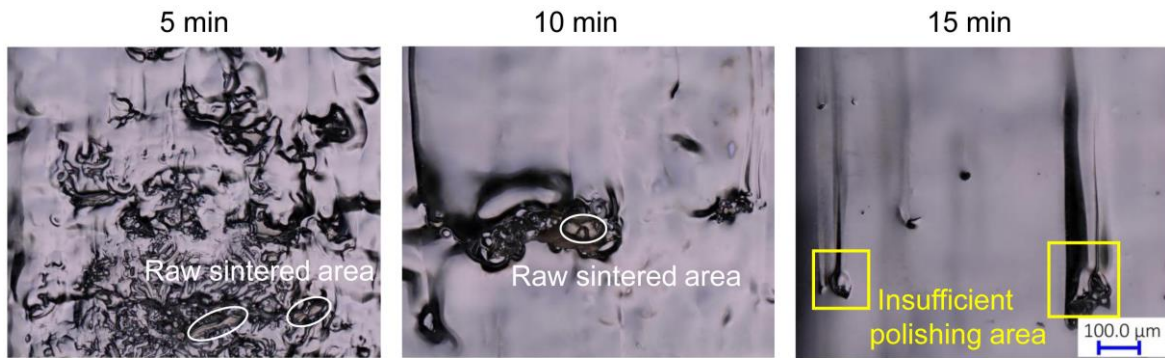
Figure 4.30 OM images of L-PBF Ti6Al4V side internal surfaces after different time of EP at a potential of 44V.

Based on the polarization curve in Figure 4.29, 20V and 32V were selected for EP of Ti6Al4V side inner surfaces. Morphology of side internal surfaces after 10 minutes of EP at different potentials are illustrated in Figure 4.31. It is obvious that nonuniform polishing phenomenon showed up at 32V, while a uniform morphology can be obtained at 20V. Therefore, 20V is selected as the potential for the first step of EP for L-PBF Ti6Al4V internal surfaces.
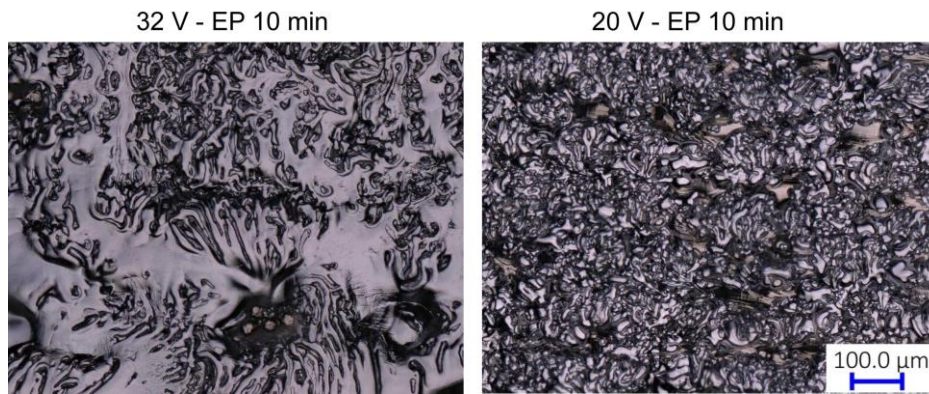
Figure 4.31 OM images of L-PBF Ti6Al4V side internal surfaces after 10 minutes of EP at potential of 32V and 20V, respectively.

4.4.3 Two-step EP

Considering the differences of morphology and roughness of various L-PBF inner surfaces, EP potential of 20V which is lower than LCPR is found to obtain uniform morphology of L-PBF Ti6Al4V inner surfaces. EP effects on morphology of top, face up, side and face down inner surfaces of L-PBF Ti6Al4V are shown in Figure 4.32. It can be seen that most of spherical adhesions on L-PBF surfaces are removed after 2.5 minutes. Meanwhile, the area ratio of raw morphology reduces gradually with an increase of EP time from 2.5 to 5 minutes and all areas are polished after 15 minutes of EP. Although some smooth and bright area shows up in the polished area, it is hard to obtain large bright area at 20V. Given that there are etching and passivation stages before LCPR [143], the material removal of EP at 20V is caused by etching based on the polarization curve (Figure 4.29) and morphological changes.

Both Ra and Rz of original and polished surfaces were measured after EP at 20V, as shown in Figure 4.33. The raw surface roughness values vary with different L-PBF surfaces due to combined effects of staircase effect, heat conduction, gravity effect, etc. [95]. Notably, Ra and Rz values on top surface gradually increase in the first 15 minutes of EP, but deteriorate substantially after 25 minutes of EP at 20V (Figure 4.33a). Different from the top surface, surface roughness of the face up and side surfaces reduce in the first 15 minutes. However, Ra and Rz values increase on the face up and side surfaces with 25 minutes of EP (Figure 4.33b and c). Only the roughness of the

face down surface shows a continuous decreasing trend with prolongation of EP time (Figure 4.33d).
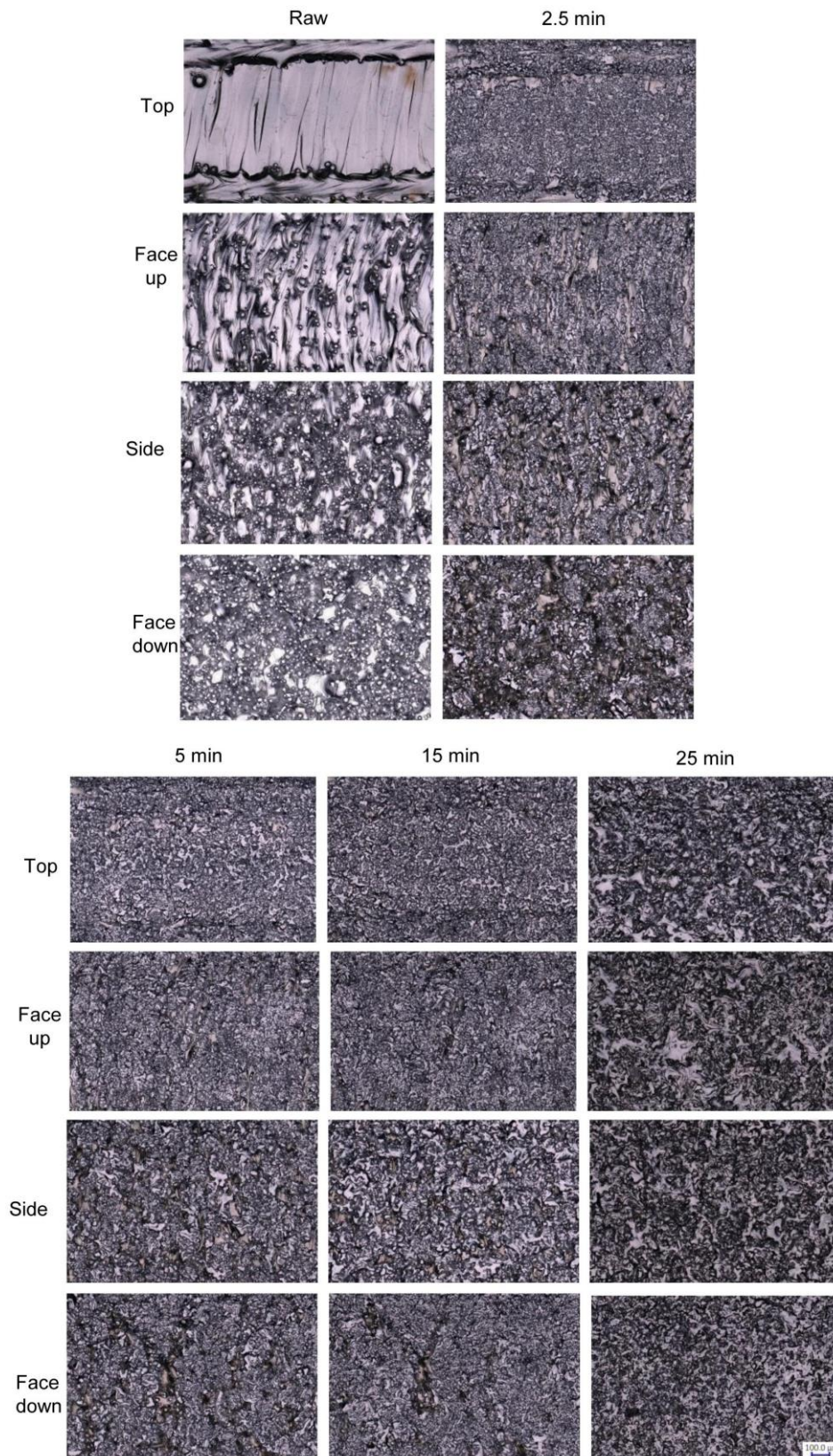
Figure 4.32 OM images of the same area on top, face up, side and face down inner surfaces of L-PBF Ti6Al4V internal channels after different time of EP at 20V.

Based on the changes of morphology and roughness values, it is found that EP at 20V could remove raw morphology of L-PBF Ti6Al4V internal surfaces by etching. However, roughness of the top surface would increase which means the etching morphology have higher Ra and Rz values than raw top surface. In addition, EP time should be carefully considered, as over-etching could greatly deteriorate surface roughness. Considering the differences of various L-PBF internal surfaces, EP at 20V can obtain close surface roughness of various surfaces. Thus, 15 minutes of EP at 20V is considered as the first step of EP for various L-PBF Ti6Al4V inner surfaces.
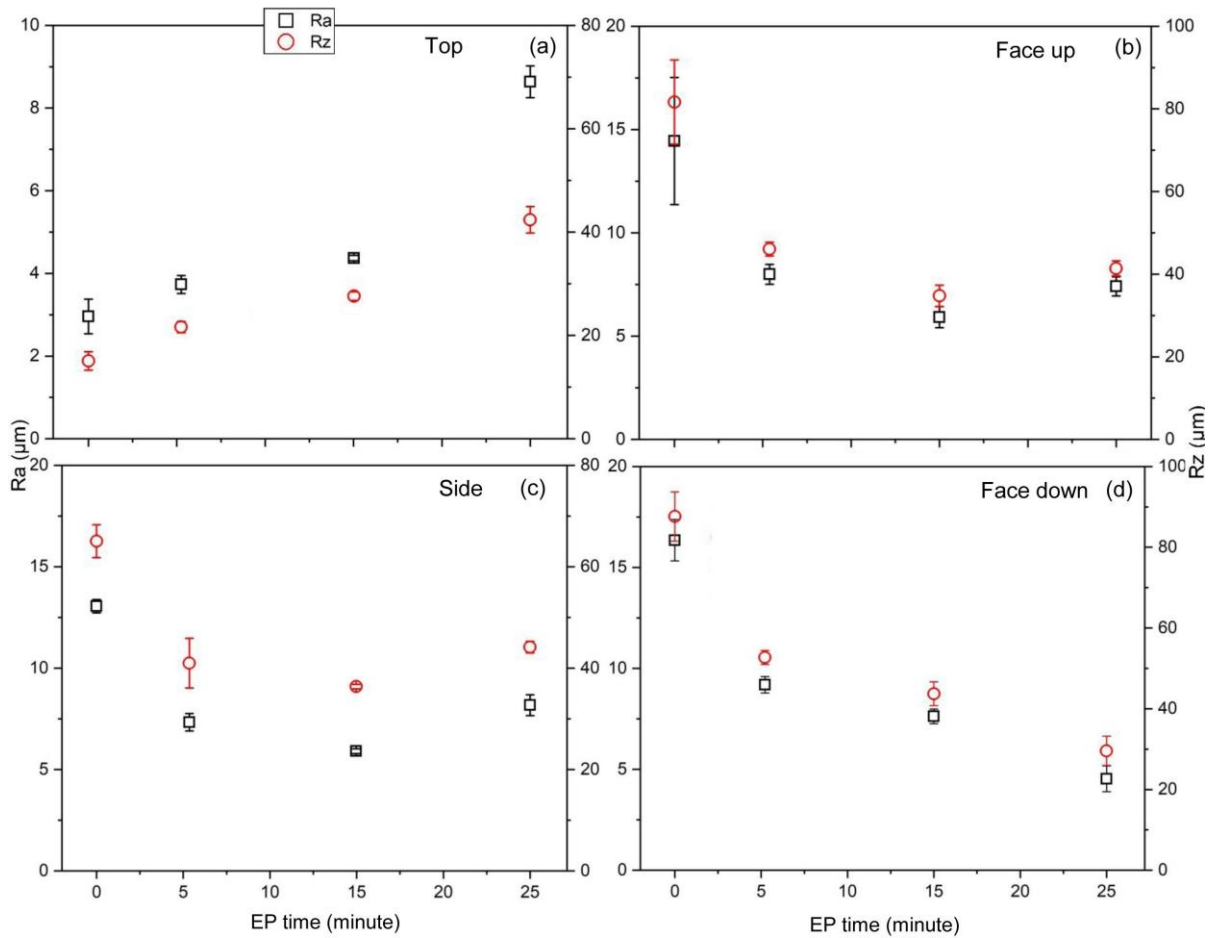
Figure 4.33 Ra and Rz values of L-PBF Ti6Al4V internal (a) top, (b) face up, (c) side and (d) face down surfaces before and after different time of EP at 20V. Note that the left vertical axis represents Ra and the right vertical axis represents Rz.

After EP at a lower potential, a second step of EP has been carried out at 44V along LCPR. Morphologies and roughness of various L-PBF surfaces on the same sample after EP are illustrated in Figure 4.34 and Figure 4.35, respectively. It is clear that there are etching traces after the first step of EP. With the action of EP at 44V,

etching morphologies are still obvious in the first 90 seconds. With an increase of EP time to 210 seconds, etching traces are dissolved visibly. Based on the simulation in Figure 4.9, protruding areas have higher current distributions than valleys during EP. Then, a smooth surface is obtained on top surface, while a few sintered areas with dark colour that located at valley positions (Figure 4.36) are still remained on face up, side and face down surface after 300 seconds. With an increase of EP time at 44V, both Ra and Rz values remain consistent reducing trends across different surfaces as can be seen in Figure 4.35. Notably, roughness reducing efficiency gradually decreases with the prolongation of EP time in the second step of EP because lower roughness values can weaken the current distribution differences between protruding and valley positions.

According to the above discussion, a two-step EP process is proposed for the polishing of various internal surfaces of L-PBF Ti6Al4V. The aim of the first step is to achieve close surface roughness values of various surfaces by applying a potential of 20V for 15 minutes, while the second step is further level the surface at a potential of 44V along LCPR in order to obtain smooth surfaces.
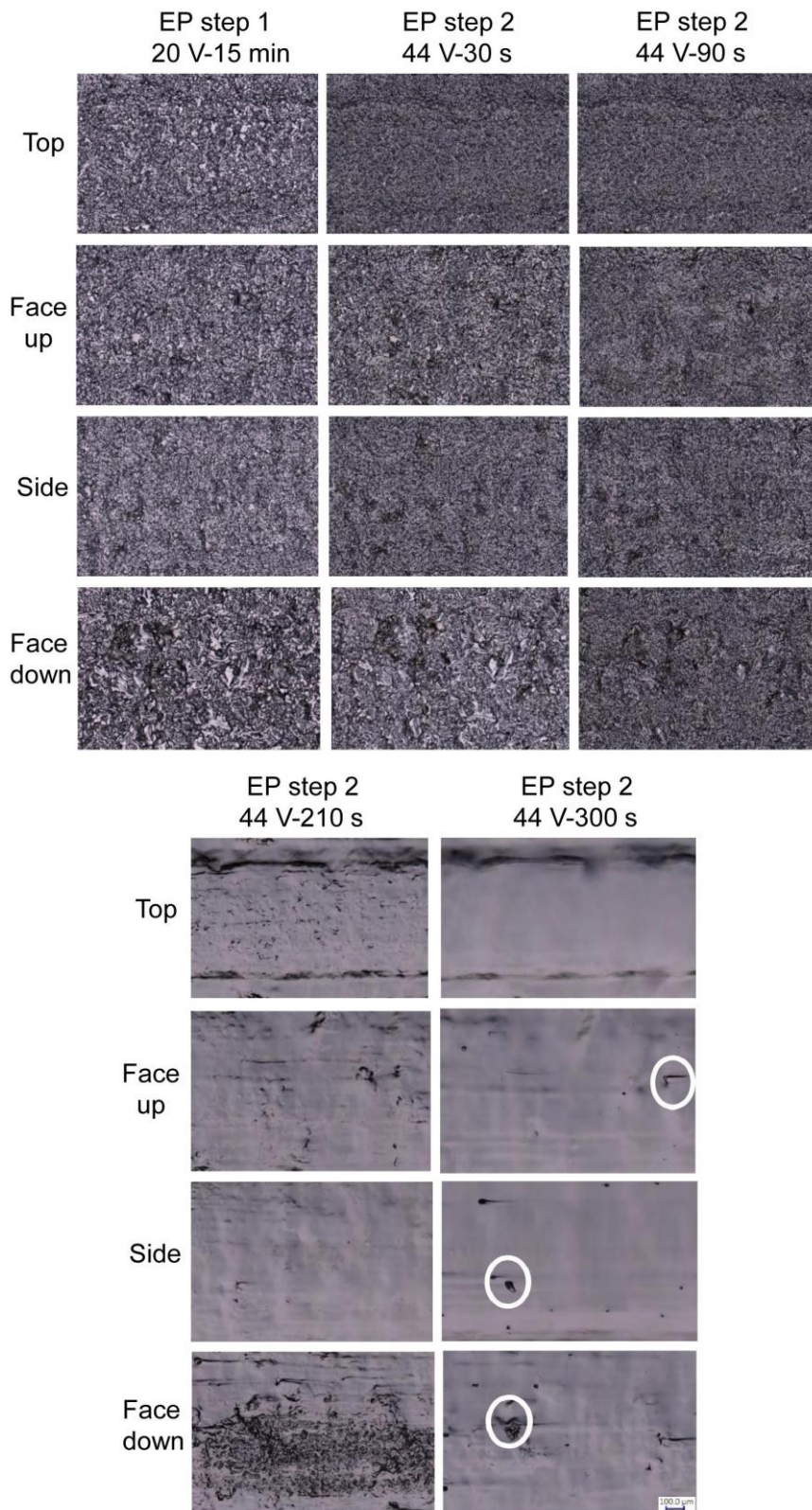
Figure 4.34 OM images of the same area on L-PBF Ti6Al4V various internal surfaces after different time of the two-step EP. Remained sintered areas were marked with white circles after 300 second of the second step of EP.
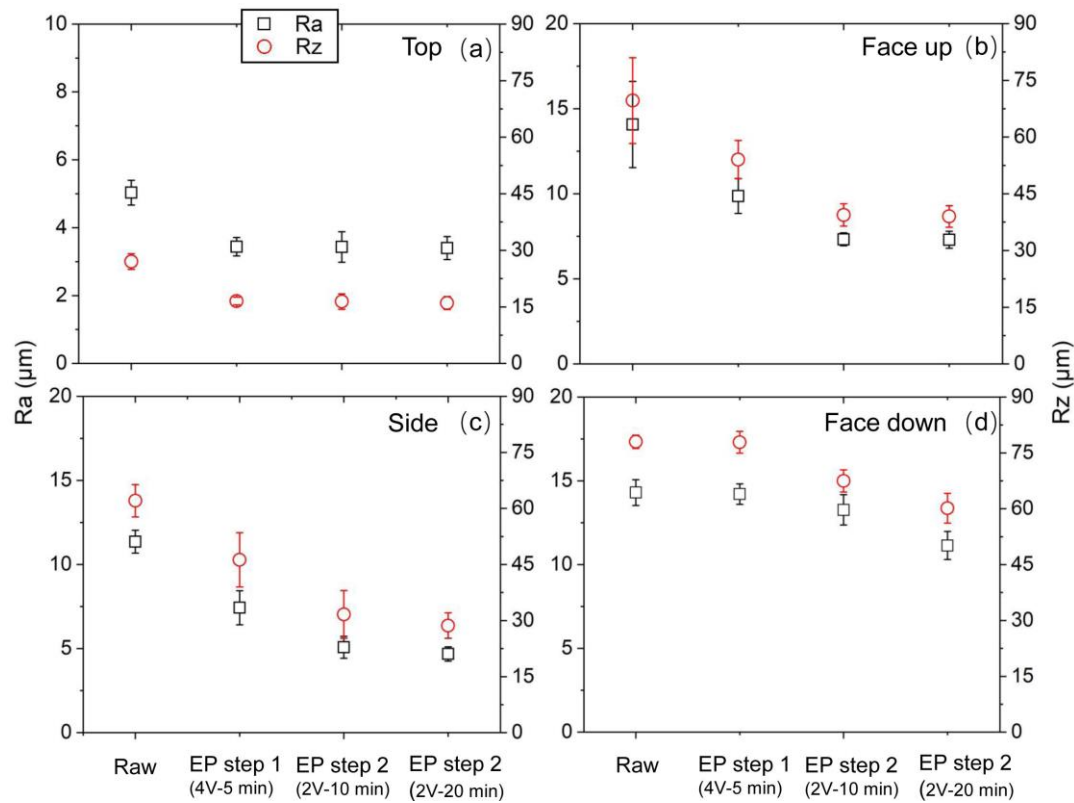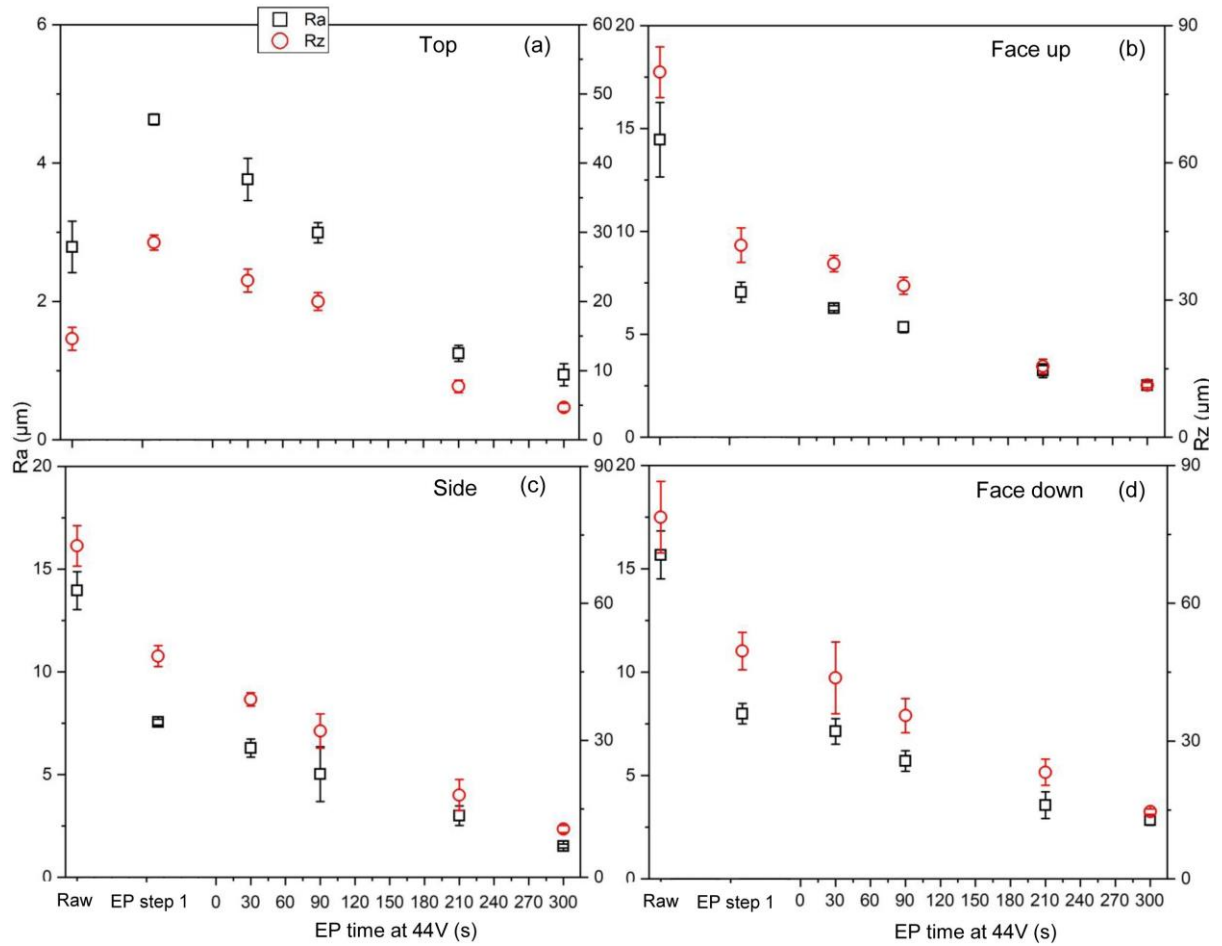
Figure 4.35 Ra and Rz values of L-PBF Ti6Al4V internal (a) top, (b) face up, (c) side and (d) face down surfaces before and after different time of the two-step EP. Note that the left vertical axis represents Ra and the right vertical axis represents Rz.
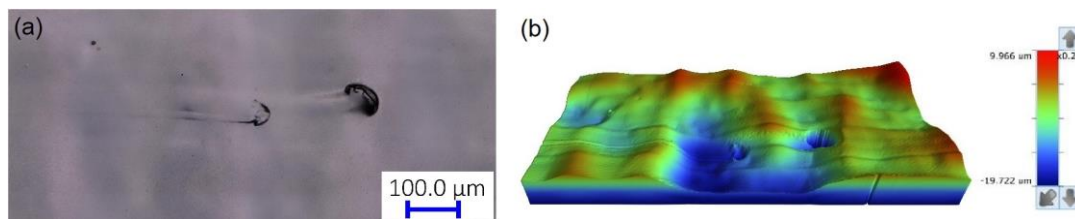
Figure 4.36 OM image of a L-PBF Ti6Al4V side internal surface after the two-step EP (a) and its topography image (b).

4.5 Summary

This chapter investigates material removal process of L-PBF inner surfaces during EP. Based on the study of traditional EP in the beaker, current density distribution differences between protruding positions and valleys on L-PBF surfaces could influence material removal process during EP. EP of various inner surfaces on L-PBF 316L stainless steel and Ti6Al4V is then performed. In order to improve polishing

efficiency, parameters such as flow rate, voltage, polishing time of EP are studied and optimized. Morphology, Ra and Rz values are evaluated to discuss EP effects on different surfaces. The cross sections of various L-PBF 316L stainless steel inner surfaces during the two-step EP are characterized to analyze its material removal process. The main conclusions are summarized as follows:

(1) Surface features on various L-PBF 316L stainless steel flat surfaces have an effect on material removal characteristics of EP. Un-sintered powders dissolve faster than sintered area during EP due to microstructure difference. Moreover, protruding positions on L-PBF surfaces have superior dissolution rate because of their higher current density distribution than recessed positions. During EP, un-sintered powders would be firstly removed. Then, sintered areas would be continuously electropolished with the extension of EP time. Roughness of L-PBF surfaces depends on the combined effect of un-sintered powder and sintered area. Ra and Rz values of polished surfaces show continuous declination from the beginning to 20 minutes of EP. The reduction degree of Rz is higher than Ra on face up and face down surfaces from 10 to 20 minutes of EP due to the high roughness of sintered area.

(2) In the EP of L-PBF 316L stainless steel inner surfaces using the developed hybrid polishing system, although LCPR can be observed at different flow rates of electrolyte, flow oscillations occur at low flow rates, and the degree of oscillation decreases greatly with an increase of flow rate. Despite un-sintered powders possess higher dissolution rate than sintered area and would be removed firstly in normal EP, the removal efficiency of un-sintered powders still needs to be improved. EP parameters are optimized by using a potential appropriately higher than the LCPR to remove most of un-sintered powders. Therefore, a two-step EP has been optimized for various internal surfaces prepared by L-PBF 316L stainless steel in which the first step of EP is to dissolve almost un-sintered powders, while the second step is to further level the remaining sintered area and obtain a smooth surface by applying a potential along the LCPR.

(3) By using an environmentally friendly electrolyte, a two-step EP is investigated for various internal surfaces on L-PBF Ti6Al4V in which the first step of EP is to polish surfaces uniformly using a lower potential, while the second step is to obtain a smooth surface by applying a potential along the LCPR.

(4) Through the analysis of EP effects on various internal surfaces of L-PBF 316L stainless steel and Ti6Al4V, it is found that EP is capable of polishing L-PBF internal surfaces with various printing angles and effectively reducing their surface roughness. In addition, the un-sintered powders would be firstly dissolved and then the sintered area could be further levelled during EP of L-PBF internal surfaces.

Despite the advantages of EP, it is necessary to balance the high material removal rate of EP and surface roughness reduction of L-PBF internal surfaces. For example, it is difficult to further reduce surface roughness of top, face up and side internal surfaces of 316L stainless steel by extending EP time after 25 minutes due to the irregular shape of molten pools on L-PBF surfaces.

It is noted that the selection of electrolytes and optimization of EP parameters are related to the polishing process of specific material. In addition, EP parameters such as composition of electrolyte, EP potential and temperature have significant impacts on material removal process and final surface finish. Although normal EP generally carries out along LCPR, the optimized two-step EP for L-PBF 316L stainless steel and Ti6Al4V demonstrate better polishing effect and efficiency by combining different potentials. This study shows great potential to develop environmentally friendly electrolytes for various L-PBF alloys and then optimize their EP parameters to improve polishing efficiency.

Chapter 5. AFP of L-PBF Internal Surfaces

5.1 AFP process optimization

To optimize AFP process in the developed polishing system (Figure 3.24, Figure 3.26a and b), AFP parameters such as pressure, volume percentage of abrasive particles, type and size of abrasives were optimized. Considering the flow rate in EP and hybrid polishing, a flow rate of 0.18 L/s was used for AFP optimization process. Given that only the internal surface of side 1/6 channels has uniform morphology, AFP parameter optimization was studied using L-PBF 316L stainless steel side inner surfaces. Meanwhile, optimized parameters were also verified on L-PBF Ti6Al4V side 1/6 channels.

5.1.1 Pressure and volume percentage of abrasive particles

Preston equation $R=K_pPV$ [151, 152], where R is material removal, P is pressure acting on workpiece, V is the relative linear velocity, and K_p is Preston constant, indicates that pressure acting on the workpiece surface relates to the material removal rate of AFP. Therefore, the value of the pressure gauge (Figure 3.24) was used to reflect pressure in the polishing chamber during AFP. Given that volume percentage (vol %) of abrasive particles affects the pressure stability, pressure values were tested using different percentages of B_4C with a particle size of 100 μm, as recorded in Table 5.1. Notably, an excessively high proportion of 6 vol% would cause unstable pressure while 2 and 4 vol% could obtain stable pressure in AFP. In addition, Figure 5.1 indicates reduction percentages of surface roughness with different volumes of abrasive particle. It is noted that 2 vol% has lowest reduction of Ra and Rz, while 4 and 6 vol% show similar reduced proportion. It can be explained that a lower percentage of abrasive particles results in a lower proportion of effective scratching particles during AFP [153]. Given that 4 vol% of abrasive particles could obtain both stable pressure and higher reduction of surface roughness, 4 volume percent of abrasive particles is used in the following sections.

Table 5.1 Pressure conditions at different volumes of B_4C with a particle size of 100 μm.

Vol% of abrasive particles	Pressure	Pressure stability
2	0.08 ± 0.01 Mpa	Stable
4	0.08 ± 0.01 Mpa	Stable
6	0 ～0.40 Mpa	Unstable
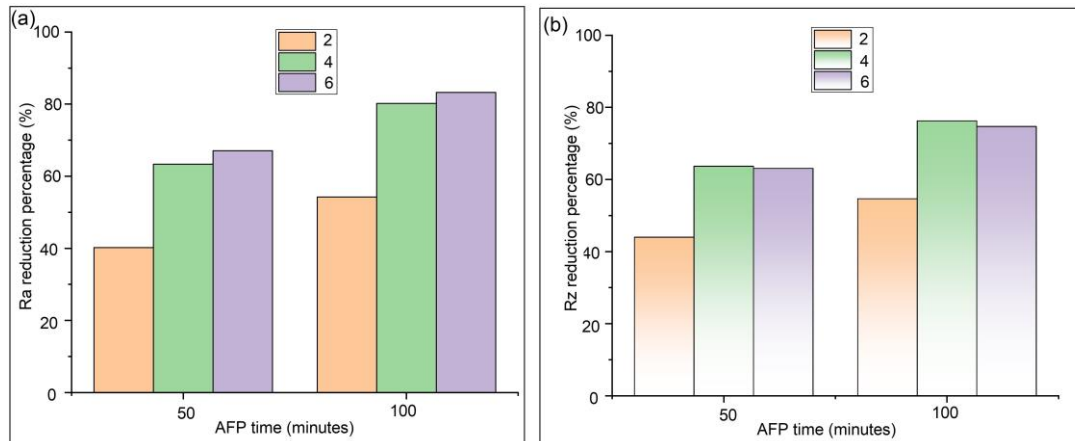
Figure 5.1 Images of surface roughness reduction percentage of (a) Ra and (b) Rz on L-PBF 316L stainless steel side inner surfaces after AFP with different volume percentages of B_4C with a particle size of 100 μm.

5.1.2 Types of abrasive particles

Based on the literature review in Chapter 2, researchers have applied various types of ceramic abrasive particles in AFP [14, 16]. In this section, three types of commercial abrasive particles were tested to optimize the type of abrasive particles. SEM images of B_4C, Al_2O_3 and SiC abrasive particles are shown in Figure 5.2. Various types of abrasive particles have irregular shape and the narrowest point of different types of particles is around 100 μm.
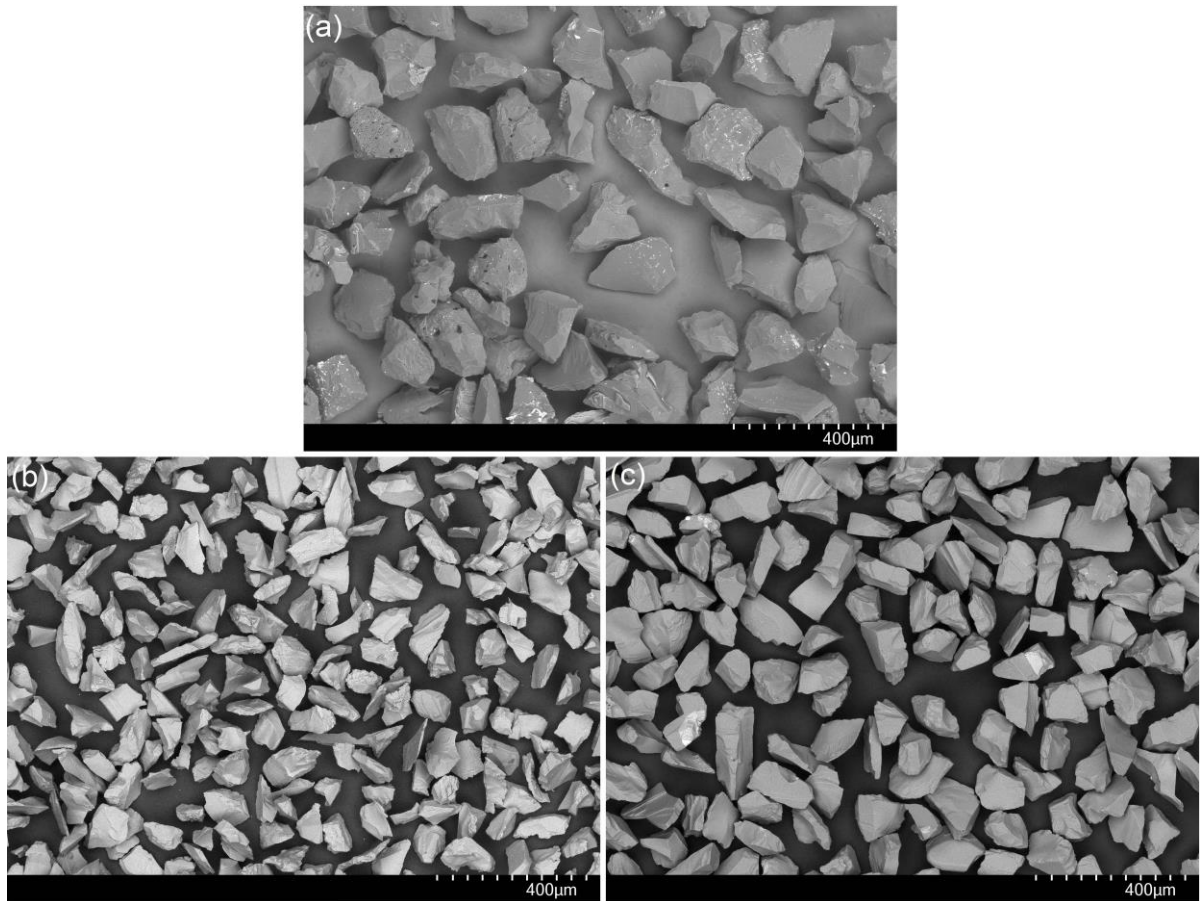
Figure 5.2 SEM images of (a) B_4C, (b) Al_2O_3 and (c) SiC with particle size of 100 μm.

As can be seen in Figure 5.3, some scratching area shows up after AFP with different types of abrasive particles and the area ratio of scratching area increases with the prolongation of AFP time. Moreover, under the same AFP time, the area ratios of scratching area using B_4C, Al_2O_3 are higher than SiC. AFP effects of different abrasive particles can be further analyzed according to the reduction percentages of surface roughness in Figure 5.4. Consistent with the scratching area ratios in Figure 5.3, SiC shows the lowest reduction of surface roughness in comparison to others. With 50 minutes of AFP, similar percentage reductions of surface roughness show up with the use of B_4C and Al_2O_3. Then, B_4C exhibits the highest reduction rate of Ra and Rz after 100 minutes of AFP. This may be caused by a combined effect of hardness and density which results in a higher impact kinetic energy of B_4C during AFP. Given that AFP generally performs hours of polishing on L-PBF inner surfaces, B_4C has demonstrated superiority to Al_2O_3 and SiC in AFP.
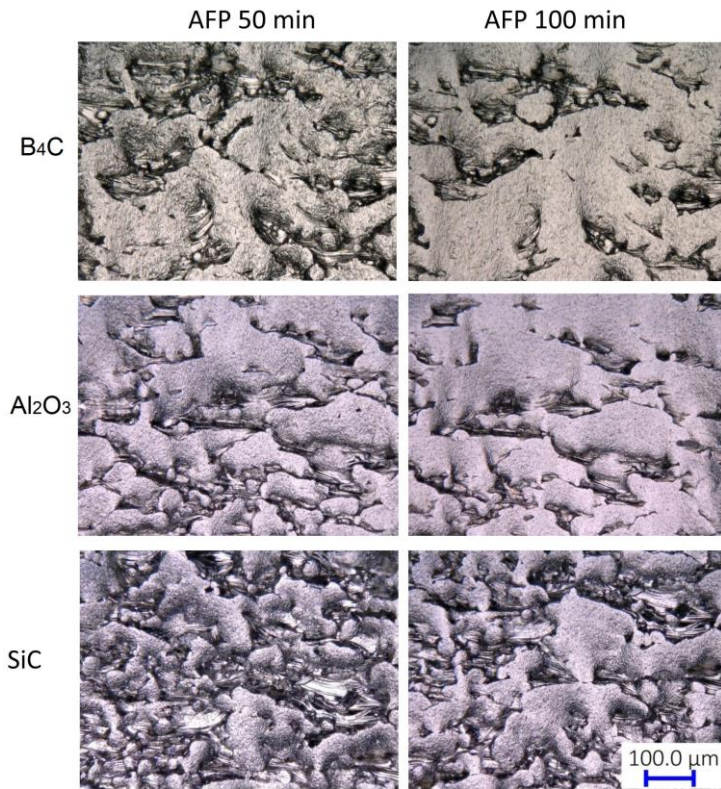
Figure 5.3 OM images of the same area on internal surfaces of L-PBF 316L stainless steel channels with an increase of AFP time using different types of abrasive particles.
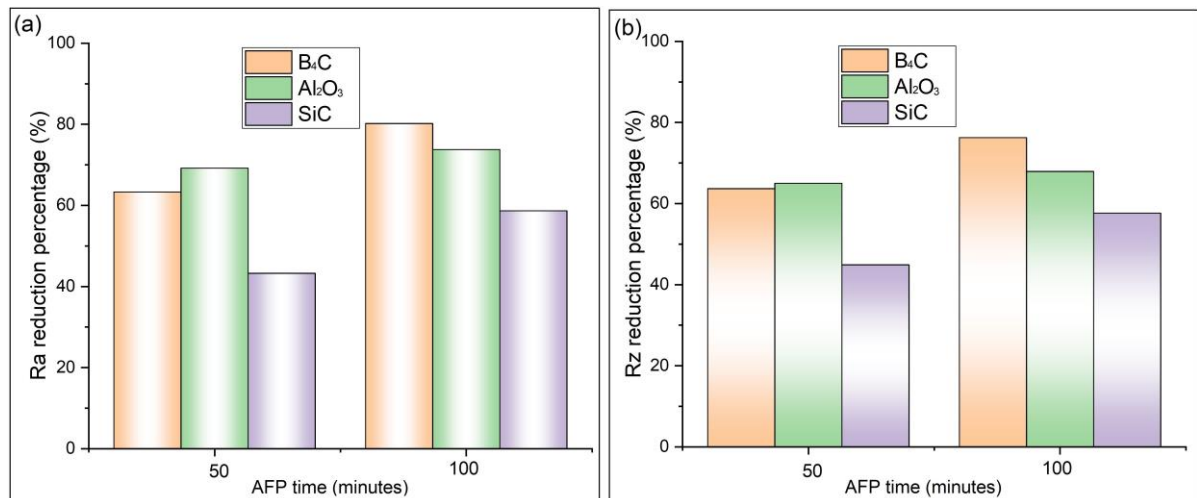
Figure 5.4 Images of surface roughness reduction percentage of (a) Ra and (b) Rz on L-PBF 316L stainless steel side inner surfaces with an increase of AFP time using different types of abrasive particles.

5.1.3 Size of abrasive particles

In terms of the particle size of B_4C, different sizes such as 50, 100 and 200 μm were optimized in order to obtain better AFP efficiency on L-PBF inner surfaces. Morphology analysis of B_4C abrasive particles with various sizes shows the irregular shape in Figure 5.5. With an increase of AFP time, the proportions of scratching area

also increase as can be seen in Figure 5.6. Compared with the size of 50 and 200 μm, the size of 100 μm shows the highest percentage of scratching area. Consistent with scratching morphology, B_4C with the size of 100 μm results in the largest reduction of Ra as shown in Figure 5.7. Because of the same density of B_4C particles, the mass of abrasive particles increases with an increase of particle size. As a result, the kinetic energy of the abrasive particles impacting workpiece surface increases with the particle size during AFP. In addition, the size of particles could also influence sharp corners of abrasive particles and the impact pressure per unit area on the workpiece surface during polishing [154]. According to the combined effects of the kinetic energy, impact pressure and sharp corners of B_4C with different sizes, B_4C with the size of 100 μm shows the best AFP efficiency and would be used in the following sections.
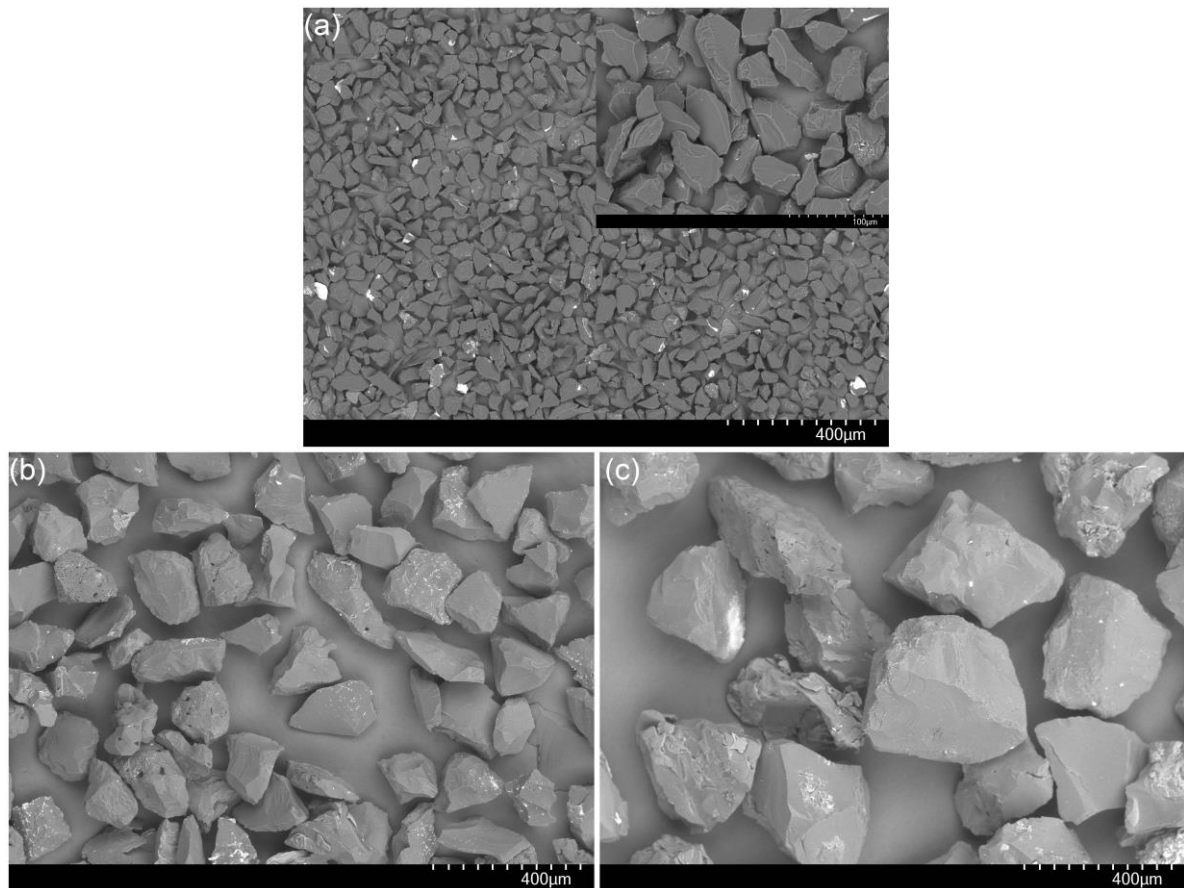
Figure 5.5 SEM images of B_4C with particle sizes of (a) 50, (b) 100 and (c) 200 μm.
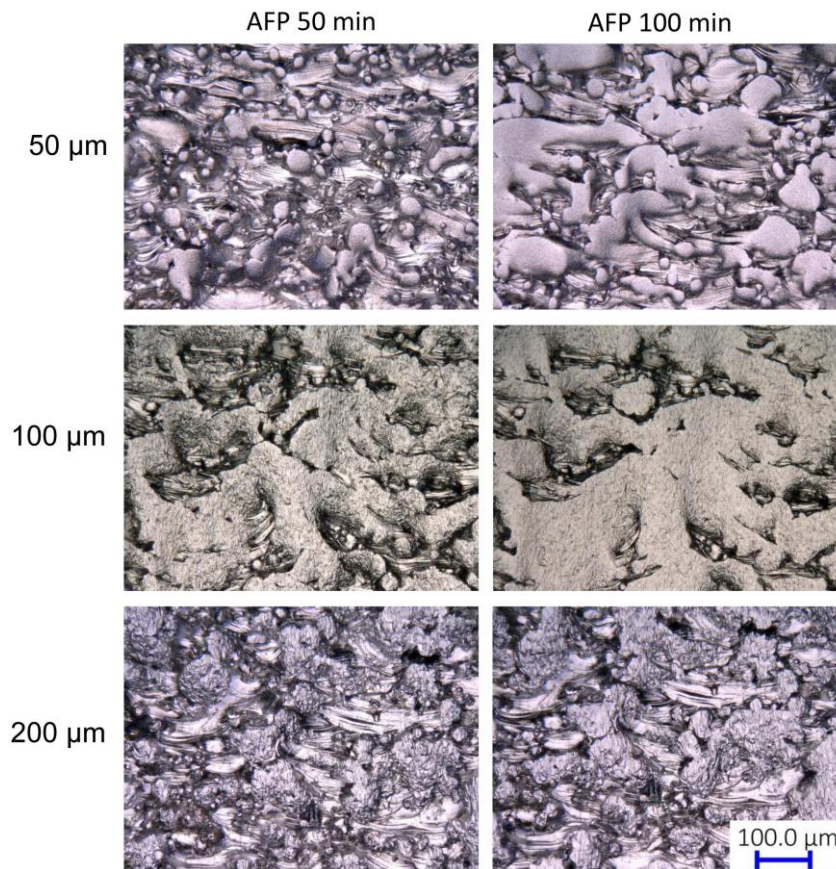
Figure 5.6 OM images of the same area on internal surfaces of L-PBF 316L stainless steel channels with an increase of AFP time using different sizes of B$_4$C.
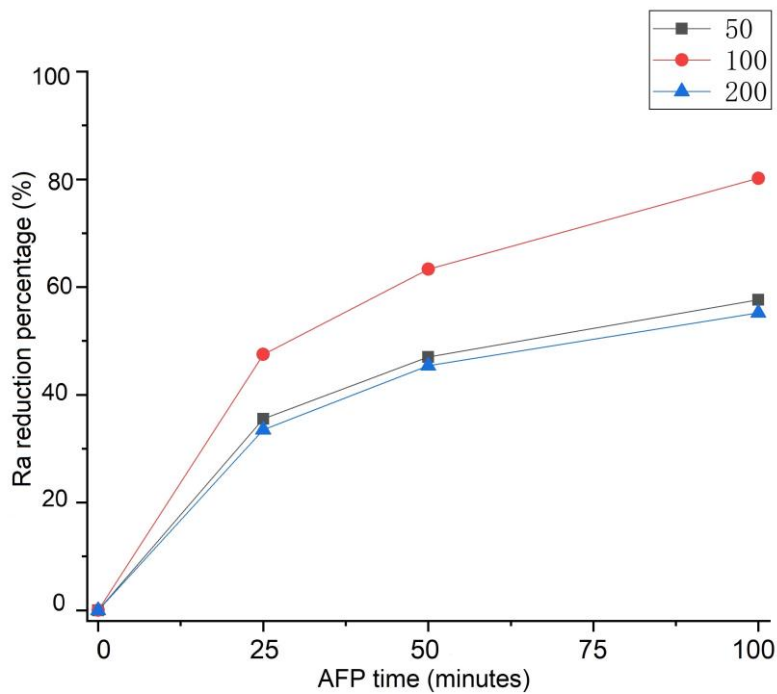
Figure 5.7 Surface roughness reduction percentages of Ra on L-PBF 316L stainless steel side inner surfaces with an increase of AFP time using different sizes of B$_4$C.

5.1.4 Use time of abrasive particles

The optimized parameters of abrasive particles in AFP are also applicable to L-PBF Ti6Al4V inner surfaces. Surface roughness reduction percentages of L-PBF Ti6Al4V side inner surfaces with different conditions of abrasive particles are summarized in Table 5.2. Compared with other abrasive particles, 4 vol% of B_4C with particle size of 100 μm also demonstrates the largest reduction in surface roughness.

Table 5.2 Surface roughness reduction percentages of L-PBF Ti6Al4V side inner surfaces after AFP with different conditions of abrasive particles.

Particle	Size (μm)	Vol%	AFP time (minutes)	Ra reduction (%)	Rz reduction (%)
B_4C	100	2	50	39.5	38.9
B_4C	100	4	50	58.4	57.8
B_4C	100	6	50	55.3	51.2
B_4C	100	4	100	71.1	63.9
Al_2O_3	100	4	100	68.3	61.2
SiC	100	4	100	62.3	56.9
B_4C	50	4	50	42.8	41.9
B_4C	200	4	50	41.5	40.6

Considering the wear of abrasive particles during AFP, morphology of raw B_4C and particles after polishing for 5 hours is compared in Figure 5.8. Despite the existence of wear, the shape and cutting edges of B_4C remains sharp before and after polishing for 5 hours. Please note that B_4C particles would be replaced after 5 hours of use in the following sections in order to ensure the consistency of AFP efficiency.
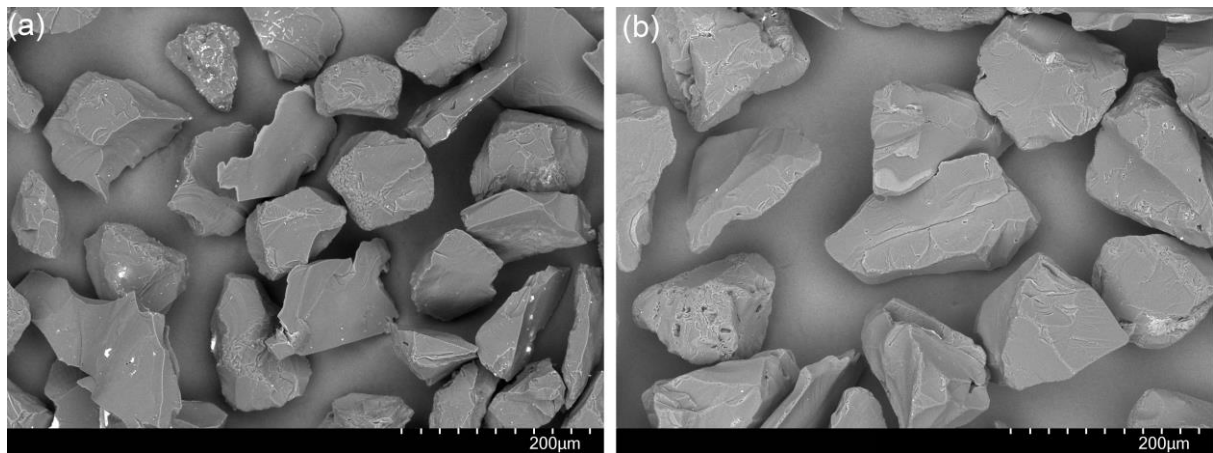
Figure 5.8 SEM images of (a) raw B_4C and (b) B_4C after 5 hours use in AFP with 4 vol% and particle size of 100 μm.

5.2 AFP of 316L stainless steel internal surfaces

5.2.1 Experimental approaches

AFP of L-PBF 316L stainless steel internal surfaces was carried out using the developed polishing system as illustrated in Figure 3.24, Figure 3.26a and b. Based on the optimized parameters in section 5.1, B_4C particles and water were mixed as polishing media with the volume percent of B_4C particles is 4. A stable flow rate of 0.18 L/s that measured from the flow meter and a stable pressure of 0.08 MPa which measured by the pressure gauge in the polishing system could be achieved during AFP. X-ray diffraction patterns of L-PBF side inner surface on the same sample were tested by a D500 X-ray diffractometer (Siemens, Germany) with Cu Kα radiation at 40 kV and 30 mA before and after AFP. Considering that traditional AFP could enlarge channel entrance and cause non-uniform final surface finish [153], the inlet of the chamber was designed for AFP of L-PBF internal straight channels as illustrated in Figure 5.9. There is a gradient change from the large size diameter of pipe to the diameter of the internal channel (Φ 5 mm). Notably, fluid would pass a length of 14mm through the flow channel before reaching the inner surface of L-PBF straight channels.
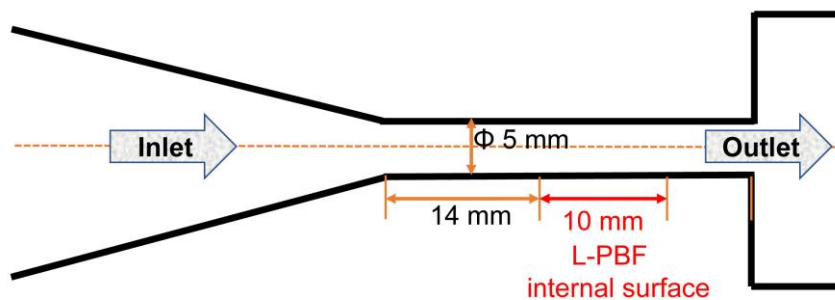
Figure 5.9 Dimension design of cross section of the inlet of polishing chamber in AFP.

5.2.2 Polishing uniformity of AFP

To demonstrate the design of the inlet during AFP, morphologies of a large-area on the inner surface of the same L-PBF Ti6Al4V side channel before and after 50, 100 and 200 minutes of AFP were measured. Based on the uniform polishing morphologies with different AFP time in Figure 5.10, the design of the inlet during AFP in this study

could effectively weaken or even eliminate hole expansion effect and non-uniform polishing problems of traditional AFP.
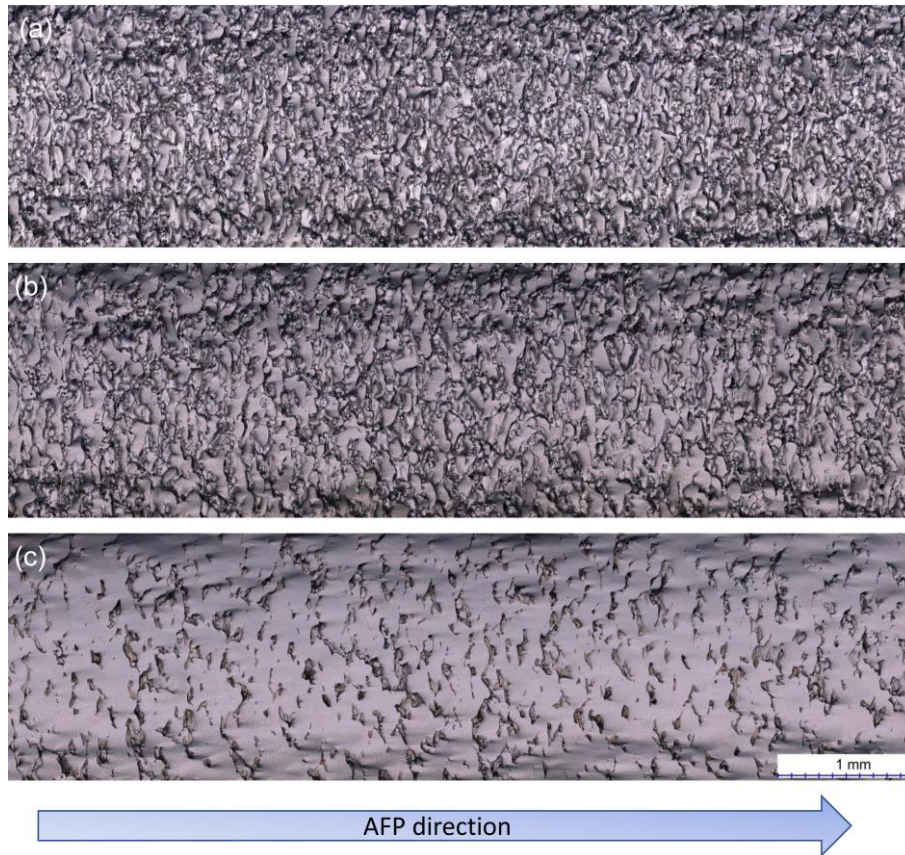
Figure 5.10 Inner surface morphology of the same inner side surface on a L-PBF Ti6Al4V channel after AFP for (a) 50, (b) 100 and (c) 300 minutes.

5.2.3 AFP effects

Both Ra and Rz values of various L-PBF 316L stainless steel internal surfaces before and after AFP were measured as shown in Figure 5.11. Although various inner surfaces have different initial surface roughness, Ra and Rz values on top (Figure 5.11a), face up (Figure 5.11b) and side (Figure 5.11c) surfaces exhibit a similar decreasing trend with three distinct regions from original to 300 minutes of AFP. The first decreasing zone is the first 25 minutes which has the fastest decline rate in roughness. Then, the rate of roughness reduction gradually slows from 25 to 200 minutes of AFP. In the third region, there is no significant decrease in Ra and Rz values from 200 to 300 minutes of AFP. Despite of the similar reduction trend, the reduction percentage of roughness on face up surface is obviously higher than top and side surfaces in the first 25 minutes. Different from other inner surfaces, multiple fluctuations

113

of changes in roughness appeared on the face down surface during AFP. For example, roughness values from 15 to 50 minutes of AFP first rises slightly and then continue to decrease as can be seen in Figure 5.11d.
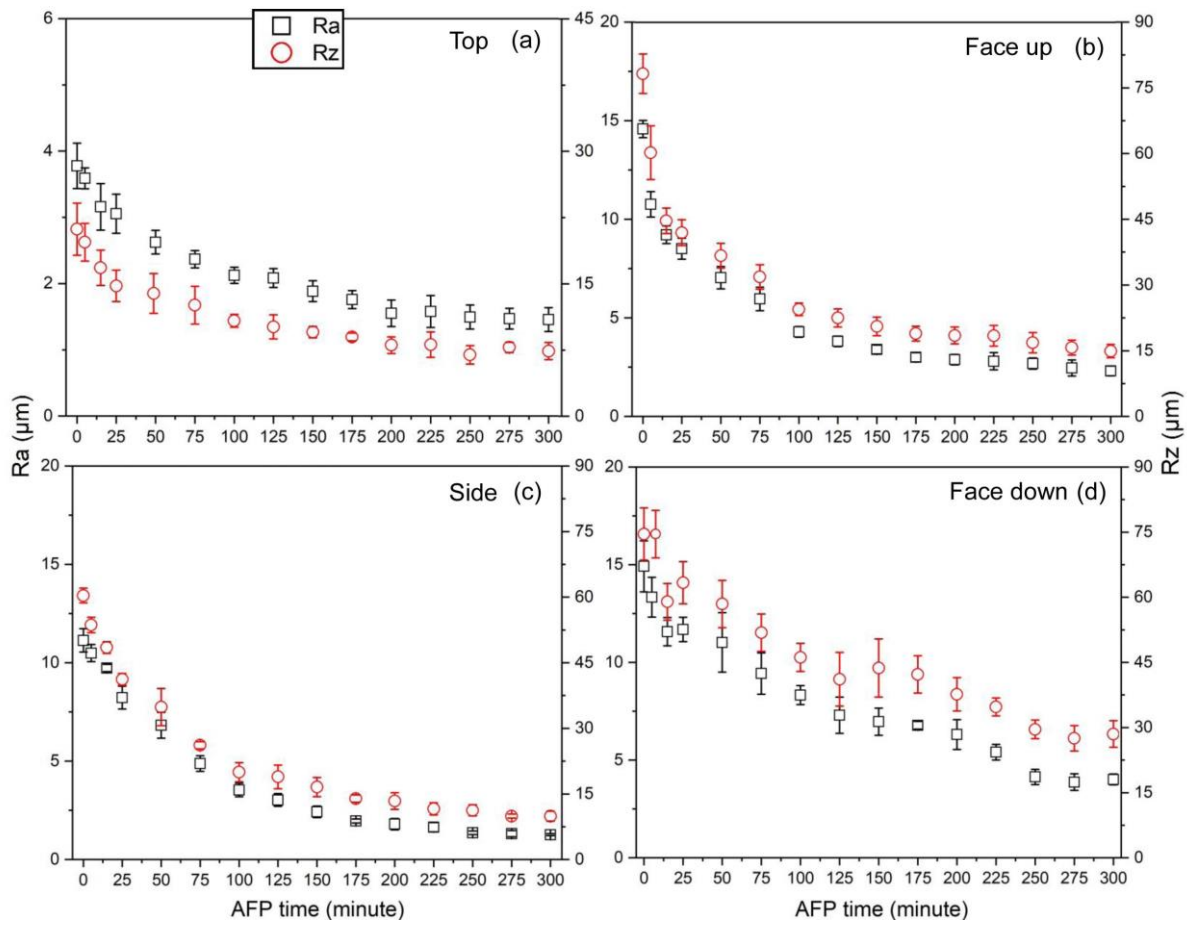
*F*igure 5.11 Ra and Rz values of L-PBF 316L stainless steel internal (a) top, (b) face up, (c) side and (d) face down surfaces before and after 5, 15, 25, 50, 75, 100, 125, 150, 175, 200, 225, 250, 275 and 300 minutes of AFP. Note that the left vertical axis represents Ra and the right vertical axis represents Rz.

Figure 5.12 and Figure 5.13 indicate morphology evaluation of different L-PBF inner surfaces over AFP processing time. In the first 25 minutes of AFP (Figure 5.12), the total area ratio with scratching traces on different surfaces increases significantly with extension of AFP time. Meanwhile, the area ratio of scratching marks on specific surface features such as raw sintered area generally increases. However, some surface features with circular morphology (marked with red circles) could be removed directly without leaving scratching morphology after 5 minutes of AFP. Moreover, some area (marked with yellow boxes) with scratching marks could also be removed directly after AFP from 5 to 15 minutes. Then, morphological changes of AFP are still obvious from 50 to 200 minutes. During this period, AFP effectively removes some original

areas and leaves scratching traces (Figure 5.13). Despite that an increase of scratching area is not significant on the top, face up and side inner surfaces from 200 to 300 minutes, the total scratching area still increases with extension of AFP time. Different from other surfaces, the increase of scratching area ratio on the face down surface is obvious from 200 to 300 minutes. In addition, raw areas could be observed on various L-PBF inner surfaces after AFP for 300 minutes as shown in Figure 5.13.
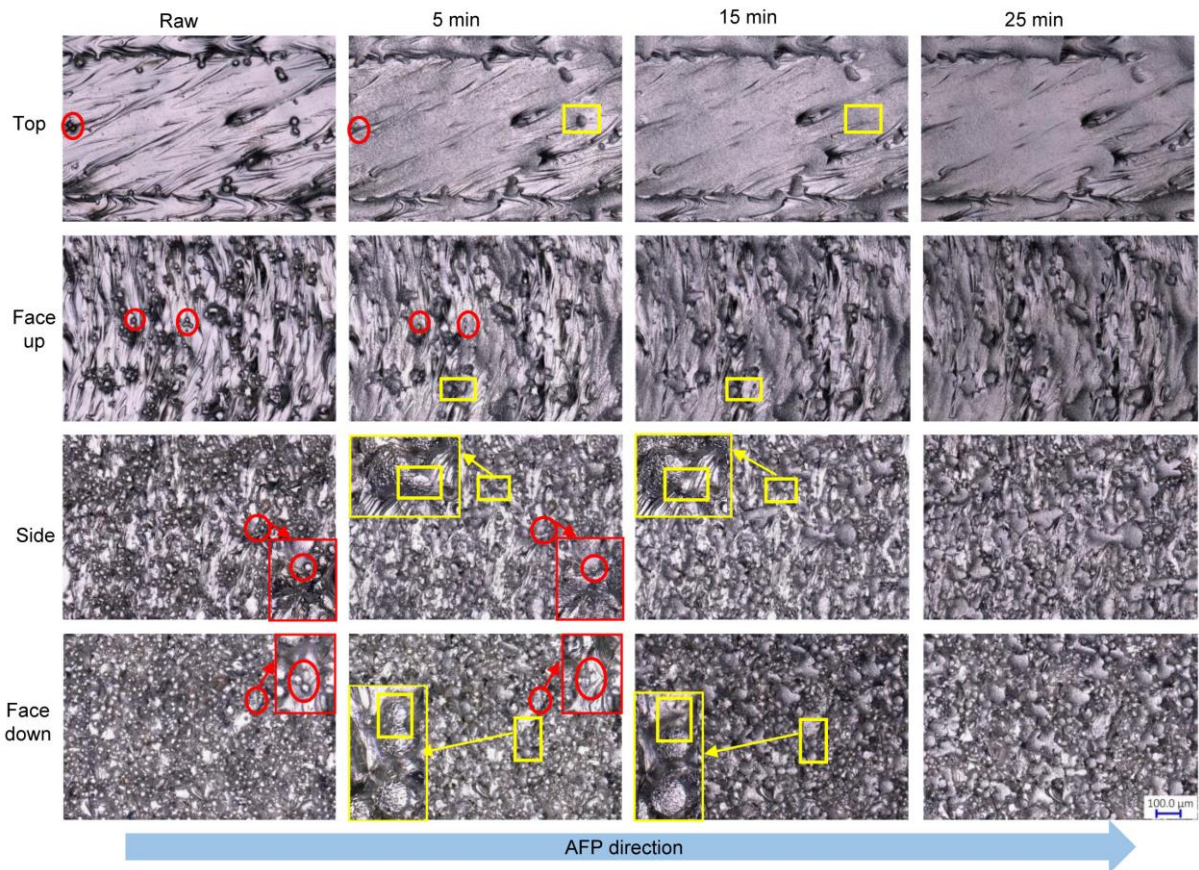
Figure 5.12 OM images of the same area on inner top, face up, side and face down surfaces on L-PBF 316L stainless steel channels after different time of AFP.
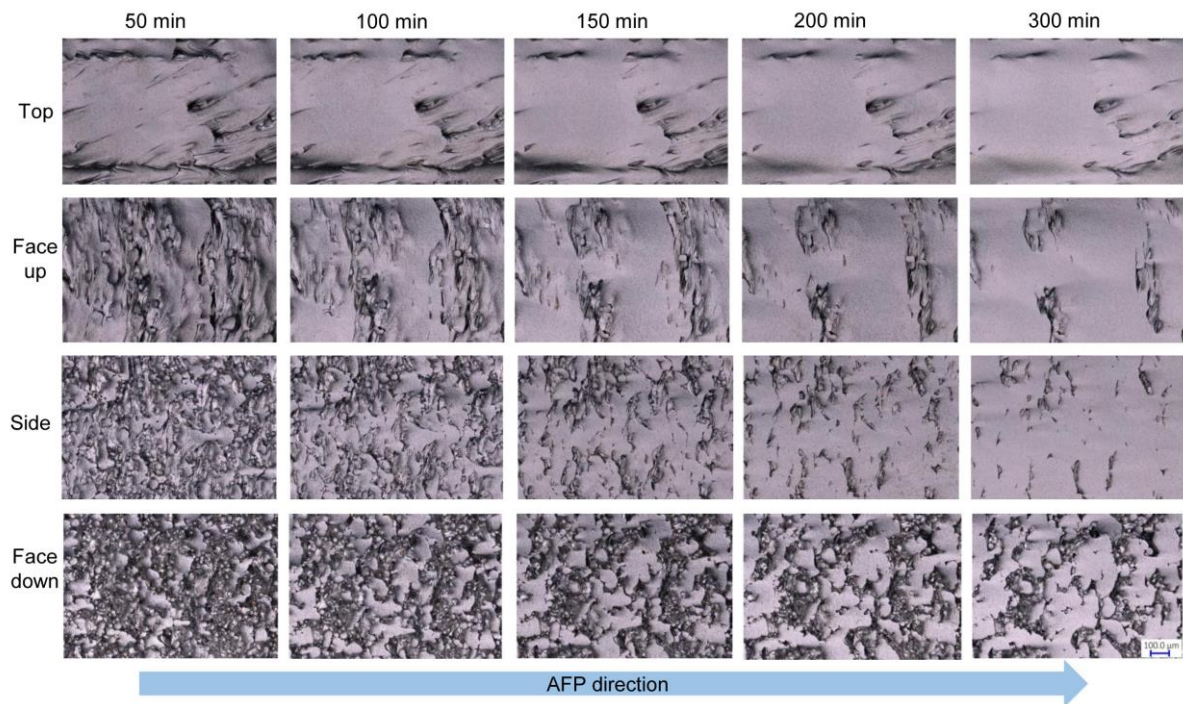
Figure 5.13 OM images of the same area on inner top, face up, side and face down surfaces on L-PBF 316L stainless steel channels after 50, 100, 150, 200 and 300 minutes of AFP.

Given that AFP is a mechanical polishing process, collision and scratching of abrasive particles with surface may cause external forces to act on L-PBF inner surfaces. As a result, there should be residual stress on inner surfaces after AFP. Residual stress is usually divided into micro stress and macro stress. The two types of stress behave differently in the X-ray diffraction spectrum. Micro stress refers to the residual stress inside grain, and its existence generally widens diffraction peaks. Different from micro stress, macro stress refers to stress that exists on multiple crystallographic scales and its performance on the X-ray diffraction spectrum is to shift the peak position. Austenite peaks of the inner surface on the same L-PBF 316L stainless steel side 1/6 channel before and after different AFP times are shown in Figure 5.14. Compared with the width of austenite peaks on raw surface, it is obvious that AFP could cause broadening of austenite peaks. However, it is difficult to determine the shifting degree of peaks since it is not significant. Thus, AFP could increase micro residual stress of L-PBF 316L stainless steel inner surfaces based on the qualitative analysis of X-ray diffraction results.
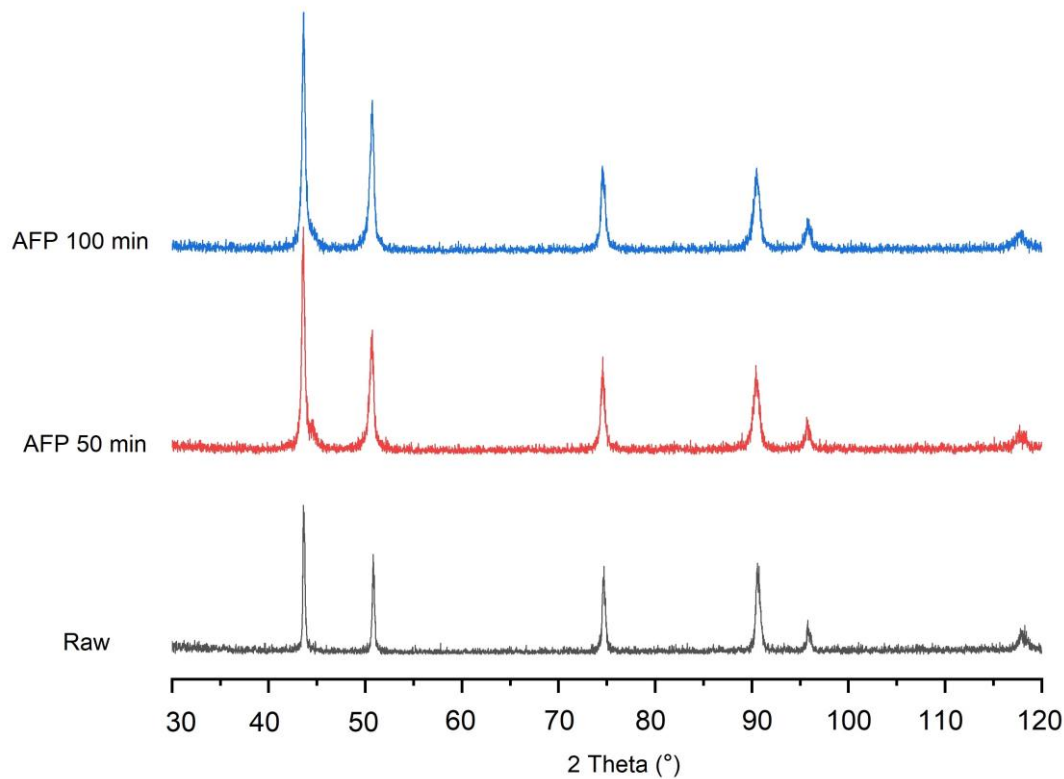
Figure 5.14 X-ray diffraction results with austenite peaks of an inner side surface on the same L-PBF 316L stainless steel side channel before and after different time of AFP.

5.2.4 Material removal mechanism

Morphology with large-area and high magnification of etched cross sections on top internal surfaces of L-PBF 316L stainless steel is shown in Figure 5.15 and Figure 5.16, respectively. In the first 25 minutes of AFP, raw surface features such as protruding sintered area still remained on surface (Figure 5.15). Then, the whole surface was further levelled from 50 to 200 minutes of AFP (Figure 5.15). Correspondingly, protruding sintered area and un-sintered powder are observed after AFP for 5 and 25 minutes (see Figure 5.16), respectively. Notably, obvious scratching marks appears on cross sections after 15 minutes of AFP which is consistent with morphology results in Figure 5.12 and Figure 5.13. Based on the lowest raw surface roughness among various L-PBF inner surfaces (Figure 5.11), most of surface area can be scratched to a relatively flat condition after 200 minutes of AFP. However, un-sintered powders at valley positions still exist after 200 minutes of AFP as illustrated in Figure 5.16.
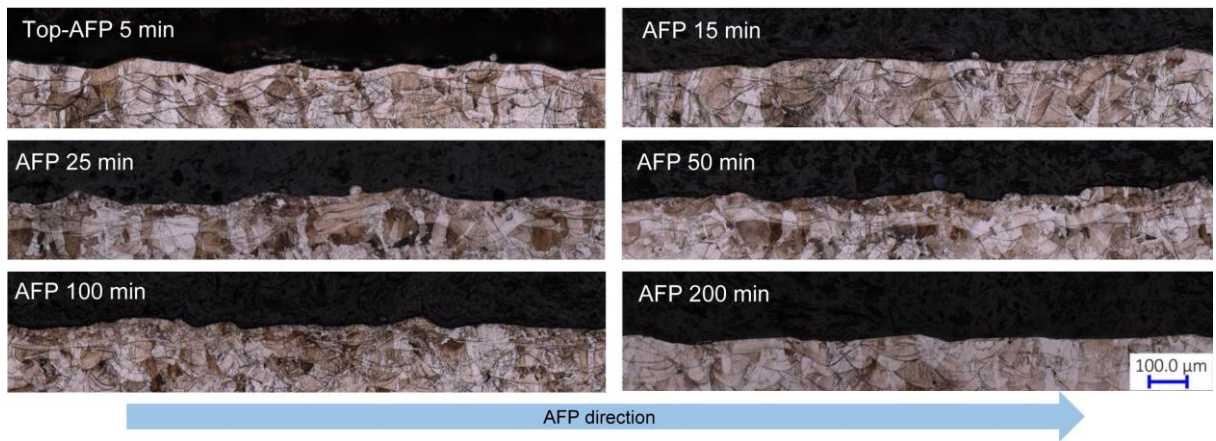
Figure 5.15 OM images of etched cross sections on inner top surfaces of L-PBF 316L stainless steel after different time of AFP.
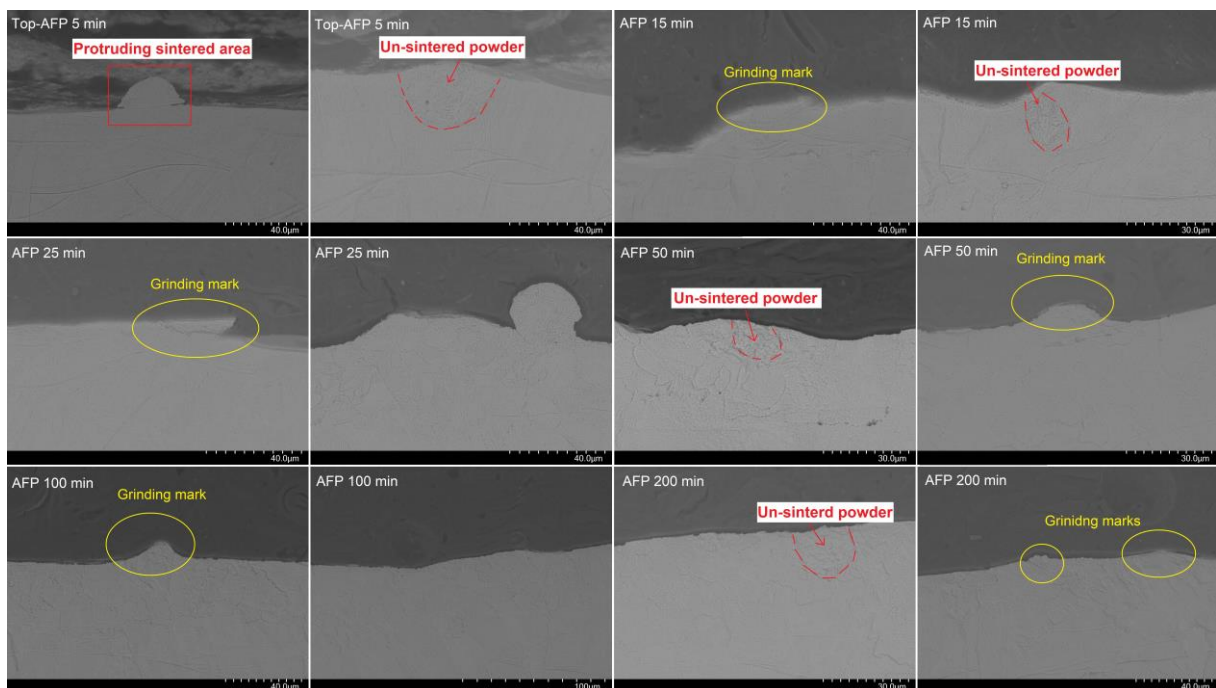
Figure 5.16 SEM images of etched cross sections on inner top surface of L-PBF 316L stainless steel after different time of AFP.

Morphology of etched cross sections on face up internal surfaces of L-PBF 316L stainless steel are illustrated in Figure 5.17, Figure 5.18 and Figure 5.19, respectively. From 5 to 25 minutes of AFP, the quantity of un-sintered powders that have necking or narrow connections with surface reduces significantly (Figure 5.17). Due to the existence of agglomeration adhesions and narrow connections between some surface features and face up surfaces, scratching marks with narrow necking morphology on cross sections are observed after AFP for 5, 15 and 25 minutes (Figure 5.18). It is worth noting that deformation of an un-sintered powder is observed after 25 minutes

118

of AFP, as shown in Figure 5.18, implying that some surface features would be deformed by collision with abrasive particles before being removed. The deformation of surface features demonstrates that the presence of forces acting on L-PBF inner surfaces during AFP, which is consistent with the X-ray diffraction results in Figure 5.14.

Despite of the same AFP direction, scratching marks in Figure 5.18 exhibit different scratching angles on face up surfaces. Meanwhile, surface features at approximate surface heights show varied degree of removal. When the flow rate is low, the fluid flows in layers without mixing, which is called laminar flow. With a gradually increase of flow velocity, streamline of the fluid begins to appear wavy swing. The frequency and amplitude of the swing increase with an increase of the flow velocity and this flow condition is called transition flow. When the flow velocity increases greatly, the streamlines are not clearly discernible, meanwhile, there are many small eddies in the flow which means that the laminar flow is destroyed. Thus, there is not only sliding but also mixing between adjacent flow layers, resulting in turbulent flow [153]. Thus, the directional and height irregularity characteristic of AFP in removing L-PBF surface features (see Figure 5.18) is related to the fact that AFP in this study is a turbulence process.
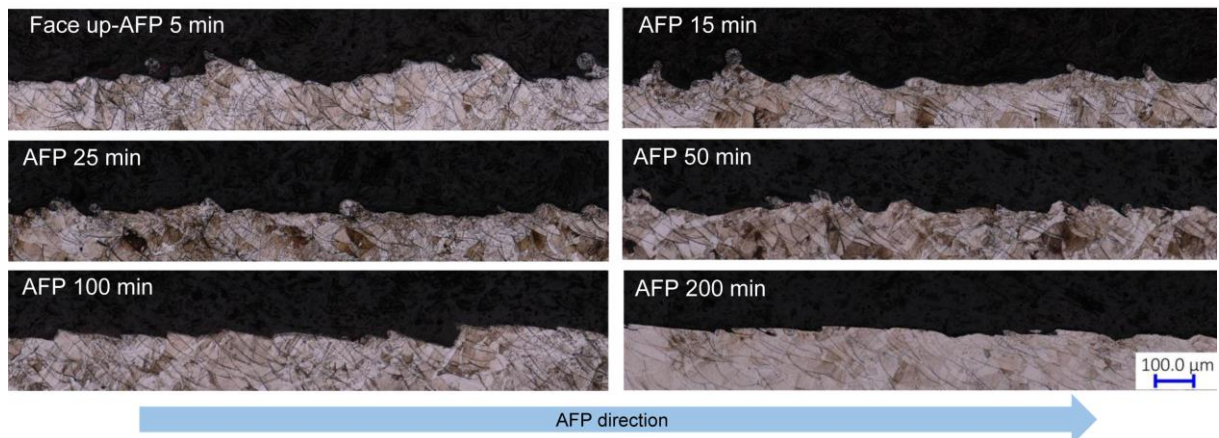
Figure 5.17 OM images of etched cross sections on inner face up surfaces of L-PBF 316L stainless steel after different time of AFP.
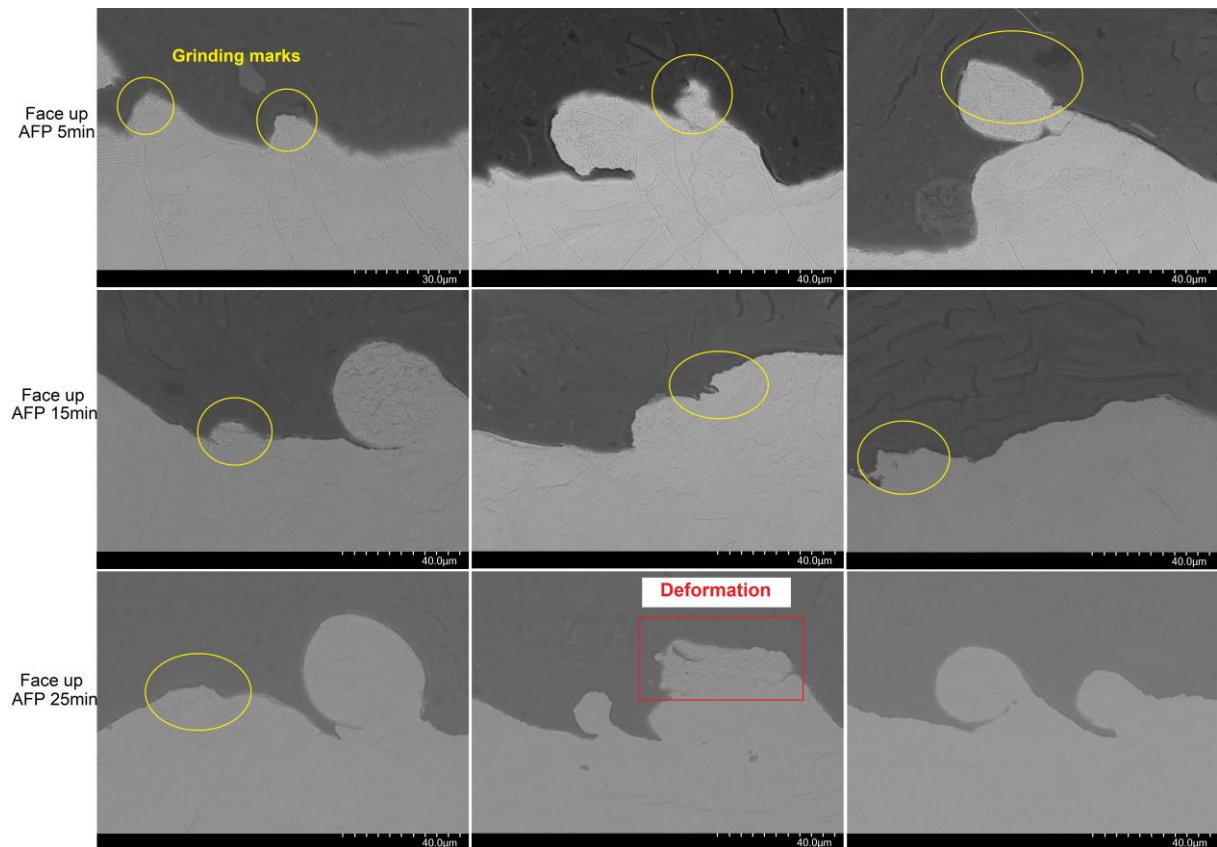
Figure 5.18 SEM images of etched cross sections on inner face up surfaces of L-PBF 316L stainless steel after 5, 15 and 25 minutes of AFP.

With an increase of AFP time, surface features at protruding positions on face up surfaces exhibit a higher degree of scratching from AFP for 50 to 200 minutes than surface features at valley positions as shown in Figure 5.17 and Figure 5.19. This can be explained that time-cumulative effect of AFP could result in a higher material removal rate for surface features at protruding locations than valley locations on L-PBF inner surfaces. After AFP for 200 minutes, most surface area has been scratched and achieved a relatively flat condition. Similar to top surfaces, un-sintered powders at valley positions still remain on the face up surface as shown in Figure 5.19.
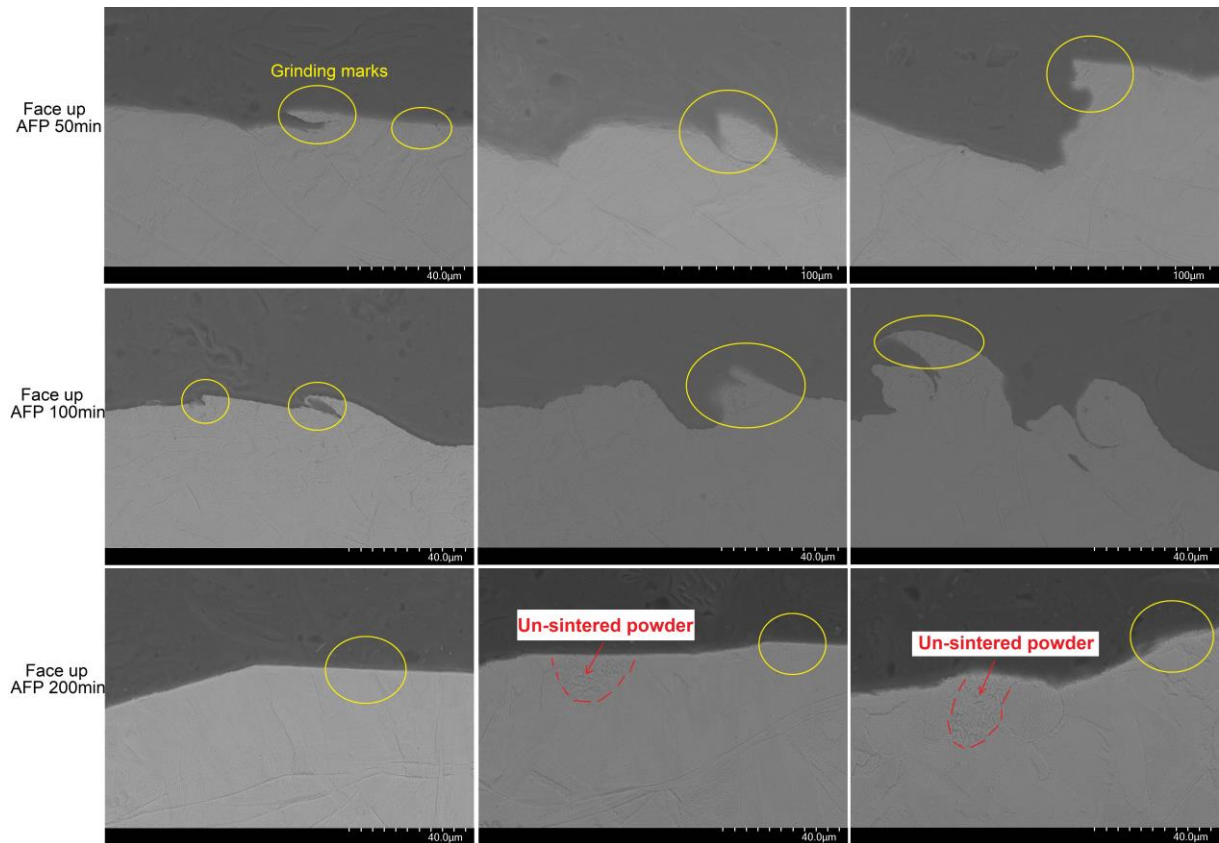
Figure 5.19 SEM images of etched cross sections on inner face up surfaces of L-PBF 316L stainless steel after 50, 100 and 200 minutes of AFP.

Morphology of etched cross sections on side internal surfaces of L-PBF 316L stainless steel is shown in Figure 5.20, Figure 5.21 and Figure 5.22, respectively. With AFP for 5 to 25 minutes, some scratching marks with narrow necking morphology occur on cross sections because there are some necking connections between surface features and side surfaces (see Figure 5.21). The irregular movement of abrasive particles during AFP can also be observed based on that scratching marks in Figure 5.21 located at different heights on side surfaces and showed various scratching angles. Consistent with face up surfaces, surface features at protruding positions on side inner surfaces exhibit a higher degree of scratching from AFP for 50 to 200 minutes (see Figure 5.20 and Figure 5.22) compared to surface features at valley positions.
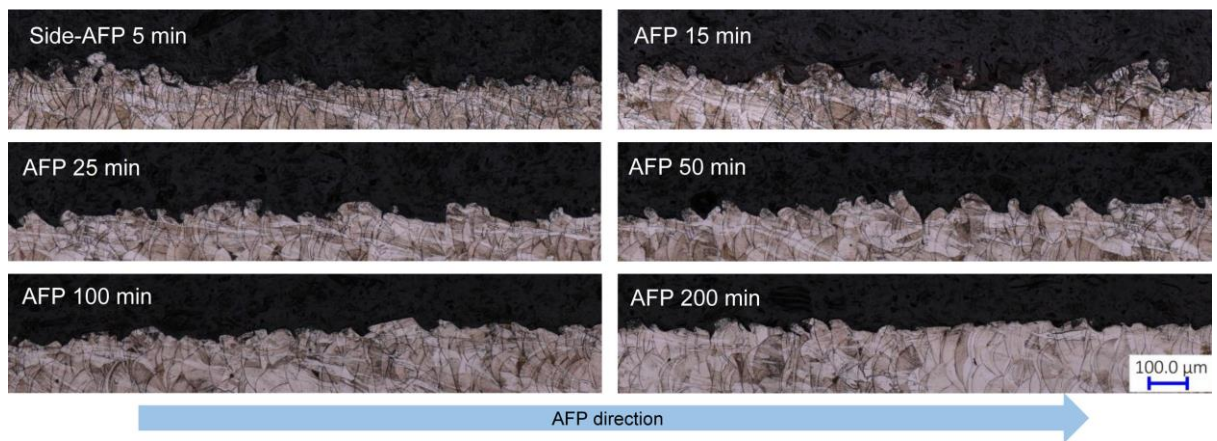
Figure 5.20 OM images of etched cross sections on inner side surfaces of L-PBF 316L stainless steel after different time of AFP.
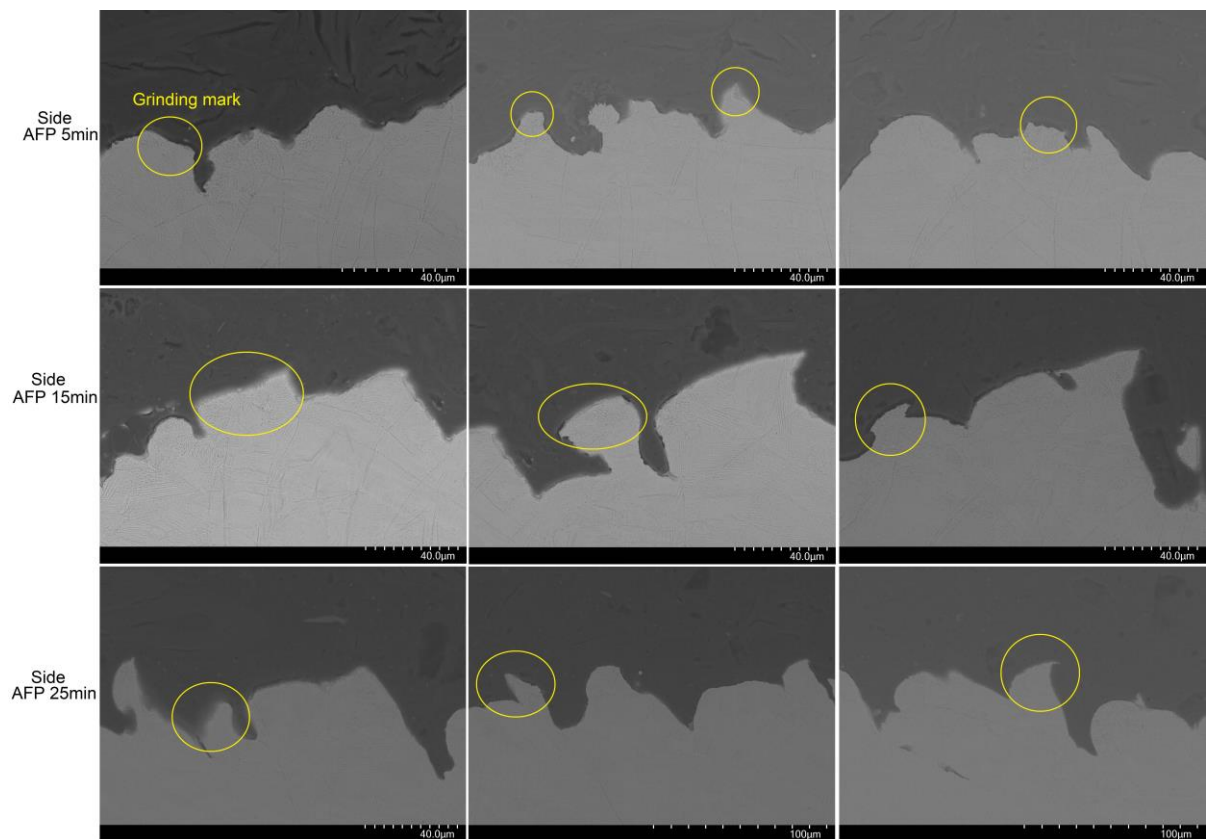
Figure 5.21 SEM images of etched cross sections on inner side surfaces of L-PBF 316L stainless steel after 5, 15 and 25 minutes of AFP.
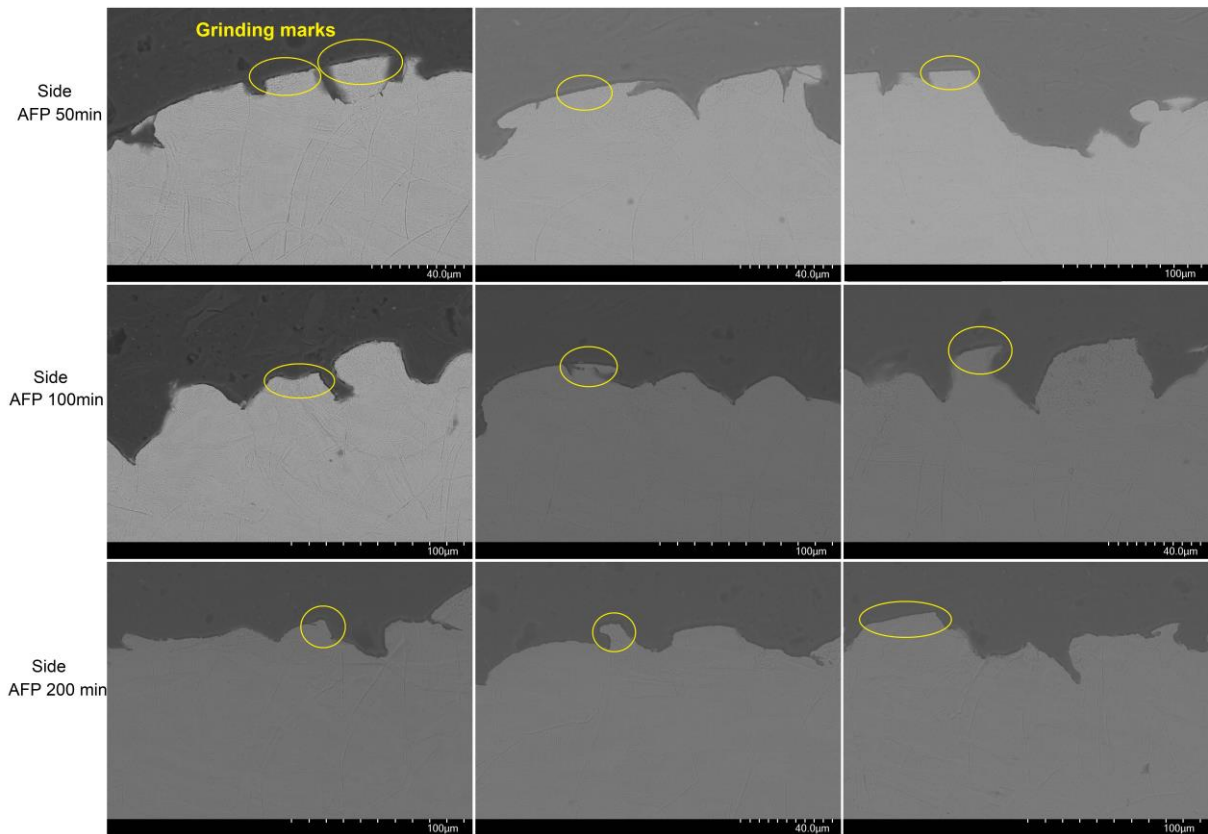
Figure 5.22 SEM images of etched cross sections on inner side surfaces of L-PBF 316L stainless steel after AFP for 50, 100 and 200 minutes.

Figure 5.23, Figure 5.24 and Figure 5.25 present morphology of etched cross sections on face down internal surfaces of L-PBF 316L stainless steel. As AFP time increased from 5 to 15 minutes, the quantity of un-sintered powders at protruding positions are reduced significantly as seen in Figure 5.23. Then, surface morphology changes slightly from 15 to 25 minutes of AFP because of the short time interval and rough face down surfaces (Figure 5.23 and Figure 5.24). Considering that surface roughness values measured in this study are based on the contact measurement principle, topographic changes of face down surfaces over AFP processing time may cause fluctuations in measured Ra and Rz values, which are due to the complexity of raw L-PBF inner face down surfaces as shown in Figure 5.11. The directional and height irregularity characteristic of AFP can also be observed in Figure 5.24 considering the turbulence state of AFP. Consistent with face up and side inner surfaces, surface features at protruding positions exhibit a higher degree of scratching from 50 to 200 minutes of AFP (Figure 5.23) than surface features at valley positions

123

on face down surfaces. In addition, face down surfaces still rough after 200 minutes and can be further smoothed which is consistent with obvious morphology change from 200 to 300 minutes of AFP in Figure 5.25.
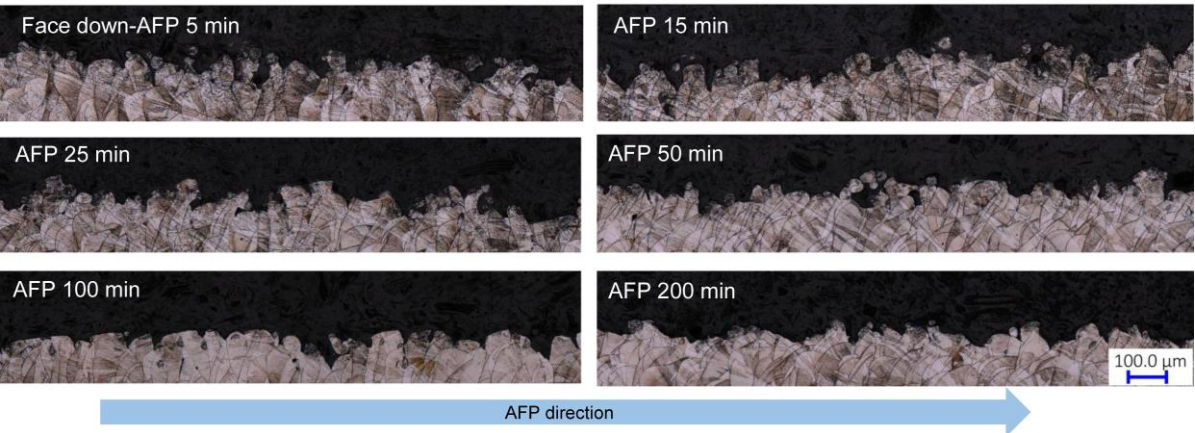
Figure 5.23 OM images of etched cross sections on inner face down surfaces of L-PBF 316L stainless steel after different time of AFP.
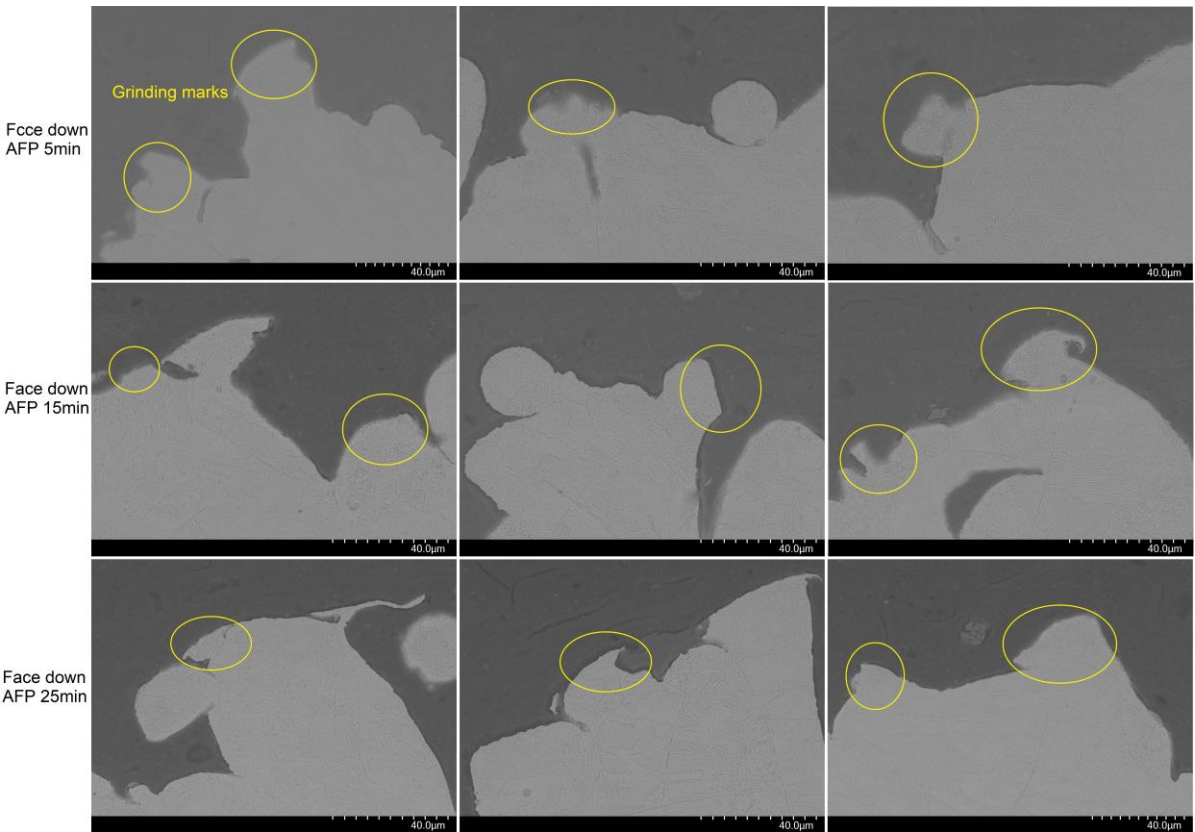
Figure 5.24 SEM images of etched cross sections on inner face down surfaces of L-PBF 316L stainless steel after 5, 15 and 25 minutes of AFP.
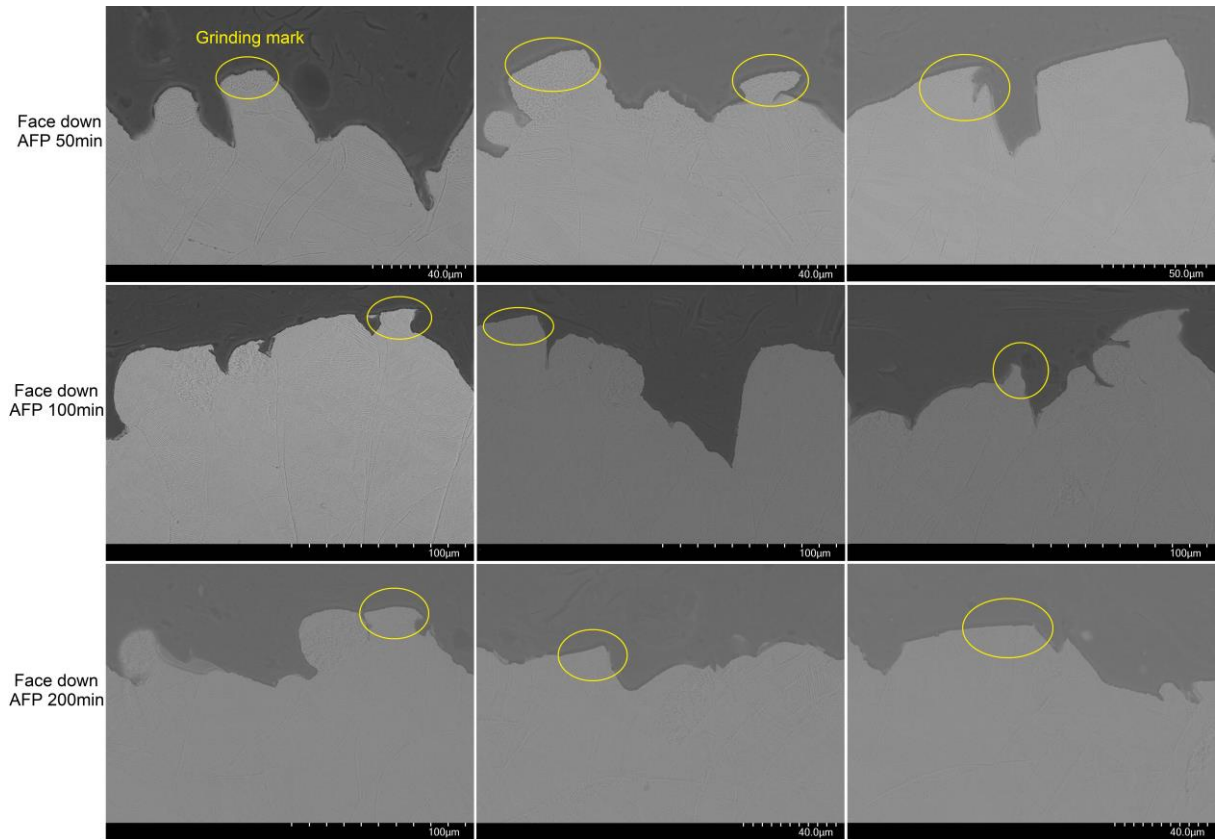
Figure 5.25 SEM images of etched cross sections on inner face down surfaces of L-PBF 316L stainless steel after 50, 100 and 200 minutes of AFP.

To further study the material removal mechanism, AFP effects on topography evolution are shown in Figure 5.26. Consistent with morphology changes of cross sections on L-PBF face up, side and face down surfaces, time-cumulative effect of AFP could result in a higher material removal rate for surface features at protruding locations than valleys on L-PBF internal surfaces despite the turbulence state of AFP.
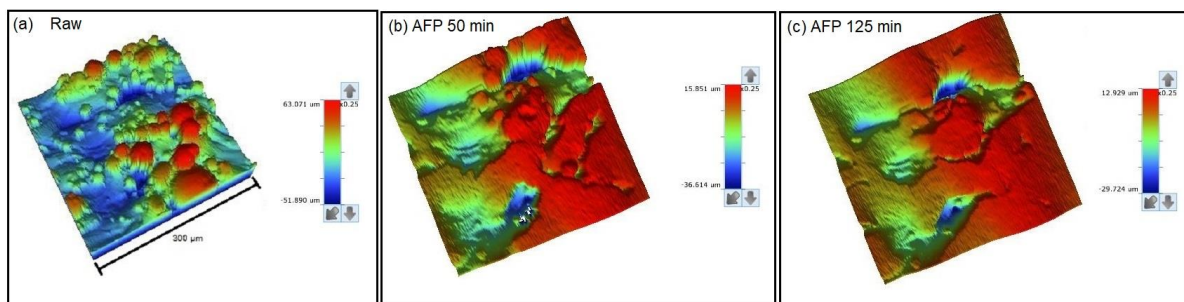
Figure 5.26 Topography evolution of the same location of side inner surface on a L-PBF 316L stainless steel side channel before and after different time of AFP.

Based on the above discussions, when looking back on Figure 5.11, Figure 5.12 and Figure 5.13, morphological evolution, reduction of surface roughness and material

removal mechanism over AFP processing time could be well explained. With a short time of AFP, collisions and scratching between abrasive particles and surface cause deformation and removal of surface features, which could effectively remove surface features that have narrow connection area with L-PBF surface. Therefore, direct removal of the surface features marked by red circles and yellow boxes could be observed in Figure 5.12 attributing to the turbulent nature of AFP. Correspondingly, the highest reduction of Ra and Rz shows up from 5 to 25 minutes on L-PBF 316L stainless steel inner top, face up and side surfaces (see Figure 5.11). Due to the higher quantity of surface features with necking connections and agglomeration adhesions than others, the reduction percentage of surface roughness of face up surfaces is higher than others in the first 25 minutes. Then, remaining surface features would be further scratched and the time-cumulative effect of AFP could result in a higher material removal rate at protruding locations than valley locations on L-PBF surfaces. With an increase of scratching area ratio, efficiency of AFP gradually decreases because more areas need to be removed until AFP could polish valley positions. Therefore, the reduction of Ra and Rz values also gradually reduce from 25 to 200 minutes of AFP surfaces (Figure 5.11). Moreover, it is difficult to further polish all areas of L-PBF inner surfaces by AFP when the area of scratched zone increases to a certain extent. Thus, raw morphology at valley positions still can be observed on various L-PBF surfaces after AFP for 300 minutes (see Figure 5.13).

The material removal mechanism and process of inner surfaces of L-PBF 316L stainless steel during AFP is shown in Figure 5.27. Considering the connection and location differences of surface features, the surface features with narrow or unstable connections can be deformed or scratched, resulting in removal directly or leaving scratching marks with various scratching angles due to the irregular movement of abrasive particles in AFP (see Figure 5.27a and b). Then, AFP is more preferable to remove surface features that located at protruding positions than valley positions on L-PBF surfaces with prolongation of AFP time (see Figure 5.27c and d).
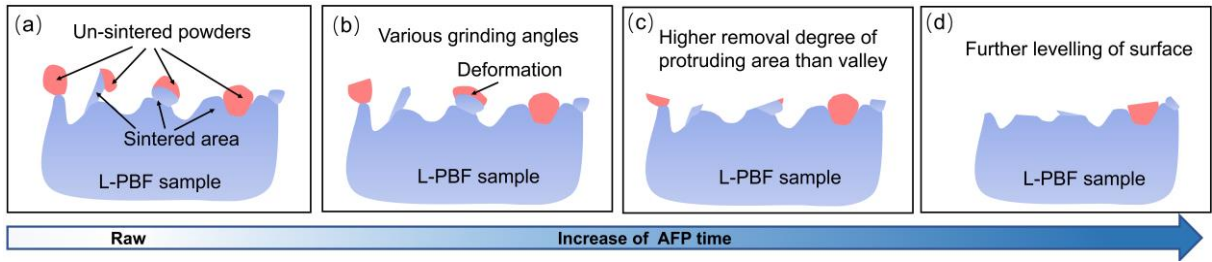
Figure 5.27 Schematic diagram of (a) raw L-PBF inner surface and (b-d) material removal process during AFP.

5.3 AFP of Ti6Al4V internal surfaces

5.3.1 Experimental approaches

AFP of L-PBF Ti6Al4V internal surfaces was carried out using the developed polishing system as illustrated in Figure 3.24, Figure 3.26a and b. Based on optimized parameters in section 5.1, B_4C particles and water was mixed as polishing media for AFP process and the volume of B_4C particles was 4%. A stable flow rate of 0.18 L/s and a stable pressure of 0.08 MPa that measured from the flow meter and pressure gauge could be achieved, respectively. In addition, X-ray diffraction patterns was performed by a D500 X-ray diffractometer (Siemens, Germany) with Cu Kα radiation at 40 kV and 30 mA on a side inner surface before and after AFP.

Considering that AFP is a mechanical process with turbulent flow and L-PBF surfaces with the same printing orientation show similar morphology, material removal mechanism of AFP that analysed for different L-PBF 316L stainless steel inner surfaces in section 5.2.2 is also applicable to various L-PBF T6Al4V inner surfaces. Therefore, morphology evolution and roughness changes of L-PBF Ti6Al4V inner surfaces after different time of AFP are discussed considering characteristics of specific inner surfaces.

5.3.2 Morphology evolution

AFP effects on morphology evaluation of different L-PBF Ti6Al4V inner surfaces are shown in Figure 5.28 and Figure 5.29. As AFP time increased from 5 to 25 minutes (Figure 5.28), the total area ratio of scratching traces on different surfaces increases. Correspondingly, the area ratio of scratching traces on specific surface features such

as raw sintered area also increases. Consistent with L-PBF 316L stainless steel (Figure 5.12), some features with circular morphologies (marked with red circles) on various surfaces could be removed directly without leaving scratching marks after 5 minutes of AFP. Moreover, some area (marked with yellow boxes) with scratching marks are also removed directly from 5 to 15 minutes. Then, morphological changes of AFP are obvious from 50 to 200 minutes which means that AFP could effectively remove some original areas and leave scratching traces during this period. Then, the increase of scratching area is insignificant on top, face up and side inner surfaces from 200 to 300 minutes of AFP. Different from other inner surfaces, the increase of scratching area ratio on face down surface is obvious from 200 to 300 minutes. In addition, there are raw areas on various L-PBF inner surfaces after 300 minutes of AFP.
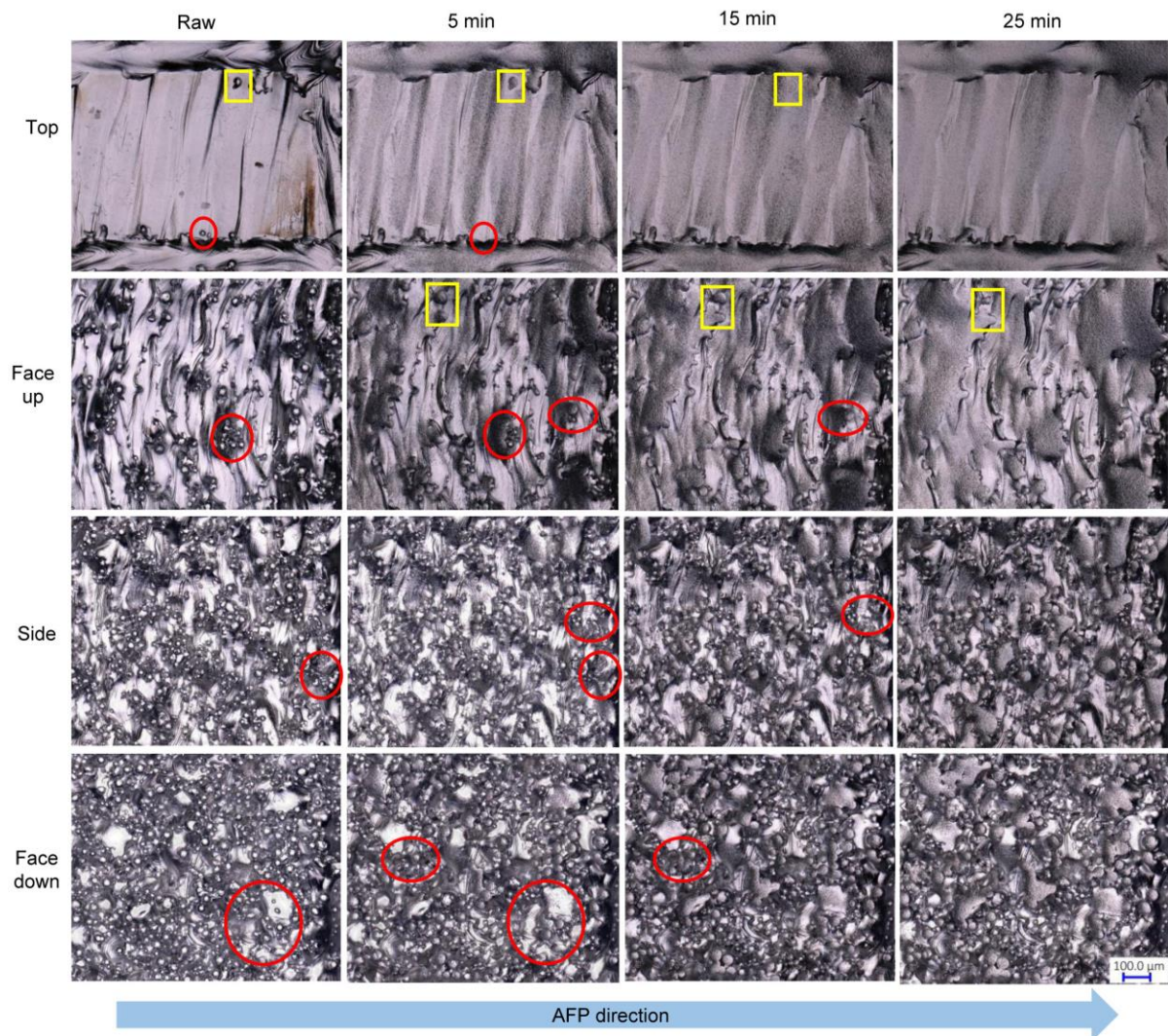
Figure 5.28 OM images of the same area on inner top, face up, side and face down surfaces on L-PBF Ti6Al4V channels after different time of AFP.
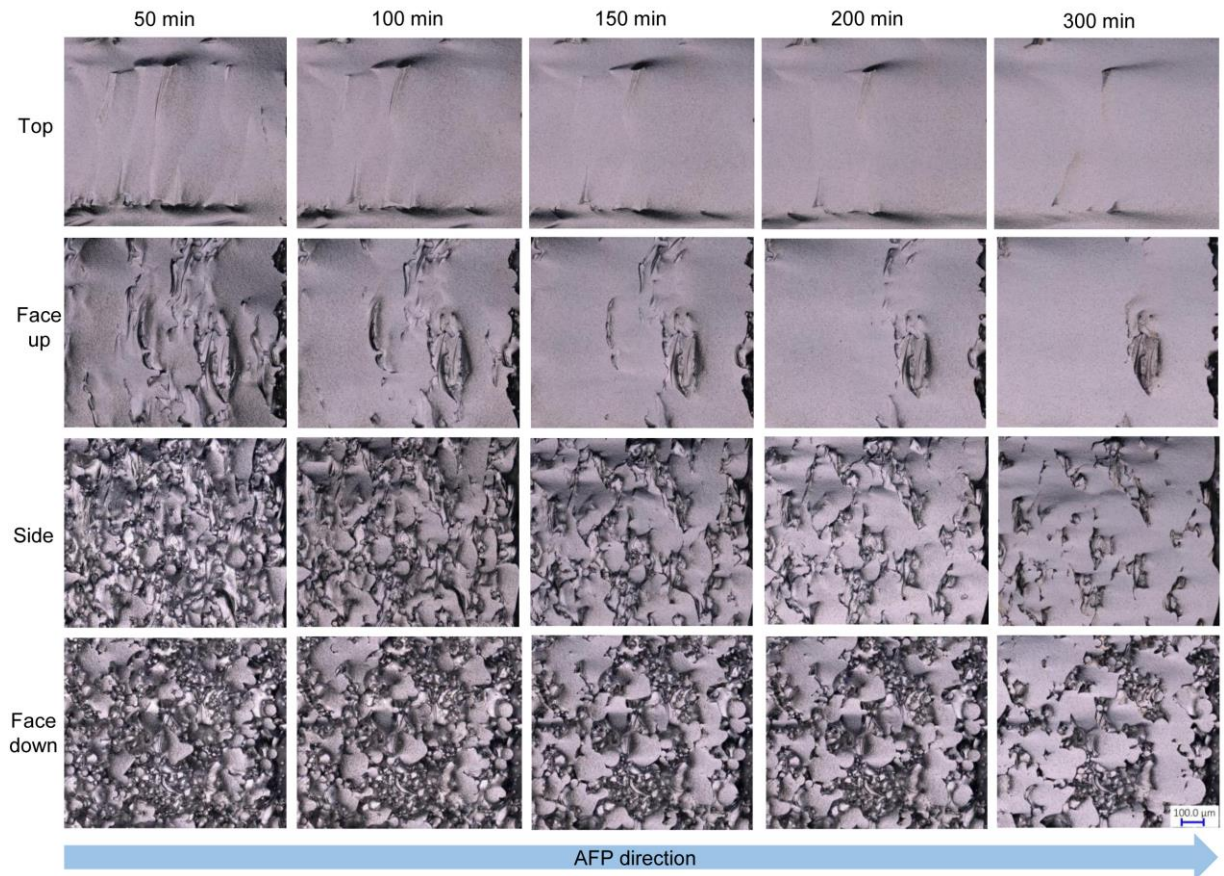
Figure 5.29 OM images of the same area on inner top, face up, side and face down surfaces on L-PBF Ti6Al4V channels after AFP for 50, 100, 150, 200 and 300 minutes.

5.3.3 Roughness and residual stress

Roughness values of various L-PBF Ti6Al4V internal surfaces before and after different time of AFP were measured and shown in Figure 5.30. Similar to L-PBF 316L stainless steel (Figure 5.11), Ra and Rz values on, face up (Figure 5.30b) and side (Figure 5.30c) surfaces have a similar decreasing trend with three distinct regions from original to 300 minutes of AFP. The first decreasing zone of the face up and side surfaces is the first 25 minutes of AFP which has the fastest rate of decline in roughness. It should be noted that the first decreasing zone for top surface (Figure 5.30a) is the first 5 minutes which differs from the face up and side surfaces. This could be explained that there are limited spherical adhesions on the top surface. Then, the reduction rate of roughness on the top, face up and side surfaces is gradually reduced until AFP reached 200 minutes. In the third region, there is no significant decrease in Ra and Rz values from 200 to 300 minutes. Despite of the similar reduction trend, the

129

reduction percentage of roughness on the face up surface is obviously higher than the top and side surfaces because AFP is capable of removing agglomerated spherical adhesions effectively on face up surfaces as analyzed in section 5.3.3. Different from other inner surfaces, multiple fluctuations appear on face down inner surface during AFP (Figure 5.30d) considering the largest amount of un-sintered powders and maximum roughness of sintered area on the raw face down surface.

Considering that AFP is a mechanical polishing process, scratching and collision of abrasive particles with L-PBF inner surface could cause external forces to act on the inner surface. α-Ti peaks [142] of an inner surface on the same L-PBF Ti6Al4V side channel before and after 50 minutes of AFP are shown in Figure 5.31. Compared with the width of peaks on raw surface, it is obvious that AFP caused broadening of α-Ti peaks. Similar to Figure 5.14, it is also hard to determine the shifting degree of peaks. Thus, AFP could increase micro residual stress of L-PBF Ti6Al4V inner surfaces based on the qualitative analysis of X-ray diffraction results.
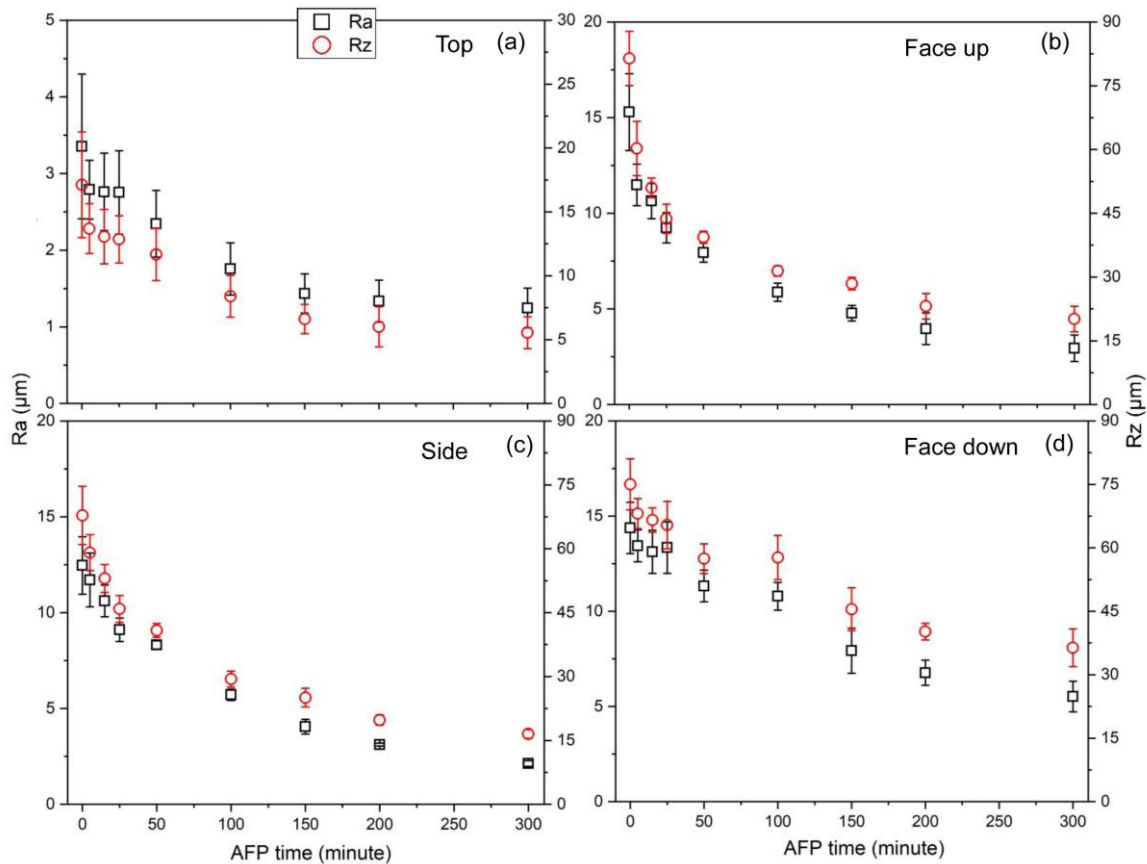
Figure 5.30 Ra and Rz values of L-PBF Ti6Al4V internal (a) top, (b) face up, (c) side and (d) face down surfaces before and after different time of AFP. Note that the left vertical axis represents Ra and the right vertical axis represents Rz.
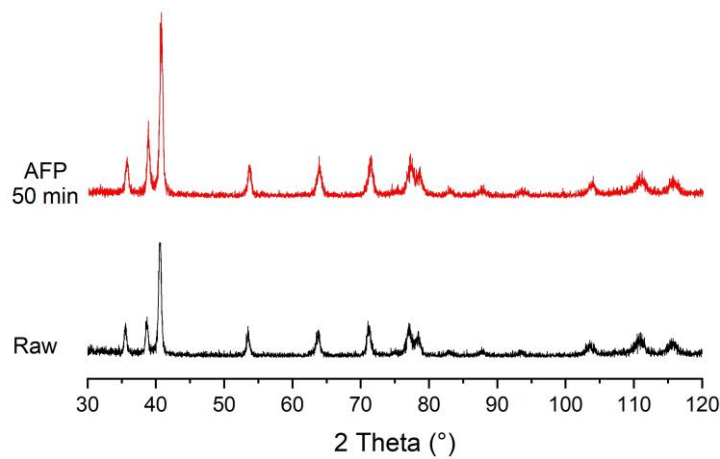
Figure 5.31 X-ray diffraction peaks of hexagonal close-packed (hcp) α-Ti of the inner surface on the same L-PBF Ti6Al4V side channel before and after 50 minutes of AFP.

5.4 Comparison

Considering the uniform inner morphology of L-PBF side 1/6 channels, roughness reduction percentages of side inner surfaces of L-PBF 316L stainless steel and Ti6Al4V before and after AFP for 25, 50, 100 and 200 minutes are shown in Figure 5.32. It could be seen that surface roughness reduction percentages of two alloys are close to each other in the first 25 minutes of AFP because surface features that have unstable connections with L-PBF side surfaces could be removed efficiently during this period. With the prolongation of AFP time, the degree of roughness reduction of AFP on the side internal surface of L-PBF 316L stainless steel is higher than that of Ti6Al4V due to the lower hardness of L-PBF 316L stainless steel than Ti6Al4V. Thus, the mechanical property of L-PBF alloys can affect AFP efficiency and needs to be considered.
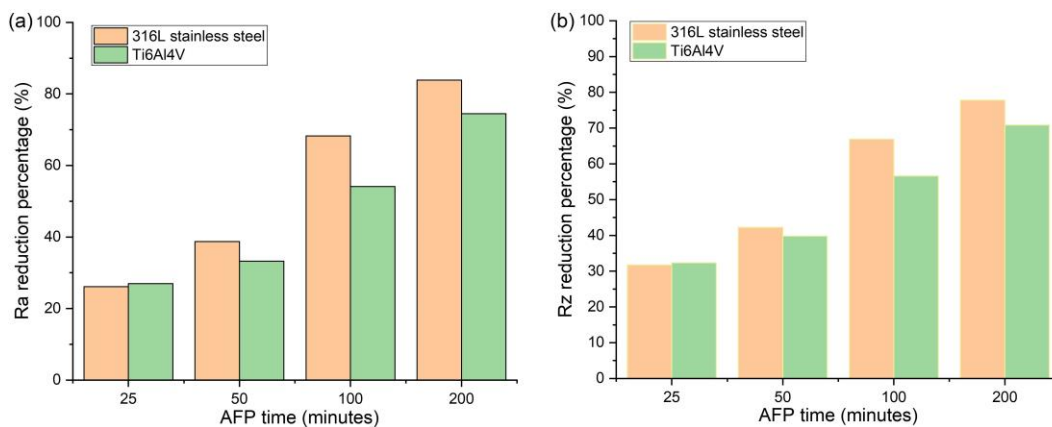
Figure 5.32 Images of (a) Ra and (b) Rz reduction percentages of inner side surfaces of L-PBF 316L stainless steel and Ti6Al4V before and after 25, 50, 100 and 200 minutes of AFP.

5.5 Summary

This chapter investigates the material removal mechanism of AFP on top, face up, side and face down internal surfaces of L-PBF 316L stainless steel and Ti6Al4V considering the characteristics of L-PBF surface features. Morphology, Ra and Rz values are evaluated to study AFP effects on different inner surfaces. The cross sections of various internal surfaces of L-PBF 316L stainless steel after different AFP times are characterized to analyze its material removal mechanism. Given that AFP is a mechanical polishing process, the material removal mechanism and removal process of surface features show consistency on L-PBF 316L stainless steel and Ti6Al4V inner surfaces during AFP. The main conclusions can be drawn as follows:

(1) By designing the inlet of the polishing chamber, a gradient change from the large size diameter of pipe to the diameter of the internal channel can be obtained to achieve uniform polishing of various L-PBF inner surfaces during AFP.

(2) AFP is capable of polishing various L-PBF internal surfaces and leave scratching marks on polished area. Based on the turbulent state of polishing media during AFP, collision and scratching between irregular movement of abrasive particles and surfaces would cause deformation and removal of surface features.

(3) Surface features with narrow or unstable connections would be firstly removed or partially scratched. Then, AFP is more efficient in removing protruding areas than valleys on L-PBF inner surfaces following the direction of height reduction.

(4) AFP exhibits superiority in the polishing of L-PBF face up surfaces because face up surfaces possess higher quantity of surface features with necking connections and agglomeration adhesions than other raw surfaces.

Chapter 6. Combination of EP and AFP to Polish L-PBF Internal Surfaces

6.1 Multiple polishing in different sequences of 316L stainless steel

6.1.1 Experimental approaches

Optimized polishing parameters of EP and AFP in the developed polishing system for L-PBF 316L stainless steel inner surfaces are used for multiple polishing in different sequences. A mixture of H_3PO_4 and glycerol with the ratio of 3:2 was heated to 55 ℃. In addition, a two-step EP using a stable flow rate of 0.18 L/s was optimized in section 4.3 for 316L stainless steel internal surfaces in which the first step of EP is to remove un-sintered powders using a potential of 4V for 5 minutes, while the second step is to further level the remaining sintered area and obtain a smooth surface by applying a potential of 2V along the LCPR for 20 minutes. Based on the optimized parameters in section 5.1, B_4C particles and water was mixed as polishing media for AFP process and the volume of B_4C particles was 4%. A stable flow rate of 0.18 L/s and a stable pressure of 0.08 MPa were achieved during AFP. There are two types of multiple polishing in different sequences for L-PBF 316L stainless steel inner surfaces in this study, the first is performing EP before AFP in section 6.1.2, while the second is conducting AFP before EP in section 6.1.3.

6.1.2 EP and AFP in sequence

Morphology evolution and topography of top, face up, side and face down inner surfaces of L-PBF 316L stainless steel after EP and then AFP are shown in Figure 6.1, Figure 6.2, Figure 6.3 and Figure 6.4, respectively. The morphology of different surfaces after two-step EP is consistent with OM images in Figure 4.21. Based on the analysis of the two-step EP in section 4.3, un-sintered powders are totally dissolved and uneven sintered areas are remained on various surfaces after 25 minutes of EP as shown in Figure 4.25. Then, morphological changes in the first 25 minutes of AFP are not obvious despite area ratios with scratching traces on various surfaces increase

with the prolongation of AFP time. Given that EP has effectively polished surface features at protruding area and reduced surface roughness, the effect of short-term AFP after EP is not significant. Therefore, a mixed morphology of scratching traces and electropolished smooth surface coexist on different L-PBF inner surfaces. From 50 to 250 minutes of AFP, the scratching degree of protruding positions is higher than that of valleys on various surfaces due to time-cumulative effect of AFP. Because of the lowest roughness of the original surface among different surfaces, EP marks are almost removed by AFP after 250 minutes on the top surface. However, several laser scanning traces at valley positions (Figure 6.1) still remain on the top surface. Different from the top surface, EP morphology with smooth surface still could be observed at some valley positions after 250 minutes of AFP on the face up (Figure 6.2), side (Figure 6.3) and face down (Figure 6.4) surfaces.

Figure 6.1 OM images and topography of the same area on a top inner surface of L-PBF 316L stainless steel before and after multiple polishing in different sequences of EP and then AFP.

Figure 6.2 OM images and topography of the same area on a face up inner surface of L-PBF 316L stainless steel before and after multiple polishing in different sequences of EP and then AFP.

Figure 6.3 OM images and topography of the same area on a side inner surface of L-PBF 316L stainless steel before and after multiple polishing in different sequences of EP and then AFP.

Figure 6.4 OM images and topography of the same area on a face down inner surface of L-PBF 316L stainless steel before and after multiple polishing in different sequences of EP and then AFP.

Ra and Rz values of various inner surfaces of L-PBF 316L stainless steel after EP and then AFP were measured and presented in Figure 6.5. It appears that EP exhibits higher efficiency as the first step of multiple polishing in different sequences. However, the fact is that extending EP time after 25 minutes is difficult to continue to reduce surface roughness of top, face up and side surfaces as analysed in section 4.3 (see Figure 4.23). Notably, both Ra and Rz values of different inner surfaces show similar

continuous decreasing trend with the application of AFP after EP. Roughness reduction efficiency of AFP on the top, face up and side surfaces gradually decreases from 25 to 175 minutes of multiple polishing and then roughness values hardly continue to decrease as can be seen in Figure 6.5a. With an increase of scratching area ratio, efficiency of AFP gradually decreases because more areas need to be removed until AFP could polish valley positions. Given that there are only sintered areas on different surfaces after EP, the application of AFP could effectively remove protruding sintered area on surfaces, resulting in lower Ra and Rz values. Different from other surfaces, there are small fluctuations in roughness reductions on the face down surface with prolonged AFP time after EP due to the rough sintered area after EP. In addition, the decreasing degree of Rz on the face up and side surfaces (Figure 6.5b and c) is higher than Ra during AFP attributing to the removal characteristic of AFP.

Figure 6.5 Ra and Rz values of L-PBF 316L stainless steel internal (a) top, (b) face up, (c) side and (d) face down surfaces before and after EP and then AFP. Note that the left vertical axis represents Ra and the right vertical axis represents Rz.

Based on above analysis, material removal process of various surface features during EP and then AFP is illustrated in Figure 6.6. After EP, un-sintered powders are totally dissolved and uneven sintered area is levelled. Then, the applying of AFP causes scratching on the surface and AFP for long time would further smooth protruding sintered area on L-PBF surfaces.
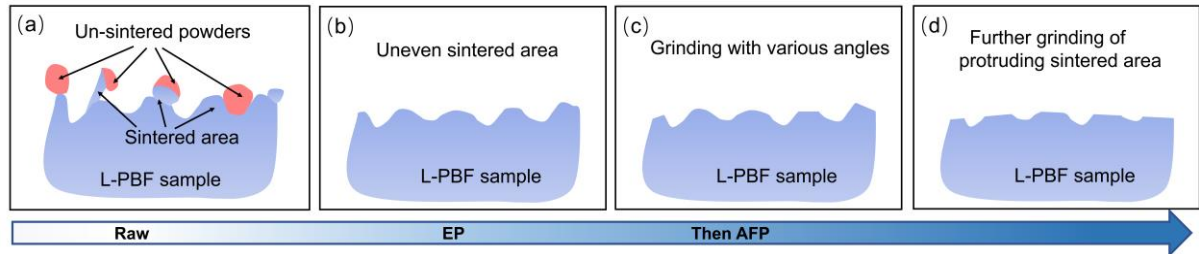
Figure 6.6 Schematic diagram of (a) raw L-PBF inner surfaces and (b-d) material removal process during multiple sequence polishing of EP and then AFP.

6.1.3 AFP and EP in sequence

Both Ra and Rz of original and polished inner surfaces of L-PBF 316L stainless steel were measured during multiple polishing in different sequences in which AFP was performed first, followed by EP. As can be seen in Figure 6.7, roughness values of various surfaces decrease significantly after 300 minutes of AFP which is consistent with the results in Figure 5.11. However, Ra and Rz values are not continued to reduce but increase with the action of the first 5 minutes of EP after AFP. Considering the changes of roughness vary among various internal surfaces, morphological evolution is characterized for further analysis.

Figure 6.7 Ra and Rz values of L-PBF 316L stainless steel internal (a) top, (b) face up, (c) side and (d) face down surfaces before and after AFP and then EP. Note that the left vertical axis represents Ra and the right vertical axis represents Rz.

OM images of the same area on top, face up, side and face down inner surfaces of L-PBF 316L stainless steel before and after the multiple polishing in different sequences are shown in Figure 6.8, Figure 6.9, Figure 6.10, and Figure 6.11, respectively. According to the material removal characteristic of AFP, raw areas with valley positions are observed after 300 minutes of AFP. By applying the first step of EP after AFP, scratching and original areas are all electropolished. Despite raw areas are polished, their morphology still could be easily identified after the first and second step of EP. Considering the changes of roughness in Figure 6.7, both Ra and Rz values increase slightly on the top, face up and side inner surfaces after the first 5 minutes of EP, and then surface roughness decreases with the prolongation of EP time and reaches a stable level after the second step of EP. Notably, the first step of EP could remove almost un-sintered powders on inner top, face up and face down surfaces as

analysed in section 4.3 (Figure 4.25). Considering the existence of un-sintered powders at valley locations on top (Figure 5.16), face up (Figure 5.19) and side (Figure 5.22) inner surfaces after AFP, the dissolution of the original morphology at valleys during the first 5 minutes of EP leads to slight increase of surface roughness. Based on the analysis in Figure 4.9, protruding area has higher current density distribution than valley positions during EP. Thus, surface roughness decreases with an extension of EP time from total 305 to 325 minutes as shown in Figure 6.7a, b and c.

Different from other surfaces, roughness of the face down surfaces increases significantly after 5 minutes of EP and roughness values continue to rise after 15 minutes of EP. Then, Ra and Rz values start to decrease as seen in Figure 6.7d. Roughness change trend of the face down surface during the multiple polishing in different sequences consisting of AFP and then EP is influenced by the largest amount of un-sintered powders and maximum roughness of sintered area on its raw surface. Based on the analysis in Figure 5.13, Figure 5.23, and Figure 5.25, rough sintered area and large quantity of un-sintered powders are remained on face down surfaces after AFP. Therefore, the remaining original morphology of the face down surface after AFP of 300 minutes is only partially dissolved after the action of EP for 5 minutes. In addition, significant morphological changes between the first and second step of EP in Figure 6.11 also demonstrate that the partially dissolved original areas are further electropolished during the second step of EP. As a result, only sintered areas exist on the face down surface after 25 minutes of EP. Considering the high roughness of sintered area on the face down surface, the changes of roughness in Figure 6.7d are consistent with morphological evolution of the face down surface (Figure 6.11) during the multiple polishing of AFP and then EP.

Figure 6.8 OM images of the same area on a top inner surface of L-PBF 316L stainless steel before and after multiple polishing in different sequences of AFP and then EP.

Figure 6.9 OM images of the same area on a face up inner surface of L-PBF 316L stainless steel before and after multiple polishing in different sequences of AFP and then EP.

Figure 6.10 OM images of the same area on a side inner surface of L-PBF 316L stainless steel before and after multiple polishing in different sequences of AFP and then EP.
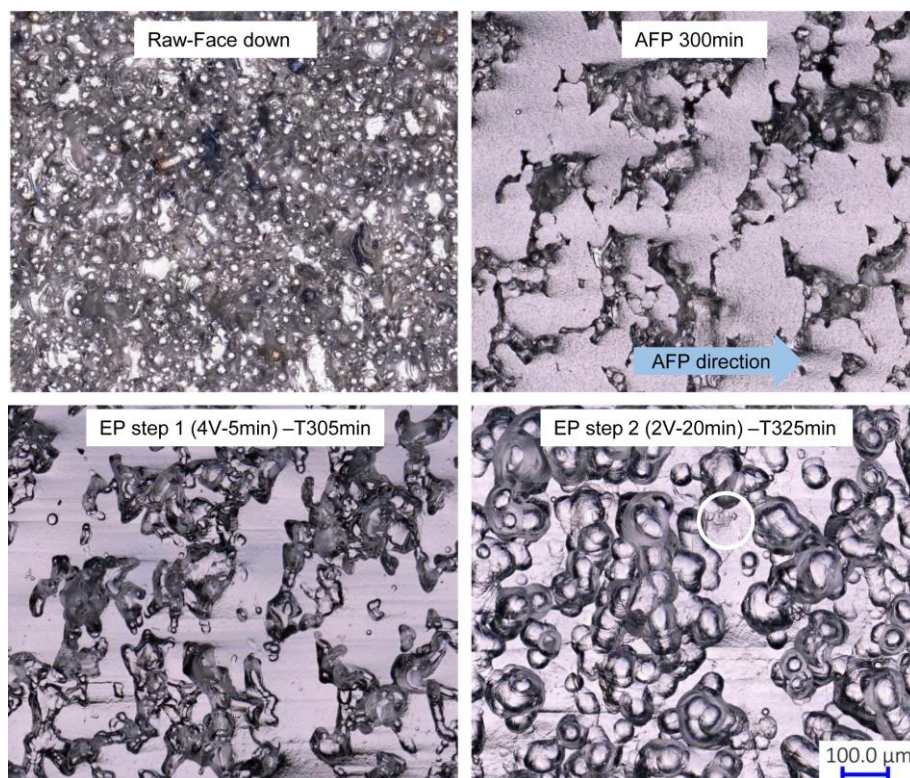
Figure 6.11 OM images of the same area on a face down inner surface of L-PBF 316L stainless steel before and after multiple polishing in different sequences of AFP and then EP.

Considering that the area ratio with scratching traces is higher than original area on various inner surfaces after AFP for 300 minutes, some etching traces that marked with white circles in Figure 6.8, Figure 6.9, Figure 6.10, and Figure 6.11 are found in previously scratched area after EP for 25 minutes. In addition, the reduction degree of roughness is limited on the top, face up and face down surfaces by applying EP after AFP as can be seen in Figure 6.7. Therefore, no further extension of the EP time is recommended in this multiple polishing. Based on above discussion, material removal process of AFP and then EP is shown in Figure 6.12. Protruding area has been effectively levelled after AFP. Then, un-sintered powders would be dissolved totally with the action of EP. With a prolongation of EP time, sintered area could be further levelled on L-PBF surfaces.
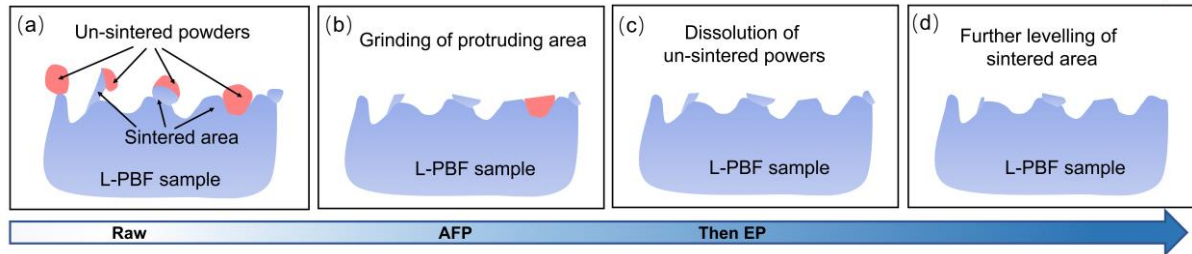
Figure 6.12 Schematic diagram of (a) raw L-PBF inner surfaces and (b-d) material removal process during multiple sequence polishing of AFP and then EP.

6.2 Multiple polishing in different sequences of Ti6Al4V

6.2.1 Experimental approaches

Optimized polishing parameters of EP and AFP for L-PBF Ti6Al4V inner surfaces were used in multiple polishing in different sequences, respectively. The electrolyte was a mixture of NaCl powder (99 %) and ethylene glycol solution (99 %) with 0.6 M Cl$^-$. Moreover, the temperature of the electrolyte was 25 ℃ during EP. It is noted that a two-step EP using a stable flow rate of 0.18 L/s was optimized in section 4.4 for Ti6Al4V internal surfaces in which the first step of EP is to polish surfaces uniformly using a potential of 20 V for 15 minutes, while the second step is to obtain a smooth surface by applying a potential of 44V along the LCPR for 5 minutes. Based on the optimized parameters in section 5.1, B$_4$C particles and water was mixed as polishing media for

AFP process and the volume of B_4C particles was 4%. A stable flow rate of 0.18 L/s and a stable pressure of 0.08 MPa were achieved during AFP.

There are two types of multiple polishing in different sequences for L-PBF Ti6Al4V inner surfaces in this study, the first is performing EP before AFP in section 6.2.2, while the second is conducting AFP before EP in section 6.2.3. For multiple polishing in different sequences consisting of EP and then AFP, the two-step EP was performed first considering the rough original surfaces. In terms of the polishing sequence of AFP and then EP, only the potential of 44V for 5 minutes was used for EP process because the potential of 20V could cause uneven etching on the scratched area after AFP.

6.2.2 EP and AFP in sequence

Morphology evolution of top, face up, side and face down inner surfaces of L-PBF Ti6Al4V after EP and then AFP are shown in Figure 6.13, Figure 6.14, Figure 6.15, and Figure 6.16, respectively. The morphology of different surfaces after the two-step EP is consistent with OM images in Figure 4.34. Based on the analysis of the two-step EP in section 4.4, some sintered areas at valley positions are remained on various surfaces after EP for 20 minutes (Figure 4.25). Then, morphological changes in the first 25 minutes of AFP are not obvious despite area ratios with scratching traces on various surfaces increase with the prolongation of AFP time. Given that EP has effectively polished surface features at protruding area and reduced surface roughness, the effect of short-term AFP is not significant. Therefore, a mixed morphology of scratching traces and electropolished surface topography coexist on different inner surfaces. From 50 to 200 minutes of AFP, sintered morphology at valley positions has been effectively scratched due to time-cumulative effect of AFP. Because of the lowest roughness of the original surface among various inner surfaces, EP marks are almost removed by AFP after 200 minutes on the top surface (Figure 6.13). Different from the top surface, several sintered areas at valley positions still can be observed after AFP for 200 minutes on the face up (Figure 6.14), side (Figure 6.15) and face down (Figure 6.16) surfaces.
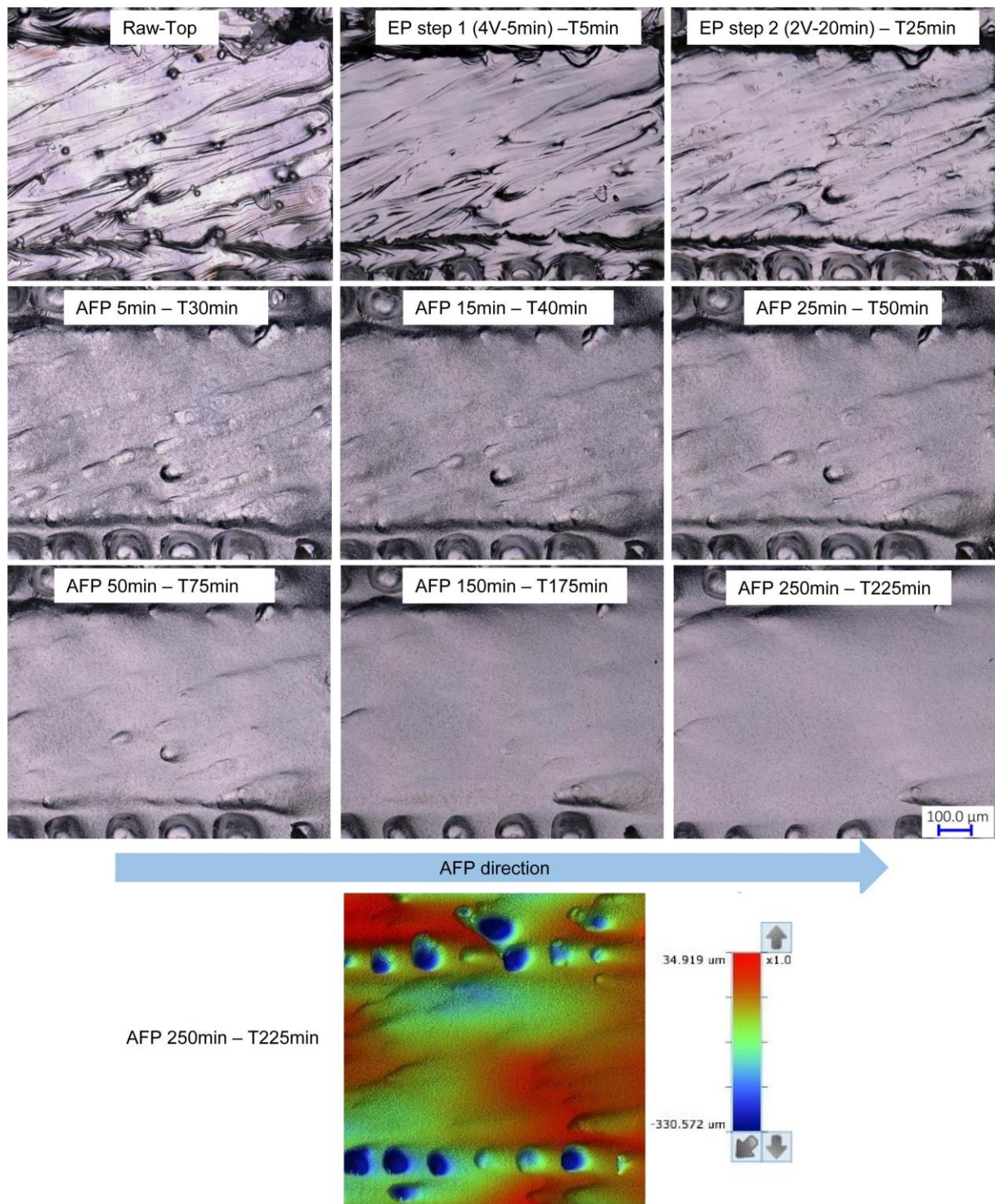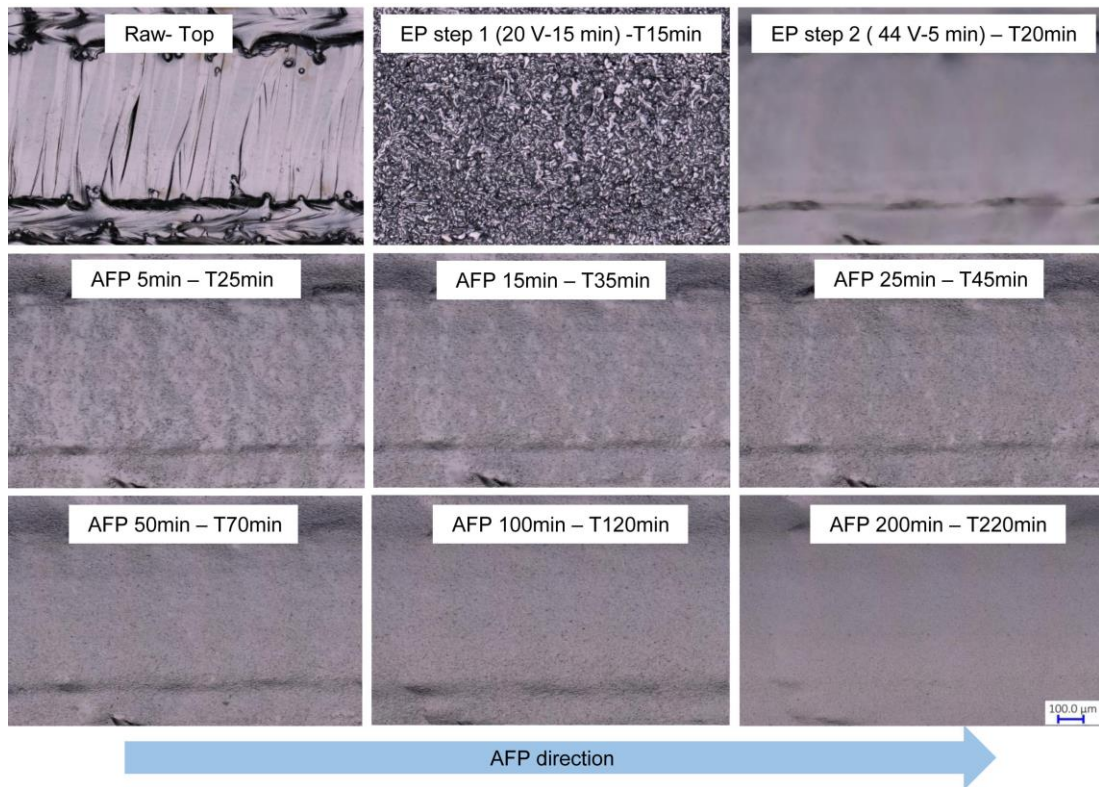
Figure 6.13 OM images of the same area on a top inner surface of L-PBF Ti6Al4V before and after multiple polishing in different sequences of EP and then AFP.
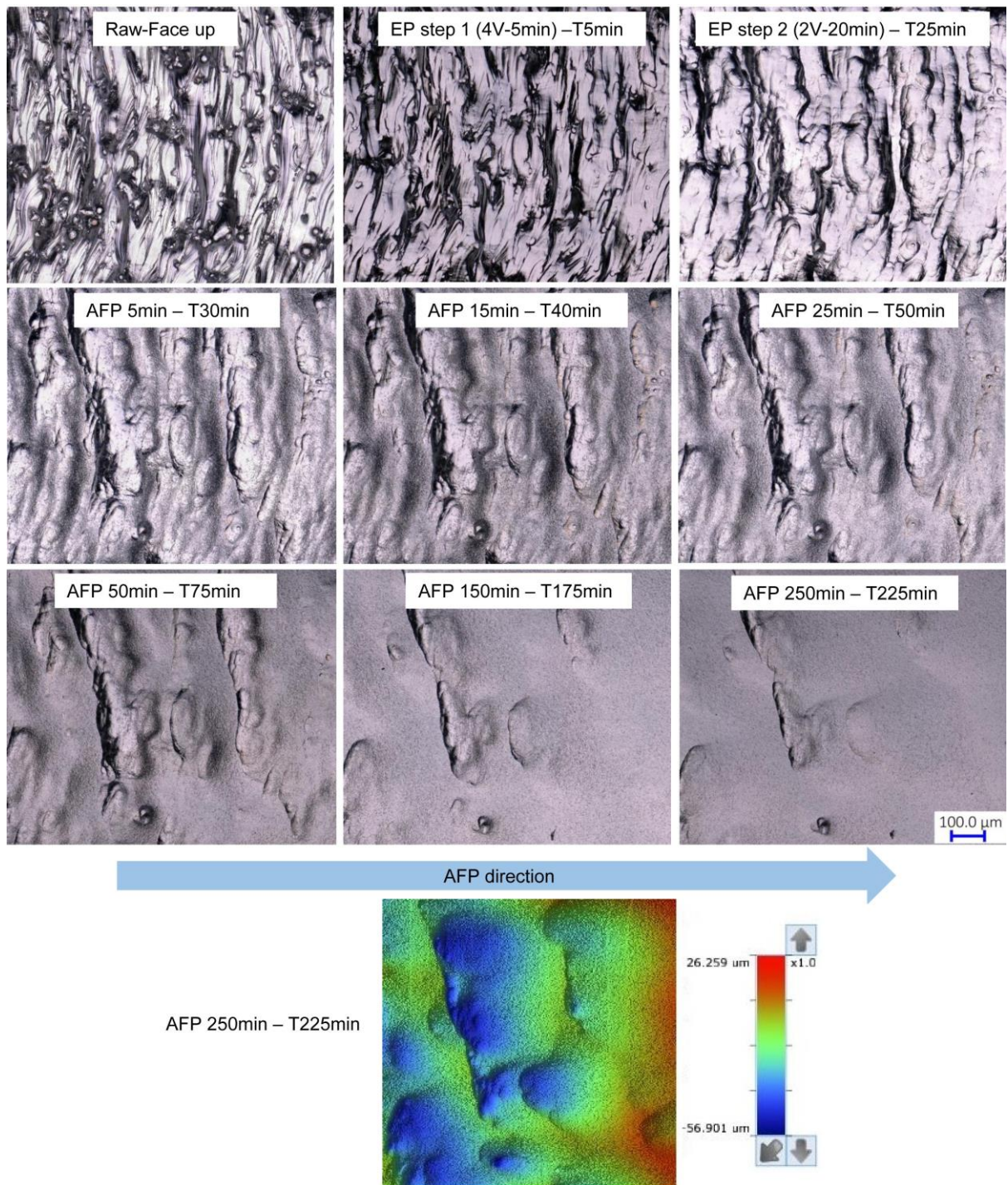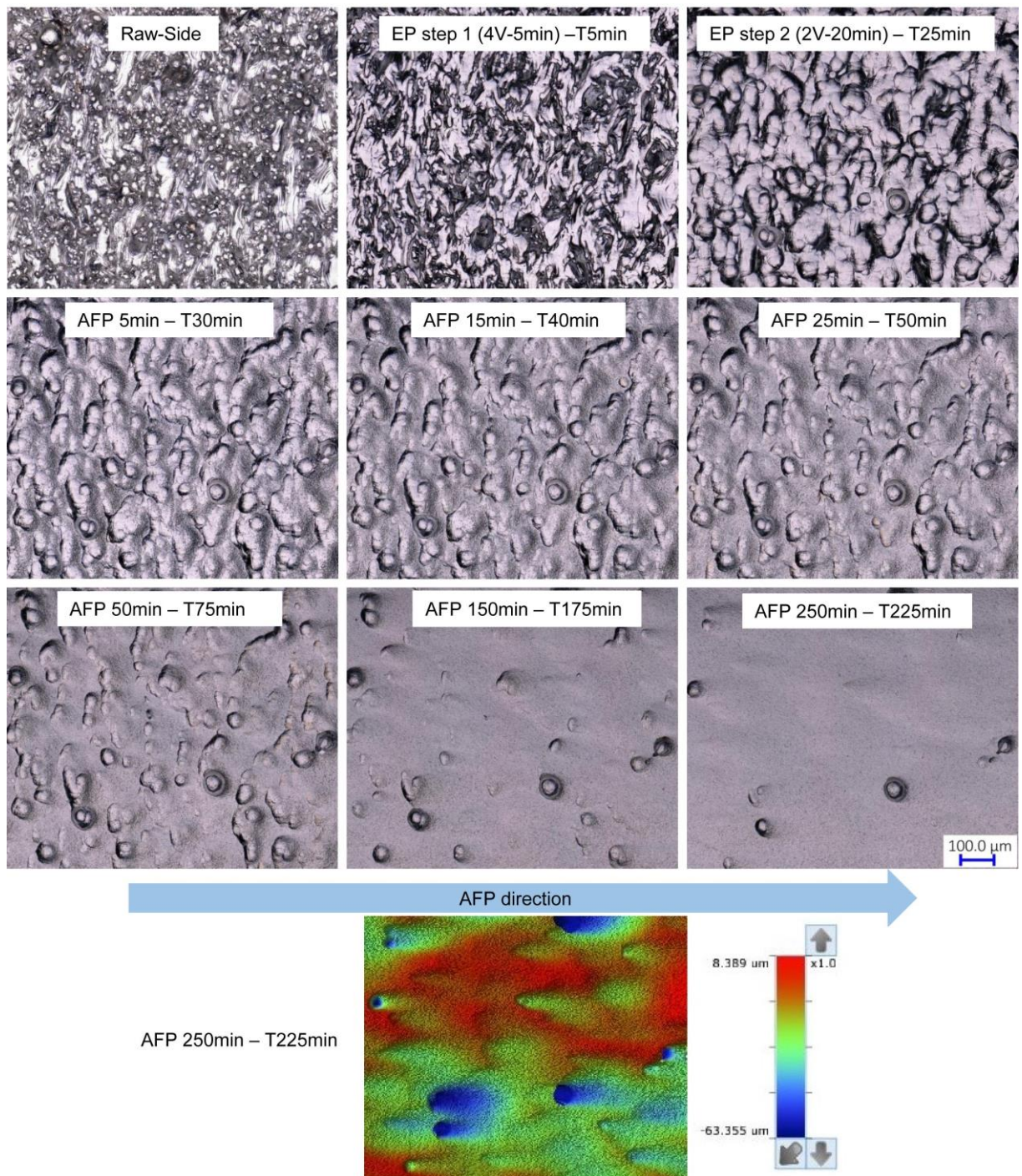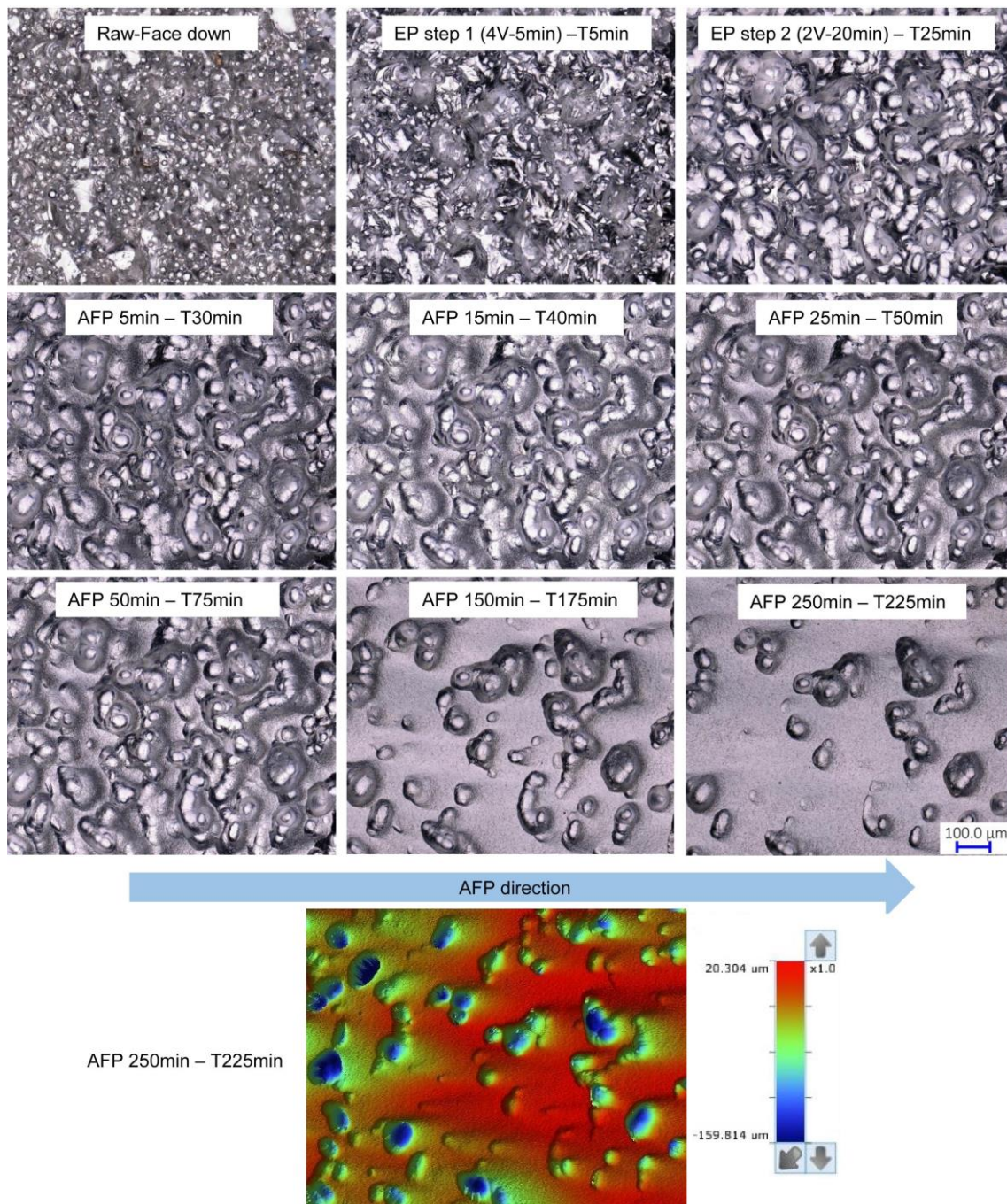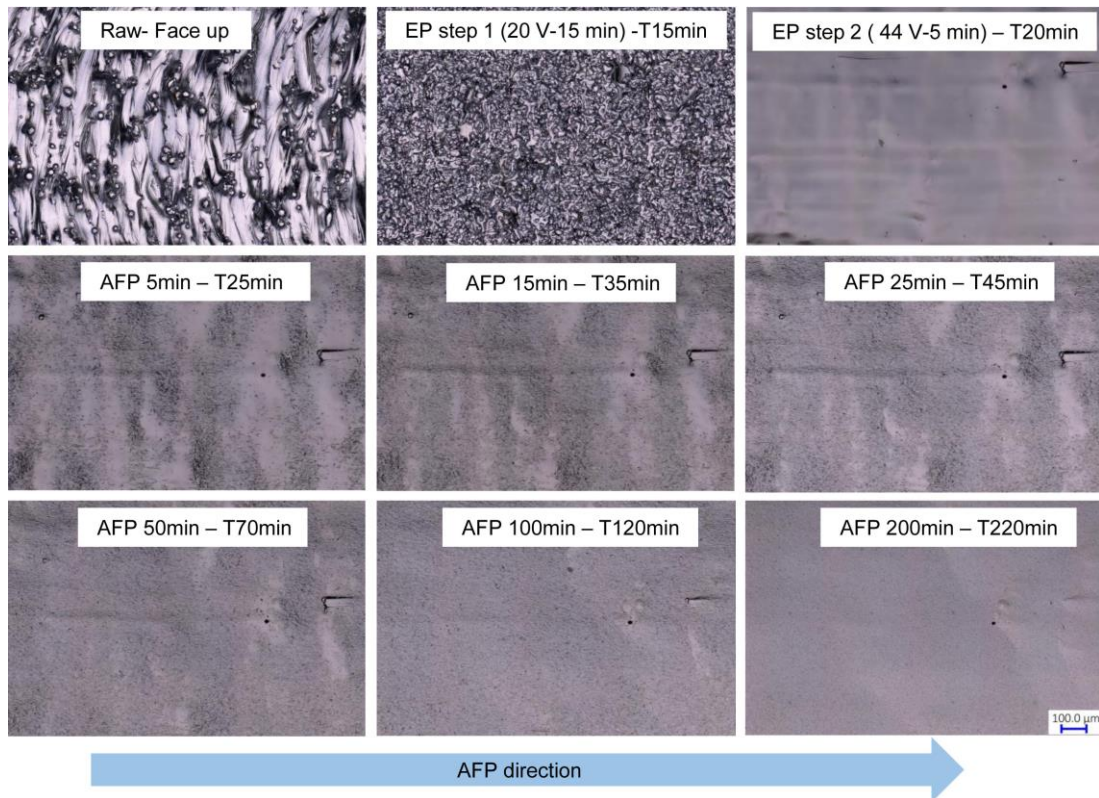

Figure 6.14 OM images of the same area on a face up inner surface of L-PBF Ti6Al4V before and after multiple polishing in different sequences of EP and then AFP.
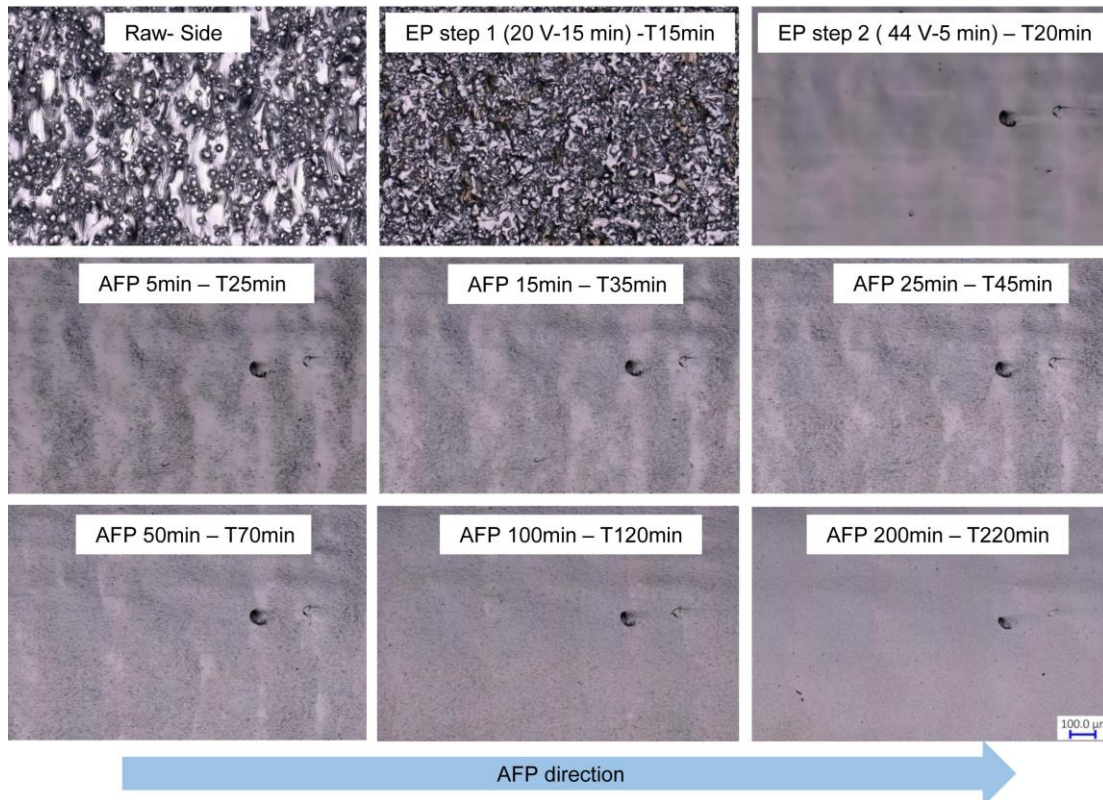
Figure 6.15 OM images of the same area on a side inner surface of L-PBF Ti6Al4V before and after multiple polishing in different sequences of EP and then AFP.
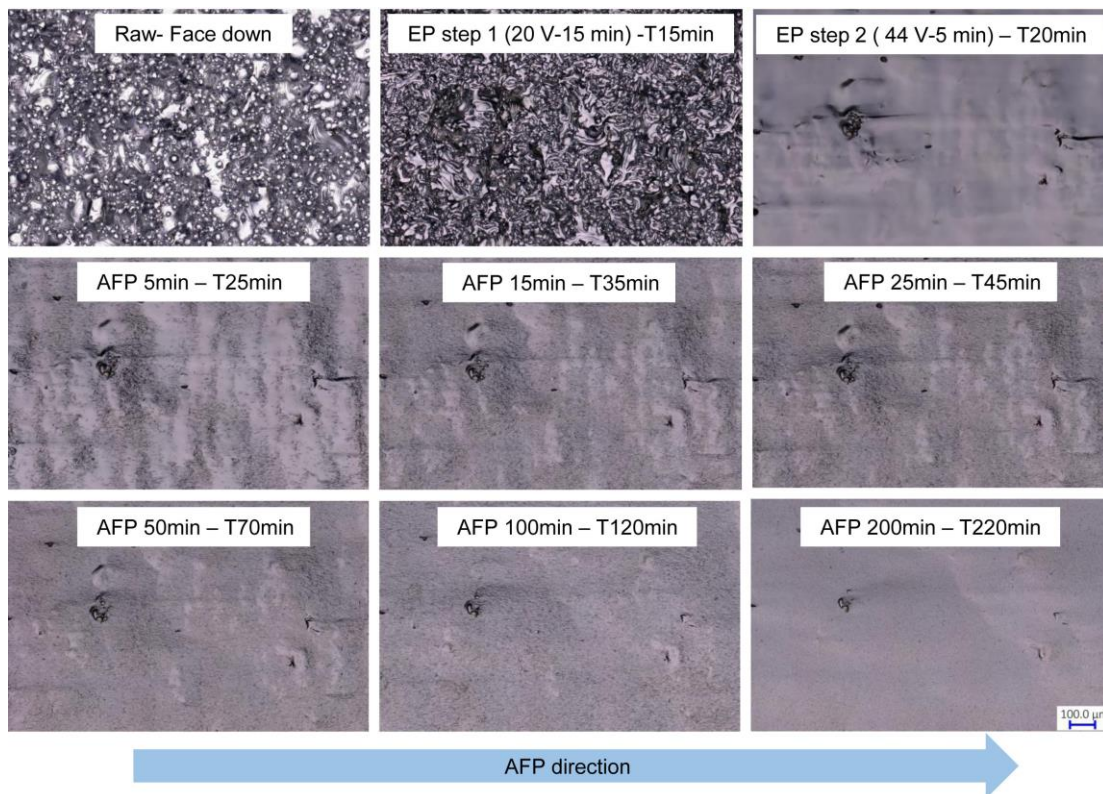
Figure 6.16 OM images of the same area on a face down inner surface of L-PBF Ti6Al4V before and after multiple polishing in different sequences of EP and then AFP.

Ra and Rz values of various inner surfaces of L-PBF Ti6Al4V after EP and AFP are shown in Figure 6.17. It is obvious that EP exhibits higher efficiency as the first step of multiple polishing in different sequences. However, it is not suggested to extending EP time after 20 minutes considering its high material removal rate as analysed in section 4.4.3. It is noted that both Ra and Rz values of different inner surfaces show similar continuous decreasing trend with the application of AFP after EP. Roughness reduction efficiency of AFP on various surfaces gradually decreases from 20 to 220 minutes of multiple polishing and then roughness values hardly continue to decrease as seen in Figure 6.17. It can be explained that with an increase of scratching area ratio, efficiency of AFP gradually decreases because more areas need to be removed before AFP could polish valley areas.
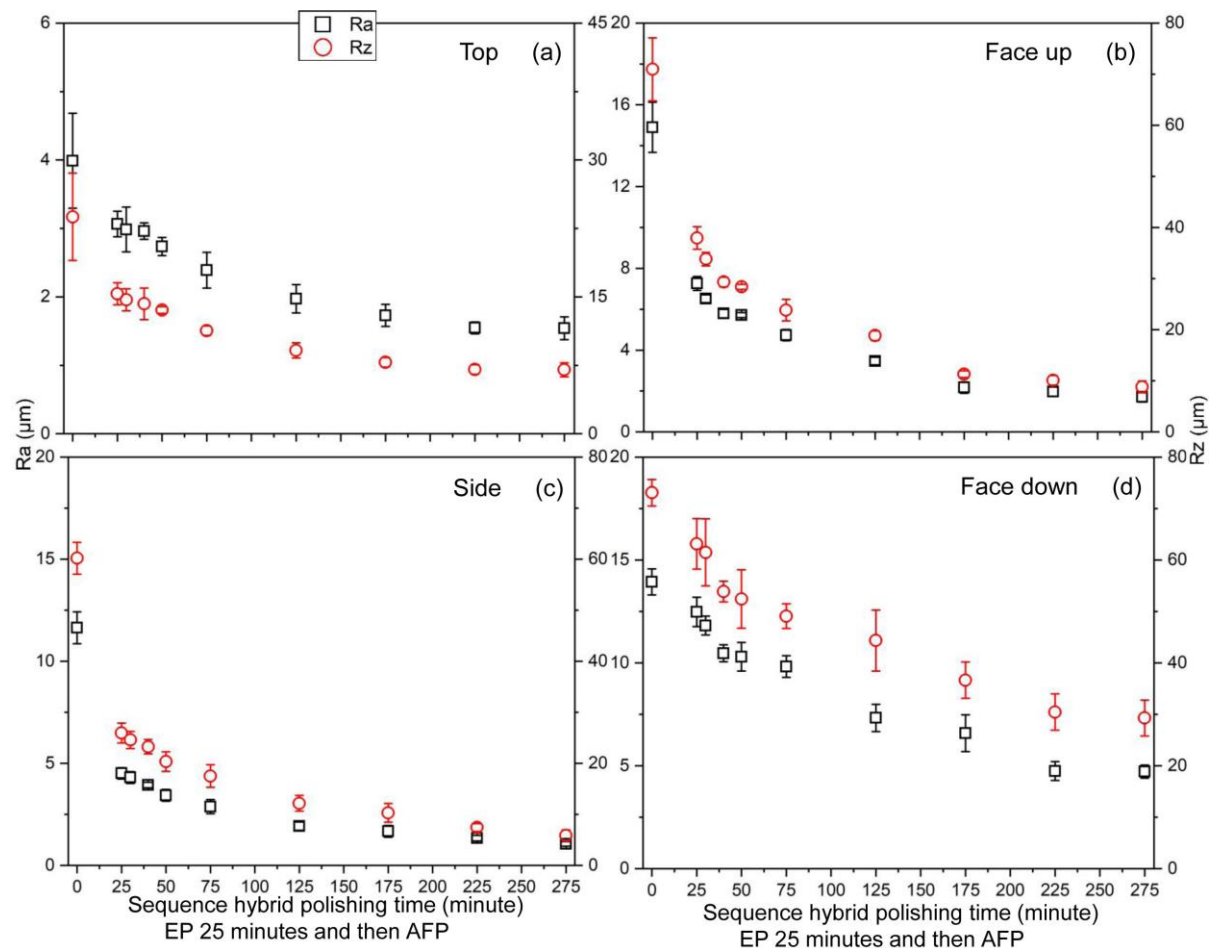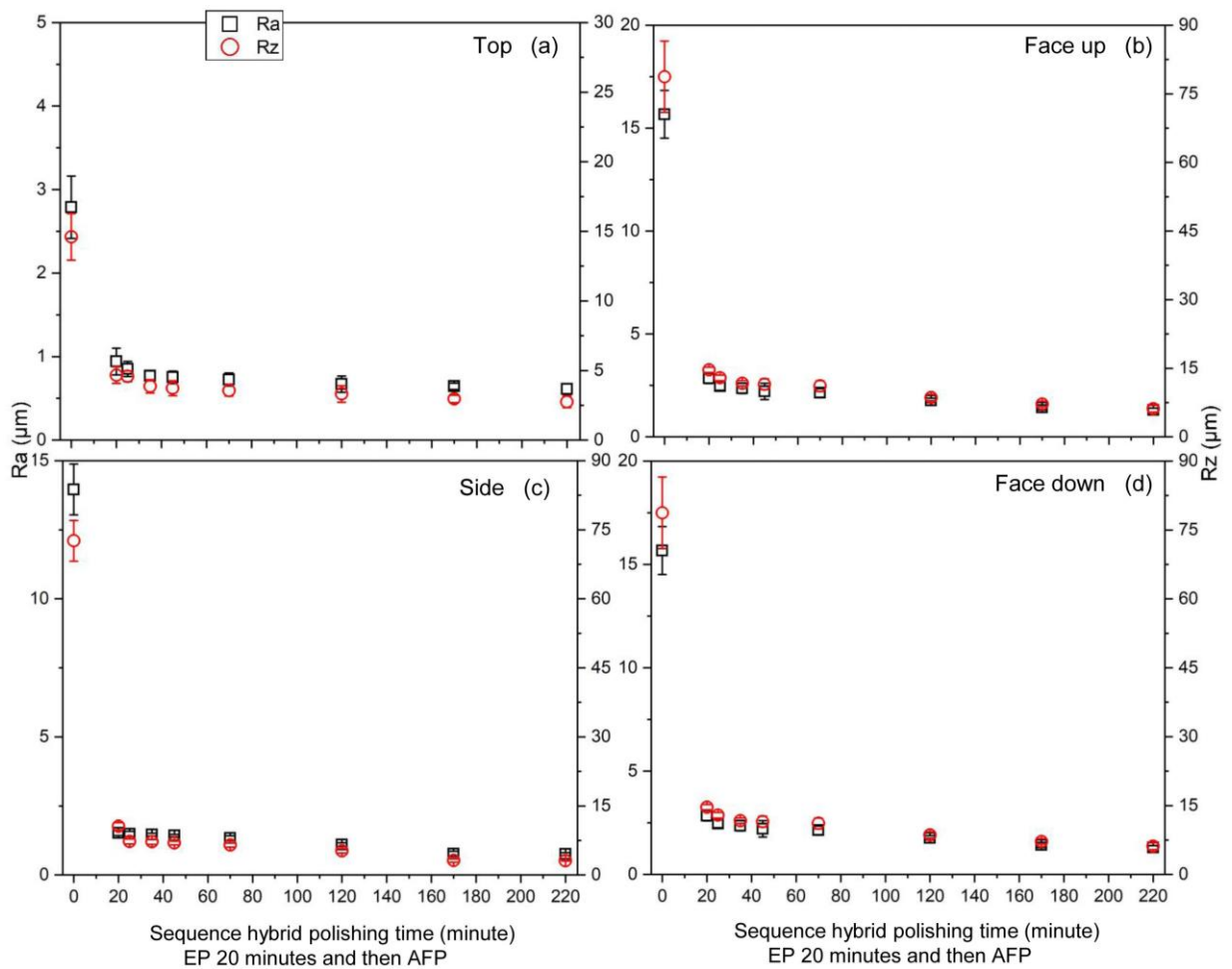

Figure 6.17 Ra and Rz values of L-PBF Ti6Al4V internal (a) top, (b) face up, (c) side and (d) face down surfaces before and after EP and then AFP. Note that the left vertical axis represents Ra and the right vertical axis represents Rz.

6.2.3 AFP and EP in sequence

Both Ra and Rz of original and polished inner surfaces of L-PBF Ti6Al4V were measured during multiple polishing in different sequences in which AFP was performed first, followed by EP. As can be seen in Figure 6.18, roughness of various surfaces decreases significantly after 300 minutes of AFP which is consistent with the results in Figure 5.30. However, Ra and Rz values have not continued to reduce but increased after the first 90 seconds of EP at 44V in the multiple polishing. Considering the changes of roughness vary among various internal surfaces, morphological evolution is characterized for further analysis.
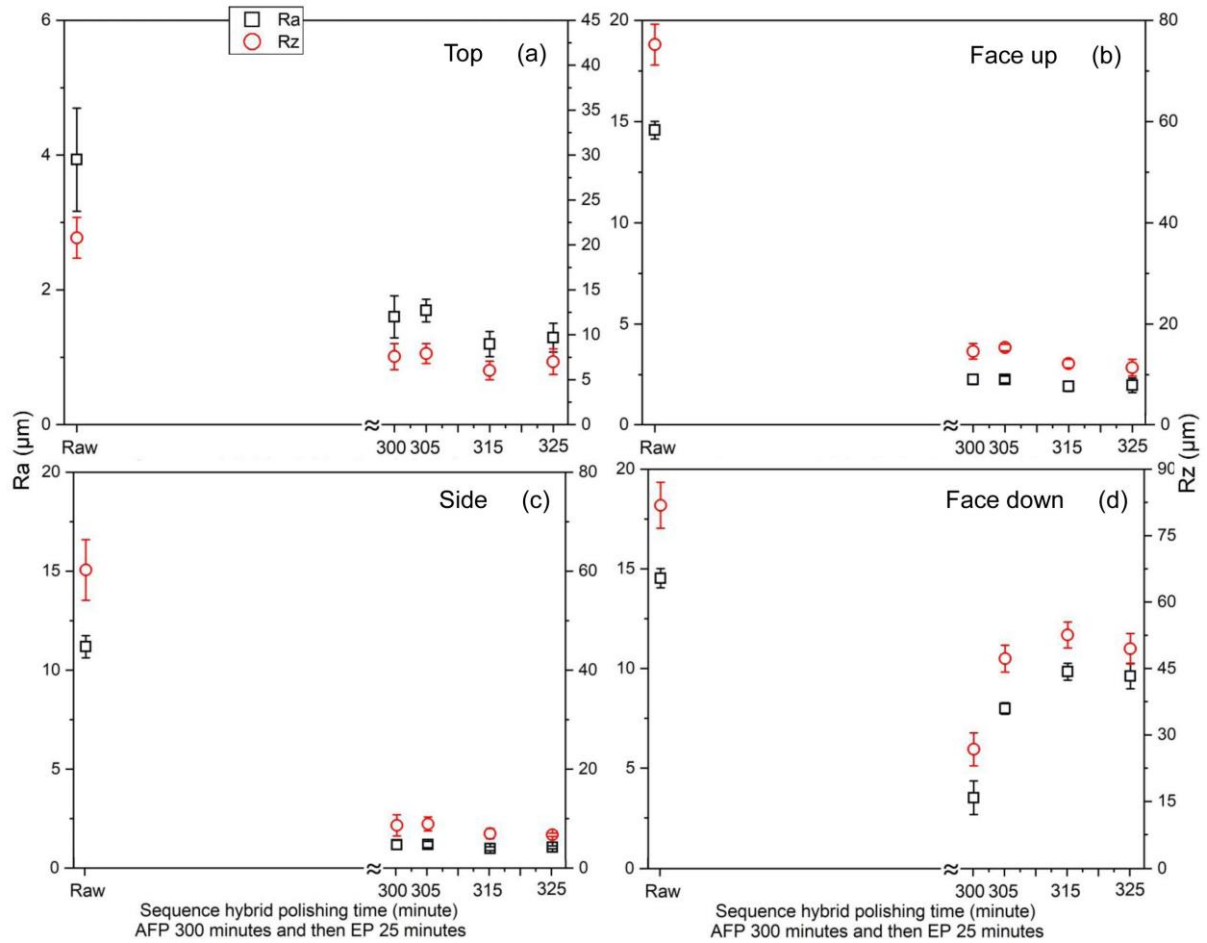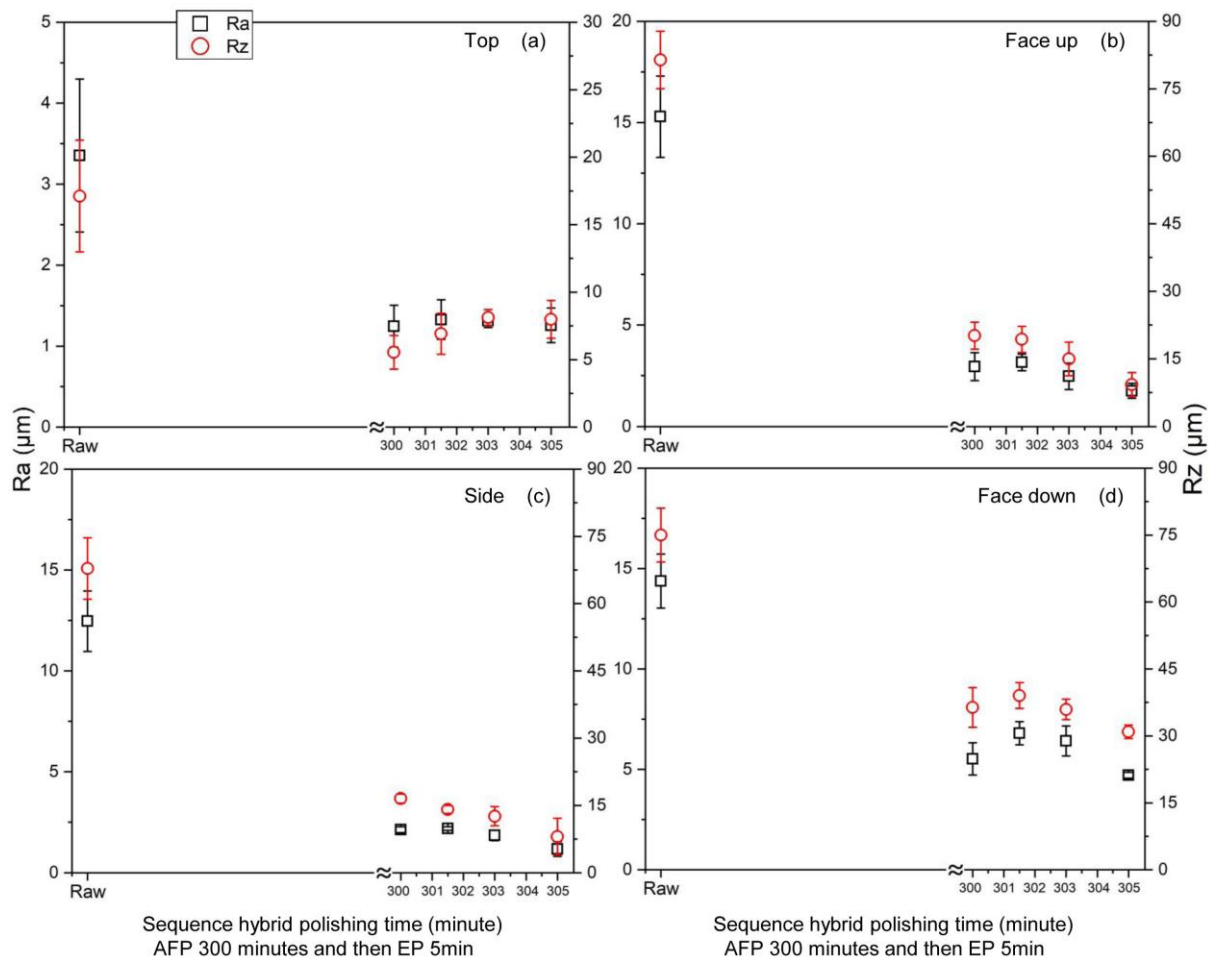

Figure 6.18 Ra and Rz values of L-PBF Ti6Al4V internal (a) top, (b) face up, (c) side and (d) face down surfaces before and after AFP and then EP. Note that the left vertical axis represents Ra and the right vertical axis represents Rz.

OM images of the same area on various inner surfaces before and after the multiple polishing in different sequences are shown in Figure 6.19, Figure 6.20, Figure

6.21, Figure 6.22, respectively. According to the material removal characteristic of AFP, valley areas are observed after 300 minutes of AFP. By applying EP at 44V for 90 seconds, scratching and original areas are partially electropolished and their morphologies still can be identified. With an extension of EP time, electropolished area ratio increases. However, new morphologies show up at previously scratched area after 90 seconds of EP on the face up surface as marked with white circles in Figure 6.20. The same phenomenon also appears on the top, side and face down surfaces after 3 and 5 minutes of EP as marked with white circles in Figure 6.19, Figure 6.21 and Figure 6.22, respectively. Given that there exists raw morphology on various surfaces after AFP, the applying of EP could further electropolish the remaining raw area at valley positions. Thus, there are fluctuations of roughness with prolongation of EP after AFP (Figure 6.18). Different from other surfaces, raw morphology still exists on the face down surface after the multiple polishing in different sequences which is caused by the largest amount of un-sintered powders and maximum roughness of sintered area on its raw surface.
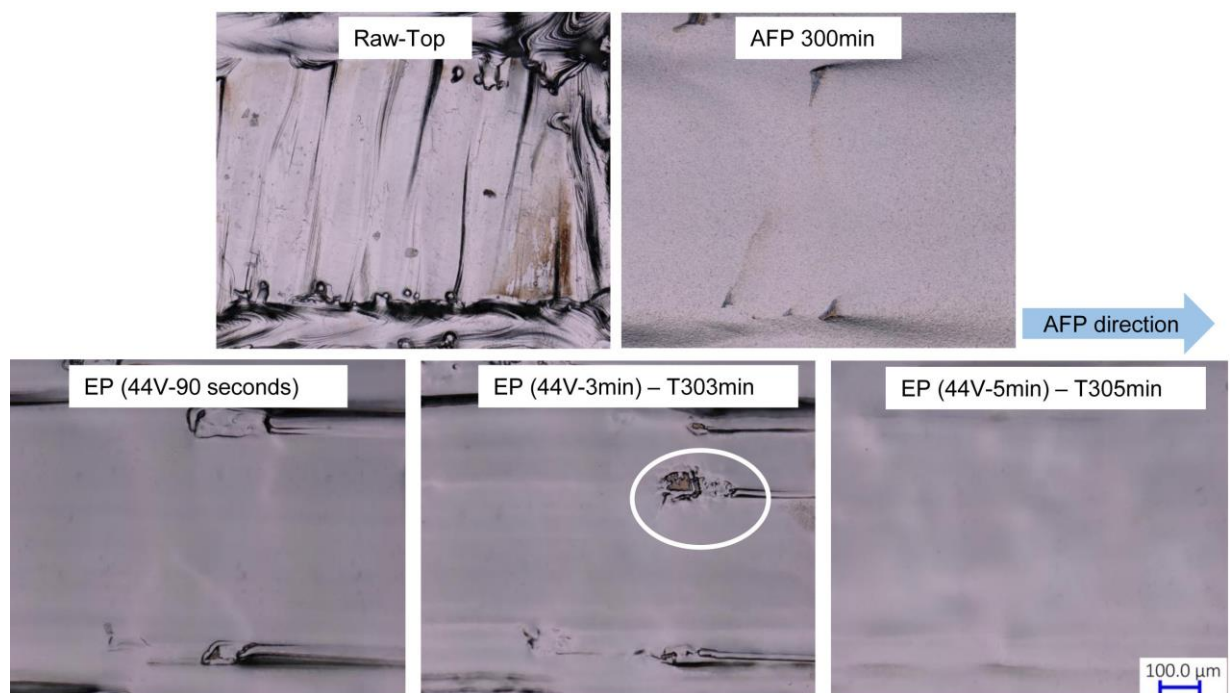
Figure 6.19 OM images of the same area on a top inner surface of L-PBF Ti6Al4V before and after multiple polishing in different sequences of AFP and then EP.
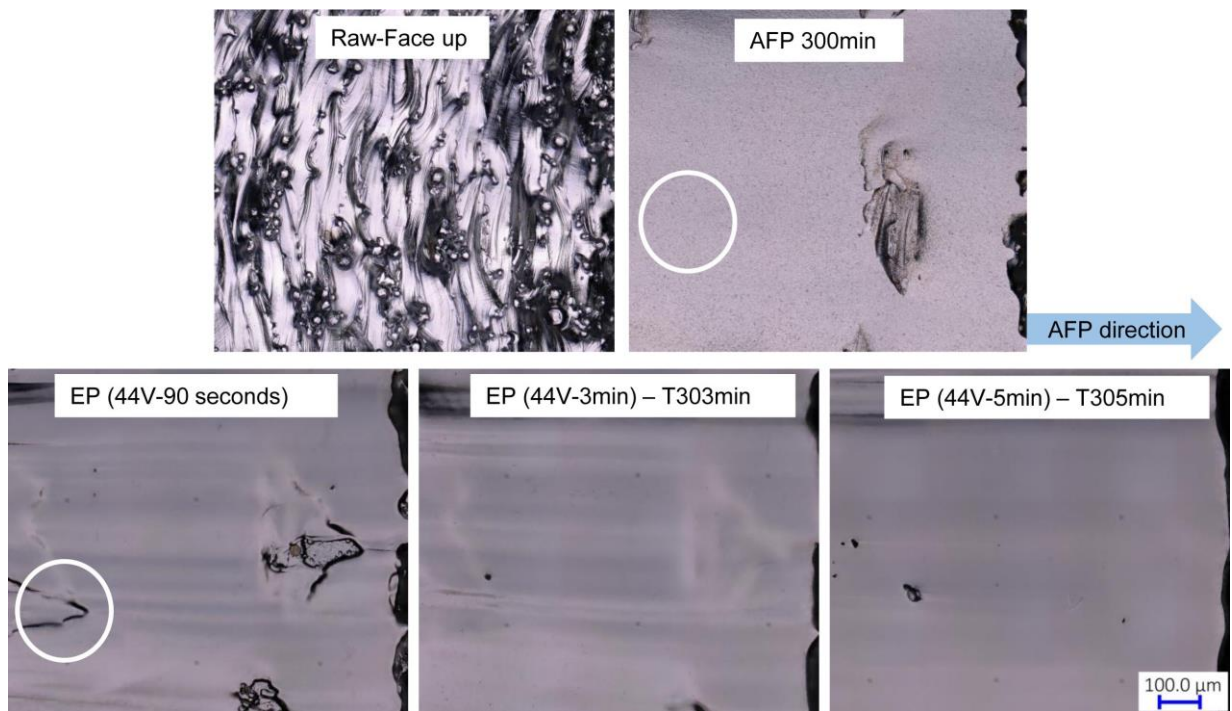
Figure 6.20 OM images of the same area on a face up inner surface of L-PBF Ti6Al4V before and after multiple polishing in different sequences of AFP and then EP.
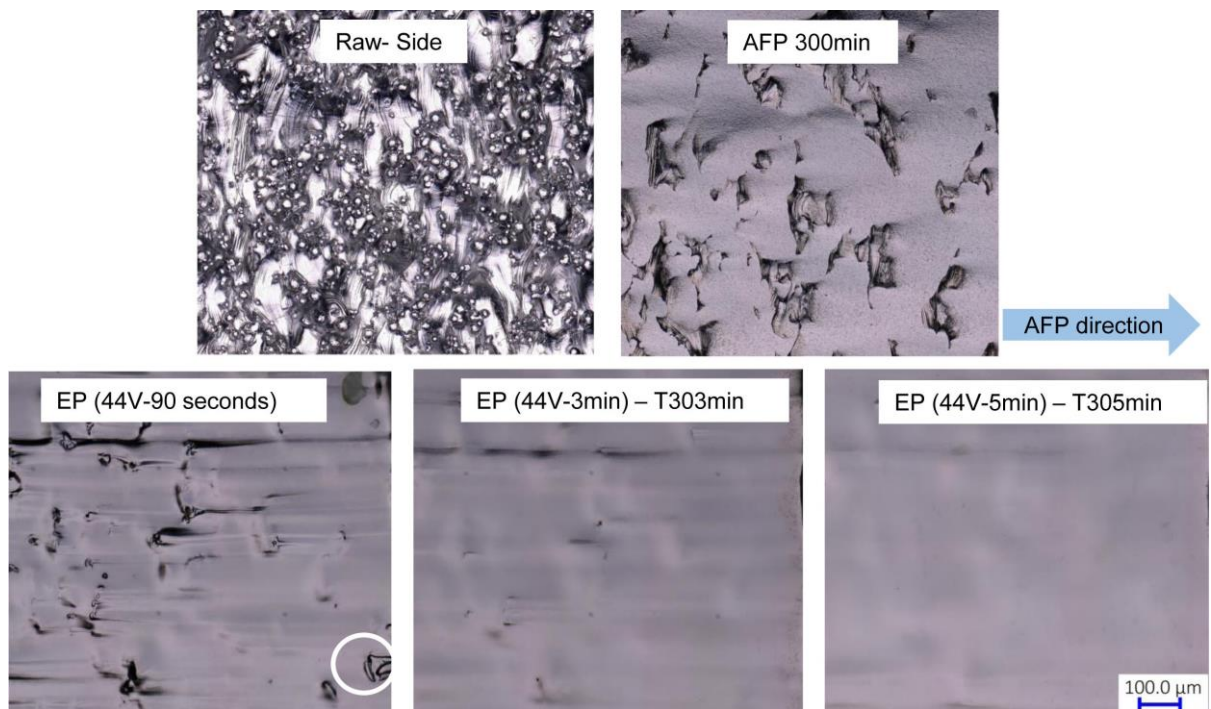
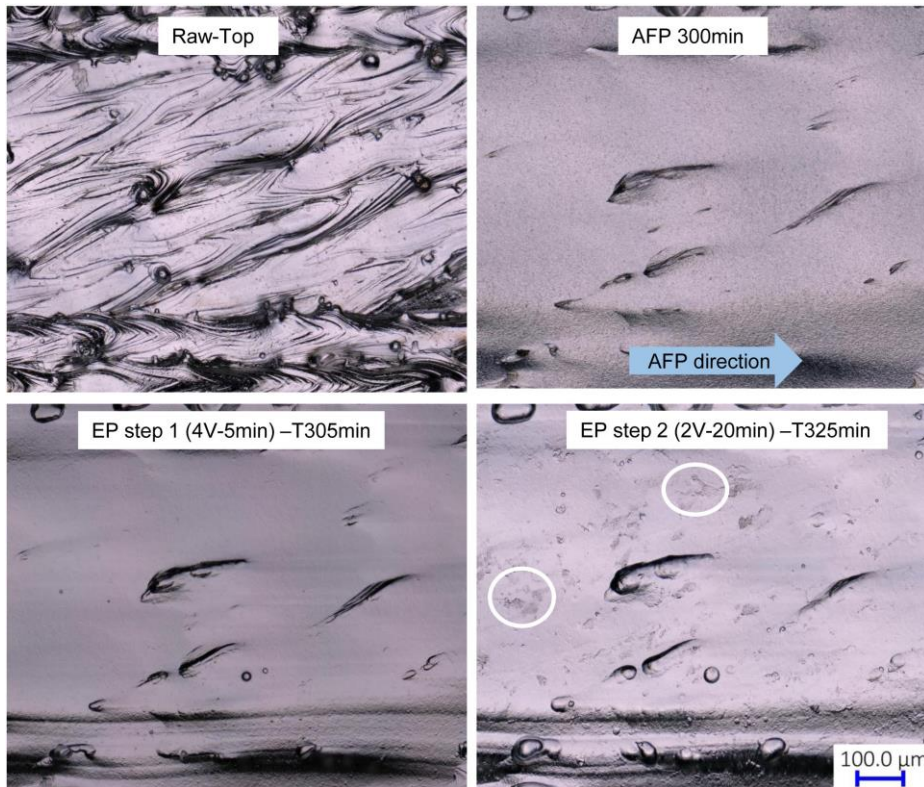Figure 6.21 OM images of the same area on a side inner surface of L-PBF Ti6Al4V before and after multiple polishing in different sequences of AFP and then EP.
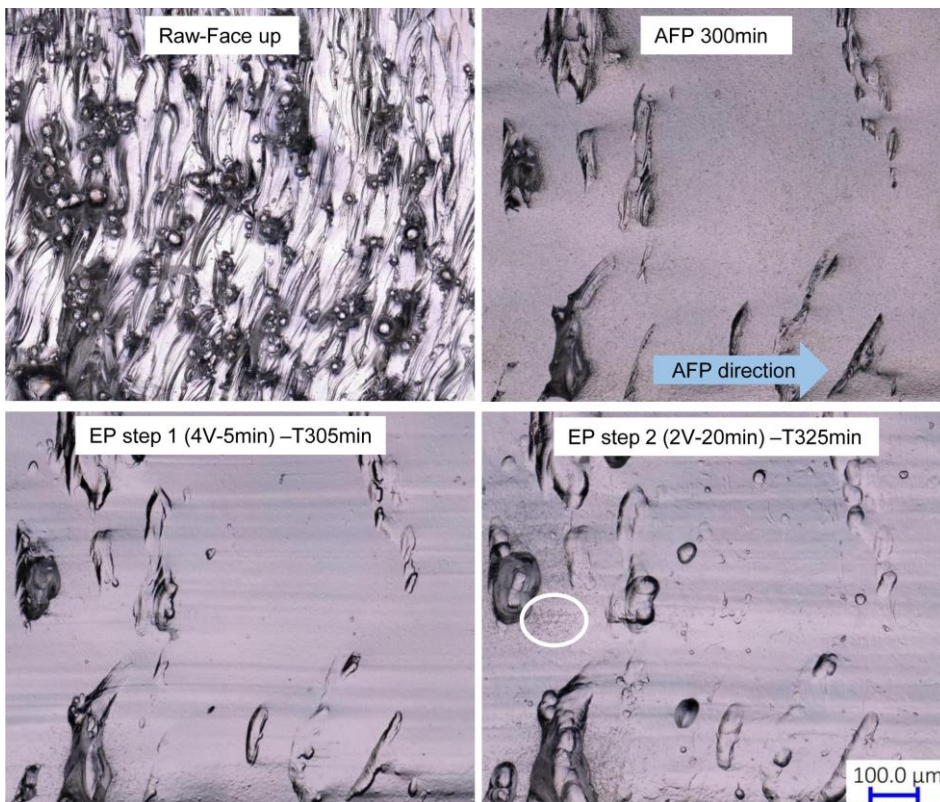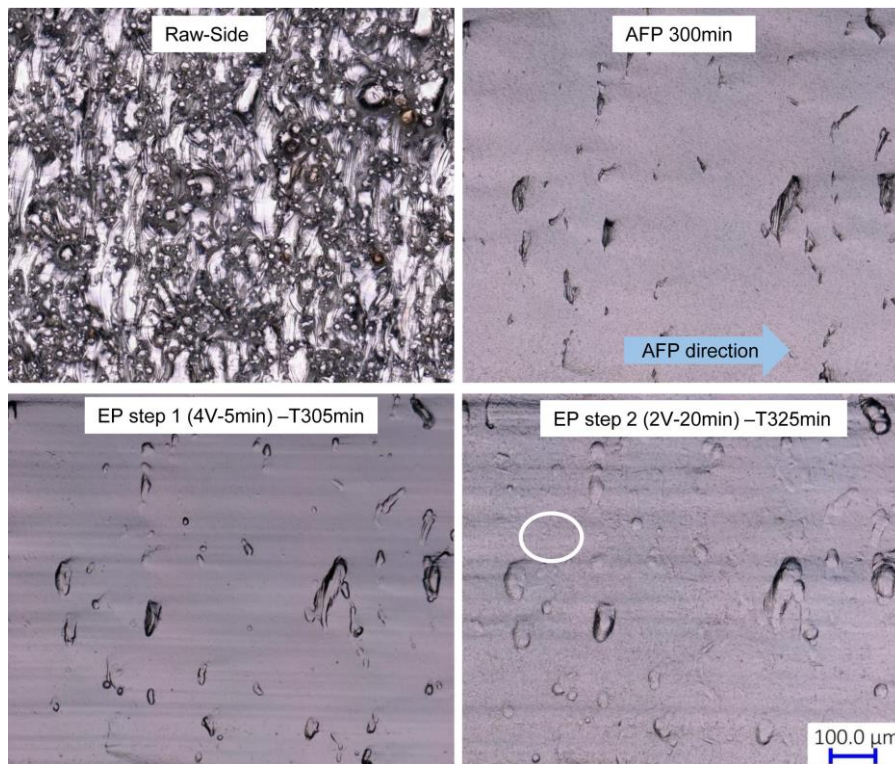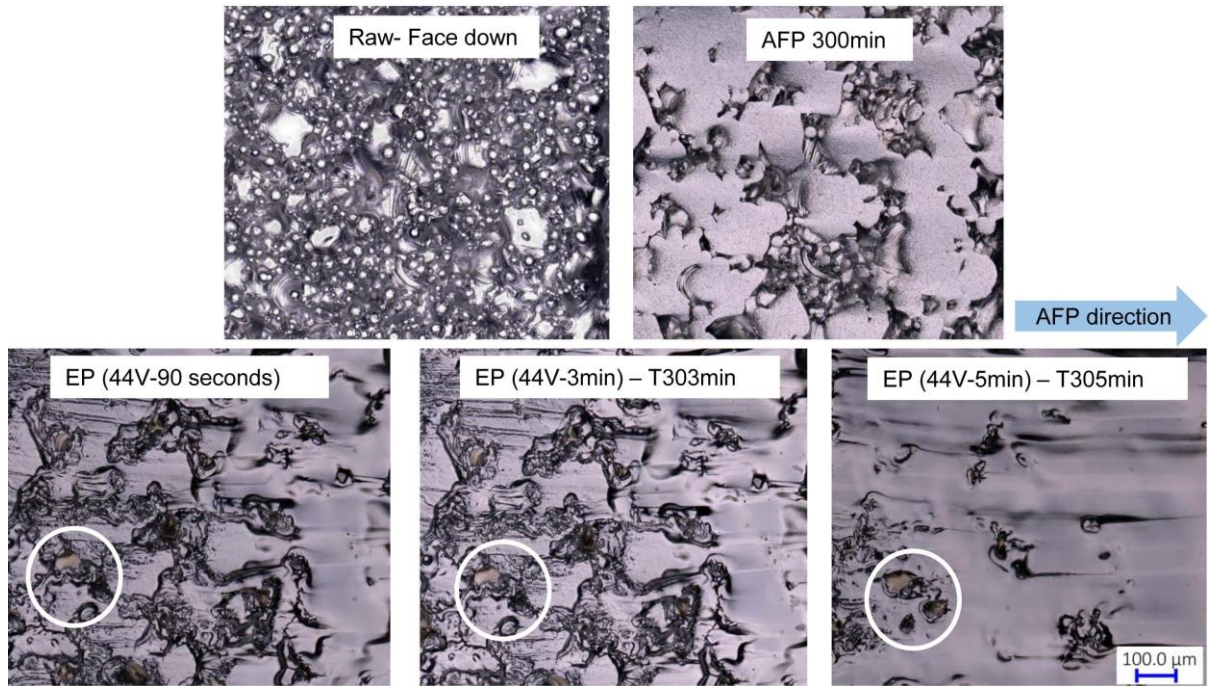
Figure 6.22 OM images of the same area on a face down inner surface of L-PBF Ti6Al4V before and after multiple polishing in different sequences of AFP and then EP.

6.3 Hybrid polishing of L-PBF internal surfaces

6.3.1 Experimental approaches

During hybrid polishing based on EP and AFP, electrolyte and abrasive particles were mixed for the polishing of L-PBF inner surfaces. For L-PBF 316L stainless steel, a mixture of H_3PO_4 and glycerol with the ratio of 3:2 was heated to 55 ℃ first. Then, B_4C particles and the electrolyte were mixed and stirred as polishing media for hybrid polishing. It is noted that the volume of B_4C particles was 4% and the size of particles was 100 μm as optimized in section 5.1. During hybrid polishing of L-PBF 316L stainless steel, a stable flow rate of 0.18 L/s and a stable pressure of 0.18 MPa were employed. Hybrid polishing was carried out based on the two-step EP in section 4.3 in which the first step is to apply a potential of 4V for 5 minutes, and the second step is to utilize a potential of 2V for 20 minutes. In terms of L-PBF Ti6Al4V, electrolyte was a mixture of NaCl powder (99 %) and ethylene glycol solution (99 %) with 0.6 M Cl^-. Then, B_4C particles and the electrolyte are mixed and stirred as polishing media for Ti6Al4V at 25 ℃. During hybrid polishing of L-PBF Ti6Al4V inner surfaces, a stable flow rate of 0.18 L/s and a stable pressure of 0.15 MPa were achieved. Hybrid polishing was

performed based on the two-step EP in section 4.4 in which the first step is to apply a potential of 20V for 15 minutes, and the second step is to utilize a potential of 44V for 5 minutes.

6.3.2 Hybrid polishing of 316L stainless steel

Considering the uniform morphology of side inner surfaces, hybrid polishing of L-PBF 316L stainless steel was conducted using L-PBF side internal surfaces first. Polarization curve was measured in hybrid polishing as shown in Figure 6.23. It is found that the curve shows a similar relationship between potential and current density to single EP (Figure 4.15). Thus, the optimized parameters in single EP can be applied in hybrid polishing.
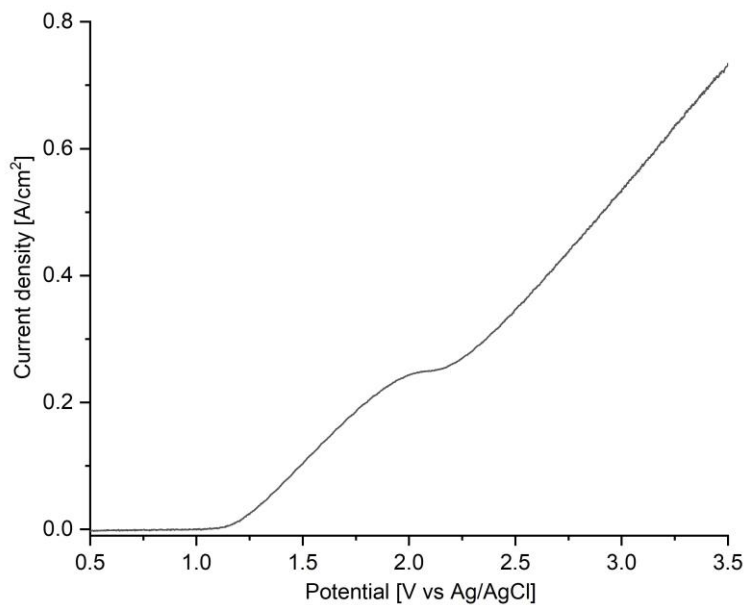
Figure 6.23 Polarization curve of L-PBF 316L stainless steel side internal surface with flow rates of 0.18 L/s at 55 ℃ in hybrid polishing.

Morphological and topographical evolutions of a side inner surface before after different time of hybrid polishing are shown in Figure 6.24 and Figure 6.25, respectively. It can be seen that a morphology similar to that of Figure 4.21 is achieved after 5 minutes (Figure 6.24), which means that un-sintered powders are almost removed. Meanwhile, scratching traces show up at protruding positions on L-PBF side surface that have been marked with red circles and yellow boxes (see Figure 6.24 and Figure 6.25). Then, smooth sintered area and scratching marks are observed after 15 minutes of hybrid polishing. It is worth noting that some scratched areas in the yellow box are

replaced by electropolished sintered areas after polishing from 5 to 15 minutes. With the prolongation of polishing time, the area ratio with scratching traces decreases continuously, and most of the surface is polished to smooth surface after 25 minutes. Based on the surface morphology after single polishing process, it is found that EP and AFP are carried out at the same time without interfering with each other during hybrid polishing of L-PBF 316L stainless steel inner surfaces. Thus, a mixed morphology of electropolished sintered areas and scratching traces are presented after different time of hybrid polishing. With the extension of polishing time, scratched area can be further electropolished and electropolished sintered area at protruding positions could also be scratched during hybrid polishing. Consist with above analysis, mixed morphologies of on top, face up and face down internal surfaces of L-PBF 316L stainless steel after 25 minutes of hybrid polishing are also obtained as can be seen in Figure 6.26.

Given that only side inner surfaces of L-PBF 1/6 straight channels have uniform surface morphology, Ra and Rz values of the side inner surface in Figure 6.24 before and after hybrid polishing were measured and compared with single polishing process as can be seen in Figure 6.27. During hybrid polishing, surface roughness continues to decrease with an increase of polishing time (see Figure 6.27a). Among different polishing processes, single AFP has the lowest polishing efficiency (Figure 6.27b). Hybrid polishing shows higher polishing efficiency in the first five minutes, then it has similar efficiency to EP. Due to a large difference of EP and AFP in polishing efficiency with the developed polishing system, hybrid polishing exhibits highest polishing efficiency in the first 5 minutes, and then the hybrid polishing process is dominated by EP.
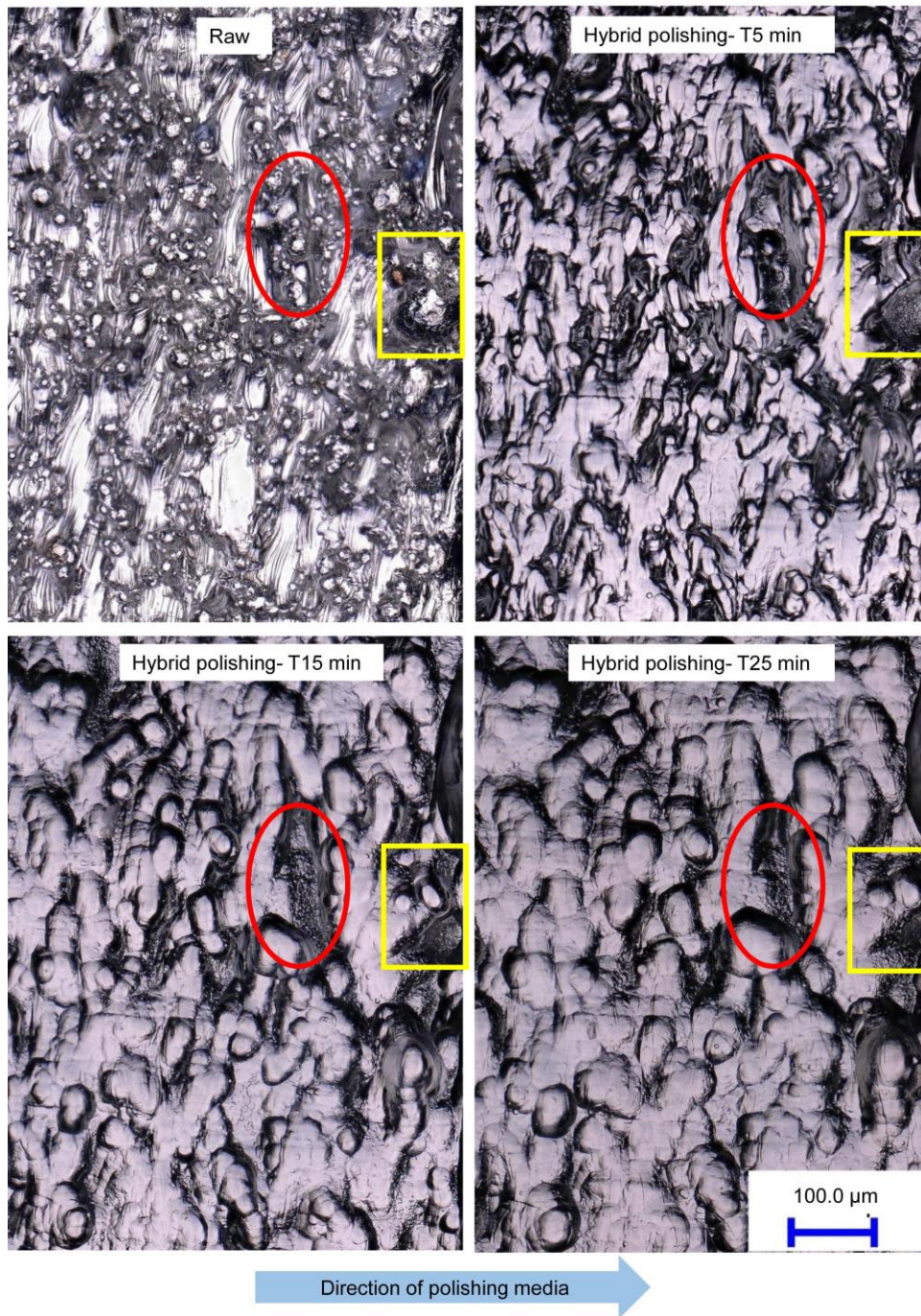
Figure 6.24 OM images of the same area on a side internal surface of L-PBF 316L stainless steel before and after different time of hybrid polishing.
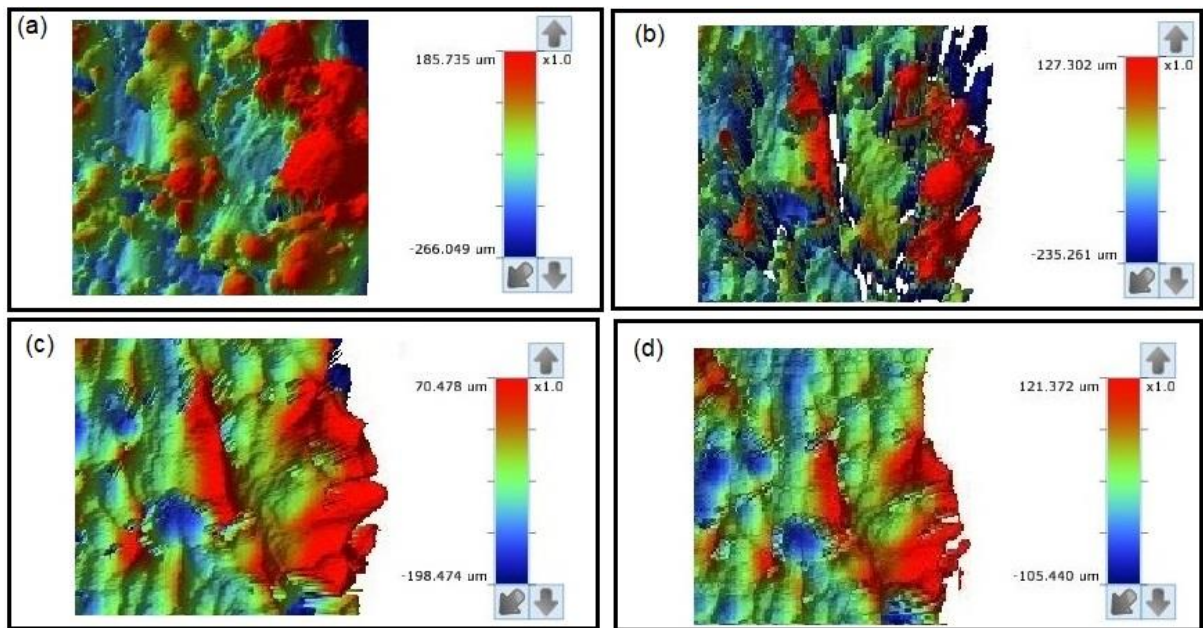
Figure 6.25 Topography images of the same area marked with red circles and yellow boxes in Figure 6.24 (a) before and after (b) 5 minutes, (c) 15 minutes and (d) 25 minutes of hybrid polishing.
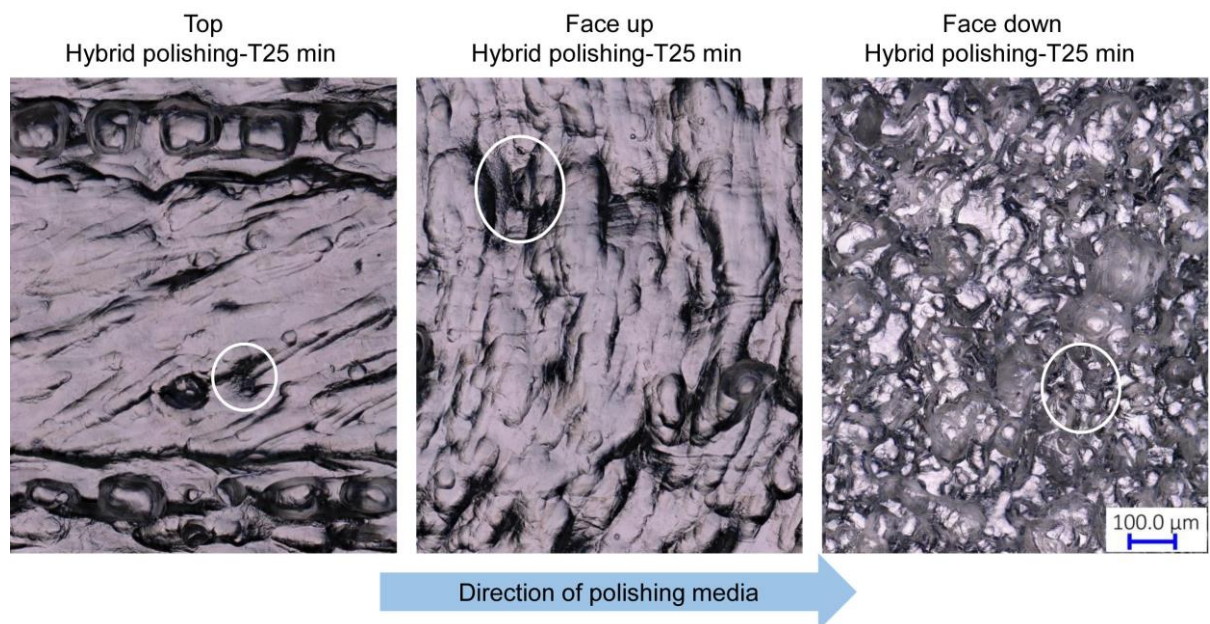
Figure 6.26 OM images of inner top, face up and face down internal surfaces of L-PBF 316L stainless steel after 25 minutes of hybrid polishing, and scratching traces are marked in white circles.

157
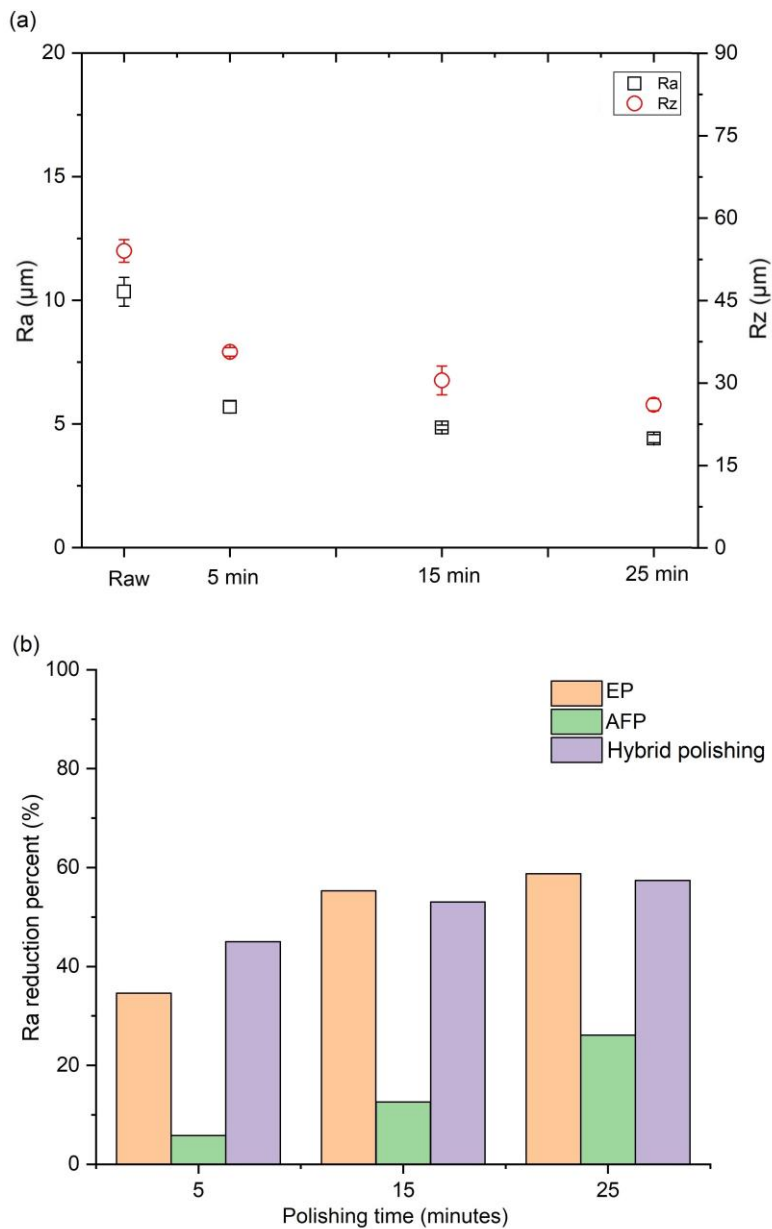
Figure 6.27 Images of (a) surface roughness of a L-PBF side surface before and after different time of hybrid polishing, and (b) Ra reduction percent of EP, AFP and hybrid polishing of L-PBF side surfaces after different polishing time. Note that the left vertical axis represents Ra and the right vertical axis represents Rz in image (a).

Based on above analysis, material removal process of hybrid polishing is illustrated in Figure 6.28. The dissolution of un-sintered powders and scratching of surfaces perform simultaneously in the initial stage of hybrid polishing. With an increase of polishing time, sintered area would be further levelled and protruding area could also be scratched at the same time in hybrid polishing.
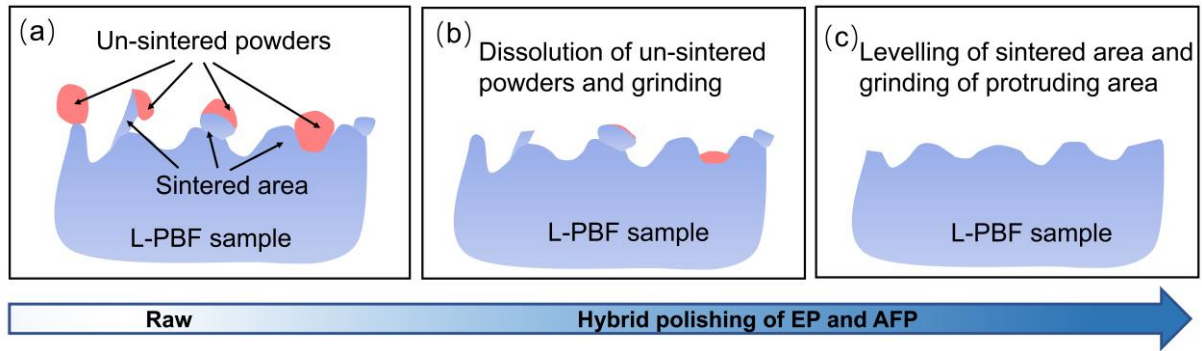
Figure 6.28 Schematic diagram of (a) raw L-PBF inner surfaces, (b) and (c) material removal process with an increase of time during hybrid polishing.

6.3.2 Hybrid polishing of Ti6Al4V

Polarization curve of L-PBF Ti6Al4V inner side surface was measured during hybrid polishing based on EP and AFP as can be seen in Figure 6.29. It is found that the curve shows a similar relationship between potential and current density to single EP (see Figure 4.29). Thus, the optimized parameters in single EP for L-PBF Ti6Al4V internal surfaces can be applied in hybrid polishing.
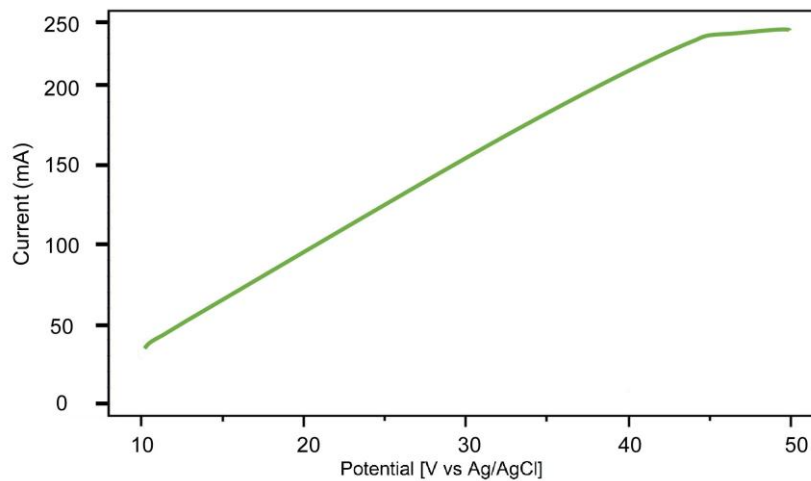
Figure 6.29 Polarization curve of L-PBF Ti6Al4V side internal surfaces with flow rates of 0.18 L/s at 25 °C during hybrid polishing.

OM images and final topography of side inner surfaces of L-PBF Ti6Al4V before and after different time of hybrid polishing are shown in Figure 6.30. It can be seen that a morphology similar to that of Figure 4.32 is achieved after 5 minutes. It is worth noting that some areas are scratched as marked with white circles, while most of the surface possesses etching morphology as marked with yellow box. After 20 minutes of hybrid polishing, most of areas obtain a bright and smooth surface with few scratching traces.

159

In addition, there are some sintered areas at valley positions as shown in the topography image. The morphology difference of side inner surfaces after 20 minutes of hybrid polishing and single EP (Figure 4.34) is that there exist few scratching traces on surface after hybrid polishing. Thus, EP and AFP are carried out simultaneously without interfering with each other during hybrid polishing of L-PBF T6Al4V inner surfaces. As a result, a mixed morphology of electropolished surface and scratching traces is shown after different time of hybrid polishing. Consist with above analysis, mixed morphologies of top, face up and face down internal surfaces of L-PBF Ti6Al4V after 20 minutes of hybrid polishing are also obtained as can be seen in Figure 6.31.
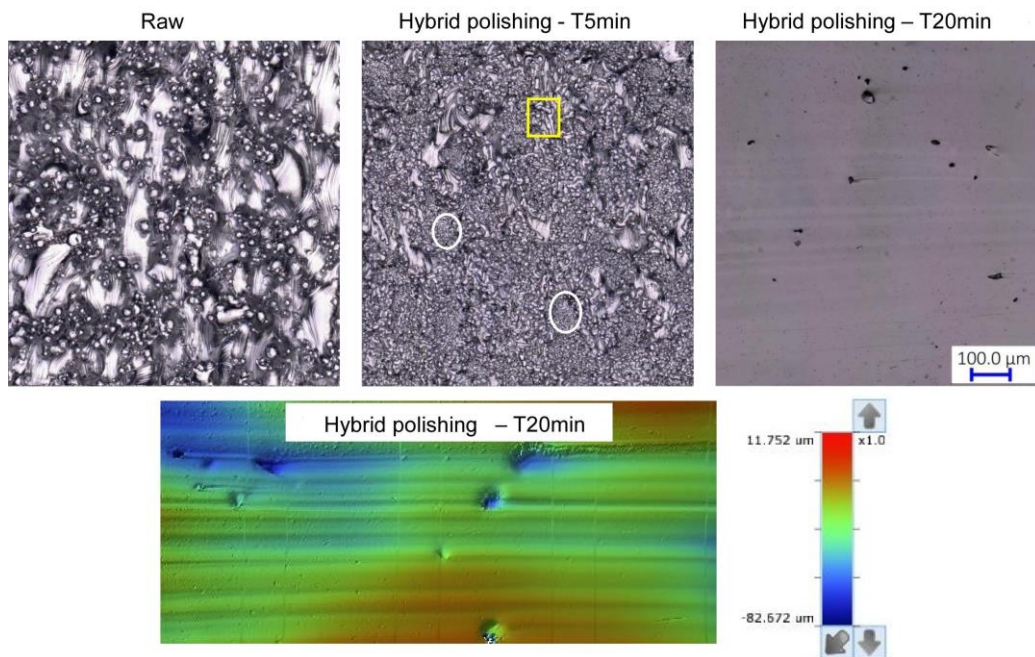
Figure 6.30 OM images and topography of side internal surfaces of L-PBF Ti6Al4V before and after different time of hybrid polishing.
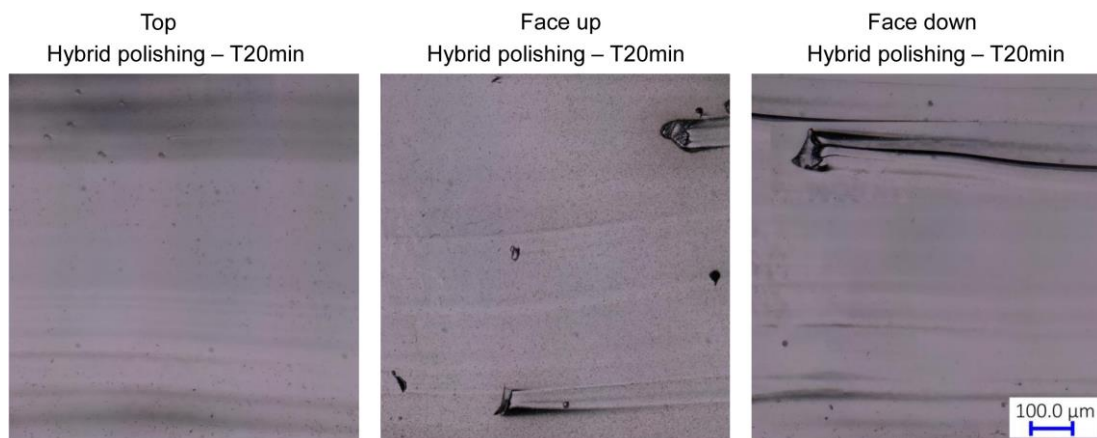
Figure 6.31 OM images of top, face up and face down internal surfaces of L-PBF Ti6Al4V after 20 minutes of hybrid polishing.

Ra values of L-PBF Ti6Al4V side inner surfaces before and after hybrid polishing and EP are compared in Figure 6.32. It could be seen that hybrid polishing shows higher polishing efficiency in the first five minutes and then it has similar efficiency to EP after 20 minutes. Consistent with hybrid polishing of L-PBF 316L stainless steel inner surfaces, it is caused by the large difference of polishing efficiency of EP and AFP in the developed polishing system.
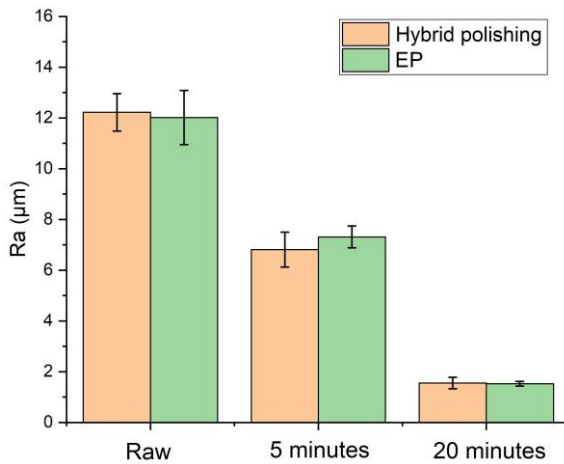
Figure 6.32 Ra values of L-PBF Ti6Al4V side inner surfaces before and after different time of hybrid polishing and EP.

6.4 Summary

This chapter investigates multiple polishing in different sequences and hybrid polishing of EP and AFP on various inner surfaces of L-PBF 316L stainless steel and Ti6Al4V. Given that it is difficult or inappropriate to further polish L-PBF inner surfaces by single EP and AFP after a certain period of time as analyzed in chapter 4 and chapter 5, it is essential to study the material removal characteristics of multiple and hybrid polishing for L-PBF inner surfaces. Based on the comprehensive characterization of morphology, roughness and microstructure on cross sections, material removal characteristics of EP and AFP on L-PBF inner structures have been discussed in previous chapters. Therefore, evolutions of morphology and roughness are characterized to study multiple and hybrid polishing processes in this chapter. The main conclusions can be drawn as follows:

(1) Multiple polishing in different sequences of EP and then AFP would continuously reduce surface roughness on various L-PBF inner surfaces because AFP is capable of removing protruding area of inner surfaces after EP. Considering the relatively low surface roughness can be obtained after EP, a longer AFP time is required to achieve a flatter inner surface.

(2) Multiple polishing in different sequences of AFP and then EP generally exhibits fluctuations of roughness on L-PBF inner surfaces during polishing process because original surface areas at valley positions are remained after AFP.

(3) A mixed morphology of EP and AFP appears on L-PBF inner surfaces after hybrid polishing. During hybrid polishing, EP and AFP can be carried out simultaneously without interfering with each other.

(4) Due to the large difference of EP and AFP in polishing efficiency using the developed polishing system, hybrid polishing of L-PBF internal surfaces shows superiority of removing surface features and reducing roughness effectively in a short period of time. Then, the reduction of surface roughness shows a similar level to that of EP in the developed hybrid polishing system.

Chapter 7. Application Development of Polishing for L-PBF Internal Structures

7.1 Polishing of Ti6Al4V straight channels

7.1.1 Experimental approach

Polishing parameters of EP and AFP were tested and applied to Ti6Al4V straight channels. Considering that the inner diameter of the straight channel is 2 mm (Table 3.2 and Figure 3.17), a cylindrical titanium rod was used as cathode as illustrated in Figure 3.25b. During EP, a stable flow rate of 0.03 L/s could be achieved due to the narrow space between the cathode and inner surface of whole channel. A two-step EP was optimized in section 4.4 for various internal surfaces prepared by L-PBF Ti6Al4V in which the first step of EP is to polish surfaces uniformly using a potential of 20V for 15 minutes, while the second step is to obtain a bright and smooth surface by applying a potential of 44V along the LCPR for 5 minutes. Given that changes of flow rate have less effect on LCPR, the two-step EP for L-PBF Ti6Al4V internal surfaces was utilized to straight channels directly in this section. In terms of AFP (Figure 3.26b), optimized parameters of abrasive particles in section 5.1 were used and a stable flow rate of 0.06 L/s can be employed. In addition, it is difficult to conduct hybrid polishing due to the limited remaining space between the cathode and the inner surface of the whole channels. Thus, EP, AFP and multiple polishing in different sequences were investigated for L-PBF Ti6Al4V whole straight channels with the inner diameter of 2 mm.

7.1.2 Polishing process

The morphology and topography of a straight channel after the two-step EP are shown in Figure 7.1a and b, respectively. Consistent with the results in Figure 4.36, most inner surface area is polished to a smooth and bright surface, but there are some remained sintered areas without bright morphology at valley positions after EP.
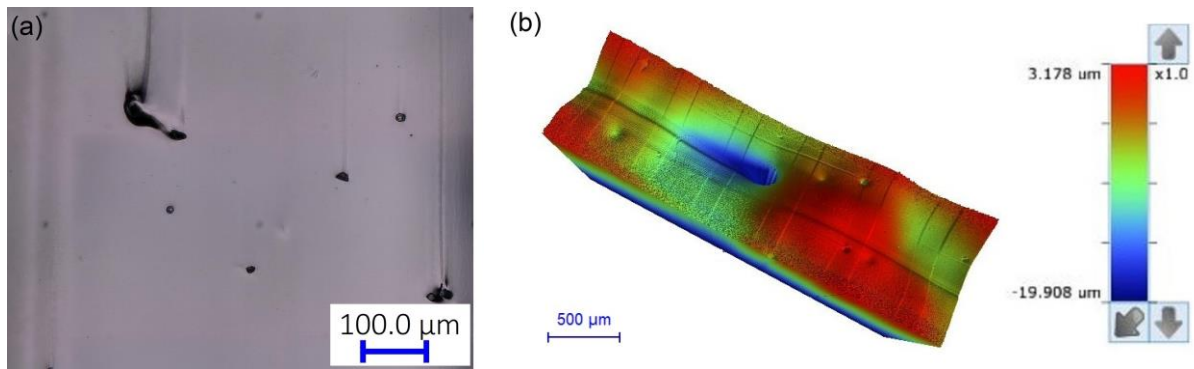
Figure 7.1 Images of morphology (a) and topography (b) of inner surfaces of L-PBF Ti6Al4V straight channels with inner diameter of 2 mm after the two-step EP.

Figure 7.2 shows the morphology of inner surfaces after different time of AFP. It can be seen that some raw area still exists after 25 minutes, while raw morphology is removed and only scratches traces are observed after 50 minutes of AFP. Therefore, single AFP time for the straight channel is optimized to 50 minutes.
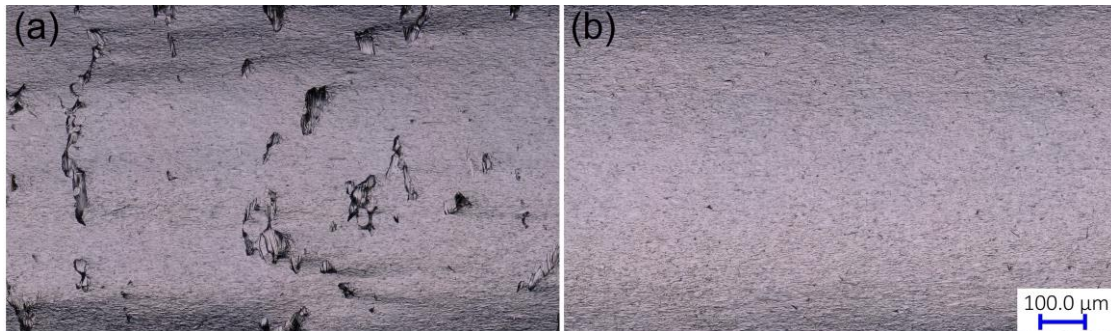
Figure 7.2 OM images of the inner surface of L-PBF Ti6Al4V straight channels with an inner diameter of 2 mm after 25 minutes (a) and 50 minutes (b) of AFP.

In order to remove the remained sintered area after EP (Figure 7.1), different AFP time was applied for multiple polishing on inner surface of straight channels. As illustrated in Figure 7.3, most sintered areas can be removed after AFP for 5 and 15 minutes (Figure 7.3a and b). With AFP time for 25 minutes, the sintered areas on the whole channel are totally removed and a uniform scratch morphology is obtained (Figure 7.3c).
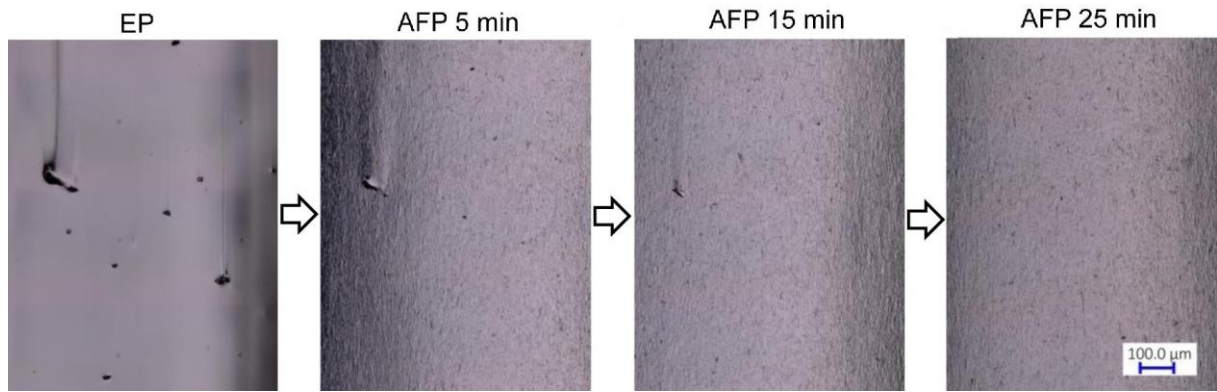
Figure 7.3 OM images of the same area on the inner surface of a L-PBF Ti6Al4V straight channel with an inner diameter of 2 mm after EP and then different time of AFP.

EP was carried out after AFP for 50 minutes for multiple polishing in different sequences and surface morphologies after different time of EP are shown in Figure 7.4. Considering the scratching morphology on the inner surface after AFP (Figure 7.2b), a potential of 44V was used for EP process. Despite the uniform morphology after AFP (Figure 7.2b), some sintered areas (Figure 7.4c) show up after EP of 90, 180 and 300 seconds. Given that current density at 44V is relatively high and could cause high material removal rate, it is not advisable to further extend EP time. The topography of the inner surface after EP for 5 minutes was measured. Consistent with the results in section 4.4.3 (Figure 4.36), it is found that the remained sintered areas are at valley positions (Figure 7.4d).

AFP 50 min
then EP 90 s

AFP 50 min
then EP 180 s

AFP 50 min
then EP 300 s

(a)

(b)

(c)

100 μm

(d)

AFP 50 min
then EP 300 s

2.674 um   x1.0

-20.499 um

500 μm
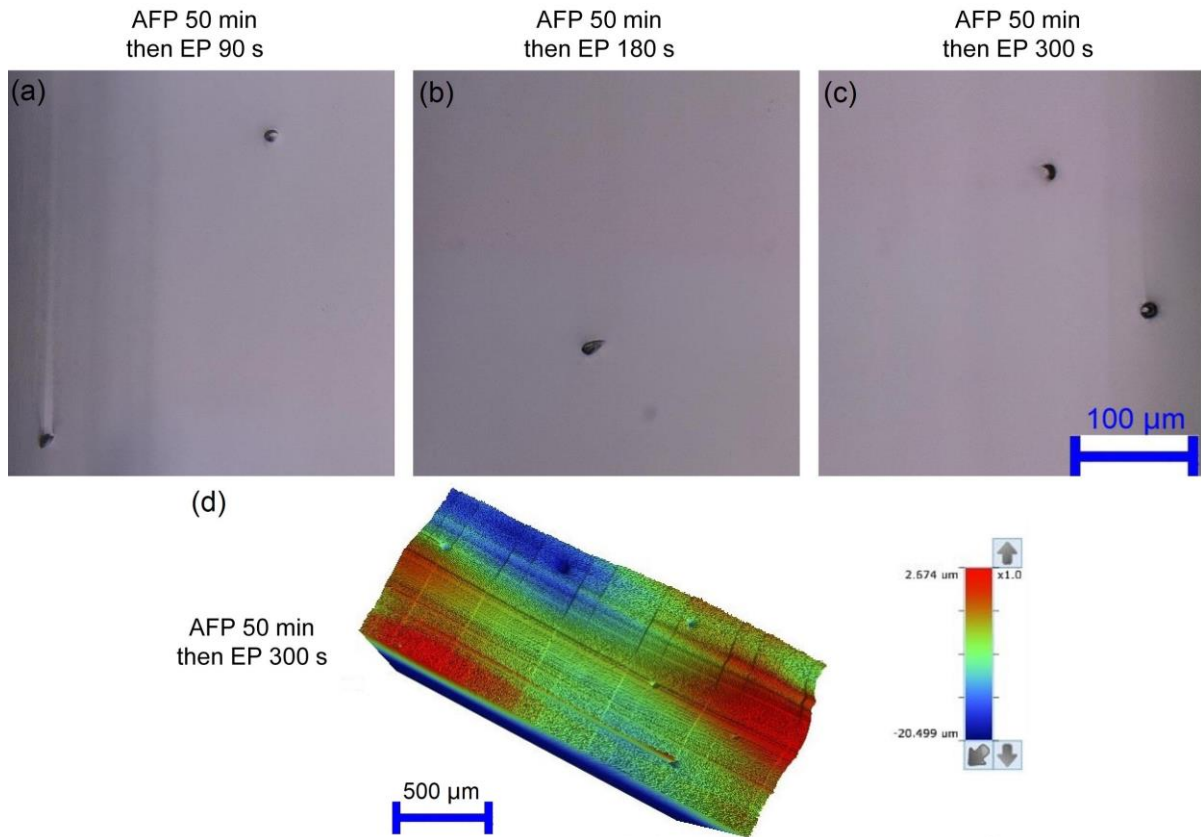
Figure 7.4 Morphology of inner surfaces of L-PBF Ti6Al4V straight channels with an inner diameter of 2 mm after AFP and then EP at 44V of (a) 90 seconds, (b) 180 seconds and (c) 300 seconds, and topography of an inner surface after (d) AFP and then EP for 300 seconds.

7.1.3 Polishing of whole straight channel

Whole straight channels before and after multiple polishing in different sequences are shown in Figure 7.5. Although smooth inner surfaces were both obtained after multiple polishing in different sequences, multiple polishing consisting of the two-step EP and then 25 minutes of AFP is more suitable for L-PBF Ti6Al4V whole straight channels with inner diameter of 2mm based on the analysis in section 7.1.2 (Figure 7.3 and Figure 7.4).

Raw

AFP+EP

EP+AFP

5 mm

Figure 7.5 L-PBF Ti6Al4V straight channels with an inner diameter of 2mm before and after multiple polishing in different sequences.

166

7.2 Polishing of Ti6Al4V BCC lattice structures

7.2.1 Experimental approach

Polishing parameters of EP and AFP were optimized for Ti6Al4V BCC lattice structures, respectively. Considering the dimension of lattice structure (Table 3.2 and Figure 3.17), a cylindrical titanium cathode was used and located inside a fixture with an inner diameter of 18 mm as illustrated in Figure 3.25c. During EP, a stable flow rate of 0.03 L/s was used. A two-step EP was optimized in section 4.4.2 for various internal surfaces prepared by L-PBF Ti6Al4V in which the first step of EP is to polish surfaces uniformly using a potential of 20V for 15 minutes, while the second step is to obtain a smooth and bright surface by applying a potential of 44V along the LCPR for 5 minutes. Moreover, changes of flow rate have less effect on LCPR. Therefore, the two-step EP and the potential of 44V with different EP time were applied to lattice structures, respectively. In terms of AFP, the optimized parameter in section 5.1 was used and a stable flow rate of 0.18 L/s can be obtained (see Figure 3.26c) inside a fixture with an inner diameter of 10 mm. Considering the use of cathode and the large diameter of the fixture in EP, it is difficult to conduct hybrid polishing in the current polishing system due to the limited flow rate of the pump. Thus, EP, AFP and multiple polishing in different sequences were investigated for BCC lattice structures of L-PBF Ti6Al4V in this section.

7.2.2 Polishing process

Given that the two-step EP for various L-PBF Ti6Al4V internal surfaces in section 4.4 has higher current density and relatively long polishing time, different combinations of potentials and polishing time were investigated for Ti6Al4V lattice structures considering the diameter of the strut is 0.45 mm in the designed model (Table 3.2 and Figure 3.17). Figure 7.6 shows the images of lattice structures at top view after different EP processes. As can be seen in Figure 7.6a, the two-step EP in section 4.4.2 was applied to BCC structures and a bright surface is obtained. However, some struts are partially dissolved after 20 minutes due to the high material removal rate. Then, 5 and 10 minutes of EP at 44V were tested considering that 44V is along LCPR (Figure 7.6).

It should be noted that 10 minutes of EP at 44V could also partially dissolve struts (Figure 7.6b), while 5 minutes of EP is more appropriate since it achieves smooth and bright surface, and avoid damaging struts on BCC structures (Figure 7.6c). Different views of a BCC lattice structure after 5 minutes of EP at 44V are illustrated in Figure 7.7. Most of adhered powders on top and side views are dissolved and smooth surfaces can be obtained. However, some raw areas remain on bottom view which is caused by the maximum quantity of un-sintered powders and highest roughness of un-sintered area on raw surface. In addition, current density distribution in the region facing the cathode is generally higher than other regions on the BCC lattice structure. Thus, it is hard to achieve absolutely uniform polishing on BCC lattice structures by EP.
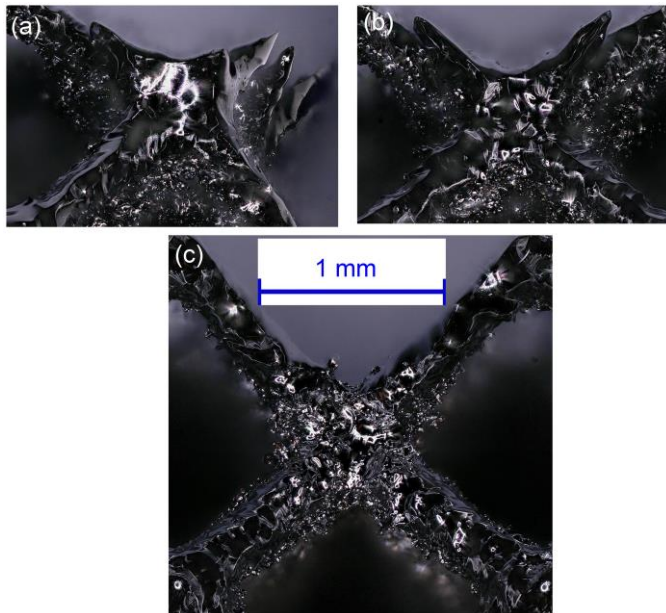
Figure 7.6 OM images of top view of Ti6Al4V lattice structures after (a) the two-step EP, (b) 10 minutes of EP at 44V and (c) 5 minutes of EP at 44V.
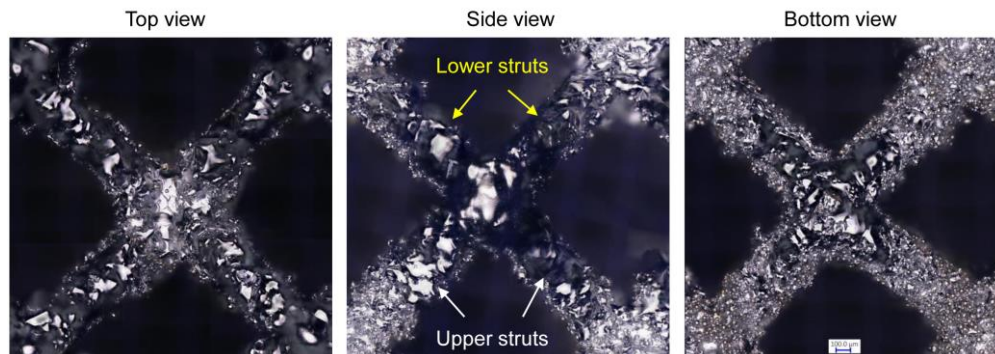
Figure 7.7 OM images of top, side and bottom views of a Ti6Al4V lattice structure after 5 minutes of EP at 44V.

Given that the strength of Ti6Al4V BCC lattice structures should be properly considered during AFP, different AFP times were optimized. Bottom view of Ti6Al4V lattice structures after 5, 15 and 25 minutes of AFP are shown in Figure 7.8. It is noted that morphologies on bottom view change significantly after AFP because of the setting of AFP direction (Figure 3.26c). Despite some adhered powders on struts are polished after 5 minutes by AFP, some raw areas still can be observed (Figure 7.8a). Moreover, obvious adhesions of un-sintered powders are remained at the center point of struts (Figure 7.8a). With an increase of AFP time, raw morphologies on struts and their center points are totally removed after 15 and 25 minutes (Figure 7.8b and c) because AFP is capable of removing un-sintered powders and levelling of sintered area. It should be noted that the diameter of struts reduces obviously after AFP of 25 minutes which may affect strength of the whole structure. Considering that excessive AFP time could continuously reduce the size of struts and result in reduced structural strength, 15 minutes of AFP is optimized for L-PBF Ti6Al4V lattice structures. Compared with bottom area, some areas on top and side views (Figure 7.9) are also partially polished because of the turbulence flow characteristic of AFP process.
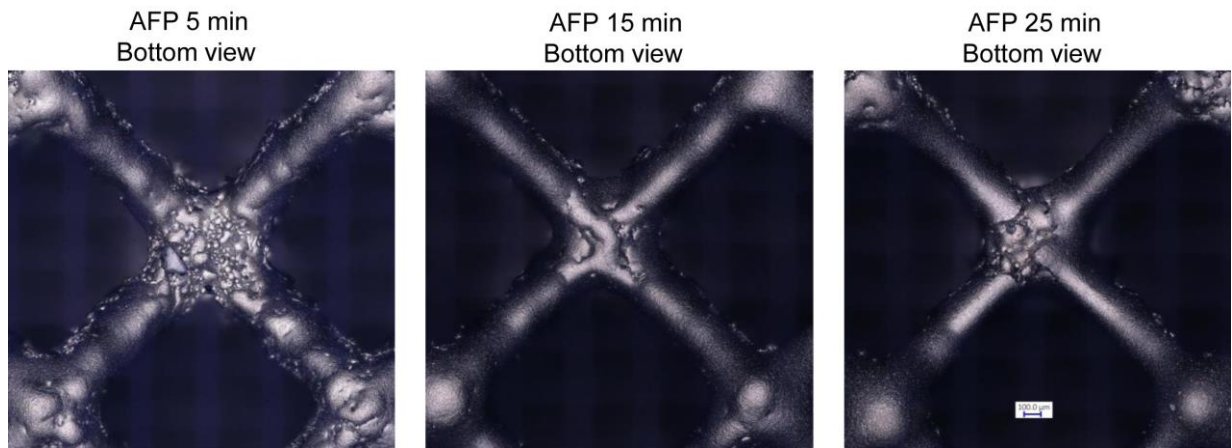
Figure 7.8 OM images of bottom views of Ti6Al4V lattice structures after different time of AFP.
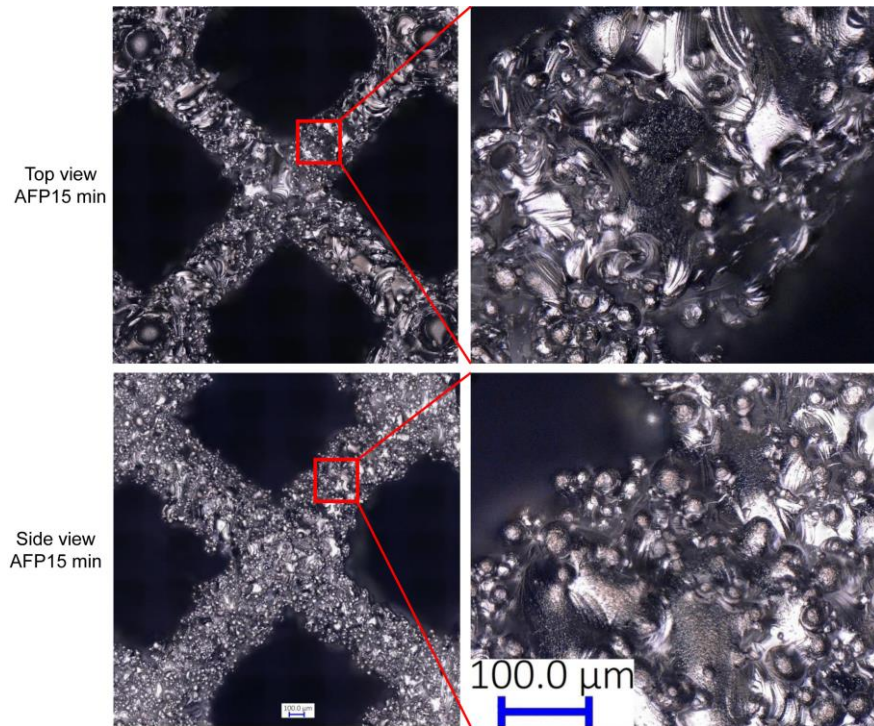
Figure 7.9 OM images of top and side views of Ti6Al4V lattice structure after 15 minutes of AFP.

To further polish the bottom view after EP (Figure 7.7), 15 minutes of AFP was applied for Ti6Al4V lattice structures. Morphology of bottom view after multiple polishing is displayed in Figure 7.10. Un-sintered powders on bottom view are totally removed and sintered area is further levelled. However, deformation of some struts occurs. It can be explained that EP reduces the dimension of struts to a certain degree, then, AFP process continuously reduces the size of struts and causes deformation.

Figure 7.10 Morphology of bottom view of Ti6Al4V lattice structure after EP and then 15 minutes of AFP.

EP was conducted after AFP of 15 minutes for multiple polishing in different sequences. Based on the morphology of that BCC lattice structure after 15 minutes of AFP in Figure 7.8 and Figure 7.9, adhered spherical morphologies are almost dissolved and bright surfaces can be obtained on the bottom view with the action of 5 minutes of EP as can be seen in Figure 7.11. Meanwhile, this multiple polishing process keeps the entire structure from being damaged.
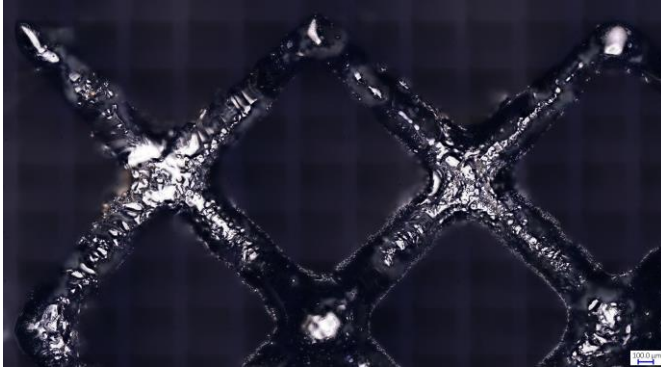
Figure 7.11 Morphology of bottom view of Ti6Al4V lattice structure after AFP and then 5 minutes of EP.

7.2.3 Polishing of lattice structures

Images of L-PBF Ti6Al4V lattice structures before and after multiple polishing in different sequences of EP and AFP are shown in Figure 7.12. Multiple polishing in different sequences based on EP and AFP using the developed polishing system could effectively remove un-sintered powders and flatten sintered area on BCC lattice structures without damaging the structure. With the optimization of polishing parameters, it is more appropriate to apply 15 minutes of AFP first and then 5 minutes of EP at 44V for L-PBF Ti6Al4V BCC lattice structures. In addition, the dimension of struts and the strength of L-PBF specific lattice structure need to be considered for the optimization of polishing process.

Figure 7.12 Images of L-PBF Ti6Al4V lattice structures before and after multiple polishing in different sequences.

7.3 Polishing of 316L stainless steel BCC lattice structures

7.3.1 Experimental approach

Given that there are two types of BCC lattice structures of L-PBF 316L stainless steel as illustrated in Table 3.2, EP, AFP and multiple polishing in different sequences were carried out on multiple BCC lattice structures, while EP, AFP and hybrid polishing were conducted on single BCC lattice structure. Meanwhile, fixtures and polishing conditions were also varied due to dimension differences of lattice structures. It is noted that a two-step EP was optimized in section 4.3 for various internal surfaces prepared by L-PBF 316L stainless steel in which the first step of EP is to remove almost un-sintered powders using a potential of 4V for 5 minutes, while the second step is to further level the remaining sintered area and obtain a bright surface by applying a potential of 2V along the LCPR for 20 minutes.

For multiple BCC lattice structures, flow rates and fixtures of EP and AFP are the same as Ti6Al4V lattice structures in section 7.2. During EP (Figure 3.25c), a stable flow rate of 0.03 L/s was used. Given that changes of flow rate have less effect on LCPR, the two-step EP in section 4.3 were applied to 316L stainless steel multiple lattice structures directly. In terms of AFP (Figure 3.26c), optimized parameters of abrasive particles in section 5.1 were used and a stable flow rate of 0.18 L/s could be obtained. Due to the use of cathode and the large diameter of the fixture during EP, it is also difficult to apply hybrid polishing to multiple BCC lattice structures. Thus, EP, AFP and multiple polishing in different sequences were investigated for multiple BCC lattice structures of L-PBF 316L stainless steel.

In terms of single BCC lattice structure, a cylindrical fixture with an inner diameter of 7 mm was used for EP, AFP and hybrid polishing (Figure 3.25c and Figure 3.26c). Different from multiple lattice structures, a potential of 2V was used during EP and hybrid polishing. Meanwhile, a flow rate of 0.18 L/s was utilized for various polishing processes of single BCC lattice structure.

7.3.2 Polishing process

7.3.2.1 Polishing of multiple BCC lattice structures

OM images of multiple BCC lattice structures after the two-step EP are shown in Figure 7.13. It can be seen that un-sintered powders are totally electropolished and smooth surfaces with sintered area on top, side and bottom views could be obtained after EP. Therefore, the two-step for various L-PBF 316L stainless steel internal surfaces is also applicable to BCC lattice structures. In addition, sintered area on bottom view can be further improved considering its highest roughness of raw surface.
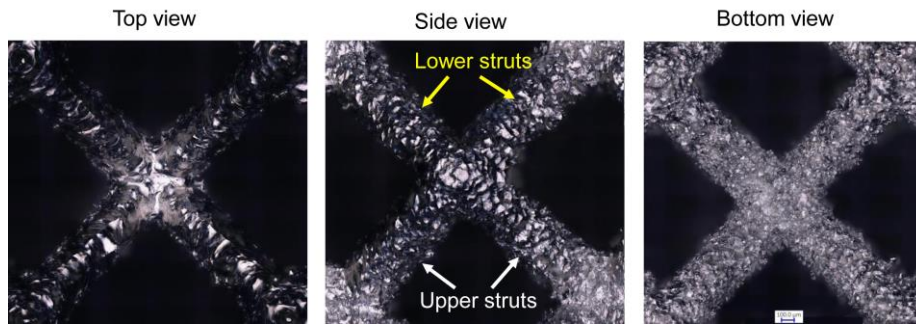
Figure 7.13 Morphology of top, side and bottom views of 316L stainless steel lattice structure after the two-step EP.

AFP time was optimized for multiple BCC structures and the bottom views after 15, 25 and 50 minutes are illustrated in Figure 7.14. Despite adhered powders on struts are removed after 15 minutes, some raw areas can still be observed. Moreover, there are obvious adhesion of un-sintered powders at the center point of struts (Figure 7.14a). With an increase of AFP time, raw morphologies are totally removed on bottom view after 25 and 50 minutes (Figure 7.14b and c). It is noted that the diameter of struts reduces obviously after AFP of 50 minutes which may affect the strength of BCC structures. Thus, AFP for 25 minutes is optimized for L-PBF 316L stainless steel BCC lattice structures. Compared with bottom view, there are scratches on some area of top and side views due to the turbulence flow characteristic of AFP process as can be seen in Figure 7.15.

Figure 7.14 OM images of bottom views of 316L stainless steel lattice structure after (a) 15, (b) 25 and (c) 50 minutes of AFP.
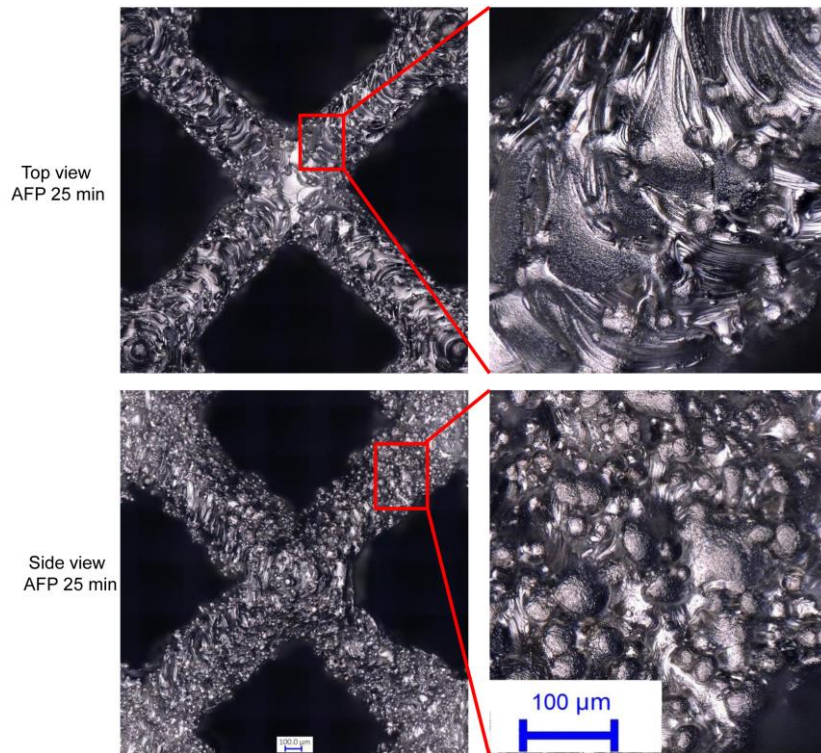
Figure 7.15 OM images of top and side views of 316L stainless steel lattice structure after 25 minutes of AFP.

The rough sintered area on bottom view after EP (Figure 7.13) could be further levelled by applying AFP. Considering that EP had reduced the dimension of struts to a certain degree, 15 minutes of AFP was utilized to multiple BCC lattice structures after EP. The morphology of bottom view after EP and then AFP is shown in Figure 7.16. It can be seen that rough sintered areas after EP (Figure 7.13) on bottom view could be effectively levelled. Meanwhile, the diameter of struts is less affected with 15 minutes of AFP. Thus, multiple polishing consisting of the two-step EP and then 15 minutes of AFP is applicable for L-PBF 316L stainless steel multiple BCC lattice structures.

Figure 7.16 Morphology of bottom view of 316L stainless steel multiple lattice structure after the two-step EP and then 15 minutes of AFP.

Multiple polishing in different sequences of AFP and then EP was carried out for multiple lattice structures. Compared with surface morphology after AFP in Figure 7.14 and Figure 7.15, un-sintered powders on the top and side views are dissolved and smooth surfaces can be obtained as can be seen in Figure 7.17. Meanwhile, this polishing process keeps the entire structure from being damaged. However, etching traces occur on the bottom view after the two-step EP due to that AFP has effectively polished surfaces on the bottom view (Figure 7.14b) and the use of 4V in the first step of EP with relatively long EP time cause etching which is consistent with the analysis in section 6.1.
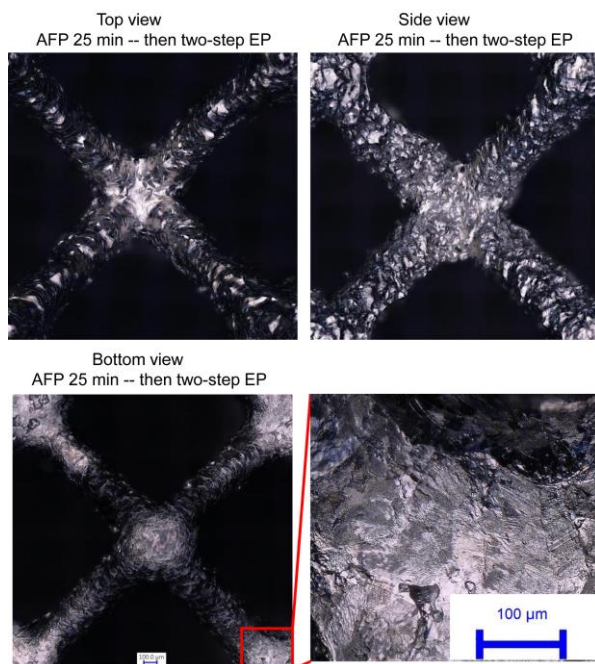
Figure 7.17 OM images of top, side and bottom views of 316L stainless steel lattice structure after 25 minutes of AFP and then the two-step EP.

7.3.2.2 Polishing of single BCC lattice structure

To study the potential of hybrid polishing on L-PBF lattice structures, OM images of single BCC lattice structures after 30 minutes of EP, AFP and hybrid polishing are shown in Figure 7.18. After EP, un-sintered powders are removed, and uneven sintered areas with bright surface show up on bottom view (Figure 7.18a). Compared with EP, AFP can remove some un-sintered powders and level surfaces on bottom view to a certain degree by scratching. However, some raw morphologies with un-sintered powders and sintered area are remained after AFP (Figure 7.18b). Different from EP and AFP, hybrid polishing can effectively remove adhered powders and level the

sintered area simultaneously (Figure 7.18c) which is consistent with the analysis in section 6.3.
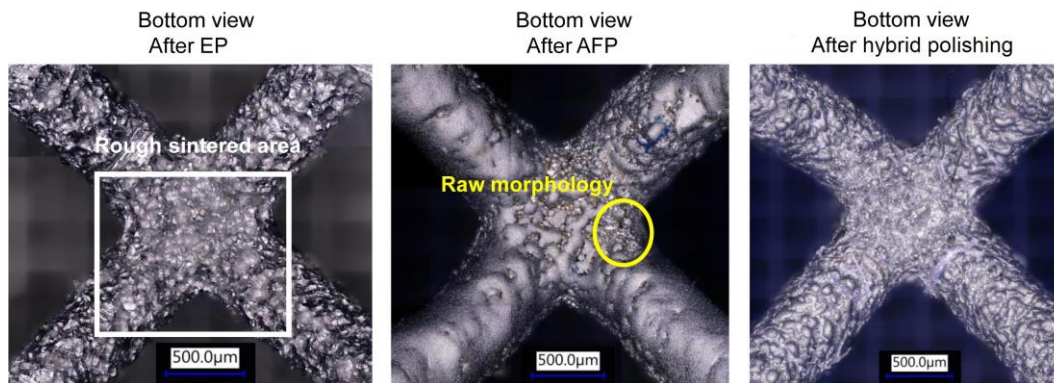
Figure 7.18 OM images of bottom views of single BCC lattice structures prepared by L-PBF 316L stainless steel after 30 minutes of EP at 2V, AFP and hybrid polishing with the potential of 2V, respectively.

7.3.3 Polishing of lattice structures

Pictures of multiple L-PBF 316L stainless steel lattice structures before and after multiple polishing in different sequences based on EP and AFP are shown in Figure 7.19. Multiple polishing in different sequences could effectively remove un-sintered powders and flatten sintered area on surfaces of L-PBF BCC lattice structures without damaging the structure. Based on the optimization of polishing parameters, it is more appropriate to apply the two-step EP first and then 15 minutes of AFP for multiple 316L stainless steel BCC lattice structures. It is noted that materials, design of unit cell, dimensions of struts, strength of L-PBF specific lattice structure, polishing effects of EP and AFP should be considered for the optimization of polishing process. In addition, hybrid polishing exhibits great potential for the polishing of L-PBF lattice structures. Moreover, the developed hybrid polishing system can be further optimized such as fixture optimization, polishing chamber optimization and using a pump with higher flow rate to improve the polishing capability of L-PBF internal structures.

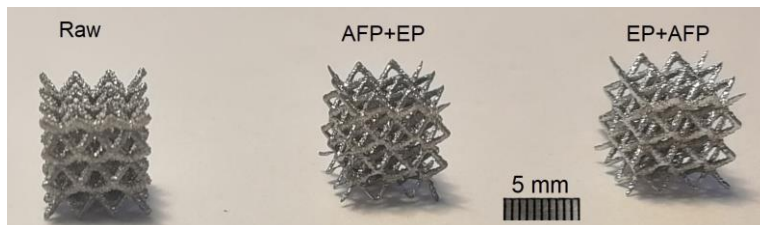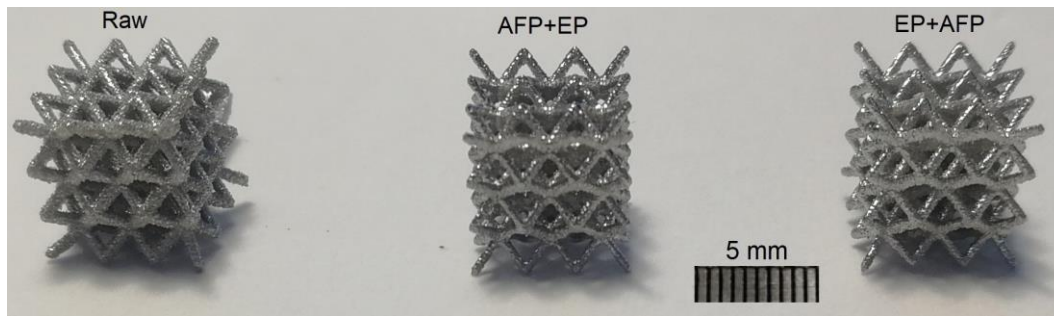Figure 7.19 Pictures of L-PBF 316L stainless steel multiple lattice structures before and after multiple polishing in different sequences.

7.4 Polishing of 316L stainless steel conformal channels

7.4.1 Experimental approach

Polishing parameters of EP and AFP were optimized for L-PBF 316L stainless steel conformal channels. During EP, a conformal titanium cathode with flexibility was designed, fabricated by titanium wire, and then used as illustrated in Figure 3.25d. Meanwhile, a stable flow rate of 0.03 L/s could be achieved. It is noted that a two-step EP was optimized in section 4.3 for various internal surfaces prepared by L-PBF 316L stainless steel in which the first step of EP is to remove almost un-sintered powders using a potential of 4V for 5 minutes, while the second step is to further level the remaining sintered area and obtain a smooth surface by applying a potential of 2V along the LCPR for 20 minutes. Given that changes of flow rate have less effect on LCPR, the two-step EP for L-PBF 316L stainless steel internal surfaces in section 4.3 was utilized to conformal channels directly. In terms of AFP (Figure 3.26d), optimized parameters of abrasive particles in section 5.1 were used and a stable flow rate of 0.15 L/s could be obtained. In addition, it is difficult to conduct hybrid polishing to 316L stainless steel conformal channels due to the use of the conformal cathode. Therefore, EP, AFP and multiple polishing in different sequences were investigated for the inner surface polishing of conformal channels.

7.4.2 Polishing process

Morphology of the internal surface of a conformal channel after the two-step EP for L-PBF 316L stainless steel is shown in Figure 7.20. Despite that EP time is 25 minutes, un-sintered powders are only partially dissolved and rough sintered area

shows up. The low efficiency of EP is a result of low current density caused by the limited size and surface area of the conformal cathode.
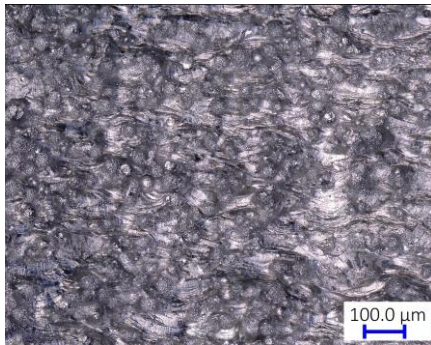
Figure 7.20 Morphology of inner surface of a L-PBF 316L stainless steel conformal channel after EP.

Different AFP times were utilized to conformal channels in order to optimize AFP process as can be seen in Figure 7.21. After AFP for 5 minutes, although face down areas would be polished efficiently (Figure 7.22), it is difficult to achieve uniform material removal process on inner surfaces of curve channels through AFP process [153]. Cumulative effect of non-uniform material removal could severely reduce the wall thickness at specific interior locations on the conformal channel after AFP for 15 minutes. With an increase of AFP time, certain locations can be worn through after 25 and 50 minutes and conformal channels are destroyed. Thus, AFP of 5 minutes is acceptable for L-PBF 316L stainless steel conformal channels in this section.
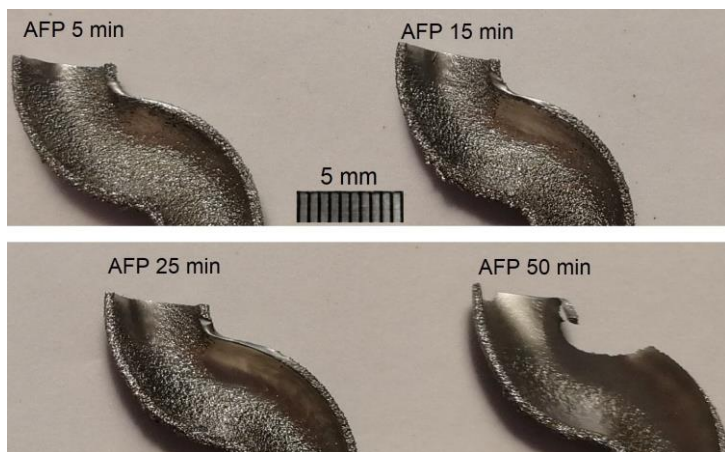
Figure 7.21 Pictures of inner surfaces of half conformal channels prepared by L-PBF 316L stainless steel after different times of AFP.

Figure 7.22 OM image of inner surface of a conformal channel prepared by L-PBF 316L stainless steel after AFP for 5 minutes.

Given that AFP in the current polishing system caused non-uniform polishing result for conformal channels and longer AFP time could destroy thin-walled conformal channels, only AFP and then EP was conducted as the multiple polishing in different sequences for 316L stainless steel conformal channels. Morphology of the internal surface on a conformal channel after multiple polishing is shown in Figure 7.23. It is obvious that most of un-sintered powders are removed. Meanwhile, all areas are effectively polished due to the combined effect of AFP and EP.
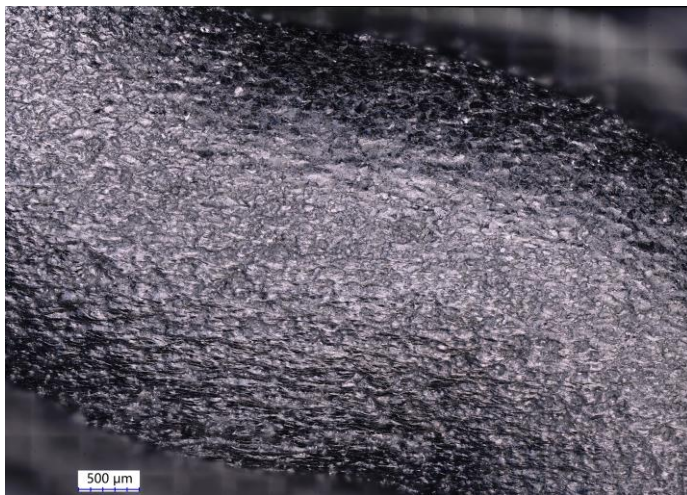
Figure 7.23 Morphology of inner surface of a conformal channel prepared by L-PBF 316L stainless steel after AFP for 5 minutes and then the two-step EP.

7.4.3 Polishing of whole conformal channels

Images of L-PBF 316L stainless steel conformal channels before and after multiple polishing in different sequences consisting of AFP and then EP are shown in Figure 7.24.Given that it is hard to show the polished condition of inner surface by directly observing a whole conformal channel as seen in Figure 7.24a, inner surfaces of half conformal channels before and after the multiple polishing of AFP and then EP are

presented in Figure 7.24b and c. It can be seen that AFP for 5 minutes and then the two-step of EP is capable of polishing the inner surface of L-PBF 316L stainless steel conformal channels. Considering the use of the conformal cathode, multiple polishing in different sequences is more appropriate for L-PBF curve channels. In addition, the optimization of flexible cathodes and simulation analysis of AFP for specific L-PBF inner structures should be further considered for the polishing optimization of L-PBF curve channels. It should be noted that designing or placing flexible cathodes in complex curve channels may be difficult to achieve in EP and hybrid polishing considering the complexity of the internal channels.
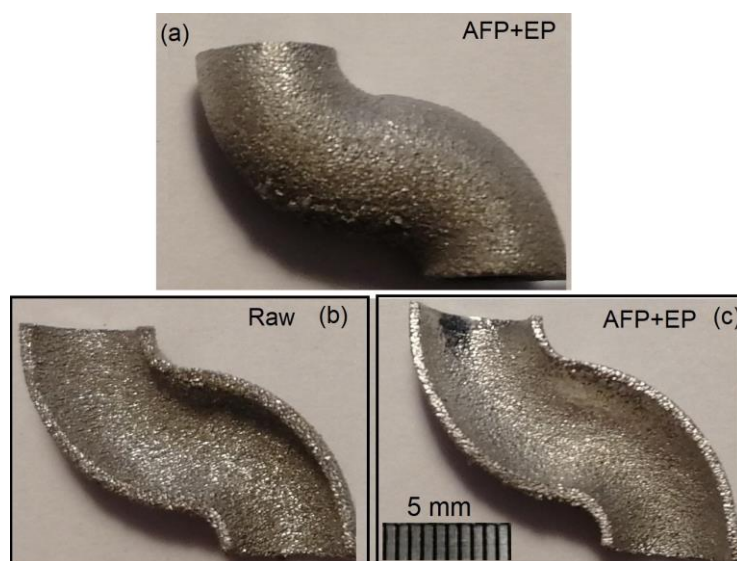
Figure 7.24 Pictures of L-PBF 316L stainless steel (a) conformal channel after multiple polishing in different sequences and (b) raw inner surface of a conformal channel and (c) an inner surface of a half conformal channel after multiple polishing in different sequences consisting of AFP and then EP.

7.5 Summary

This chapter applies different polishing processes to straight channels with small inner diameter, lattice structures and conformal channels prepared by L-PBF for application development. The polishing capability of the developed hybrid polishing system for L-PBF internal structures is demonstrated. The main conclusions can be drawn as follows.

(1) Multiple polishing of EP and AFP in different sequences shows better polishing ability than single polishing process on L-PBF lattice structures, straight and conformal channels.

(2) Hybrid polishing can effectively remove un-sintered powders and smooth sintered area at the same time in the polishing of L-PBF BCC lattice structures and exhibits higher polishing efficiency than single polishing process.

(3) The selection of an appropriate polishing process should consider characteristics of specific L-PBF internal structures, such as the placement of cathode and the structure strength.

Chapter 8. Conclusions and Perspectives

8.1 Conclusions

The objective of this thesis is to develop an efficient polishing process for L-PBF internal structures and establish the relationship between polishing process and surface features of L-PBF various inner surfaces using environmentally friendly polishing media. Based on the characterization of surface features of L-PBF 316L stainless steel and Ti6Al4V, establishment of the innovative hybrid polishing system, fundamental study of EP, AFP, multiple polishing in different sequences and hybrid polishing effects on various L-PBF inner surfaces, this study provides a theoretical basis for the application of the hybrid polishing system in the polishing of various L-PBF internal structures. The main conclusions of the study are summarized as follows:

(1) There exists un-sintered powders and sintered area as common surface features on L-PBF top, face up, side and face down surfaces. One or different types of surfaces may present on L-PBF internal structures based on the variation of printing angles.

(2) The developed hybrid polishing system can successfully perform EP, AFP, multiple polishing in different sequences and hybrid polishing based on EP and AFP to obtain reliable polishing results on L-PBF inner surfaces and internal structures.

(3) The two-step EP using different potentials and polishing times can be more efficiently applied to polish all areas of L-PBF 316L stainless steel and Ti6Al4V inner surfaces with environmentally friendly electrolytes. Although a smooth surface can be obtained by first dissolving un-sintered powders, and then further levelling of sintered area, EP is more suitable to reduce surface roughness to a certain extent considering the uneven sintered area on L-PBF surfaces and high material removal rate of EP.

(4) The gradient design of the polishing media inlet can realize uniform polishing of various L-PBF inner surfaces in the fundamental study of AFP. It is notified that

L-PBF surface features at protruding areas can be removed more effectively than valleys by collision and scratching in AFP.

(5) Multiple polishing of EP and AFP in different sequences breaks the limitations of single polishing process, and is capable of reducing surface roughness of various L-PBF inner surfaces more effectively than single polishing method. Performing EP before AFP is shown to be more efficient in smoothing all areas of L-PBF inner surfaces.

(6) The innovative hybrid polishing combines the advantages of EP and AFP, which can effectively polish all areas of L-PBF inner surfaces because EP and AFP can be performed simultaneously during the hybrid polishing without interfering with each other. Although polishing efficiencies of EP and AFP differ greatly in the developed polishing system, hybrid polishing exhibits higher efficiency than single polishing in a short period of time, which shows its research value and great potential in improving polishing efficiency of internal structures.

(7) By using the developed hybrid polishing system, internal surfaces of L-PBF straight channels, lattice structures and conformal channels can be efficiently polished. Multiple polishing in different sequences and hybrid polishing based on EP and AFP is capable of polishing inner structures, and achieving flexible control of the final surface quality for various L-PBF internal structures.

8.2 Perspectives

Perspectives of this study can be summarized as follows:

(1) Although various polishing processes for L-PBF inner surfaces using the same polishing system have been investigated, there is a further need for the comprehensive performance evaluation of polished surfaces. Considering the importance of surface quality in practical applications, it is recommended to test surface properties such as biocompatibility, corrosion resistance, friction and wear after polishing to provide positive feedback for polishing optimization of components for specific applications.

(2) The surface analysis and various polishing processes developed in this study can be extended to polish surfaces prepared by electron beam powder bed fusion and materials such as L-PBF CoCr alloy. In addition, environmentally friendly polishing media for different materials can be further developed.

(3) The superiority of hybrid polishing based on EP and AFP has been demonstrated in this study. Further investigation of hybrid polishing is necessary by optimizing the polishing system because it is essential to reduce the efficiency gap between EP and AFP. In addition, the optimization of polishing chamber and fixtures can be further considered in order to improve the polishing efficiency for various inner structures.

(4) Given that different polishing processes in this study are based on the material removal process, the impact of polishing on the dimension and shape of component surface needs to be further considered.

(5) To accelerate the industrial application of L-PBF internal structures, the connection between CAD model design, optimization of L-PBF process, polishing process etc. should be strengthened.

(6) Although this study focuses on the polishing of L-PBF inner surfaces and internal structures, further consideration can be given to applying the developed hybrid polishing system to the polishing of internal structures and external surfaces prepared by various fabrication techniques.

References

[1] Han S, Salvatore F, Rech J, Bajolet J. Abrasive flow machining (AFM) finishing of conformal cooling channels created by selective laser melting (SLM). Precision Engineering 2020;64:20-33. https://doi.org/10.1016/j.precisioneng.2020.03.006.

[2] Huo P, Zhao Z, Bai P, Yuan X, Wang Q, Zhao R, Zhang L, Du W, Han B, Wang Y. Deformation evolution and fracture mechanism of porous TC4 alloy scaffolds fabricated using selective laser melting under uniaxial compression. Journal of Alloys and Compounds 2021;861:158529. https://doi.org/10.1016/j.jallcom.2020.158529.

[3] Nakazawa K, Ozawa S, Iwata F. Additive Manufacturing of Metal Micro-ring and Tube by Laser-Assisted Electrophoretic Deposition with Laguerre–Gaussian Beam. Nanomanufacturing and Metrology 2021;4(4):271-7. https://doi.org/10.1007/s41871-020-00087-y.

[4] Fang FZ, Zhang XD, Gao W, Guo YB, Byrne G, Hansen HN. Nanomanufacturing—Perspective and applications. CIRP Annals 2017;66(2):683-705. https://doi.org/10.1016/j.cirp.2017.05.004.

[5] Yan X, Li Q, Yin S, Chen Z, Jenkins R, Chen C, Wang J, Ma W, Bolot R, Lupoi R, Ren Z, Liao H, Liu M. Mechanical and in vitro study of an isotropic Ti6Al4V lattice structure fabricated using selective laser melting. Journal of Alloys and Compounds 2019;782:209-23. https://doi.org/10.1016/j.jallcom.2018.12.220.

[6] Yadroitsev I, Thivillon L, Bertrand P, Smurov I. Strategy of manufacturing components with designed internal structure by selective laser melting of metallic powder. Applied Surface Science 2007;254(4):980-3. https://doi.org/10.1016/j.apsusc.2007.08.046.

[7] Gu DD, Meiners W, Wissenbach K, Poprawe R. Laser additive manufacturing of metallic components: materials, processes and mechanisms. International Materials Reviews 2013;57(3):133-64. https://doi.org/10.1179/1743280411y.0000000014.

[8] Ghorbani J, Li J, Srivastava AK. Application of optimized laser surface re-melting process on selective laser melted 316L stainless steel inclined parts. Journal of Manufacturing Processes 2020;56:726-34. https://doi.org/10.1016/j.jmapro.2020.05.025.

[9] Yadroitsev I, Krakhmalev P, Yadroitsava I. Selective laser melting of Ti6Al4V alloy for biomedical applications: Temperature monitoring and microstructural evolution. Journal of Alloys and Compounds 2014;583:404-9. https://doi.org/10.1016/j.jallcom.2013.08.183.

[10] Zhong T, He K, Li H, Yang L. Mechanical properties of lightweight 316L stainless steel lattice structures fabricated by selective laser melting. Materials & Design 2019;181. https://doi.org/10.1016/j.matdes.2019.108076.

[11] Yan C, Hao L, Hussein A, Young P, Raymont D. Advanced lightweight 316L stainless steel cellular lattice structures fabricated via selective laser melting. Materials & Design 2014;55:533-41. https://doi.org/10.1016/j.matdes.2013.10.027.

[12] Singla AK, Banerjee M, Sharma A, Singh J, Bansal A, Gupta MK, Khanna N, Shahi AS, Goyal DK. Selective laser melting of Ti6Al4V alloy: Process parameters, defects and post-treatments. Journal of Manufacturing Processes 2021;64:161-87. https://doi.org/10.1016/j.jmapro.2021.01.009.

[13] Aufa AN, Hassan MZ, Ismail Z. Recent advances in Ti-6Al-4V additively manufactured by selective laser melting for biomedical implants: Prospect development. Journal of Alloys and Compounds 2022;896:163072. https://doi.org/10.1016/j.jallcom.2021.163072.

[14]   Furumoto T, Ueda T, Amino T, Hosokawa A. A study of internal face finishing of the cooling channel in injection mold with free abrasive grains. Journal of Materials Processing Technology 2011;211(11):1742-8. https://doi.org/10.1016/j.jmatprotec.2011.05.018.

[15]   Chang S, Liu A, Ong CYA, Zhang L, Huang X, Tan YH, Zhao L, Li L, Ding J. Highly effective smoothening of 3D-printed metal structures via overpotential electrochemical polishing. Materials Research Letters 2019;7(7):282-9. https://doi.org/10.1080/21663831.2019.1601645.

[16]   Mohammadian N, Turenne S, Brailovski V. Surface finish control of additively-manufactured Inconel 625 components using combined chemical-abrasive flow polishing. Journal of Materials Processing Technology 2018;252:728-38. https://doi.org/10.1016/j.jmatprotec.2017.10.020.

[17]   Zhao C, Qu N, Tang X. Electrochemical mechanical polishing of internal holes created by selective laser melting. Journal of Manufacturing Processes 2021;64:1544-62. https://doi.org/10.1016/j.jmapro.2021.03.003.

[18]   Nagalingam AP, Yuvaraj HK, Yeo SH. Synergistic effects in hydrodynamic cavitation abrasive finishing for internal surface-finish enhancement of additive-manufactured components. Additive Manufacturing 2020;33:101110. https://doi.org/10.1016/j.addma.2020.101110.

[19]   Baicheng Z, Xiaohua L, Jiaming B, Junfeng G, Pan W, Chen-nan S, Muiling N, Guojun Q, Jun W. Study of selective laser melting (SLM) Inconel 718 part surface improvement by electrochemical polishing. Materials & Design 2017;116:531-7. https://doi.org/10.1016/j.matdes.2016.11.103.

[20]   Liang Y, Chen W, Sun Y, Yu N, Zhang P, Liu H. An expert system for hydro/aero-static spindle design used in ultra precision machine tool. Robotics and Computer-Integrated Manufacturing 2014;30(2):107-13. https://doi.org/10.1016/j.rcim.2013.09.006.

[21]   Zhou H, Bennett A, Castelli M, Jourdain R, Guo J, Yu N. Design of a motorised plasma delivery system for ultra-precision large optical fabrication. International Journal of Extreme Manufacturing 2020;2(4). https://doi.org/10.1088/2631-7990/abab49.

[22]   Vayre B, Vignat F, Villeneuve F. Metallic additive manufacturing: state-of-the-art review and prospects. Mechanics & Industry 2012;13(2):89-96. https://doi.org/10.1051/meca/2012003.

[23]   Boschetto A, Bottini L, Veniali F. Surface roughness and radiusing of Ti6Al4V selective laser melting-manufactured parts conditioned by barrel finishing. The International Journal of Advanced Manufacturing Technology 2017;94(5-8):2773-90. https://doi.org/10.1007/s00170-017-1059-6.

[24]   Strano G, Hao L, Everson RM, Evans KE. Surface roughness analysis, modelling and prediction in selective laser melting. Journal of Materials Processing Technology 2013;213(4):589-97. https://doi.org/10.1016/j.jmatprotec.2012.11.011.

[25]   Cabanettes F, Joubert A, Chardon G, Dumas V, Rech J, Grosjean C, Dimkovski Z. Topography of as built surfaces generated in metal additive manufacturing: A multi scale analysis from form to roughness. Precision Engineering 2018;52:249-65. https://doi.org/10.1016/j.precisioneng.2018.01.002.

[26]   Kasperovich G, Hausmann J. Improvement of fatigue resistance and ductility of TiAl6V4 processed by selective laser melting. Journal of Materials Processing Technology 2015;220:202-14. https://doi.org/10.1016/j.jmatprotec.2015.01.025.

[27]   Qiu C, Panwisawas C, Ward M, Basoalto HC, Brooks JW, Attallah MM. On the role of melt flow into the surface structure and porosity development during selective laser melting. Acta Materialia 2015;96:72-9. https://doi.org/10.1016/j.actamat.2015.06.004.

[28]   Sun Z, Tan X, Tor SB, Yeong WY. Selective laser melting of stainless steel 316L with low porosity and high build rates. Materials & Design 2016;104:197-204. https://doi.org/10.1016/j.matdes.2016.05.035.

[29]   Zhang L-C, Attar H. Selective Laser Melting of Titanium Alloys and Titanium Matrix Composites for Biomedical Applications: A Review Advanced Engineering Materials 2016;18(4):463-75. https://doi.org/10.1002/adem.201500419.

[30]   Yadroitsev I, Gusarov A, Yadroitsava I, Smurov I. Single track formation in selective laser melting of metal powders. Journal of Materials Processing Technology 2010;210(12):1624-31. https://doi.org/10.1016/j.jmatprotec.2010.05.010.

[31]   Rombouts M, Kruth JP, Froyen L, Mercelis P. Fundamentals of Selective Laser Melting of alloyed steel powders. CIRP Annals 2006;55(1):187-92. https://doi.org/10.1016/s0007-8506(07)60395-3.

[32]   Mills KC. Marangoni effects in welding, in Marangoni and interfacial phenomena in materials processing. IOM Communications, London; 1998.

[33]   Shifeng W, Shuai L, Qingsong W, Yan C, Sheng Z, Yusheng S. Effect of molten pool boundaries on the mechanical properties of selective laser melting parts. Journal of Materials Processing Technology 2014;214(11):2660-7. https://doi.org/10.1016/j.jmatprotec.2014.06.002.

[34]   Xu W, Brandt M, Sun S, Elambasseril J, Liu Q, Latham K, Xia K, Qian M. Additive manufacturing of strong and ductile Ti–6Al–4V by selective laser melting via in situ martensite decomposition. Acta Materialia 2015;85:74-84. https://doi.org/10.1016/j.actamat.2014.11.028.

[35]   Qiu C, Adkins NJE, Attallah MM. Microstructure and tensile properties of selectively laser-melted and of HIPed laser-melted Ti–6Al–4V. Materials Science and Engineering: A 2013;578:230-9. https://doi.org/10.1016/j.msea.2013.04.099.

[36]   Li R, Shi Y, Wang Z, Wang L, Liu J, Jiang W. Densification behavior of gas and water atomized 316L stainless steel powder during selective laser melting. Applied Surface Science 2010;256(13):4350-6. https://doi.org/10.1016/j.apsusc.2010.02.030.

[37]   Ma M, Wang Z, Gao M, Zeng X. Layer thickness dependence of performance in high-power selective laser melting of 1Cr18Ni9Ti stainless steel. Journal of Materials Processing Technology 2015;215:142-50. https://doi.org/10.1016/j.jmatprotec.2014.07.034.

[38]   Xin XZ, Chen J, Xiang N, Wei B. Surface properties and corrosion behavior of Co-Cr alloy fabricated with selective laser melting technique. Cell Biochem Biophys 2013;67(3):983-90. https://doi.org/10.1007/s12013-013-9593-9.

[39]   Li Y, Gu D. Parametric analysis of thermal behavior during selective laser melting additive manufacturing of aluminum alloy powder. Materials & Design 2014;63:856-67. https://doi.org/10.1016/j.matdes.2014.07.006.

[40]   Read N, Wang W, Essa K, Attallah MM. Selective laser melting of AlSi10Mg alloy: Process optimisation and mechanical properties development. Materials & Design (1980-2015) 2015;65:417-24. https://doi.org/10.1016/j.matdes.2014.09.044.

[41]   Niu X, Singh S, Garg A, Singh H, Panda B, Peng X, Zhang Q. Review of materials used in laser-aided additive manufacturing processes to produce metallic products. Frontiers of Mechanical Engineering 2018;14(3):282-98. https://doi.org/10.1007/s11465-019-0526-1.

[42]   Harrison NJ, Todd I, Mumtaz K. Reduction of micro-cracking in nickel superalloys processed by Selective Laser Melting: A fundamental alloy design approach. Acta Materialia 2015;94:59-68. https://doi.org/10.1016/j.actamat.2015.04.035.

[43] Carter LN, Martin C, Withers PJ, Attallah MM. The influence of the laser scan strategy on grain structure and cracking behaviour in SLM powder-bed fabricated nickel superalloy. Journal of Alloys and Compounds 2014;615:338-47. https://doi.org/10.1016/j.jallcom.2014.06.172.

[44] Gu D, Dai D, Chen W, Chen H. Selective Laser Melting Additive Manufacturing of Hard-to-Process Tungsten-Based Alloy Parts With Novel Crystalline Growth Morphology and Enhanced Performance. Journal of Manufacturing Science and Engineering 2016;138(8):081003. https://doi.org/10.1115/1.4032192.

[45] Iveković A, Omidvari N, Vrancken B, Lietaert K, Thijs L, Vanmeensel K, Vleugels J, Kruth J-P. Selective laser melting of tungsten and tungsten alloys. International Journal of Refractory Metals and Hard Materials 2018;72:27-32. https://doi.org/10.1016/j.ijrmhm.2017.12.005.

[46] Yves-Christian H, Jan W, Wilhelm M, Konrad W, Reinhart P. Net shaped high performance oxide ceramic parts by selective laser melting. Physics Procedia 2010;5:587-94. https://doi.org/10.1016/j.phpro.2010.08.086.

[47] Attar H, Bönisch M, Calin M, Zhang L-C, Scudino S, Eckert J. Selective laser melting of in situ titanium–titanium boride composites: Processing, microstructure and mechanical properties. Acta Materialia 2014;76:13-22. https://doi.org/10.1016/j.actamat.2014.05.022.

[48] Vrancken B, Thijs L, Kruth JP, Van Humbeeck J. Microstructure and mechanical properties of a novel β titanium metallic composite by selective laser melting. Acta Materialia 2014;68:150-8. https://doi.org/10.1016/j.actamat.2014.01.018.

[49] Chekurov S, Lantela T. Selective Laser Melted Digital Hydraulic Valve System. 3D Printing and Additive Manufacturing 2017;4(4):215-21. https://doi.org/10.1089/3dp.2017.0014.

[50] Romei F, Grubišić AN, Gibbon D. Manufacturing of a high-temperature resistojet heat exchanger by selective laser melting. Acta Astronautica 2017;138:356-68. https://doi.org/10.1016/j.actaastro.2017.05.020.

[51] Ho JY, Leong KC, Wong TN. Experimental and numerical investigation of forced convection heat transfer in porous lattice structures produced by selective laser melting. International Journal of Thermal Sciences 2019;137:276-87. https://doi.org/10.1016/j.ijthermalsci.2018.11.022.

[52] Zhang L, Zhang S, Zhu H. Effect of scanning strategy on geometric accuracy of the circle structure fabricated by selective laser melting. Journal of Manufacturing Processes 2021;64:907-15. https://doi.org/10.1016/j.jmapro.2021.02.015.

[53] Bai Y, Zhao C, Wang D, Wang H. Evolution mechanism of surface morphology and internal hole defect of 18Ni300 maraging steel fabricated by selective laser melting. Journal of Materials Processing Technology 2022;299:117328. https://doi.org/10.1016/j.jmatprotec.2021.117328.

[54] Turalıoğlu K, Taftalı M, Yetim F. Determining the tribological behavior of 316L stainless steel with lubricating micro-channels produced by the selective laser melting (SLM) method. Industrial Lubrication and Tribology 2021;73(5):700-7. https://doi.org/10.1108/ilt-11-2020-0393.

[55] Khan HM, Waqar S, Koç E. Evolution of temperature and residual stress behavior in selective laser melting of 316L stainless steel across a cooling channel. Rapid Prototyping Journal 2022;28(7):1272-83. https://doi.org/10.1108/rpj-09-2021-0237.

[56] Santhoshsarang DM, Divya K, Telasang G, Soundarapandian S, Bathe R, Padmanabham G. Additively Manufactured High-Performance Conformally Cooled H13 Tool Steel Die Insert for Pressure Die Casting. Transactions of the Indian National Academy of Engineering 2021;6(4):1037-48. https://doi.org/10.1007/s41403-021-00233-y.

[57] Nagalingam AP, Santhanam V, Dachepally NKG, Yeo SH. Multiphase hydrodynamic flow characterization for surface finishing the laser powder bed fused AlSi10Mg conformal cooling channels. Journal of Manufacturing Processes 2021;68:277-92. https://doi.org/10.1016/j.jmapro.2021.05.040.

[58] Pakkanen J, Calignano F, Trevisan F, Lorusso M, Ambrosio EP, Manfredi D, Fino P. Study of Internal Channel Surface Roughnesses Manufactured by Selective Laser Melting in Aluminum and Titanium Alloys. Metallurgical and Materials Transactions A 2016;47(8):3837-44. https://doi.org/10.1007/s11661-016-3478-7.

[59] Qu H, Li J, Zhang F, Bai J. Anisotropic cellular structure and texture microstructure of 316L stainless steel fabricated by selective laser melting via rotation scanning strategy. Materials & Design 2022;215:110454. https://doi.org/10.1016/j.matdes.2022.110454.

[60] Maskery I, Aboulkhair NT, Aremu AO, Tuck CJ, Ashcroft IA, Wildman RD, Hague RJM. A mechanical property evaluation of graded density Al-Si10-Mg lattice structures manufactured by selective laser melting. Materials Science and Engineering: A 2016;670:264-74. https://doi.org/10.1016/j.msea.2016.06.013.

[61] Dhiman S, Sidhu SS, Bains PS, Bahraminasab M. Mechanobiological assessment of Ti-6Al-4V fabricated via selective laser melting technique: a review. Rapid Prototyping Journal 2019;25(7):1266-84. https://doi.org/10.1108/rpj-03-2019-0057.

[62] Mahmoud D, Al-Rubaie KS, Elbestawi MA. The influence of selective laser melting defects on the fatigue properties of Ti6Al4V porosity graded gyroids for bone implants. International Journal of Mechanical Sciences 2021;193:106180. https://doi.org/10.1016/j.ijmecsci.2020.106180.

[63] Pei X, Wu L, Lei H, Zhou C, Fan H, Li Z, Zhang B, Sun H, Gui X, Jiang Q, Fan Y, Zhang X. Fabrication of customized Ti6Al4V heterogeneous scaffolds with selective laser melting: Optimization of the architecture for orthopedic implant applications. Acta Biomater 2021;126:485-95. https://doi.org/10.1016/j.actbio.2021.03.040.

[64] Zhang P, Z.Zhang D, Zhong B. Constitutive and damage modelling of selective laser melted Ti-6Al-4V lattice structure subjected to low cycle fatigue. International Journal of Fatigue 2022;159:106800. https://doi.org/10.1016/j.ijfatigue.2022.106800.

[65] Maconachie T, Leary M, Lozanovski B, Zhang X, Qian M, Faruque O, Brandt M. SLM lattice structures: Properties, performance, applications and challenges. Materials & Design 2019;183:108137. https://doi.org/10.1016/j.matdes.2019.108137.

[66] Echeta I, Feng X, Dutton B, Leach R, Piano S. Review of defects in lattice structures manufactured by powder bed fusion. The International Journal of Advanced Manufacturing Technology 2019;106(5-6):2649-68. https://doi.org/10.1007/s00170-019-04753-4.

[67] Solyaev Y, Rabinskiy L, Tokmakov D. Overmelting and closing of thin horizontal channels in AlSi10Mg samples obtained by selective laser melting. Additive Manufacturing 2019;30:100847. https://doi.org/10.1016/j.addma.2019.100847.

[68] Seharing A, Azman AH, Abdullah S. A review on integration of lightweight gradient lattice structures in additive manufacturing parts. Advances in Mechanical Engineering 2020;12(6):1-21. https://doi.org/10.1177/1687814020916951.

[69] Zhu Y, Zhou L, Wang S, Zhang C, Zhao C, Zhang L, Yang H. On friction factor of fluid channels fabricated using selective laser melting. Virtual and Physical Prototyping 2020;15(4):496-509. https://doi.org/10.1080/17452759.2020.1823093.

[70] Xiong YZ, Gao RN, Zhang H, Dong LL, Li JT, Li X. Rationally designed functionally graded porous Ti6Al4V scaffolds with high strength and toughness built via selective laser melting for

load-bearing orthopedic applications. Journal of the Mechanical Behavior of Biomedical Materials 2020;104:103673. https://doi.org/10.1016/j.jmbbm.2020.103673.

[71] Wally ZJ, Haque AM, Feteira A, Claeyssens F, Goodall R, Reilly GC. Selective laser melting processed Ti6Al4V lattices with graded porosities for dental applications. Journal of the Mechanical Behavior of Biomedical Materials 2019;90:20-9. https://doi.org/10.1016/j.jmbbm.2018.08.047.

[72] Seltzman AH, Wukitch SJ. Nuclear response of additive manufactured GRCop-84 copper for use in Lower hybrid launchers in a fusion environment. Fusion Engineering and Design 2020;159:111726. https://doi.org/10.1016/j.fusengdes.2020.111726.

[73] Liu S, Shin YC. Additive manufacturing of Ti6Al4V alloy: A review. Materials & Design 2019;164:107552. https://doi.org/10.1016/j.matdes.2018.107552.

[74] Jafari D, Wits WW. The utilization of selective laser melting technology on heat transfer devices for thermal energy conversion applications: A review. Renewable and Sustainable Energy Reviews 2018;91:420-42. https://doi.org/10.1016/j.rser.2018.03.109.

[75] Yang J, Wu W, Wang C, Liu C, Wang S, Yang D, Zhou Z, Xu H. Development status and typical application of selective laser melting technology applications in aerospace field. Journal of Aeronautical Materials 2021;41:1-15. https://doi.org/10.11868/j.issn.1005-5053.2020.000158.

[76] Langi E, Zhao LG, Jamshidi P, Attallah MM, Silberschmidt VV, Willcock H, Vogt F. Microstructural and Mechanical Characterization of Thin-Walled Tube Manufactured with Selective Laser Melting for Stent Application. Journal of Materials Engineering and Performance 2021;30(1):696-710. https://doi.org/10.1007/s11665-020-05366-9.

[77] Hassanin H, Finet L, Cox SC, Jamshidi P, Grover LM, Shepherd DET, Addison O, Attallah MM. Tailoring selective laser melting process for titanium drug-delivering implants with releasing micro-channels. Additive Manufacturing 2018;20:144-55. https://doi.org/10.1016/j.addma.2018.01.005.

[78] Cooper DE, Stanford M, Kibble KA, Gibbons GJ. Additive Manufacturing for product improvement at Red Bull Technology. Materials & Design 2012;41:226-30. https://doi.org/10.1016/j.matdes.2012.05.017.

[79] Mazur M, Brincat P, Leary M, Brandt M. Numerical and experimental evaluation of a conformally cooled H13 steel injection mould manufactured with selective laser melting. The International Journal of Advanced Manufacturing Technology 2017;93(1-4):881-900. https://doi.org/10.1007/s00170-017-0426-7.

[80] Yan C, Hao L, Hussein A, Young P. Ti-6Al-4V triply periodic minimal surface structures for bone implants fabricated via selective laser melting. Journal of the Mechanical behavior of Biomedical Materials 2015;51:61-73. https://doi.org/10.1016/j.jmbbm.2015.06.024.

[81] Xiao Z, Yang Y, Xiao R, Bai Y, Song C, Wang D. Evaluation of topology-optimized lattice structures manufactured via selective laser melting. Materials & Design 2018;143:27-37. https://doi.org/10.1016/j.matdes.2018.01.023.

[82] Kirchheim A, Katrodiya Y, Zumofen L, Ehrig F, Wick C. Dynamic conformal cooling improves injection molding. The International Journal of Advanced Manufacturing Technology 2021;114(1-2):107-16. https://doi.org/10.1007/s00170-021-06794-0.

[83] Yadroitsev I, Krakhmalev P, Yadroitsava I. Hierarchical design principles of selective laser melting for high quality metallic objects. Additive Manufacturing 2015;7:45-56. https://doi.org/10.1016/j.addma.2014.12.007.

[84]   Tromme E, Kawamoto A, Guest JK. Topology optimization based on reduction methods with applications to multiscale design and additive manufacturing. Frontiers of Mechanical Engineering 2019;15(1):151-65. https://doi.org/10.1007/s11465-019-0564-8.

[85]   Kimura F, Kadoya S, Kajihara Y. Active Air Venting of Mold Cavity to Improve Performance of Injection Molded Direct Joining. Nanomanufacturing and Metrology 2021;4(2):109-17. https://doi.org/10.1007/s41871-021-00097-4.

[86]   Fang FZ, Gu C, Hao R, You K, Huang S. Recent Progress in Surface Integrity Research and Development. Engineering 2018;4(6):754-8. https://doi.org/10.1016/j.eng.2018.11.005.

[87]   Stempin J, Tausendfreund A, Stöbener D, Fischer A. Roughness Measurements with Polychromatic Speckles on Tilted Surfaces. Nanomanufacturing and Metrology 2021;4(4):237-46. https://doi.org/10.1007/s41871-020-00093-0.

[88]   Urlea V, Brailovski V. Electropolishing and electropolishing-related allowances for powder bed selectively laser-melted Ti-6Al-4V alloy components. Journal of Materials Processing Technology 2017;242:1-11. https://doi.org/10.1016/j.jmatprotec.2016.11.014.

[89]   Kruth JP, Froyen L, Van Vaerenbergh J, Mercelis P, Rombouts M, Lauwers B. Selective laser melting of iron-based powder. Journal of Materials Processing Technology 2004;149(1-3):616-22. https://doi.org/10.1016/j.jmatprotec.2003.11.051.

[90]   Gu D, Shen Y. Balling phenomena during direct laser sintering of multi-component Cu-based metal powder. Journal of Alloys and Compounds 2007;432(1-2):163-6. https://doi.org/10.1016/j.jallcom.2006.06.011.

[91]   Li R, Liu J, Shi Y, Wang L, Jiang W. Balling behavior of stainless steel and nickel powder during selective laser melting process. The International Journal of Advanced Manufacturing Technology 2011;59(9-12):1025-35. https://doi.org/10.1007/s00170-011-3566-1.

[92]   Swee L, Sing., Wai Y, Yeong., Florencia E, Wiria., bee Y, Tay., Ziqiang Z, Lin Z, Zhiling T, Shoufeng Y. Direct selective laser sintering and melting of ceramics: a review. Rapid Prototyping Journal 2017;23(3):611-23. https://doi.org/10.1108/RPJ-11-2015-0178

[93]   Bai Y, Zhao C, Yang J, Fuh JYH, Lu WF, Weng C, Wang H. Dry mechanical-electrochemical polishing of selective laser melted 316L stainless steel. Materials & Design 2020;193:108840. https://doi.org/10.1016/j.matdes.2020.108840.

[94]   Nasab MH, Gastaldi D, Lecis NF, Vedani M. On morphological surface features of the parts printed by selective laser melting (SLM). Additive Manufacturing 2018;24:373-7. https://doi.org/10.1016/j.addma.2018.10.011.

[95]   Tian Y, Tomus D, Rometsch P, Wu X. Influences of processing parameters on surface roughness of Hastelloy X produced by selective laser melting. Additive Manufacturing 2017;13:103-12. https://doi.org/10.1016/j.addma.2016.10.010.

[96]   Laleh M, Hughes AE, Yang S, Li J, Xu W, Gibson I, Tan MY. Two and three-dimensional characterisation of localised corrosion affected by lack-of-fusion pores in 316L stainless steel produced by selective laser melting. Corrosion Science 2020;165:108394. https://doi.org/10.1016/j.corsci.2019.108394.

[97]   Bi J, Wu L, Liu Z, Wang H, Jia X, Chen X, Starostenkov MD, Dong G. Formability, surface quality and compressive fracture behavior of AlMgScZr alloy lattice structure fabricated by selective laser melting. Journal of Materials Research and Technology 2022;19:391-403. https://doi.org/10.1016/j.jmrt.2022.05.051.

[98]   Bennett A, Yu N, Castelli M, Chen G, Balleri A, Urayama T, Fang F. Characterisation of a microwave induced plasma torch for glass surface modification. Frontiers of Mechanical Engineering 2020;16(1):122-32. https://doi.org/10.1007/s11465-020-0603-5.

[99]   Kumbhar NN, Mulay AV. Post Processing Methods used to Improve Surface Finish of Products which are Manufactured by Additive Manufacturing Technologies: A Review. Journal of The Institution of Engineers (India): Series C 2016;99(4):481-7. https://doi.org/10.1007/s40032-016-0340-z.

[100]   Utela BR, Storti D, Anderson RL, Ganter M. Development Process for Custom Three-Dimensional Printing (3DP) Material Systems. Journal of Manufacturing Science and Engineering 2010;132(1):011008. https://doi.org/10.1115/1.4000713.

[101]   Butscher A, Bohner M, Roth C, Ernstberger A, Heuberger R, Doebelin N, von Rohr PR, Muller R. Printability of calcium phosphate powders for three-dimensional printing of tissue engineering scaffolds. Acta Biomater 2012;8(1):373-85. https://doi.org/10.1016/j.actbio.2011.08.027.

[102]   Ahn D, Kweon J-H, Kwon S, Song J, Lee S. Representation of surface roughness in fused deposition modeling. Journal of Materials Processing Technology 2009;209(15-16):5593-600. https://doi.org/10.1016/j.jmatprotec.2009.05.016.

[103]   Boschetto A, Bottini L, Veniali F. Integration of FDM surface quality modeling with process design. Additive Manufacturing 2016;12:334-44. https://doi.org/10.1016/j.addma.2016.05.008.

[104]   Mohamed OA, Masood SH, Bhowmik JL. Optimization of fused deposition modeling process parameters for dimensional accuracy using I-optimality criterion. Measurement 2016;81:174-96. https://doi.org/10.1016/j.measurement.2015.12.011.

[105]   Reddy V, Flys O, Chaparala A, Berrimi CE, V A, Rosen BG. Study on surface texture of Fused Deposition Modeling. Procedia Manufacturing 2018;25:389-96. https://doi.org/10.1016/j.promfg.2018.06.108.

[106]   Tronvoll SA, Elverum CW, Welo T. Dimensional accuracy of threads manufactured by fused deposition modeling. Procedia Manufacturing 2018;26:763-73. https://doi.org/10.1016/j.promfg.2018.07.088.

[107]   Evren. Yasa, Jan. Deckers, Kruth. J-P. The investigation of the influence of laser re-melting on density, surface quality and microstructure of selective laser melting parts. Rapid Prototyping Journal 2011;17(5):312-27. https://doi.org/10.1108/13552541111156450

[108]   Newman ST, Zhu Z, Dhokia V, Shokrani A. Process planning for additive and subtractive manufacturing technologies. CIRP Annals 2015;64(1):467-70. https://doi.org/10.1016/j.cirp.2015.04.109.

[109]   Zhu Z, Dhokia V, Nassehi A, Newman ST. Investigation of part distortions as a result of hybrid manufacturing. Robotics and Computer-Integrated Manufacturing 2016;37:23-32. https://doi.org/10.1016/j.rcim.2015.06.001.

[110]   Junghoon H, Kunwoo L, Zhu-hu., Jongwon K. Hybrid rapid prototyping system using machining and deposition. Computer-Aided Design 2002;34:741-54.

[111]   Maleki E, Bagherifard S, Bandini M, Guagliano M. Surface post-treatments for metal additive manufacturing: Progress, challenges, and opportunities. Additive Manufacturing 2021;37:101619. https://doi.org/10.1016/j.addma.2020.101619

[112]   Günther J, Leuders S, Koppa P, Tröster T, Henkel S, Biermann H, Niendorf T. On the effect of internal channels and surface roughness on the high-cycle fatigue performance of Ti-6Al-4V processed by SLM. Materials & Design 2018;143:1-11. https://doi.org/10.1016/j.matdes.2018.01.042.

[113] Leuders S, Meiners S, Wu L, Taube A, Tröster T, Niendorf T. Structural components manufactured by Selective Laser Melting and Investment Casting—Impact of the process route on the damage mechanism under cyclic loading. Journal of Materials Processing Technology 2017;248:130-42. https://doi.org/10.1016/j.jmatprotec.2017.04.026.

[114] Kumar SS, Hiremath SS. A Review on Abrasive Flow Machining (AFM). Procedia Technology 2016;25:1297-304. https://doi.org/10.1016/j.protcy.2016.08.224.

[115] Han S, Salvatore F, Rech J, Bajolet J, Courbon J. Effect of abrasive flow machining (AFM) finish of selective laser melting (SLM) internal channels on fatigue performance. Journal of Manufacturing Processes 2020;59:248-57. https://doi.org/10.1016/j.jmapro.2020.09.065.

[116] Ferchow J, Baumgartner H, Klahn C, Meboldt M. Model of surface roughness and material removal using abrasive flow machining of selective laser melted channels. Rapid Prototyping Journal 2020;26(7):1165-76. https://doi.org/10.1108/rpj-09-2019-0241.

[117] Guo J, Au KH, Sun C-N, Goh MH, Kum CW, Liu K, Wei J, Suzuki H, Kang R. Novel rotating-vibrating magnetic abrasive polishing method for double-layered internal surface finishing. Journal of Materials Processing Technology 2019;264:422-37. https://doi.org/10.1016/j.jmatprotec.2018.09.024.

[118] Tan KL, Yeo S-H, Ong CH. Nontraditional finishing processes for internal surfaces and passages: A review. Proceedings of the Institution of Mechanical Engineers, Part B: Journal of Engineering Manufacture 2016;231(13):2302-16. https://doi.org/10.1177/0954405415626087.

[119] Dixit N, Sharma V, Kumar P. Research trends in abrasive flow machining: A systematic review. Journal of Manufacturing Processes 2021;64:1434-61. https://doi.org/10.1016/j.jmapro.2021.03.009.

[120] Ji S, Cao H, Zhao J, Pan Y, Jiang E. Soft abrasive flow polishing based on the cavitation effect. The International Journal of Advanced Manufacturing Technology 2018;101(5-8):1865-78. https://doi.org/10.1007/s00170-018-2983-9.

[121] Furumoto T, Ueda T, Amino T, Kusunoki D, Hosokawa A, Tanaka R. Finishing performance of cooling channel with face protuberance inside the molding die. Journal of Materials Processing Technology 2012;212(10):2154-60. https://doi.org/10.1016/j.jmatprotec.2012.05.016.

[122] Boschetto A, Bottini L, Macera L, Veniali F. Post-Processing of Complex SLM Parts by Barrel Finishing. Applied Sciences 2020;10(4):1382. https://doi.org/10.3390/app10041382.

[123] Khorasani M, Gibson I, Ghasemi A, Brandt M, Leary M. On the role of wet abrasive centrifugal barrel finishing on surface enhancement and material removal rate of LPBF stainless steel 316L. Journal of Manufacturing Processes 2020;59:523-34. https://doi.org/10.1016/j.jmapro.2020.09.058.

[124] Łyczkowska E, Szymczyk P, Dybała B, Chlebus E. Chemical polishing of scaffolds made of Ti–6Al–7Nb alloy by additive manufacturing. Archives of Civil and Mechanical Engineering 2014;14(4):586-94. https://doi.org/10.1016/j.acme.2014.03.001.

[125] Zhang Y, Li J, Che S, Yang Z, Tian Y. Chemical leveling mechanism and oxide film properties of additively manufactured Ti–6Al–4V alloy. Journal of Materials Science 2019;54(21):13753-66. https://doi.org/10.1007/s10853-019-03855-4.

[126] Pyka G, Burakowski A, Kerckhofs G, Moesen M, Van Bael S, Schrooten J, Wevers M. Surface Modification of Ti6Al4V Open Porous Structures Produced by Additive Manufacturing. Advanced Engineering Materials 2012;14(6):363-70. https://doi.org/10.1002/adem.201100344.

[127] Han W, Fang FZ. Orientation effect of electropolishing characteristics of 316L stainless steel fabricated by laser powder bed fusion. Frontiers of Mechanical Engineering 2021;16(3):580-92. https://doi.org/10.1007/s11465-021-0633-7.

[128] Han W, Fang FZ. Fundamental aspects and recent developments in electropolishing. International Journal of Machine Tools and Manufacture 2019;139:1-23. https://doi.org/10.1016/j.ijmachtools.2019.01.001.

[129] He B, Tian X-J, Cheng X, Li J, Wang H-M. Effect of weld repair on microstructure and mechanical properties of laser additive manufactured Ti-55511 alloy. Materials & Design 2017;119:437-45. https://doi.org/10.1016/j.matdes.2017.01.054.

[130] Dong G, Marleau-Finley J, Zhao YF. Investigation of electrochemical post-processing procedure for Ti-6Al-4V lattice structure manufactured by direct metal laser sintering (DMLS). The International Journal of Advanced Manufacturing Technology 2019;104:3401-17. https://doi.org/10.1007/s00170-019-03996-5.

[131] Demir AG, Previtali B. Additive manufacturing of cardiovascular CoCr stents by selective laser melting. Materials & Design 2017;119:338-50. https://doi.org/10.1016/j.matdes.2017.01.091.

[132] Mingear J, Zhang B, Hartl D, Elwany A. Effect of process parameters and electropolishing on the surface roughness of interior channels in additively manufactured nickel-titanium shape memory alloy actuators. Additive Manufacturing 2019;27:565-75. https://doi.org/10.1016/j.addma.2019.03.027.

[133] Sun Y, Bailey R, Moroz A. Surface finish and properties enhancement of selective laser melted 316L stainless steel by surface mechanical attrition treatment. Surface and Coatings Technology 2019;378:124993. https://doi.org/10.1016/j.surfcoat.2019.124993.

[134] Tyagi P, Goulet T, Riso C, Stephenson R, Chuenprateep N, Schlitzer J, Benton C, Garcia-Moreno F. Reducing the roughness of internal surface of an additive manufacturing produced 316 steel component by chempolishing and electropolishing. Additive Manufacturing 2019;25:32-8. https://doi.org/10.1016/j.addma.2018.11.001.

[135] Nagalingam AP, Yuvaraj HK, Santhanam V, Yeo SH. Multiphase hydrodynamic flow finishing for surface integrity enhancement of additive manufactured internal channels. Journal of Materials Processing Technology 2020;283:116692. https://doi.org/10.1016/j.jmatprotec.2020.116692.

[136] Nagalingam AP, Yeo SH. Controlled hydrodynamic cavitation erosion with abrasive particles for internal surface modification of additive manufactured components. Wear 2018;414-415:89-100. https://doi.org/10.1016/j.wear.2018.08.006.

[137] Gunasekaran J, Sevvel P, John Solomon I. Metallic materials fabrication by selective laser melting: A review. Materials Today: Proceedings 2021;37:252-6. https://doi.org/10.1016/j.matpr.2020.05.162.

[138] Sun S, Brandt M, Easton M. Powder bed fusion processes. In: Laser Additive Manufacturing; 2017, p. 55-77.

[139] Yasa E. Selective laser melting. In: Additive Manufacturing; 2021, p. 77-120.

[140] Casati R, Lemke J, Vedani M. Microstructure and Fracture Behavior of 316L Austenitic Stainless Steel Produced by Selective Laser Melting. Journal of Materials Science & Technology 2016;32(8):738-44. https://doi.org/10.1016/j.jmst.2016.06.016.

[141] Shen M, Kang C, Fang FZ. Material removal characteristics of various surface features on selective laser melted 316L stainless steel during electropolishing. Journal of Manufacturing Processes 2022;79:639-53. https://doi.org/10.1016/j.jmapro.2022.04.072.

[142]   Yang J, Yu H, Yin J, Gao M, Wang Z, Zeng X. Formation and control of martensite in Ti-6Al-4V alloy produced by selective laser melting. Materials & Design 2016;108:308-18. https://doi.org/10.1016/j.matdes.2016.06.117.

[143]   Han W, Fang FZ. Fundamental aspects and recent developments in electropolishing. International Journal of Machine Tools and Manufacture 2019;139:1-23. https://doi.org/10.1016/j.ijmachtools.2019.01.001.

[144]   Han W, Fang FZ. Eco-friendly NaCl-based electrolyte for electropolishing 316L stainless steel. Journal of Manufacturing Processes 2020;58:1257-69. https://doi.org/10.1016/j.jmapro.2020.09.036.

[145]   Han W, Fang FZ. Two-step electropolishing of 316L stainless steel in a sulfuric acid-free electrolyte. Journal of Materials Processing Technology 2020;279:116558. https://doi.org/10.1016/j.jmatprotec.2019.116558.

[146]   Bagehorn S, Wehr J, Maier HJ. Application of mechanical surface finishing processes for roughness reduction and fatigue improvement of additively manufactured Ti-6Al-4V parts. International Journal of Fatigue 2017;102:135-42. https://doi.org/10.1016/j.ijfatigue.2017.05.008.

[147]   Matlosz M, Magaino S, Landolt D. Impedance Analysis of a Model Mechanism for Acceptor-Limited Electropolishing. Journal of the Electrochemical Society 1994;141(2):410-8. https://doi.org/https://doi.org/10.1149/1.2054741.

[148]   Matlosz M. Modeling of impedance mechanisms in electropolishing. Electrochimica Acta 1995;40:393-401. https://doi.org/https://doi.org/10.1016/0013-4686(94)00287-B.

[149]   Zhang Y, Li J, Che S, Tian Y. Electrochemical Polishing of Additively Manufactured Ti–6Al–4V Alloy. Metals and Materials International 2019. https://doi.org/10.1007/s12540-019-00556-0.

[150]   Deguchi T, K. C. Development of electropolishing method of tatinum materials - electropolishing of tatinum by safety electrolyte composed of ethylene glycol. Proc 2005 Annu Meet Japan Soc Precis Eng 2005:539-40.

[151]   Zhang T, Wang Z, Yu T, Chen H, Dong J, Zhao J, Wang W. Modeling and prediction of generated local surface profile for ultrasonic vibration-assisted polishing of optical glass BK7. Journal of Materials Processing Technology 2021;289. https://doi.org/10.1016/j.jmatprotec.2020.116933.

[152]   Ji S, Xiao F, Tan D. Analytical method for softness abrasive flow field based on discrete phase model. Science China Technological Sciences 2010;53(10):2867-77. https://doi.org/10.1007/s11431-010-4046-9.

[153]   Chen F, Hao S, Miao X, Yin S, Huang S. Numerical and experimental study on low-pressure abrasive flow polishing of rectangular microgroove. Powder Technology 2018;327:215-22. https://doi.org/10.1016/j.powtec.2017.12.062.

[154]   Zhao J, Huang J, Wang R, Peng H, Hang W, Ji S. Investigation of the optimal parameters for the surface finish of K9 optical glass using a soft abrasive rotary flow polishing process. Journal of Manufacturing Processes 2020;49:26-34. https://doi.org/10.1016/j.jmapro.2019.11.011.

Appendix A. Authors' s List of Patent and Publications

Patent:

Title of the developed polishing system: Hybrid polishing; UK patent application number: 2107777.1

Inventors: Fengzhou Fang, Mingyue Shen

Publications in peer-reviewed journals:

1. Shen MY, Kang CW, Fang FZ. Material removal characteristics of various surface features on selective laser melted 316L stainless steel during electropolishing. Journal of Manufacturing Processes 2022. https://doi.org/10.1016/j.jmapro.2022.04.072 (**Impact factor 5.684**)

2. Shen MY, Fang FZ. Advances in polishing of internal structures on parts made by laser-based powder bed fusion. Frontiers of Mechanical Engineering 2023. https://doi.org/10.1007/s11465-022-0724-0 (**Impact factor 4.063)**

3. Shen MY, Fang FZ. Two-step electropolishing of internal surfaces of 316L stainless steel made by laser-based powder bed fusion. Journal of Manufacturing Processes 2023. https://doi.org/10.1016/j.jmapro.2023.01.052 (**Impact factor 5.684)**

4. Shen MY, Fang FZ. Polishing of internal surfaces of 316L stainless steel made by laser-based powder bed fusion. (To be submitted)

5. Shen MY, Fang FZ. Polishing of internal surfaces of Ti6Al4V made by laser-based powder bed fusion. (To be submitted)